A Study on the Effect of Thin Object Shading on the Performance of Photovoltaic Modules

Matthew Axisa

Supervised by Prof. Luciano Mule'Stagno
and Dr. Ing. Marija Demicoli

Institute for Sustainable Energy
University of Malta

May, 2025

A Thesis submitted in fulfilment of the requirements for the degree of Doctor of Philosophy (Ph.D.)

L-Università ta' Malta

University of Malta Library – Electronic Thesis & Dissertations (ETD) Repository

The copyright of this thesis/dissertation belongs to the author. The author's rights in respect of this work are as defined by the Copyright Act (Chapter 415) of the Laws of Malta or as modified by any successive legislation.

Users may access this full-text thesis/dissertation and can make use of the information contained in accordance with the Copyright Act provided that the author must be properly acknowledged. Further distribution or reproduction in any format is prohibited without the prior permission of the copyright holder.

Declaration of Authenticity for Doctoral Students

(a) Authenticity of Dissertation

I hereby declare that I am the legitimate author of this Thesis and that it is my original work.

No portion of this work has been submitted in support of an application for another degree or qualification of this or any other university or institution of higher education.

I hold the University of Malta harmless against any third-party claims with regard to copyright violation, breach of confidentiality, defamation and any other third party right infringement.

(b) Research Code of Practice and Ethics Review Procedures

I declare that I have abided by the University's Research Ethics Review Procedures. Furthermore, the UM Research Ethics and Data Protection (REDP) application ID **ENG-2024-00038** covers any research ethics approvals required for this thesis.

□ As a Ph.D. student, as per Regulation 66 of the Doctor of Philosophy Regulations, I accept that my thesis be made publicly available on the University of Malta Institutional Repository.

_____

Matthew Axisa

To all my beloved family especially my father Tonio, my mother Elaine, my girlfriend Amberlynn and my late grandfather Michael Bonnici, whose life and legacy remain a guiding light.

Thank you for your endless support.

Acknowledgements

I am sincerely grateful to my supervisor and Director of the Institute for Sustainable Energy (ISE), Prof. Luciano Mule' Stagno, for his academic, practical and technical guidance throughout this journey. I would also like to express my gratitude to my co-supervisor, Dr. Ing. Marija Demicoli, for her invaluable insights and continuous support throughout the course of this study. Her guidance and contributions were instrumental in providing the necessary resources and direction for this thesis.

I would like to express my heartfelt appreciation to the Ministry for Education, Sport, Youth (MEYR), Research and Innovation for awarding me the Tertiary Education Scholarship Scheme (TESS), which covered my Ph.D. tuition fees. My sincere thanks also goes to the Doctoral School for its continued support through a variety of engaging and insightful workshops offered as part of the Professional Development Programme. In addition, I am truly grateful for the opportunity to attend and present at the 41st edition of EU PVSEC, the largest European conference dedicated to photovoltaics (PVs), made possible through the Research Innovation and Development Trust (RIDT) Doctoral Overseas Conferences Grant.

I am also grateful to the ISE's staff namely Mr. Aaron Grech for his administrative guidance, Mr. Terence Cilia, Mr. Paul Bonnici and Mr. Davide La Fata for their technical support. I would like to give a special acknowledgement to Prof. Ing. Charles Yousif for providing weather data, which was essential for various parts of the research. I would like to express my gratitude to Mr. Karl Azzopardi and Mr. Jesmond Farrugia for kindly providing the full-scale PV module used in the validation section of the thesis.

I am also deeply thankful to my family for their unwavering support. In particular, I am especially grateful to my father, Tonio Axisa, for his constant encouragement throughout this journey, and to my beloved mother, Elaine Axisa Bonnici, whose inspiration guided me every step of the way. Last but not least, I would like to thank my girlfriend, Amberlynn Bonello, who provided me with immense support, unwavering patience, and constant encouragement throughout this journey. Her belief in me, even during the most challenging moments, has been a source of strength and motivation that I will always cherish.

Abstract

This study investigates a specific and underexplored aspect of partial shading of photovoltaic (PV) systems that is caused by thin horizontal objects. Following a review of both fundamental principles and current state-of-the-art, the primary aims were to examine differences in shadow formation and associated power loss between laboratory and outdoor environments, quantify shadow formation characteristics, and to assess the scientific validity of commonly used simplifications in representing penumbra shadows.

This study presents a comparative analysis of thin object shadows under laboratory environment conditions using a solar simulator, and under outdoor environmental conditions. Using a 156.0 × 156.0 mm solar cell, 56 thin object shading cases were compared using thin objects of thicknesses of ⌀2.0 mm - ⌀20.0 mm at distances between 10 cm – 40 cm in 5 cm increments. The solar cell placed in outdoor conditions produced higher power losses in the range of 0.34 W - 0.67 W, equivalent to 8.18% to 16.13% power loss respectively, when converted to standard test conditions (STC). This observation was validated by producing a quantitative factor which incorporated both the size and intensity of the overall shadow at equal weight where clearly the outdoor environment produced stronger shadow formation. Moreover, the image capture of all 56 cases found evidence of the laboratory environment producing fringed shadow patterns caused by Fresnel diffraction on the thin objects, most evidently in the shadows of the smallest thin object (⌀2 mm).

This thesis also implemented a novel methodology to quantify the shadow formation and the power loss of 104 thin object shading cases, using custom made image analysis tool named ThinShadePV. This tool utilises image analysis and Random Forest machine learning to determine the size and intensity of umbra and penumbra shadow regions from captured shadow images and predict the associated power losses. Validation through 15 real-world thin shadow cases demonstrated strong agreement between predicted and actual power loss values, with a mean deviation of just 0.48% and an accuracy range of –3.68% to +2.71%. Moreover, Spearman correlation and sensitivity analyses revealed that penumbra intensity is the most influential factor for smaller

objects (⌀2.8–⌀8.0 mm thick), while the size of the umbra shadow dominates in larger objects (⌀10–⌀16.0 mm) thick.

The study also assessed the validity of approximating varying-intensity penumbra shadows with constant-intensity penumbra representations using neutral density (ND) filters. While constant-intensity shadows closely replicated the relationship profile, they consistently overestimated power loss, despite matching the size and average varying intensity shadows. A large effect size (Cohen's d = –0.893) confirmed a significant discrepancy, indicating that varying-intensity penumbra shadows should not be simplified to constant-intensity models in analytical or simulation contexts.

One of the key contributions of this study lies in its significant advancement of current knowledge by empirically quantifying the effects of horizontal thin object shading on PV performance and establishing key relationships between shading parameters and power loss. The development of ThinShadePV, a purpose-built image analysis tool, enables quantitative measurement of shadow characteristics and power loss prediction. Moreover, ThinShadePV holds strong potential for integration into commercial PV simulation software, enhancing the accuracy of performance forecasts under real-world shading conditions.

Table of Contents

Chapter 1 Introduction **1**
1.1 An Overview of the PV Landscape in the Maltese Islands 1
1.2 Common Types of Thin Objects 2
1.3 Simulation as a Prospect for Analysing and Quantifying Thin Object Shading 4
1.4 Factors Determining the Impact of a Shadow Transposed by a Thin Object 4
1.5 Structure of Thesis 5
1.6 Research Boundaries 6
Chapter 2 Fundamentals **8**
2.1 Theory of Solar Radiation 8
2.1.1 Direct, Diffused and Ground-reflected Radiation 11
2.1.2 Sun Position 13
2.2 Basic Operation of a PV Source 15
2.3 Theory of Shadow Optics 18
2.4 The Principles of Shadow Intensity Variations in Imagery 21
2.5 Conclusion 25
Chapter 3 Literature Review **26**
3.1 Introduction to the State-of-the-art on Thin object Shading 26
3.2 Comparative Effects of Thin versus Hard Object Shading 28
3.3 Shading Mitigation Techniques 30
3.3.1 Hotspot Formation 31
3.3.2 Bypass Diodes 34
3.3.3 Maximum Power Point Tracking (MPPT) 35
3.4 Experimental Impact of Partial and Thin Object Shading 38
3.4.1 Outdoor Experimental Studies on PV shading 38
3.4.2 Laboratory Experimental Studies on PV shading 44
3.4.3 Shadow Modelling using Simulation Tools 46
3.5 Image Analysis Techniques used in PV Shading Studies 51
3.5.1 Shadow Detection 52

3.6 Shadow Image Segmentation 56
3.6.1 Image Enhancement Techniques and Filtering 59
3.7 Machine Learning and Statistical Approaches in Predicting Shading 63
3.8 Current Challenges and Gaps in the Literature Identified Gaps in Literature, Aims and Objectives of this Study 66
3.8.1 Main Research Gaps Identified from the State of the art 66
3.8.2 Aims and Objectives 68
Chapter 4 Outdoor vs Laboratory Environmental Conditions 72
4.1 Introduction 72
4.2 Methodology 73
4.2.1 Experimentation Biases and Assumptions 74
4.2.2 Outdoor Experimentation Method and Setup 76
4.2.3 Laboratory Experimentation Method and Setup 86
4.2.4 Image Capture and Quantification Methodology 89
4.2.5 Combined Shadow Factor (CSF) 91
4.3 Results and Discussion 96
4.3.1 Analysing the Significance of Experimental Bias 1 and Bias 2 96
4.3.2 Comparative Baseline Analysis at Control Conditions between Laboratory and Outdoor conditions 101
4.3.3 Comparative Difference between Laboratory and Outdoor Environment at Thin Object Shading Conditions 103
4.3.4 Outdoor and Laboratory Comparative Shadow Formation Analysis 111
4.4 Conclusion 117
Chapter 5 Shadow Quantification using Image-based Analysis 119
5.1 Introduction 119
5.2 Methodology 119
5.2.1 Outdoor Experimentation Setup for Thin Object Shading on a Small-scale PV Module 119
5.2.2 Operation of ThinShadePV (Image Analysis Tool) 129
5.2.3 Setup and Procedure for Validating ThinShadePV 156
5.3 Results and Discussion 168
5.3.1 The Quantifiable Effect of Various Sized Thin Object Shading on a Small-Scale PV Module (ThinShadePV Training) 169

5.3.2 Analysing the Size and Intensity of Umbra and Penumbra as Distance Increases. 174
5.3.3 Correlation and Sensitivity Analysis of Factors Affecting Shadow Formation and Resulting Power Loss on the Small-Scale PV Module 184
5.3.4 Validating the Performance of ThinShadePV in Real Case Scenarios. 190
5.4 Conclusion 201
Chapter 6 The Penumbra Shadow Representation 204
6.1 Introduction 204
6.2 Materials and Methods 206
6.2.1 Choosing the Appropriate Material to Replicate a Varying-Intensity Penumbra-Only Shadow 207
6.2.2 Setup Conditions and PV Sources Utilised 210
6.2.3 Quantifying the Intensity Associated with each ND Filter 211
6.2.4 Direct Comparable Method used Between a Varying-Intensity Penumbra Shadow and Constant-Intensity Shadow 217
6.3 Results and Discussions 221
6.3.1 Preliminary Experimentation results and Discussion for ND Filters 222
6.3.2 Comparative Analysis of the Intensities Between a Varying-Intensity Penumbra-Only Shadow and a Constant-Intensity Shadow 226
6.3.3 Comparative Analysis of the Size of a Varying-Intensity Penumbra-Only Shadow and a Constant-Intensity Shadow 230
6.3.4 Analysing the Difference in Power Loss Between the Varying-Intensity Shadow and the Constant-Intensity Shadow created by the ND filters. 232
6.4 Conclusion 236
Chapter 7 Conclusions 237
7.1 Achieved Aims and Objectives 237
7.2 Contribution to Knowledge and Key Findings 243
7.3 Research Limitations 244
7.4 Recommendations for Future Work 246
7.5 Final Remarks 247
References 249
Appendices 270
Appendix A 270
Appendix B 273

Appendix B.1 - Uncertainty Analysis for Chapter 4 Section 4.3.3, Chapter 5 Section 5.3.1, Chapter 5, Section 5.3.4 and Chapter 6 Section 6.3 273
Appendix B.2 - Uncertainty Analysis for Chapter 4 Section 4.3.1 and 4.3.3 277
Appendix B.3 - Uncertainty Analysis for Chapter 4 Section 5.3.3 Sensitivity Analysis..... 279
Appendix C - Datasheets and Conformities..... 281
Appendix D – Tabulated Laboratory Dataset 299
Appendix E – Supporting Calculations for Key Chapter Developments 302
Appendix E.1 - The One-Way Anova used in Section 4.3.1 302
Appendix E.2 – Additional information on the Random Forest Prediction Model used in Section 5.3.2 306
Appendix E.3 – Spearman Correlation Matrix used in Section 5.3.3 307
Appendix E.4 – Sensitivity Analysis used in Section 5.3.3 308
Appendix E.5 – Bland-Altman Analysis used in Section 5.3.4.2 310
Appendix E.6 – Mann–Whitney U Test used in Section 6.3.4 313
Appendix E.7 – Cohen's Effect Size Analysis used in Section 6.3.3 315
Appendix F - CSF Score Script 318
Appendix G - ThinShadePV Script..... 320
Appendix H - Other Supporting Scripts Used in this Thesis 343

List of Figures

Figure 1.1. Example of a real case scenario of thin objects found on a roof space before PV installation. xxv

Figure 1.2. A second exemplary scenario of thin objects shading an existing PV system. xxvi

Figure 1.3. An example of a case where the wooden pergola is not considered as a thin object. xxvi

Figure 1.4. Horizontally transposed thin shadow on a PV module. xxvii

Figure 2.1. Flow chart demonstrating the structure of Chapter 2. 8

Figure 2.2. Spectrum comparison between the UXL-10S Series Xenon lamp used as the light source unit in the solar simulator in Chapter 4 and daylight [32]. 9

Figure 2.3. Solar radiation spectrum and spectral response of a Si solar cell [33]. 10

Figure 2.4. Schematic of Air-Mass spectra definition [37]. 11

Figure 2.5. Direct, Diffuse and ground reflection (Albedo) [39]. 12

Figure 2.6. Comparative diagram of Bifacial technology tacking advantage of the ground reflectance and traditional monofacial PV modules [42]. 13

Figure 2.7. Visual diagram of the sun position angles described in this theory [46]. .. 14

Figure 2.8. A visual representation of the common PV sources used [48]. 15

Figure 2.9. I-V curve of a typical PV cell and a resistive load [50]. 16

Figure 2.10. Characteristic I-V and P-V curves of a PV module [58]. 17

Figure 2.11. A representation of umbra and penumbra shadow with penumbra being shown as a varying-intensity shadow [62]. 18

Figure 2.12. The principle of shadow formation indicating umbra and penumbra [63]. Penumbra is presented as having a uniform grey intensity, rather than a gradient effect. 19

Figure 2.13. Geometrical representation of calculating umbra and penumbra as derived by the Similar triangles theorem [66]. 19

Figure 2.14. The individual pixels are arranged in *x*, *y* coordinate space with grey level, or intensity, associated with each one [72]. 21

Figure 2.15. (a) A shaded small-scale PV module, **(b)** Intensity distribution equivalent of the image clearly indicating the shadow area due to darker grey level range [81]. .23

Figure 3.1. (a) An example of hard shading by a building [90], **(b)** An example of a thin object shading from a rod [91]. 26

Figure 3.2. An example of **(a)** hard shading [93] in contrast to **(b)** thin object shading [10]. 29

Figure 3.3. I-V curve under partial shading conditions [96]. 29

Figure 3.4. PV module with different case shading where **(a)** demonstrates horizontal shading, **(b)** visualises vertical shading, **(c)** illustrates a single cell shading and **(d)** shows a diagonal coverage [100]. 30

Figure 3.5. Example of a hotspot formation indicated **(a)** by a red spot on a **(b)** 10 W PV Module (right image) [21]. 33

Figure 3.6. The difference between the two most commercially available bypass diode design on PV modules [113]. 34

Figure 3.7. A P-V Curve of a PV system under partial shading conditions showing a power loss due to MPPT failure [125]. 37

Figure 3.8. A visualisation of the shading case scenarios studied by Numen et al. [100] where **(a)** represents the horizontal shading **(b)** singe cell shading **(c)** vertical shading. 39

Figure 3.9. Percentage shading a single row of cells using a physical experimental methodology [24]. 39

Figure 3.10. The power output of the whole PV module under the shading scenarios depicted on the right side legend, corresponding to the shading scenario in the upper portion of this figure [130]. 40

Figure 3.11. The PV plant Dolara et al. [10] used to analyse the overhead line shading. 42

Figure 3.12. The structure built by the Dolara et al. [132] to simulate the MV line shading. 42

Figure 3.13. A visualised figure of the three thin object shading cases outlined by Teneta et al. [23] where **(a)** represents shading scenario 1, **(b)** shading scenario 2 and **(c)** shading scenario 3. 43

Figure 3.14. PV shadow modelling using PVSOL for partial shading analysis where **(a)** represents the PV with simulated shadows at a given time of day and **(b)** illustrating the value of direct radiation lost due to array shading [16]. 47

Figure 3.15. A screenshot of the interactive GUI created by PVsyst [154]. 49

Figure 3.16. Flowchart of the three of the shade detection method by Bognár et al. [169] 52

Figure 3.17. Graphic representation of a simple pole shading on 3 PV modules (plan view) [170]. 53

Figure 3.18. (a) represents the captured RGB Image, (b) represents the left hand side image translated into binary, specifically focusing on the extracted shading portion [172]. 54

Figure 3.19. Block diagram for the proposed shading detection system first adopted by [175]. 55

Figure 3.20. Shadow cast on a white paper by building [183]. 57

Figure 3.21. (a) depicts the shadow being analysed where w represents the penumbra region and x depicts the distance of pixels, (b) represents the corresponding sigmoidal function for the RGB image [183]. 58

Figure 3.22. Points of interests on the sigmoidal curve, outlined by Mirylenka et al. [184]. 59

Figure 3.23. The difference between the histogram intensity distribution of an unshaded PV module observed in (a) and when a shadow is applied in (b) [81]. 61

Figure 3.24. Different shadow removal results based on applying gaussian filters where the final two images on the right are the removal result using proposed filtering method in [196]. 62

Figure 3.25. A comparative model performance using MAE, RMSE, and R^2 Score metrics [202]. 64

Figure 3.26. An example of a Pearson correlation matrix used in the realm of PV's [201]. 65

Figure 4.1. The 4-busbar monocrystalline solar cell used in this study. 73

Figure 4.2. A conceptual 3D visual of the outdoor experimental setup including the yearly sun paths. 77

Figure 4.3. Sun position 1: A 3D model of the geometrical sun position model based on the location of ISE Marsaxlokk at 12:30 on the 23rd of May 2024. 78

Figure 4.4. Sun position 2: A 3D model of the geometrical sun position model based on the location of ISE Marsaxlokk at 13:00 (Solar Noon) on the 23rd of May 2024. . 78

Figure 4.5. Sun position 3: A 3D model of the geometrical sun position model based on the location of ISE Marsaxlokk at 13:30 on the 23rd of May 2024. 79

Figure 4.6. Physical outdoor experimental setup for the solar cell, taken facing the North direction. 80

Figure 4.7. (a) A reference image of the datalogger DATAQ DI-808, **(b)** Custom circuit wiring diagram for the operation of the DATAQ DI-808. 82

Figure 4.8. I-V curve electrical characteristic for the chosen solar cell. 84

Figure 4.9. The laboratory experimentation setup. 86

Figure 4.10. An I-V curve generated for a laboratory environmental setting depicting the MPP at control conditions and the measured power point corresponding with the outdoor experimentation for a ⌀20.0 mm thin object shading scenario between 10 cm and 40 cm distance from the solar cell. 88

Figure 4.11. The reference silicon solar cell used as reference for the calibration process of the solar simulator. 89

Figure 4.12. Typical captured image of a ⌀10.0 mm thin object shading at 40 cm distance from the solar cell on a white background under laboratory environmental conditions. **(a)** RGB, **(b)** Converted to greyscale. 91

Figure 4.13. Visual representation of the shadow and background intensity and size capture indicated. 92

Figure 4.14. (a) representation of the pixel intensity darkness range, **(b)** a scaled down version of each pixel intensity value of the image, **(c)** the average column pixel intensity distribution resembling a histogram. 93

Figure 4.15. A comparative difference between black absorbent (solid lines) and silver reflective (dashed) coated thin objects in a laboratory environment. 97

Figure 4.16. A comparative difference between horizontal (solid lines) and vertical (dashed) aligned thin object shadow on the solar cell in a laboratory environment. 99

Figure 4.17. A comparative understanding between the **(a)** Horizontal transposed shadow on the busbars contacts **(b)** Vertical transposed shading on the busbars. 100

Figure 4.18. Comparative control conditions between outdoor (red point) and laboratory environment (blue point and curve) using identical PV solar cells. 102

Figure 4.19. A visual bar graph representing the power loss due to thin object shading scenarios in an **outdoor** environment. 104

Figure 4.20. A visual bar graph representing the power loss due to thin object shading scenarios in a **laboratory** environment. 104

Figure 4.21. A comparative visual representation between the rate of power loss in outdoor environment shown in blue and laboratory environment shown in red at 10 cm distance from the solar cell. 106

Figure 4.22. A heat map visualising the area where the highest discrepancy in power output between outdoor and laboratory environment is observed. 106

Figure 4.23. Comparative interpretation of the ⌀10.0 mm thickness thin objects between outdoor and laboratory environment. 108

Figure 4.24. Comparative visual representation of the CSF factor between outdoor and laboratory environment. 109

Figure 4.25. A Comparative analysis of detailed images for a ⌀10.0 mm thin object at each distance range. 112

Figure 4.26. (a) Schematic diagram of the laboratory I-V solar simulator, **(b)** The collimating lens inside the I-V solar Simulator. 113

Figure 4.27. Fringes evidently transposed from the slit of the solar simulator. 114

Figure 4.28. (a) Diffraction patterns of a slit noted by Luo et al. [229] **(b)** Rotated images from the image dataset, captured in the laboratory environment of this study, are presented. These images show the same slit diffraction pattern observed using objects of different sizes, demonstrating similar diffraction behaviour at comparable distances from the source. 115

Figure 4.29. A comparative detail between outdoor and laboratory setting for a ⌀2.0 mm thick object at ⌀40 cm distance from the solar cell. 116

Figure 4.30. A comparative detail between outdoor and laboratory setting for a ⌀20.0 mm thick object at 40 cm distance from the solar cell. 116

Figure 5.1. (a) Plan view of the small-scale PV module, **(b)** A schematic of the dimensions of the PV module **(c)** A visual representation of the horizontal position of the thin object shadow on the PV module. 120

Figure 5.2. Solar cell level operation under thin object shading conditions on the small-scale PV module consisting of 36 quarter cut solar cells. 121

Figure 5.3. (a) Conceptual visual of the outdoor methodology, (b) In-situ outdoor experimentation setup. 124

Figure 5.4. The image capture setup showing the fixed mounted device as well as the shadow cast by the thin object higher than the camera setup. 127

Figure 5.5. Varying-intensity range of greyscale pixels. 130

Figure 5.6. (a) A typical thin object shadow case transposed on a white background in RGB colour format, **(b)** The same image converted to greyscale. 131

Figure 5.7. Visual representation of the dual sigmoidal curve (Section A) extrapolated from a sample image (Section B) which shows thin object shading. 133

Figure 5.8. A typical image case classified as **(a)** umbra and penumbra case, **(b)** penumbra-only shadow case. 136

Figure 5.9. An illustrative example of the methodology utilised to quantify the shadow size. 137

Figure 5.10. (a) Shadow case indicated no umbra shadow due to the presence of the peak (no plateau), (b) Shadow case indicating a significant amount of umbra shadow due to plateau. 138

Figure 5.11. The shadow quantification algorithm based on key literature aspects by Huang et al. 's [183] and Mirylenka et al. [184] identified in Chapter 3 and methodologically outlined in this chapter, and Section 5.2.2.1. 139

Figure 5.12. Initial main window prompt of ThinShadePV. To move to the subsequent section, either function 1 or function 2 buttons must be selected according to the shading case scenario. 147

Figure 5.13. A conceptual scenario where a PV module is already installed on the roof with a horizontal thin object casting a shadow on the PV module. The photo of the rooftop was taken facing south as indicated by the cardinal compass direction indicator. 148

Figure 5.14. Reference surface placed on a single solar cell of the PV module. 149

Figure 5.15. The window prompt upon selecting the Function 1 in the main menu. Insert image of the shading case and press the '*Process & Predict'* button to predict the power loss. 152

Figure 5.16. A typical scenario involves a roof that is currently unoccupied by any PV modules but is intended to accommodate a PV system in the future. The photo of the rooftop was taken facing south as indicated by the cardinal compass direction indicator. 153

Figure 5.17. An indicative conceptual diagram of measurements required to be logged by the user of ThinShadePV, applicable to the case when a PV module is under design planning stage. The photo was taken from the south side of the roof. 154

Figure 5.18. A snapshot of function 2 in ThinShadePV demonstrating the capabilities of predicting power loss based on distance and thickness measurements when the PV system is at design stage. 155

Figure 5.19. The vacant roof area used for validation of ThinShadePV consisting of full sun exposure without any hard shading from nearby walls. The photo was taken from the north side of the roof. 157

Figure 5.20. (a) The front elevation of the full-scale monocrystalline PV module, **(b)** Schematic diagram of the same full-scale PV module, **(c)** Wiring diagram of the three diodes located in the full-scale PV module used for ThinShadePV validation. 159

Figure 5.21. The position of the horizontal thin object shadow on the PV module. . 160

Figure 5.22. A visual explanation of the percentage shadow cast on the small-scale PV module.....161

Figure 5.23. A visual explanation of the percentage shadow cast on the full-scale PV module used in the validation process. 161

Figure 5.24. (a) The Seaward PV 200 tester and I-V tracer, (b) The Seaward Survey 200R multi-function irradiance meter with suction mount on the full-scale PV module. 164

Figure 5.25. The outdoor validation experimentation setup of ThinShadePV at a real thin object shading scenario.....165

Figure 5.26. The matte white PVC sheet covering a single shaded solar cell of the full scale PV module as image capture for the ThinShadePV prediction. 166

Figure 5.27. The measured points used for validation indicated as P_{load} by the red point marker where the measured I-V curve intersects with the simulated diagonal fixed load denoted as R_{load}. 167

Figure 5.28. (a) a visual representation of the shadow and PV module setup investigating the impact of large cross sectional diameter object shading, **(b)** The resultant power loss for objects transposing shadows whose thickness exceeds the width of the solar cell on the small-scale PV module.....170

Figure 5.29. Analysing the various power loss levels as the distance between the two categories of thin objects and the small-scale PV module increases. 172

Figure 5.30. The identification of a case where the shadow consists of both umbra and penumbra derived from the dual sigmoidal curve method and generated by ThinShadePV. 174

Figure 5.31. The identification of a case where the shadow consists of only penumbra derived from the dual sigmoidal curve method and generated by ThinShadePV.....175

Figure 5.32. An illustration of the umbra and penumbra size and intensity results for the small thin objects. **(a)** ⌀2.8 mm, **(b)** ⌀3.2 mm, **(c)** ⌀6.0 mm, **(d)** ⌀8.0 mm 176

Figure 5.33. Image sample dataset illustrating the transition from umbra and penumbra shadows at a distance of 25 cm, to a penumbra-only shadow at the maximum distance of 400 cm for a small thin object (⌀8.0 mm).....177

Figure 5.34. A detailed view of the shadow created by a ⌀2.8 mm thin object at **(a)** a distance of 25 cm and **(b)** a distance of 400 cm from the small-scale PV module.....178

Figure 5.35. A detailed view of the shadow created by a ⌀8.0 mm thin object at **(a)** a distance of 25 cm and **(b)** a distance of 375 cm from the small-scale PV module.....179

Figure 5.36. An illustration of the umbra and penumbra size and intensity results for the large thin objects. (a) ⌀10.0 mm, (b) ⌀12.0 mm, (c) ⌀14.0 mm, (d) ⌀16.0 mm ...180

Figure 5.37. Image sample dataset illustrating image analysis performed on a large thin object (⌀16.0 mm).....182

Figure 5.38. The model created by Tenata et al. [23] where the normalised brightness on the y-axis representing the intensity in this study is plotted against the (x) representing the size of the shadow. 183

Figure 5.39. (a) Spearman correlation matrix heatmap **(b)** Sensitivity Analysis based on the Random forest model created for small thin objects (⌀2.8 mm – ⌀8.0 mm). ..186

Figure 5.40. (**a)** Spearman correlation matrix heatmap **(b)** Sensitivity Analysis based on the Random forest model created for large thin objects (⌀10.0 mm – ⌀16.0 mm). 188

Figure 5.41. Example output from ThinShadePV for Case 14, showing automated detection of umbra and penumbra. The red and blue lines represent the detected shadow boundaries, while the total umbra and penumbra areas are displayed on the right-hand side of the image. 192

Figure 5.42. A bar graph comparing the predicted percentage power loss visualised in red and the measure percentage power loss visualised in blue. 195

Figure 5.43. Bland–Altman plot showing the agreement between predicted and measured percentage power loss. The x-axis represents the mean of the predicted and measured values, while the y-axis shows their difference (measured minus predicted). Each data point is labelled with an "×" to indicate the corresponding case. 196

Figure 5.44. An example image of the inconsistent upper and lower background intensity 198

Figure 5.45. A comparative visual **(a)** representing the ideal background intensity where the brightness level is consistent for both left and right sigmoidal curves **(b)** representing inconsistent left and right background intensity. 199

Figure 6.1. (a) The principle of shadow formation indicating umbra and penumbra where penumbra is presented as having a uniform grey intensity value, rather than a gradient effect [63] **(b)** A representation of umbra and penumbra shadow with penumbra being shown as a varying-intensity penumbra shadow [258]. 204

Figure 6.2. (a) The formation of a sample varying-intensity shadow by a thin sample object. **(b)** the corresponding constant-intensity, bearing the same overall size and average intensity. 206

Figure 6.3. (a) A constant transmittance light ND filter [282], **(b)** An ND filter representing a graduated light transmittance [283]. 209

Figure 6.4. A single ND filter rated at 95% TR covering the PV module. 213

Figure 6.5. (a) The ND Filter positioned at 10 cm from the PV module, **(b)** The ND filter repositioned at 50 cm from the PV module to accommodate for image capture. 214

Figure 6.6. Spectroscopy data for the ND filters used in this work as provided by the manufacture. 215

Figure 6.7. The image capture setup involving a white surface sheet placed over the PV module, with an ND filter positioned on top. 216

Figure 6.8. A visual comparison between **(a)** the setup used for penumbra-only cases and **(b)** the setup used for replicating the shadow transposed using the ND filter. 218

Figure 6.9. The PV module covered with strips of ND filters replicating the constant-intensity ND filter shadow consisting of a single intensity where **(a)** represents a coverage of 10% by the shaded strip on the PV module and **(b)** represents a fully shaded PV row with 100% coverage by the strip. 220

Figure 6.10. Flowchart outlining the methodological steps illustrated by the blue border and the forthcoming results represented by the process with the red border. . 222

Figure 6.11. The image captured intensity (orange) and the gamma-corrected pixel intensity values (blue) plotted against each ND filter TR level sourced. 225

Figure 6.12. The extracted power loss from each of the 29 varying-intensity penumbra-only cases in Chapter 5 Section 5.3.1 227

Figure 6.13. (a) A penumbra-only shadow created by the thin object, **(b)** the constant-intensity shadow using ND filter strips. 228

Figure 6.14. A graph comparing the gamma-corrected intensity values of the 29 penumbra-only cases represented as the varying-intensity penumbra-only shadow in blue and the constant-intensity ND filter intensities shown in red. 229

Figure 6.15. Comparison of percentage area covered by the shadow on the solar cell for the varying-intensity penumbra-only shadow and the constant-intensity shadow produced from the ND filter strips. 230

Figure 6.16. Comparison of the percentage power loss for the varying-intensity penumbra-only shadow and the constant-intensity shadows created by the ND filters. 231

Figure 6.17. Comparison between varying-intensity shadow and constant-intensity shadow created by ND filters. 233

List of Tables

Table 3.1. The comparative results by Kumari et al. between laboratory and outdoor experimentation on a full sized PV module with percentage solar cell shading [138]. 45

Table 3.2. An overview of the PV source, environmental condition, date and time each experimentation in the subsequent chapters was conducted. 70

Table 4.1. Examples of the sun position correction factor workings for the three sun positions. 80

Table 4.2. The range of thin object thicknesses used in both laboratory and outdoor experimentation. 81

Table 4.3. Operating conditions of outdoor environmental experimentation. 85

Table 4.4. Comparing the CSF score between outdoor and laboratory environment shadows between 10 – 40 cm distance from solar cell at the consolidated thin object thickness range. 109

Table 4.5. The difference and average value of the CSF score between outdoor and laboratory environment shadows between 10 – 40 cm distance from solar cell at the consolidated thin object thickness range. 109

Table 5.1. Electrical characteristics of the PV module used in the power loss experimentation, extracted from the manufacturer datasheet in Appendix C. 123

Table 5.2. Shading object thicknesses as categorized for the purpose of correlation in this work. 125

Table 5.3. Summary nomenclature for Figure 5.7. 132

Table 5.4. Correlation coefficient metric [244]. 141

Table 5.5. Electrical characteristics of the full size PV module used to validate ThinShadePV. 159

Table 5.6. A description of the 15 cases selected as the validation dataset. Each case shall be tested on the full-scale PV module. 163

Table 5.7. Validation results between predicted power loss generated by ThinShadePV denoted in red and the measured power loss on the full-scale PV module denoted in blue. 193

Table 6.1. The electrical characteristics of the PV module used for the preliminary experimentation. 211

Table 6.2. The single layer ND filters used during the experimentation with the converted TR level determined using Equation (26). 215

Table 6.3. Comparative value sourcing table between the varying-intensity penumbra shadow and the constant-intensity shadow. 218

Table 6.4. The resultant intensity level and power loss difference when elevating the ND filter from the PV module between 10 cm and 50 cm; in increments of 10 cm for the 95% TR ND filter. 223

Table 6.5. Comparative summary of model fit, group statistical differences, and prediction errors for the varying-intensity penumbra-only shadow and the constant-intensity ND shadows. 234

Nomenclature

Abbreviations

AC	Alternating Current
ADC	Analog-to-digital converter
AI	Artificial Intelligence
Albedo	Ground Reflectance
AM	Air Mass
APC	Article Processing Charge
BIPV	Building-Integrated Photovoltaics
cm	Centimeter
CCD	Charge Coupled Device
CMOS	Metal-Oxide-Semiconductor
CNN	Convolutional Neural Network
CS	Clear Sky
CSF	Combined Shadow Factor
CT	Computerised Tomography
CV	Computer Vision
CO_2	Carbon Dioxide
DAQ	Data Acquisition card
DC	Direct Current
DHI	Diffuse Horizontal Irradiance
DL	Daylight
DNI	Direct Normal Irradiance
DV	Darkest Pixel Value
E	East
EU	European Union
eV	Electron Volt
GHI	Global Horizontal Irradiance
GP	Global Peak
HDR	High Dynamic Range
HPSL	High Pressure Sodium Lamp
HSV	Hue, Saturation, Value
I	Current
IEC	International Electrotechnical Commission
IF	Intensity Factor
IR	Infrared
ISE	Institute for Sustainable Energy

ISO	International Organization for Standardization
ISO	International Standards Organization
IV Curve	Current-Voltage Curve
K	Kelvin
LED	Light Emitting Diode
m	Meters
MAE	Mean Absolute Error
MATLAB	Matrix Laboratory
MC4	Multi Contact 4
MDPI	Multidisciplinary Digital Publishing Institute
mm	Millimetres
MPP	Maximum Power Point
MPPT	Maximum Power Point Tracking
MRI	Magnetic Resonance Imaging
MV	Medium Voltage
N	North
nm	Nanometre
ND	Neutral Density
NOCT	Nominal Operating Cell Temperature
OD	Optical Density
P	Power
PID Controller	Proportional Integral Derivative Controller
POA	Plane of Array
PR	Performance Ratio
PS	Partial Shading
PSO	Particle Swarm Optimization
PV	Photovoltaic
PVsyst	Photovoltaic System Simulation Software
RGB	Red, Green, Blue
RMSE	Root Mean Square Error
ROI	Return on Investment
RQ	Research Question
R^2	Coefficient of Determination
S	South
SF	Size Factor
SLR	Single-Lens Reflex
SMT	Solar Module Tester
SR	Shadow Ratio
SI	Silicon
STC	Standard Testing Conditions
TAM	Tricolor Attenuation Model

TR	Transmittance Reduction
UI	Umbra Intensity
US	Umbra Size
UV	Ultraviolet
UVA	Ultraviolet A
V	Voltage
W	West
YOLO	You Only Look Once

Symbols

⌀	Diameter
P_{MPP}	Maximum Power Output (W)
G_{PV}	Solar Radiation Received by Module (W/m²)
T_c	Temperature of the Solar Cells (°C)
η_{Tref}	Photoelectric Conversion Efficiency (%)
A	Surface Area of the PV Module (m²)
T_{ref}	Reference Temperature (25°C)
β_{rel}	Temperature Coefficient
V_{MPP}	Maximum Power Point Voltage (V)
I_{MPP}	Maximum Power Point Current (A)
I_{ph}	Light-Generated Current (A)
ID	Diode Current (A)
I_{SC}	Short Circuit Current (A)
V_{OC}	Open Circuit Voltage (V)
P_{oper}	Operating Power (W)
R_{Load}	Resistive Load (Ω)
I_{oper}	Operating Current (I)
V_{oper}	Operating Voltage (V)
G_1	Irradiance measured at operating conditions (W/m²)
a	Irradiance correction factor for the open circuit voltage (W/m²)
R_s'	Internal series resistance of the test specimen (Ω)
k'	Temperature coefficient of the internal series resistance
ρ	p-value / significance level
Point A	Start of Penumbra Upper Region
Point B	End of Penumbra Lower Region
Point C	End of Penumbra Upper Region
Point D	Start of Penumbra Lower Region
UI_{Total}	Total Umbra Intensity
PI_1	Penumbra Intensity Upper region

$\mathbf{PI_2}$	Penumbra Intensity Lower region
$\mathbf{PI_{Total}}$	Total Penumbra Intensity
$\mathbf{PS_1}$	Penumbra Size Upper region
$\mathbf{PS_2}$	Penumbra Size Lower region
$\mathbf{PS_{Total}}$	Total Penumbra Size
$\boldsymbol{\gamma}$	Gamma Correction Factor
$\boldsymbol{\gamma_t}$	Tilt angle
$\boldsymbol{\omega}$	Uncertainty
$\boldsymbol{\mu}$	Micro (10^{-6})
m	Milli (10^{-3})
o	Degrees
$\mathbf{g^{-1}}(\boldsymbol{u})$	The inverse gamma pixel intensity value
$\boldsymbol{u}$	The normalised pixel intensity (ranging from 0 to 1)
$\mathbf{G_{PV}}$	Solar radiation received by the module
$\boldsymbol{\beta_o}$	Temperature coefficient
$\mathbf{I_{ph}}$	Light generated current
$\mathbf{I_D}$	Diode current
$\mathbf{I_{sh}}$	Shunt Leakage current
Kt	Clearness index
€/Wp	Euro per watt peak
kWp	Kilo Watt peak

Definitions

The following terms are used consistently throughout this study. For clarity, their definitions are outlined below:

‘Thin object’

There is no universally precise definition of a thin object, as it depends on the specific circumstances. However, for this study, a thin object will be considered as an obstruction whose characteristic width is small relative to the total active PV area it affects. Its shading impact is localised and does not significantly obstruct large portions of the active surface.

To provide clarity, one can consider both Figure 1.1 and Figure 1.2 as examples of thin objects, whereas Figure 1.3 does not classify as such. This distinction ensures consistency in categorizing shading effects throughout the study.



Figure 1.1. Example of a real case scenario of thin objects found on a roof space before PV installation.



Figure 1.2. A second exemplary scenario of thin objects shading an existing PV system.



Figure 1.3. An example of a case where the wooden pergola is not considered as a thin object.

Furthermore, thin objects can cast shadows on a PV module at various angles and in different patterns, influencing shading effects. However, unless otherwise stated, this study analyses shading as occurring horizontally across the entire PV source as seen in Figure 1.4, perpendicular to its width, to maintain consistency in evaluating its impact. Moreover, within the context of this work, small thin objects are defined as having

thicknesses of between ⌀2.8 mm – ⌀8.0 mm, and large thin objects between ⌀10 mm – ⌀16.0 mm

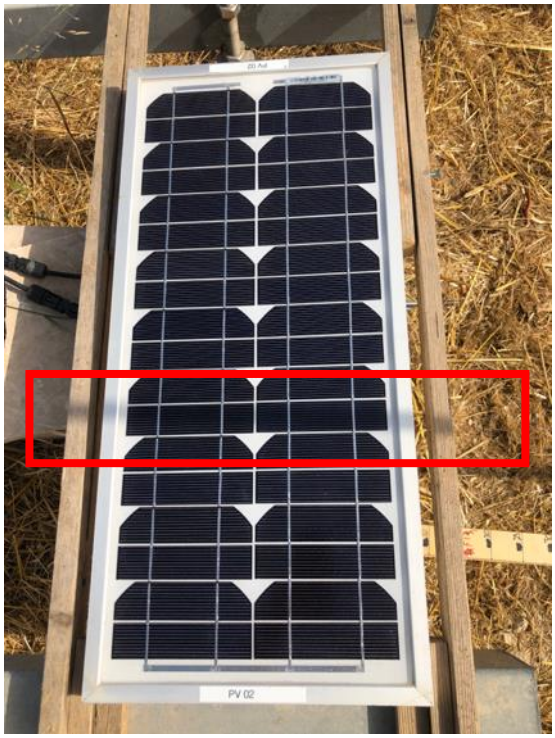


Figure 1.4. Horizontally transposed thin shadow on a PV module.

‘Single Solar Cell’

A single solar cell is a semiconductor electrical device that converts light energy directly into electricity through the PV effect. It is a type of photoelectric cell, defined as an un encapsulated device whose electrical characteristics such as current, voltage, or resistance vary when exposed to light. A single solar cell can be cut into a desired size in its raw form where a typical size would be 156.0 mm × 156.0 mm, though they are often cut in half or quarter cut cells to improve efficiency.

‘PV Source’

A PV source is a non mechanical device that converts sunlight into electrical energy using the PV effect. It typically consists of one or more solar cells, usually made from

semiconductor materials like mono-crystalline silicon, which generate direct current (DC) electricity when exposed to sunlight.

‘PV Module’

A PV module is an assembly of PV solar cells mounted in a framework for installation. Each module consists of a number of solar cells, which are electrically connected and encapsulated to protect them from the environment. The size of a PV module may vary significantly depending on the wattage and cell technology used.

‘Distance’

In this thesis, the term 'distance' is defined as the vertical separation between the thin object under study and the PV source under experimentation, unless otherwise stated. To maintain consistency and ensure precision in both experimental and theoretical calculations, all distances are meticulously measured and consistently reported in centimetres (cm). This unit was specifically chosen not only for its suitability in capturing the precise increments in a range extending up to 400 cm but also to avoid confusion with measurements of thickness, which will be recorded in different units (mm). Consequently, this standardisation facilitates the reliability and comparability of data across various experiments and analytical discussions presented within this research. All distance measurements in this thesis were made using a measuring tape with 1 cm increments. Therefore, any distance values reported carry an uncertainty of ±0.5 cm, based on half the smallest division. Furthermore, in all distance measurements, the distance refers to the vertical separation between the lowest point of the cylindrical thin object and the surface of the PV module.

‘Thickness’

For the duration of this thesis, 'thickness' pertains to the diameter (⌀) of the thin object under examination. It is crucial to distinguish this measurement from the vertical

distances explored elsewhere in this study. To ensure accuracy and uniformity across various experiments and theoretical discussions, thickness is invariably measured and documented in millimetres (mm). This choice of unit allows for detailed precision necessary for assessing the minute variations in the cross-sectional profiles of thin objects, thereby providing an essential metric for comprehensive analysis within the scope of this research. All cross sectional diameter thickness expressed in mm measurements in this thesis were made using a digital vernier calliper with 0.01 mm increments. Therefore, any distance values reported carry this uncertainty, resulting in an uncertainty of ±0.005 mm, based on half the smallest division.

Chapter 1 Introduction

Hours of sunlight vary significantly across the globe, with the optimal latitudes for PV systems typically falling between 23.5° North and 23.5° South. The Maltese islands are considered one of the most promising locations for photovoltaic (PV) solar energy generation among European Union (EU) member states. Situated at a latitude of 35.9°, Malta receives approximately 3,100 hours of sunshine annually [1], positioning it as an excellent location for both residential and large-scale PV system installations [2]. Despite this advantage, as of 2023, Malta has recorded the third lowest renewable energy share amongst the 27 members of the EU, reaching only 15.1% in 2023, with solar energy being the primary contributor [3]. This figure places Malta 10% below the EU's renewable energy average of 24.5% [3]. In 2024, the Maltese government set a target to reach the 2023 EU average, aiming for a 25% renewable energy share by 2030. This substantial increase is expected to come primarily from upcoming offshore wind and solar farm projects, as available land for PV installations is becoming increasingly scarce [4]. This will be discussed in more depth in the next sub-section.

1.1 An Overview of the PV Landscape in the Maltese Islands

Malta, together with all other EU member states, was required to update the National Energy and Climate Plan (NECP) 2021–2030 with the previous target set at 25%. Now, the NECP must align with the more ambitious 42.5% renewable energy share set by the EU by 2030 [5].

In Malta, Eurostat reports that over 97% of the country's renewable energy generation is derived from PV systems. Consequently, ensuring the optimal performance of PV installations across the Maltese Islands is of importance [6]. Nevertheless, operational inefficiencies are inevitable and may arise from several factors, including PV module degradation, debris accumulation, and partial shading resulting from increasing building heights, among others [7]. These inefficiencies are often overlooked in renewable

energy share calculations, potentially leading to an overestimation of actual contributions. Furthermore, the Maltese Planning updated the local development control design policy, guidelines and standards published in 2015 (DC15) [8] to accommodate for the rise in new apartment development buildings replacing traditional terraced development. On page 147, the DC15 opens the possibility for placing PV systems directly mounted flat on the roof space [8]. This provision also creates potential for installing PV modules on Malta's lower terraces at a 0-degree tilt, a configuration whose performance this study aims to investigate, particularly in relation to thin objects situated on such DC15-compliant flat-roof setups.

Contradictory to the government's efforts to promote sustainable energy from natural resources as per the Regulator Energy Water Services (REWS) Act, Chapter 545.11 of the Maltese laws [9], an article emphasised the fact that "the DC15 guidelines conflict with the requirements of installing unshaded PV systems" [8]. This issue arises from the introduction of the 1 meter parapet wall for roof service areas in new developments. As a result, PV modules are often confined within these walls and subjected to shading for the majority of the year. The increasing demands of development, coupled with taller building heights and restricted roof service spaces, have proven to create some of the most challenging shading conditions especially on rooftops, where such factors are largely beyond individual control. These factors will be elaborated in the forthcoming sub-section.

1.2 Common Types of Thin Objects

Overhead power lines are a common feature observed both locally and globally. These horizontal power lines are typically seen crossing over the balconies of terraced developments. However, for low-lying buildings such as bungalows and villas, they often run above the roof level to allow clearance for large vehicles. This arrangement can result in potential shadowing effects on the rooftops. Another common feature of rooftops in the Maltese islands is the widespread use of passive air clothes drying lines. These are particularly prevalent in multi-storey roof spaces, terraced houses, and duplex maisonette housing types that constitute a significant portion of the national property market. Passive air clothes-drying lines commonly span large sections of the roof, with

multiple thin ropes or wires stretched across the area. These create shading from flexible thin objects positioned above the roofline. This setup significantly reduces the potential for installing PV systems on these areas of the roof, limiting their capacity for solar energy generation and potentially impacting the potential for efficient solar energy generation. On a global scale, larger countries with abundant land resources face similar challenges with Medium Voltage (MV) power lines. These often cross large valleys and building blocks, also contributing to thin object shading, as demonstrated in [10]. In the study by Dolara et al. [10], the authors illustrate how a single overhead power line can impact hundreds of PV modules when positioned above a solar farm.

In a more commercial setting, fall protection such as safety lines and railings have become essential features on pitched roofs due to modern safety regulations by the Occupational Health and Safety Administration (OHSA) [11]. Often overlooked, these small but essential objects on rooftops can have a significant impact on the performance of PV systems, inadvertently contributing to thin object shading.

Shading induced inefficiencies in PV systems often lead to the need of installing additional PV sources to compensate for energy losses and meet target energy goals. However, this approach hinders achieving the targets set out by the United Nations' Sustainable Development Goal (SDG) Target 7.3, which aims to double the global rate of energy efficiency [12]. Achieving this target necessitates optimizing solar performance under real-world conditions to maximize efficiency. In this context, power loss becomes a critical metric for evaluating the performance of PV systems, particularly under partial shading caused by thin objects. The approach of measuring power loss is also evident in existing literature, such as in studies conducted by Al-Smadi et al. [13] and Craciunescu et al. [14]. These studies highlight the importance of accurately assessing inefficiencies induced by shading, to improve overall PV system output.

1.3 Simulation as a Prospect for Analysing and Quantifying Thin Object Shading

Currently, the analysis and quantification of shading effects caused by thin objects, such as poles, antennas, and wires, in PV systems typically involve simulation-based methodologies implemented through specialised software tools such as PVsyst v8 [15], PVSOL 2025 [16], and MATLAB® R2024b Simscape [17]. PVsyst employs a simplified yet practical approach by using a predefined "thin object" parameterisation, allowing users to assign a fractional electrical shading effect to account for partial shading scenarios [18]. PVSOL, in contrast, primarily relies on detailed three-dimensional geometric modelling to accurately predict shading patterns and their temporal variations, providing quantification of shading losses through a heatmap over different solar positions based on the difference in irradiance loss. MATLAB® Simscape offers a more flexible and detailed modelling framework, enabling users to develop customised, cell-level simulations to capture fine-grained shading effects [19]. Despite these varying approaches, common practice largely centres around evaluating shading through irradiance reduction metrics and energy yield losses, although differences exist in the balance between modelling complexity, accuracy, and shading computational demands among these tools. These discrepancies arise from multiple factors as shall be discussed in the upcoming section.

1.4 Factors Determining the Impact of a Shadow Transposed by a Thin Object

The extent to which thin object shading impacts a PV source is primarily governed by three interrelated factors: object size, object shape, and the distance between the thin object and the PV source [20], [21], [22]. Firstly, object size is a critical determinant, as increased overall object size results in greater shadow coverage and consequently reduced incident solar irradiance on PV cells.

The second factor relates to the shape of the object, which affects the uniformity and distribution of shading. The shadow can either appear smooth and uniform on a circular surface or vary significantly when the object has sharp edges. In round thin objects the

shadow transposed tends to be less sharp due to light diffraction around the round object whilst hard-edged objects produce a peripherally well-defined edge shadow. Finally, the distance between the shading object and the PV surface significantly influences shadow characteristics; objects positioned closer to the PV surface produce sharp and well-defined shadows, whereas increasing the distance leads to more diffuse and elongated shadow patterns [23].

Together, the preceding factors contribute to the overall shadow impact on PVs. Moreover, this study will endeavour to investigate these factors through an image analysis and predictive modelling. To provide a clear roadmap for this investigation, the following section outlines the structure of the thesis and concisely explains the content of each chapter.

1.5 Structure of Thesis

This thesis is organised with the following outline in sequential order:

- **Chapter 2** lays the theoretical foundation of this study by exploring solar radiation, shadow optics, and the principles of shadow image intensity, while defining key terms used throughout.

- **Chapter 3** reviews state-of-the-art methodologies for quantifying partial and thin object shading, including predictive modelling and image analysis. This forms the basis for the study's aims, objectives and research questions.

- **Chapter 4** provides a comparative analysis of thin object shading effects between the outdoor experiments and the laboratory setups, highlighting discrepancies in both quantitative loss in power and shadow formation.

- **Chapter 5** quantifies the impact of thin object shading on PV modules using outdoor experimentation and analyses correlations and feature importance between influencing factors. It also introduces an innovative image analysis

tool, ThinShadePV, designed to predict power loss and shadow formation from images of horizontal thin object shading scenarios.

- **Chapter 6** investigates whether the simplification of the varying-intensity penumbra shadow into the average constant-intensity shadow as observed in the state of the art is scientifically valid.

- **Chapter 7** concludes the study by summarising the key findings, contributions to the body of knowledge and evaluating the extent to which the research has achieved its aims and objectives. It also acknowledges the study's limitations and provides recommendations for future research.

1.6 Research Boundaries

This section aims to clearly outline the research boundaries adopted for this study. These boundaries are applied to define the scope of experimental setups, data collection methods, and analytical approaches, ensuring the research remains focused, manageable, and aligned with the study's objectives.

- Unless otherwise stated, this study uses a worst-case scenario approach to approximate power loss, based on the altitude correction factor introduced in Chapter 4. By selecting periods of peak solar irradiance to cast the shadows, the analyses focuses on conditions where shading effects are most pronounced. While this may not reflect days with higher diffuse radiation, it provides a strong baseline.

- The study will focus exclusively on thin object shadows at a horizontal setting due to the lack of research in the field. For a more detailed and comprehensive analyses focusing specifically on vertical thin object shading, the reader is invited to refer to the research work carried out by Teneta et al. [24] and Galeano et al. [25] .

- Throughout each experimentation conducted in this study, the analysis was conducted at either single solar cell or PV module level with all varying parameters stated in the methods section of each chapter. This therefore excludes analysis at inverter level, at plant level and any consideration of Maximum Power Point Tracking (MPPT) algorithms.

- The development and application of the ThinShadePV tool are limited to static image-based analysis of thin object shading under controlled lighting conditions. The tool is designed to predict power loss and shadow distribution using images captured at specific moments in time, and does not account for dynamic shading changes throughout the day or year. Its accuracy is therefore most applicable to high-contrast, well-defined shadow scenarios.

- The predictions from ThinShadePV are based on still images under consistent irradiance, offering estimated rather than exact power loss values. They are intended for comparative analysis in controlled conditions, with factors like weather variability and module-specific performance falling outside this study's scope.

- This research excludes external influence from components like bypass diodes and optimisation devices. ThinShadePV predictions are solely based on a monocrystalline PV module with all cells connected in series.

Chapter 2 Fundamentals

This chapter outlines the fundamental theory behind solar radiation, shadow optics, and shadow intensity variations in imagery with focus on solar energy. This knowledge serves as the foundation for the methodologies, correction factors, and PV principles discussed in later chapters. It should be noted that this chapter comprises only the theory that shall be relevant towards the later chapters of the study, and thus excludes theoretical concepts that are beyond the scope of the study moving forward. Figure 2.1 outlines the structure of the fundamental theory, highlighting the key components that will be examined in detail in the following sections.

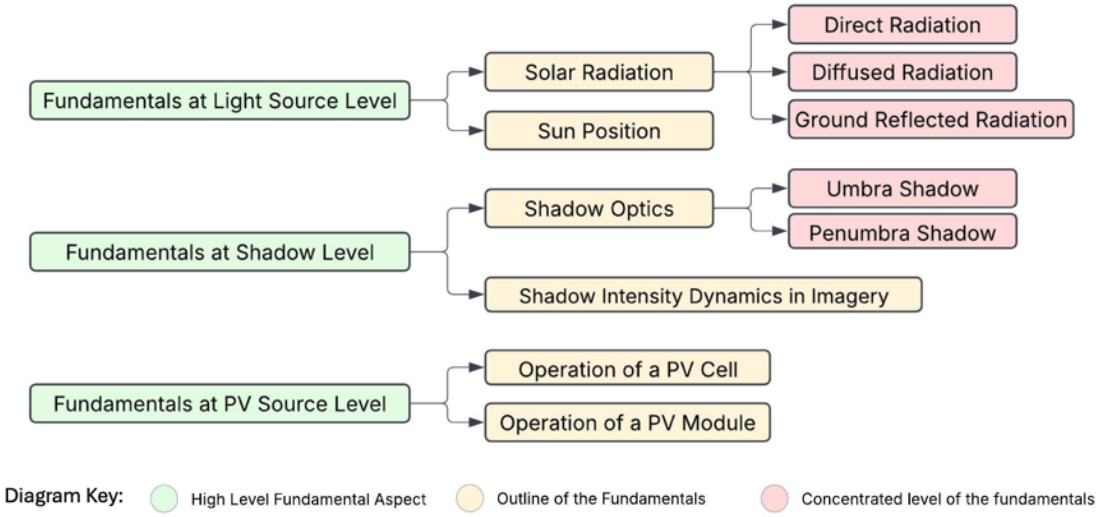


Figure 2.1. Flow chart demonstrating the structure of Chapter 2.

2.1 Theory of Solar Radiation

Solar irradiation is the energy emitted by the sun per square meter (Wh/m^2) in the form of electromagnetic waves, mainly consisting of visible light, ultraviolet (UV), and infrared (IR) radiation. Sunlight is a broad spectrum of electromagnetic radiation emitted by the Sun, spanning wavelengths from approximately 290 nm (UV rays) to 2500 nm (IR rays), with the visible light portion falling between 380 and 700 nm [26]. Consequently, visible light carries a significant portion of the sun's energy that reaches Earth, making it the primary driver in the PV energy conversion. Light can be produced

naturally by the sun or artificially through various technologies. Artificial light typically focuses on visible light wavelengths, with heat as a by-product depending on the technology used [27]. Sunlight has a more even colour distribution when compared to other commonly found artificial light sources such as Light Emitting Diodes (LEDs) and High Pressure Sodium Lamps (HPSL) [28], making it more aligned with human visual perception. The Sun behaves approximately like a blackbody radiator with an effective temperature of about 5778 Kelvin (K), resulting in the emission of a continuous and broad spectrum of electromagnetic radiation, which includes visible light [29]. In contrast, artificial light spectra vary by technology, with the xenon short-arc lamp being the closest match to natural daylight. This emits a bright flux (3000 candela per 1000 W) at a colour temperature of 6200 K [30],[31]. To exemplify, Figure 2.2 visualises the spectrum comparison between the UXL-10S Xenon lamp used in experimentation involving a solar simulator in Chapter 4 of this study and natural midday sunlight. While both sources exhibit peak light relative intensities around the visible spectrum (particularly near 500 nm), the Xenon lamp demonstrates a sharper intensity spike and greater fluctuations across the electromagnetic spectrum. In contrast, natural sunlight shows a smoother distribution with generally lower relative intensity at shorter wavelengths, indicating a discrepancy in spectral uniformity between the artificial and natural light sources. The outlined fundamental discrepancy could lead to varying effects on the PV source being tested. This will be explored further in Chapter 4.

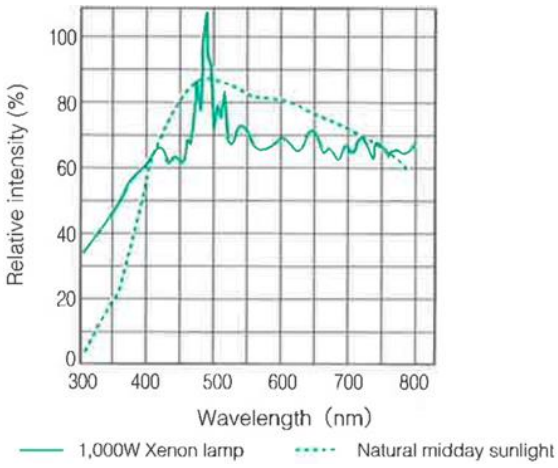


Figure 2.2. Spectrum comparison between the UXL-10S Series Xenon lamp used as the light source unit in the solar simulator in Chapter 4 and daylight [32].

Silicon (Si) PV cells are widely used for solar energy conversion, with their performance strongly linked to the amount of direct sunlight and the material's characteristics. Moreover, Si has a bandgap energy of approximately 1.1 electron volts (eV) and demonstrates the spectral ability to work between 300 nm and 1100 nm [33], as illustrated in Figure 2.3. Within this spectral range, the inclusion of ultraviolet (UV) wavelengths (approximately 300–400 nm) is particularly significant, as the high-energy photons in this region exceed the bandgap of Si and thus release excess energy upon absorption. However, this surplus energy is not converted into electrical power; instead, it is rapidly lost through thermalisation, generating heat within the cell and contributing to increased thermal losses rather than improving PV performance [34], whilst also inducing interface defects [35]. Furthermore, whilst the sun emits solar IR radiation up to 2500 nm, the upper bound of the Si bandgap is around 1100 nm, as can be identified from Figure 2.3. This implies that only the range between the upper bound of visible light (>700 nm) and the upper bound of the Si bandgap is useful for electricity production. Moreover, the wavelengths between 1100 nm and the upper solar IR radiation of 2500 nm do not contain the properties to produce electricity but rather decrease the efficiency of the solar cell due to thermal heat production [36].

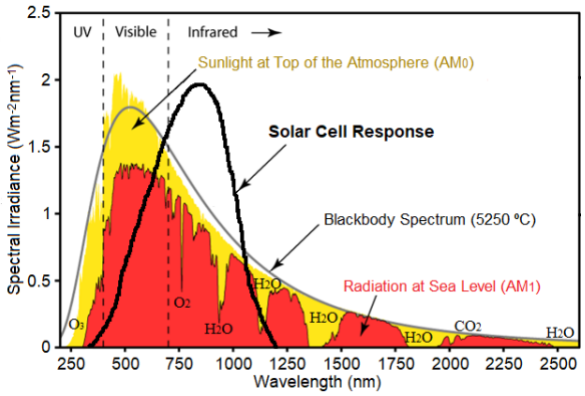


Figure 2.3. Solar radiation spectrum and spectral response of a Si solar cell [33].

While solar radiation from the sun's surface is relatively constant, atmospheric absorption and scattering cause variability by the time it reaches Earth. Maximum radiation occurs under clear skies when the sun is directly overhead at a given location. This pathlength is usually referred to as the air mass (AM) through which solar radiation must pass to reach the earth's surface. The sun's photosphere as observed just outside earth's atmosphere (AM 0). The airmass of AM 1.5 G equivalent to a sun angle of 48.2°

overhead is the standard used for PV studies because it represents an average solar radiation condition for mid-latitude locations where most PV systems are deployed as illustrated in Figure 2.4. It is also common in research to split the global radiation of AM 1.5 G into direct radiation from the sun and diffused radiation from the sky.

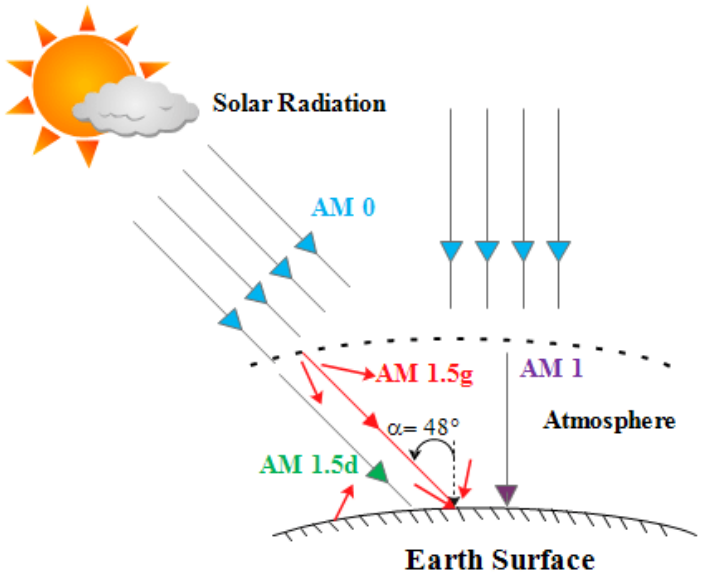


Figure 2.4. Schematic of Air-Mass spectra definition [37].

2.1.1 Direct, Diffused and Ground-reflected Radiation

The earth's surface receives three main solar radiation components, beam radiation (direct radiation), diffused radiation and Albedo (ground reflectance) as illustrated in Figure 2.5. Direct radiation refers to solar radiation that travels in a straight line from the Sun to the Earth's surface without being scattered by the atmosphere. This phenomenon is known as the principle of rectilinear propagation, which states that light travels in straight lines through a homogeneous medium, such as air, water, or glass [38]. It is the most intense form of solar energy and is most prominent under clear sky conditions. In contrast, diffused radiation revolves around Rayleigh scattering of molecules in the atmosphere, scattering by dust particles and absorption gases such as oxygen, ozone, water vapour and carbon dioxide (CO_2).

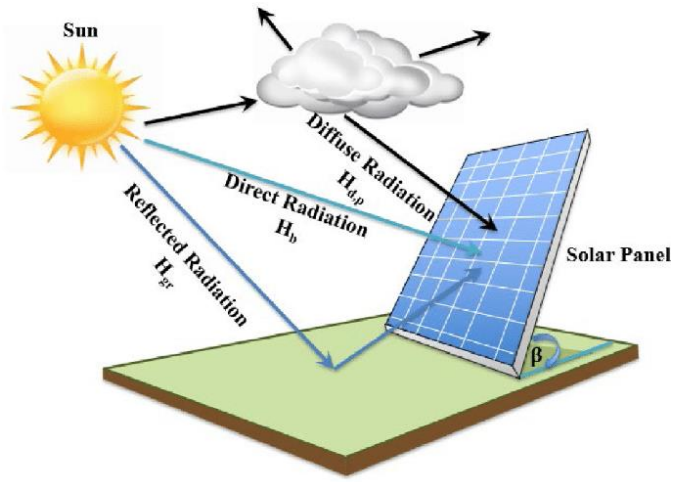


Figure 2.5. Direct, Diffuse and ground reflection (Albedo) [39].

The proportions of diffuse and beam radiation are strongly dependent on weather conditions. From research, it is difficult to quantify a general ratio of the amount of diffuse to direct radiation, but in sunny weather with clear skies, some 30% of the radiation is diffused by the time sunlight reaches the earth [29]. This theoretical rule of thumb is almost identical to the average percentage of diffuse radiation to the direct radiation observed in the Maltese Islands at 29.7% [40]. In cloudy weather with a lack of bright sunshine, most of the incident radiation is diffused. Since the shadow effect is substantially diminished at high rate of diffused radiation in comparison to the direct radiation, such weather conditions (cloudy skies) were excluded throughout the outdoor experiments conducted in this study.

A third component of solar radiation that must be considered in solar energy applications is albedo radiation, which is the portion of solar radiation reflected from the ground and surrounding objects onto a surface. The amount received depends on the ground's reflectance and on the tilt and orientation of the surface. Modern advancements in PV systems have introduced bifacial solar technology, which enables energy generation from both faces of a PV module as illustrated in Figure 2.6. This is accomplished by harnessing reflected solar radiation, termed surface reflectance, from the ground or nearby surfaces onto the rear side of the module. By capturing the reflected light from surfaces such as white or silver painted roofs, bifacial panels can achieve energy gains of up to 10–30% compared to traditional monofacial panels, depending on surface reflectance and environmental conditions [41].

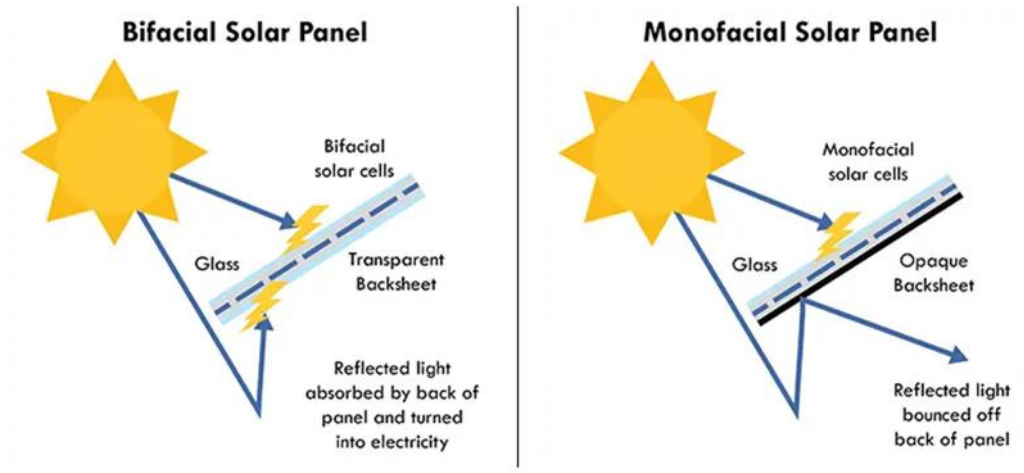


Figure 2.6. Comparative diagram of Bifacial technology tacking advantage of the ground reflectance and traditional monofacial PV modules [42].

With the global irradiance on a horizontal surface, $(E_{G,hor})$, and the Albedo (A); the ground reflected irradiance on a surface with tilt angle γ_t $(E_{refl,tilt})$ becomes:

$$E_{refl,tilt} = E_{G,hor}\, A\, \frac{1}{2}\,(1 - cos\gamma_t) \tag{1}$$

During this study, the focus was solely on the front monofacial side and does not include any bifaciality energy capture. Moreover, to maintain consistency in the fundamental settings of the forthcoming experimental setups in this thesis and to minimise ground reflections, the PV sources will be installed flat at 0° without any inclination.

2.1.2 Sun Position

The sun's position, depicted in Figure 2.7, plays a crucial role in solar energy systems, affecting both solar radiation intensity and shading patterns. Understanding parameters such as solar altitude, azimuth, and the sun's path is essential for the forthcoming chapters. Solar position or sun-path diagrams are essential tools for visualising the sun's path throughout the day. These diagrams can even take the form of 3D models, such as the one developed by Andrew Marsh [43]. They illustrate the sun's altitude and azimuth for each minute and hour of selected days, with curves connecting the plotted points to represent the sun's trajectory. While various tools are now available to estimate the sun's position for a given date and time, the fundamental factors for determining sun position at a specific location have been detailed in [44], are summarised below and will serve as the basis for the experiments in the upcoming chapters.

γ_S represents the solar altitude angle, or the elevation angle. This is defined as the angle of the sun relative to the earth's horizon [45].

α_s represents the sun's azimuth, which represents the angle between geographical north and the vertical circle through the centre of the sun.

The **zenith** is the point in the sky directly above an observer, while the **meridian** is an imaginary line that runs from the north to the south point on the horizon, passing through the zenith.

With the latitude represents by **φ** of the location and the hour angle **ω.**

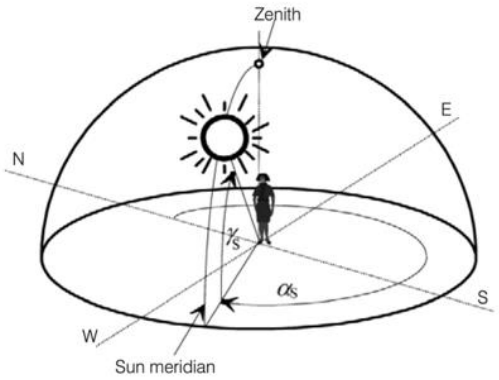


Figure 2.7. Visual diagram of the sun position angles described in this theory [46].

The angle of solar altitude (γ_S) and angle of solar azimuth (α_s) becomes:

$$\boldsymbol{\gamma_S} = arcsin(cos\omega \bullet cos\varphi \bullet cos\delta + sin\varphi \bullet sin\delta) \tag{2}$$

On condition that Solar time ≤ 12:00 h:

$$\boldsymbol{\alpha_s} = 180° - \arccos \frac{sin\,\gamma_S \bullet sin\varphi_s - sin\,\delta}{cos\,\gamma_S \bullet \cos\varphi_s} \tag{3}$$

On condition that Solar time > 12:00 h

$$\boldsymbol{\alpha_s} = 180° + \arccos \frac{sin\,\gamma_S \bullet sin\varphi_s - sin\,\delta}{cos\,\gamma_S \bullet \cos\varphi_s} \tag{4}$$

Equations (2) - (4) were adopted in Chapters 4-6 of this study as foundation for a code using the Python repository in Appendix H. The code utilises the 'ephem' and 'geopy' libraries to calculate solar positions at 15-minute intervals for every day of the year.

2.2 Basic Operation of a PV Source

Building on the importance of imaging and diagnostic analysis in PV systems, it is essential to first understand the fundamental operating principles of PV cells and modules, and how they contribute to power generation. A PV source may consist of a single solar cell or, more commonly, multiple cells connected in series to form a module. Several modules can be further interconnected to form a PV string, and multiple strings are combined to constitute a complete PV array or system, as illustrated Figure 2.8. These components are typically connected in series, which has implications for system performance under non-uniform conditions. For cases, when a portion of the PV source is shaded, a condition referred to as a 'current mismatch' arises, meaning that the "total current from the series-connected elements is limited to that of the lowest-producing unit" [47, p. 17].

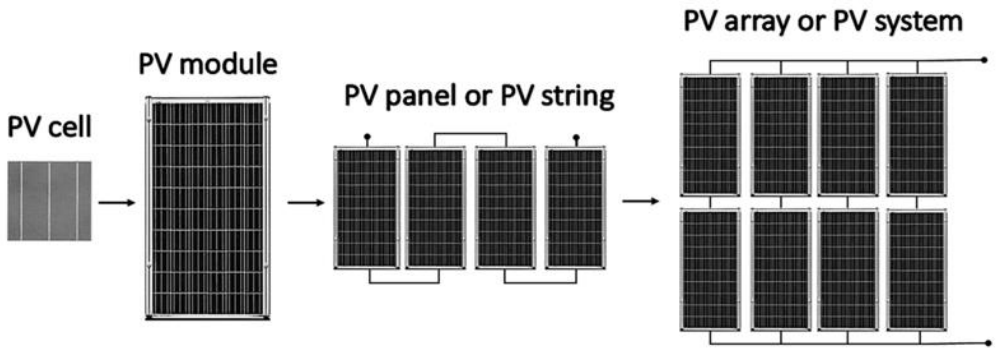


Figure 2.8. A visual representation of the common PV sources used [48].

The maximum power point (MPP) output, P_{MPP} (W) generated by a PV module during a specific time interval is influenced by two key factors. These include the solar radiation received by the module, G_{PV} (W/m²) and the temperature of the solar cells, T_c (°C). The temperature of the solar cells is itself affected by the level of incident solar radiation, the wind speed, the cells' efficiency, and the standard reference temperature, T_{ref} (°C). The maximum power output can be determined using Equation (5) [18], where A represents the surface area of the PV module (m²), T_{ref} refers to the standard reference temperature (typically set at 25°C), and β_0 is the temperature coefficient that quantifies how temperature influences the efficiency of the solar cell.

$$P_{MPP} = \eta_{T_{ref}} A\, G_{PV}\, (1 - \beta_0(T_c - T_{ref})) \quad (5)$$

The P_{MPP} is achieved when the PV module operates at a specific voltage and current corresponding to the module's characteristic I-V curve as seen in Figure 2.9 [49] [50]. This condition occurs under a fixed load that matches the internal impedance of the module. The relationship between the voltage (V_{MPP}) and current (I_{MPP}) at the MPP is given in Equation (6).

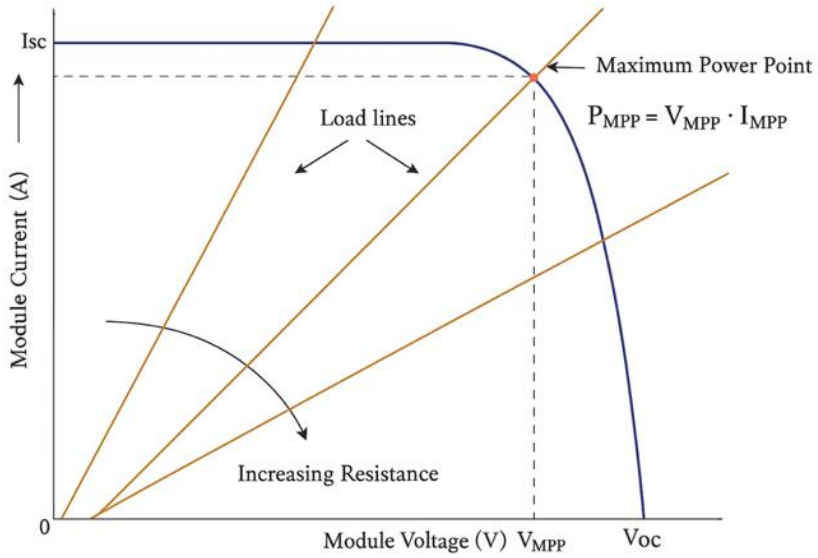


Figure 2.9. I-V curve of a typical PV cell and a resistive load [50].

$$P_{MPP} = V_{MPP}\, I_{MPP} \quad (6)$$

In modern PV systems, MPPT (Maximum Power Point Tracking) algorithms continuously adjust the load and optimise power output under varying environmental conditions [51] [52]. In principle, the current generated by a solar cell is directly proportional to the sunlight it receives. Under shading conditions at cell level, a single shaded cell in a string of PV modules limits the current flow of all other cells in that string. Furthermore, at the PV module level, it is characterised by non-homogeneous components across the entire panel surface. Even minimal shading in a non-uniform pattern can significantly impact the energy output [53]. Therefore, when a PV cell is shaded, the light-generated current (I_{ph}) decreases because fewer photons are available to excite electrons across the p-n junction. The total output current of a PV cell is given in Equation (7):

$$I = I_{ph} - I_D - I_{sh} \quad (7)$$

Where I is the output current of the PV cell, I_{ph} is the photocurrent generated by the incident light, $I_D = I_0 (e^{qV/kT} - 1)$ is the diode current and $I_{sh} = V / R_{sh}$ is the shunt leakage current. All units are in Amps (A).

A reduction in I_{ph} leads to an overall decrease in the output current. This results in a lower short-circuit current (I_{sc}), causing the entire I-V curve to contract downward as demonstrated by the red I-V curve seen in Figure 2.10. However, if a bypass diode is present and activated, the I-V curve exhibits a discontinuity or step where the diode takes over conduction. If bypass diodes are absent or ineffective, the shaded cell can go into reverse bias mode. Instead of generating power, it starts dissipating power as heat. In his study, Kumar et al. [54] reports that temperature has minimal effect on the I_{sc} at a rate of 0.4%/°C over Standard Test Conditions (STC). In contrast, both [55] and [56] observed that on the other hand, voltage is sensitive to light intensity but not as much as I_{sc}. Wolf et al. [57] show that the open circuit voltage (V_{oc}) varies logarithmically with light intensity but is less predictable since light intensity varies according to time of day and the size of the object obstructing the light source.

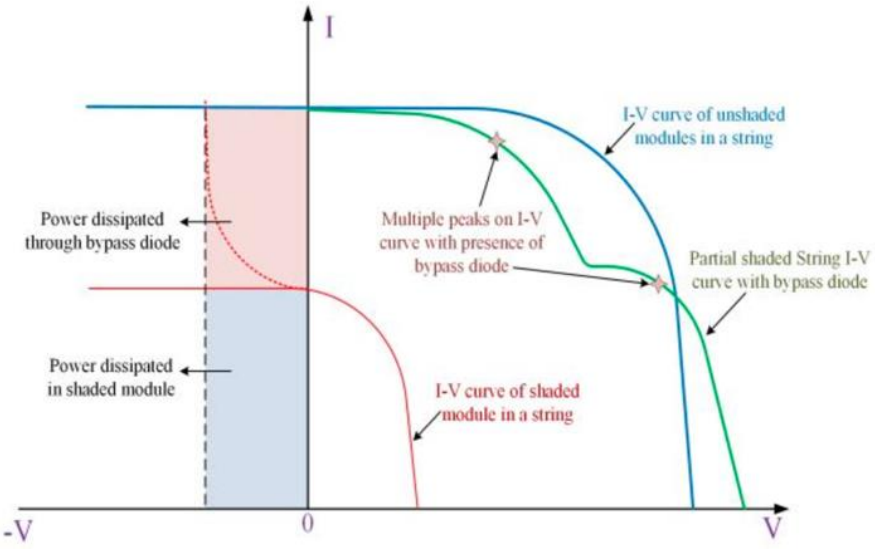


Figure 2.10. Characteristic I-V and P-V curves of a PV module [58].

2.3 Theory of Shadow Optics

The term ‘shadow’ is not scientifically defined as a phenomenon in which light is removed, but rather as an interpretation of the absence of light [59]. As mentioned in Section 2.1.1, the behaviour of light can be explained by the principle of rectilinear propagation. When light encounters an opaque object, some rays are blocked while others continue to travel in straight paths, forming distinct shadow regions on the surface where the shadow is cast. The size, shape, and clarity of these shadows depend on the relative positions and sizes of the light source, object, and surface. From this point onward, this study focuses solely on obstacles that yield thin object shading.

A shadow can be categorised into two distinct parts, the umbra and the penumbra [60]. The umbra is located directly in line with the object and the light source on the surface, creating the darkest part of the shadow. Moreover, surrounding the umbra is the penumbra, which extends outward and forms a partially lit region [61],[62] as seen in Figure 2.11. The penumbra exhibits a gradient effect, transitioning from complete darkness in the umbra to partial shading in the penumbra.

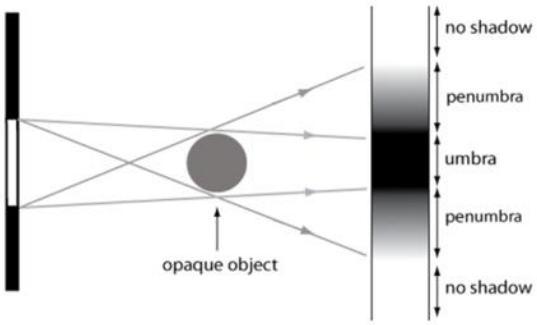


Figure 2.11. A representation of umbra and penumbra shadow with penumbra being shown as a varying-intensity shadow [62].

Nonetheless, in some research articles, diagrams may depict the penumbra as having a uniform grey intensity as seen in Figure 2.12, as opposed to a gradient effect. This simplification is intended for clarity, as a true penumbra always features a gradual transition in intensity toward the non-shaded region, labelled “no shadow” in Figure 2.11

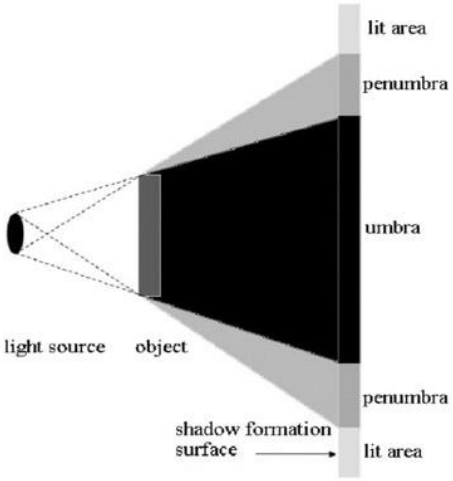


Figure 2.12. The principle of shadow formation indicating umbra and penumbra [63]. Penumbra is presented as having a uniform grey intensity, rather than a gradient effect.

The geometrical derivation of the size of the umbra and penumbra has been well established in astronomical studies conducted by NASA [64]. The Greek mathematician Thales, introduced the Basic Proportionality Theorem, often referred to as the Similar Triangles Theorem illustrated in Figure 2.13 [65], [66].. This theorem has been widely applied in geometry, including derivations based on Pythagorean and trigonometric principles, to estimate the size of the umbra using Equation (8) and penumbra using Equation (9), at a given distance. Key variables, such as the diameter of the Sun (approximately 1.4 million km) and the average distance between the Sun and Earth (149 million km), have been consistently validated by NASA [67] and Rozelot [68]. However, for a more precise calculation of the umbra and penumbra's size, additional factors such as the time of day and the day of the year must also be considered.

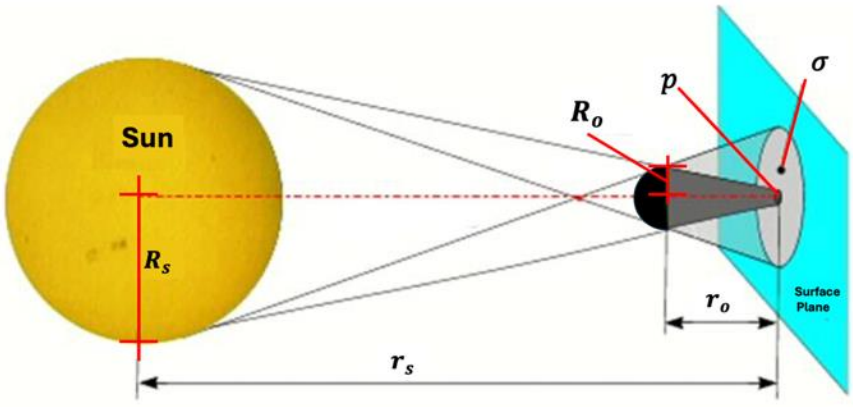


Figure 2.13. Geometrical representation of calculating umbra and penumbra as derived by the Similar triangles theorem [66].

where p is the size of the darker shade (Umbra), σ the size of the partially shaded (Penumbra), R_s the size of the source of light (The Sun), r_s is distance between the sun and the surface plane, R_o is the radius of the obstructing object whilst r_o is the distance between the obstructing object and the surface plane.

By using the similar triangles principle previously mentioned, the umbra and penumbra mathematical formulas can be deduced from Figure 2.13 as follows:

Therefore:

$$p = R_o - r_o\left(\frac{R_s - R_o}{r_s - r_o}\right) \tag{8}$$

$$\sigma = R_o + r_o\left(\frac{R_s + R_o}{r_s - r_o}\right) \tag{9}$$

With regards to the intensity of the umbra shadow, Pogge [61] observes that while Demouth et al. [69] describe the umbra as a region of total darkness with no light penetration, in practice, the umbra is not always completely dark. Therefore, total darkness is rarely achieved in shadow regions. This apparent contradiction highlights that in theory, an umbra shadow has an absolute value of zero, representing complete darkness; however, in reality, factors such as reflected radiation and the distance between the object and the surface cause variations in its intensity [70]. Furthermore, given that the distance between the sun and earth is far greater in proportion than the diameter of the object casting the shadow, the similar triangle theorem offers an approximate indication rather than a precise measurement. This concept is mostly applicable to the theoretical framework of space; however, when the object is on Earth, additional factors such as atmospheric scattering, surface reflections, and environmental conditions come into play, affecting the shadow's accuracy and intensity.

2.4 The Principles of Shadow Intensity Variations in Imagery

An image is defined as a "two-dimensional function, $f(x, y)$, where x and y are spatial (plane) coordinates, and the amplitude of f at any pair of coordinates (x, y) is called the intensity or grey level of the image at that point."[71, p. 50]. Digital images are primarily categorized into greyscale and colour images based on how pixel intensity values are represented and interpreted, as depicted in Figure 2.14. Greyscale images encode each pixel with a single intensity value, typically ranging from 0 (black) to 255 (white) in an 8-bit representation, capturing variations in brightness. In contrast, colour images, such as those in the RGB (red, green and blue) format, encode each pixel using three separate intensity values corresponding to the red, green, and blue channels, enabling a wide spectrum of colours through their combination.

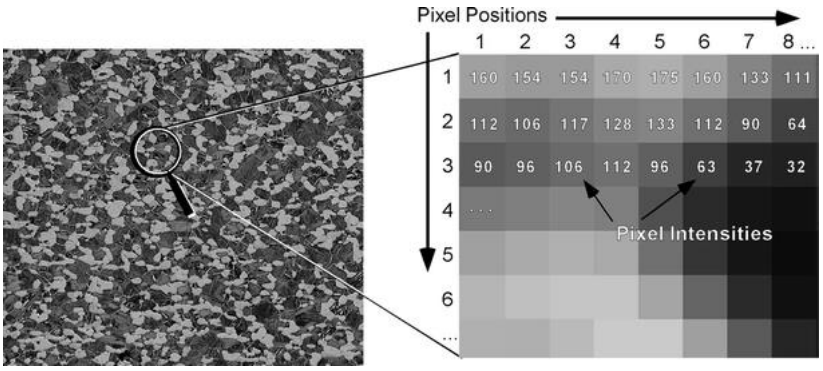


Figure 2.14. The individual pixels are arranged in x, y coordinate space with grey level, or intensity, associated with each one [72].

The precision of pixel intensity representation varies with bit depth. The conversion from RGB to greyscale is quite an intricate process especially to maintain the contrast, sharpness, shadow and structure as described by [73]. In 8-bit images, each pixel supports 256 intensity levels per channel, which are the most commonly used in images for day to day observations as exemplified by [74]. On the other hand, 16-bit images expand this range to 65,536 levels, offering finer gradations and greater precision. 32-bit images are often used for high dynamic range (HDR) imaging or for formats requiring additional channels, such as an alpha channel for transparency. Throughout this study, 8-bit images will be used for ease of functionality on a standard computer. Furthermore, pixel values can be normalised using min-max normalisation, mapping the

original 0–255 range to 0–1, allowing greater flexibility in scientific imaging applications [75].

Pixel intensity digitally represents real-world factors such as light intensity and surface reflectance, converting these physical properties into measurable image values. Brighter light produces a higher pixel intensity value, reflecting an increase in illumination [76]. A digital camera uses an image sensor and in the early stages of imagery, Charge Coupled Device (CCD) was the default option, however now it has been replaced by Complementary Metal-Oxide-Semiconductor (CMOS) which is a more cost effective option while using less power compared to CCD with equal performance [77]. This charge is then digitized by an analogue to digital converter (ADC) into pixel values, representing the intensity and colour of the light at each pixel. Imaging sensors, such as camera photodiodes, convert incoming light into electrical signals, which are then digitized into intensity values based on the sensor's dynamic range and bit depth.

The intensity pixel distribution within an image is traditionally represented using histograms [78]. These provide a visual summary of how pixel values are distributed across different intensity levels, enabling the analysis of shadow patterns, contrast, and overall image characteristics [79]. An image usually consists of a background which in a histogram will have the majority of pixels, whilst the ‘noise’ or subject in question will stand out. Figure 2.15a visualises a case where a small-scale PV module shaded by a foreign object is captured by the corresponding intensity distribution curve as seen in Figure 2.15b. Furthermore, shadows are almost always present in any image to provide a level of depth and realism of the image in question. According to Hussein et al. “The best definition of image noise is known as any degradation in the signal of the image and the external disturbance is the major reason for that noise” [80, p. 28]. Two very common types of noise in an image are ‘Gaussian noise’ and ‘salt and pepper noise’ which are increasingly common in low lighting scenarios especially in a laboratory environment.

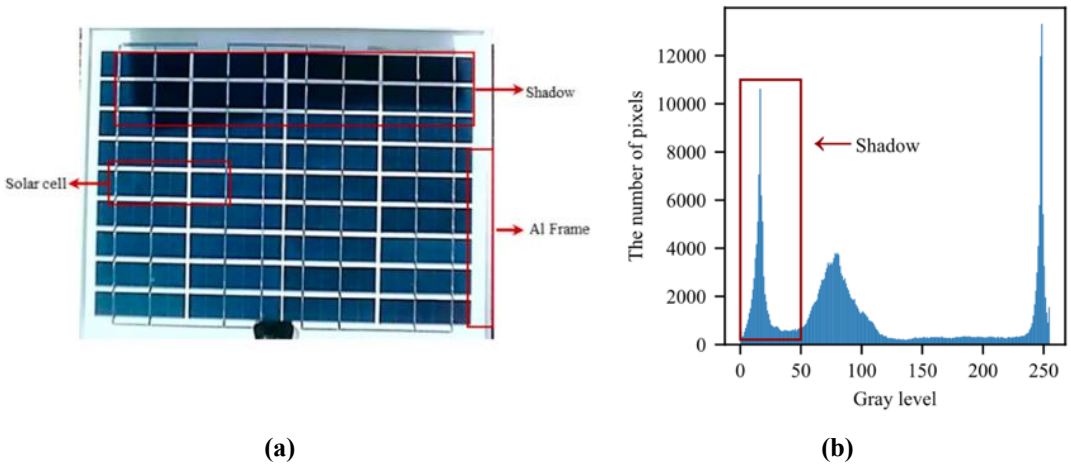


Figure 2.15. (a) A shaded small-scale PV module, **(b)** Intensity distribution equivalent of the image clearly indicating the shadow area due to darker grey level range [81].

In contrast to various noise levels in a laboratory setting, for well-lit up areas such as outdoor environment, certain camera sensors automatically adjust pixel values which does not fully match the actual reduction in light intensity. This discrepancy stems from the digital cameras' setting to apply a nonlinear response to light named as gamma correction settings [82]. Gamma correction is applied to sensor data to better match the human eye's sensitivity, which perceives brightness changes more acutely in darker regions than in brighter ones. As a result, when applicable, the camera's pixel intensity does not scale linearly with the reduction in light intensity. This nonlinear relationship means that a significant light reduction may correspond to only a modest drop in pixel intensity. Therefore, to correct such a fundamental principle when the gamma correction setting is active, in digital imaging and photometric analysis, inverse gamma correction can be applied to accurately map the pixel values to real-world light intensity levels, allowing for precise scientific measurements [83]. It is essential to determine the gamma correction of the specific devices that will be used according to the make and model. The equation to apply the inverse gamma correction is denoted in equation (10) where,

$\boldsymbol{g^{-1}(u)}$ is the inverse gamma pixel intensity value

$\boldsymbol{u}$ represents the normalised pixel intensity (ranging from 0 to 1)

$\boldsymbol{\gamma}$ is the gamma value that defines the degree of correction.

$$g^{-1}(u) = u^{\frac{1}{\gamma}} \tag{10}$$

By applying inverse gamma correction, one can mathematically reverse the exponential scaling to approximate a direct relationship between pixel intensity and incident light from the sun.

In image analysis, external objects such as camera filters are used to manipulate pixel intensity to enhance image quality, extract features, or enable analysis. Spatial filters, like Gaussian filters, smooth images by averaging neighbouring pixel values [84], while median filters reduce 'salt and pepper noise' by replacing pixels with the median of their neighbours [85]. Sharpening filters, such as the Laplacian filter, emphasise edges by enhancing intensity differences. Colour absorption filters adjust pixel intensity by selectively enhancing or reducing specific colour channels using mathematical matrices. Neutral Density (ND) filters uniformly reduce the intensity of all wavelengths of light, effectively controlling exposure without altering colour balance, which is particularly useful in high-intensity or overexposed images [86]. Thresholding filters simplify images into binary forms by setting intensity cutoffs, and high-pass and low-pass filters in the frequency domain emphasise or suppress certain spatial frequencies. These operations rely on mathematical techniques like convolution, scaling, and normalisation to ensure pixel values stay within valid ranges.

Pixel intensity analysis plays a crucial role in a wide range of fields, enabling tasks such as edge detection, thresholding, and segmentation to extract meaningful information from images. Techniques like the Canny Edge Detection method are widely used for identifying object boundaries and detecting fine details in images such as microcracks in Si solar cells [87]. Furthermore, classification of objects using the detection algorithm You Only Look Once (YOLO) is widely used in image processing tasks, dealing with pixel intensity analysis to detect and classify objects within an image or video frame with high accuracy and speed. Applications of YOLO include the detection of hotspots on PV modules placed in solar farms [88], as well as image collection using drones to conduct maintenance and multi fault identification on PV systems as described by Yin et al. [89] Furthermore, technicians use IR image analysis to detect abnormal pixel intensities, identifying defective cells, shading, cracks, or dirt in PV systems. Techniques like thresholding and intensity mapping enable precise fault detection, improving diagnostics, efficiency, and maintenance. Pixel intensity is also applied in

other sectors such as medical imaging which helps identify anomalies in X-rays, magnetic resonance imaging (MRI), and computerized tomography (CT) scans, aiding in the detection of tumours, fractures, or other irregularities. This highlights the significant impact of imagery and pixel intensity analysis, not only in renewable energy research but also in advancing critical applications across diverse fields. This section has thus established the foundational principles necessary for understanding shadow intensity in image analysis, particularly addressed in Chapters 4–6.

2.5 Conclusion

This chapter has outlined the fundamental principles essential for understanding the key factors that influence solar energy generation. These include the theory of solar radiation, the basic operation of a PV source, the theory of shadow optics and the variations of shadow intensity in imagery. A key takeaway from Section 2.1.2 on solar radiation is that the sun's position significantly influences the size and shape of shadows, depending on its altitude at a given time of day. This highlights the importance of applying a correction factor when conducting experiments over varying times throughout the day. Moreover, the theory of shadow formation, including the scientific categorization of shadows into penumbra and umbra, is key for subsequent chapters. Furthermore, the variations of shadow imagery have been explored, providing a foundation for deriving shadow intensity through innovative methodologies such as image analysis and pixel distribution. This includes emphasizing the importance of interpreting data from images captured using different photographic sources. The upcoming chapter, Chapter 3, shall build upon the theoretical fundamentals introduced in this chapter to present the current state-of-the-art in the realm of thin object shading.

Chapter 3 Literature Review

This chapter presents a review of existing literature in the realm of thin, partial and general shading on PV's. The purpose of this literature review is to identify current gaps in the field, provide context for the study, and support the development of the research. By examining key theories, findings, and methodologies used by researchers in area of study, this chapter begins to lay the foundation for deriving the research questions in the subsequent chapters. Key subtopics discussed include shading mitigation techniques, the impact of partial shading in a laboratory and outdoor environment, image analysis techniques, shadow image segmentation and the use of ML in shadow prediction.

3.1 Introduction to the State-of-the-art on Thin object Shading

PV systems are essential for renewable energy, directly converting sunlight into electricity, thus reducing the reliance on fossil fuels. However, shadows on PV modules present unique challenges, disrupting the performance of PV modules through localised power losses . Unlike hard uniform obstructions such as building shading, as defined previously in the definitions section of this thesis, thin object shading produces irregular and localised patterns of reduced sunlight on PV panels. This is discussed in detail in Section 3.2.



(a) **(b)**

Figure 3.1. (a) An example of hard shading by a building [90], **(b)** An example of a thin object shading from a rod [91].

These disruptions can lead to significant power losses, disproportionate to the size of the shadow on the PV source. Furthermore, shadows arising from thin object are dynamic and can vary in intensity, size and position throughout the day. Ignoring these characteristics can lead to significant underestimations of the adverse effects on energy production and module longevity. However, despite the importance of understanding the implications of thin object shading, this topic has received relatively little attention in the scientific literature. This absence of literature highlights the need for a more targeted investigation into the effect of thin object shading on a PV source.

The objective of this literature review is to provide a comprehensive analysis of current research on the factors influencing thin object shading, as well as methods to quantify the shadows they produce. This includes exploring findings and methods, such as algorithms developed by other researchers to model thin object shading both in outdoor and laboratory environmental conditions in the realm of PVs. Additionally, the review seeks to identify the limitations of existing methods, research gaps, and opportunities to improve the quantification and assessment of the impact of thin object shading and the complex varying shadow patterns they create.

This chapter shall proceed with the following order. Section 3.2 compares the effects of thin versus hard object shading. Section 3.3 outlines various shading mitigation components, including bypass diodes in Section 3.3.2 and MPPTs in Section 3.3.3. Moreover, in Section 3.4, focus is concentrated on outdoor environmental experimentation outlined in Section 3.4.1, and contrastingly, laboratory environment experimentation in Section 3.4.2. Simulation-based shadow modelling is discussed in Section 3.4.3. Image-based shadow analysis is covered in Section 3.5, focusing on shadow edge detection in Section 3.5.1, while Section 3.6.1 expands on image segmentation methods and enhancement techniques. Section 3.7 explores machine learning (ML) and statistical approaches in shading prediction. The chapter concludes in Section 3.8 by identifying current challenges and gaps in the literature.

3.2 Comparative Effects of Thin versus Hard Object Shading

The comparative effect of thin and hard shading arises from the distinct ways each type of shading forms shadows. To better understand their differing impacts on PVs, it is essential to examine the underlying reasons for the variations in shadow formation on PV modules.

Hard shading occurs when an object obstructs, either fully or partially, a PV module. This arises from large opaque objects such as buildings, which cast a sharp, well-defined shadow with minimal transition between light and dark intensity [92]. The shadow cast is mainly in the umbra form, (refer to Section 2.3 for a description of umbra and penumbra) the darkest shadow region, where no light reaches. The shadow's intensity is due to the obstruction being large or close enough to fully block the light, creating a high-contrast shadow with a sharply defined boundary and little gradation. A study by Al-Jumaili [92] specifically investigating hard shading effects utilised artificial irradiance generated by a Solar Module Tester (SMT) equipped with a pulsed and decaying light solar simulator, allowing for precise control over irradiance levels. Experiments were conducted in a laboratory environment under STC (1000 W/m², 25°C). Hard shading was simulated by applying opaque carton tape to selected cells of the module. The PV module used was a Solara® 130 W polycrystalline panel comprising 36 series-connected cells. The study found that shading just 25% of the panel area , results in a 41% loss in power output and the power of module was observed to be zero at complete hard shading case [92]. Contrastingly, thin object shading on a PV module involves shadows with a gradual transition between light and dark, often including both the umbra and penumbra. These shadows are lighter and less intense than those from larger objects, with decreasing intensity as they move away from the obstruction. This contrast is shown in Figure 3.2a and Figure 3.2b. Figure 3.2a shows hard shading on the PV module with a distinctive dark colour and a defined shadow region contrasting to Figure 3.2b which visualises a lighter thin object on the PV module spanning across multiple solar cells.



(a) **(b)**

Figure 3.2. An example of **(a)** hard shading [93] in contrast to **(b)** thin object shading [10].

In terms of the impact on PVs, studies such as Zulu and Kashweka [94] conducted experimentation using incandescent bulbs and cardboard to simulate artificial lighting and shading on a polycrystalline PV panel. Their results showed that hard shading caused significant efficiency losses and sharp dips in the I-V curve, even at 25% coverage. Similarly, Bimenyimana et al. [95] used MATLAB simulations and physical tests on monocrystalline, polycrystalline, and amorphous modules, shading 50% of each with cardboard. Their findings confirmed that hard shading leads to abrupt declines in I-V performance, especially in crystalline modules. A similar sudden dip was observed by Maghami [96], as illustrated in Figure 3.3, where the analysis under partial shading conditions was likely influenced by external shading mitigation mechanisms, such as bypass diodes, which are discussed further in Section 3.3.2.

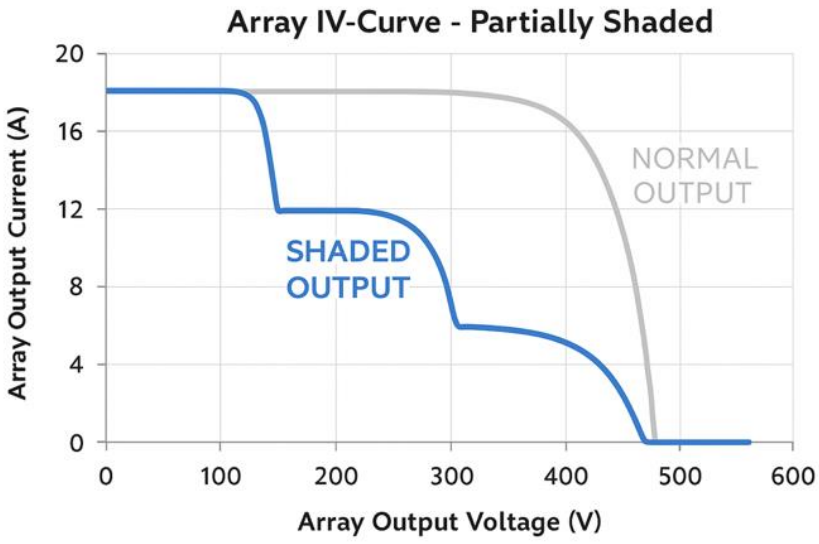


Figure 3.3. I-V curve under partial shading conditions [96]

A commonality between hard and thin object shading is that the impact is dependent on the orientation of the shadow. Indeed, authors such as Abdulridha [97] and Kareem [98] emphasised that the orientation and density of shading, are critical factors in determining the severity of energy losses, with horizontal patterns generally causing greater disruptions in both hard and thin object shading scenarios. Hard shading transposed horizontally on the PV module, has been shown to produce more severe losses than vertical shading due to the way the bypass diode configuration on traditional PV modules [99]. This is because horizontal shadows often span multiple solar cells as seen in the difference between the first and second image of Figure 3.4, creating greater disruption in current flow, as demonstrated by Kashweka et al. [94] .



Figure 3.4. PV module with different case shading where **(a)** demonstrates horizontal shading, **(b)** visualises vertical shading, **(c)** illustrates a single cell shading and **(d)** shows a diagonal coverage [100].

Similarly, while thin object shading may not always cause widespread effect on the PV module, it can result in significant power loss when aligned directly across the busbar pathways, leading to localised power losses, as noted by Kareem [98]. Moreover, Dorobantu et al. [28] showed that bypass diodes are effective at mitigating energy losses caused by hard shading by isolating portions of the PV module. However, their effectiveness diminishes in cases of thin object shading, where the localised nature of the shadow on the PV module does not trigger the bypass diode as efficiently due to the shadow being distributed with lower intensity across multiple areas of the PV module rather than concentrated on one cell.

3.3 Shading Mitigation Techniques

Over the years, researchers have developed and refined various components at both the module and inverter levels to mitigate the effects of shading, outlined in the review by Osmani et al. [101], and in the control and circuit techniques case example by Bidram

et al. [102]. However, not all shading mitigation innovations have been deemed financially viable for commercialization [103]. Santosh et al. [104] demonstrated that innovative reconfigurable topologies of the PV system such as including 25 extra Total cross tied configurations would increase the cost of each PV array by $50 which although justifiable in small scale PV systems, the economies of scale may not be justifiable for full-scale PV systems. However, significant advancements have been achieved to address long-term shading effects, which are economically feasible, reduce electrical mismatch, and prevent hotspot formation. Among these, bypass diodes and MPPT algorithms stand out as key solutions, successfully commercialised by leading PV manufacturers to mitigate the detrimental shading effect.

3.3.1 Hotspot Formation

Dhimish et al. [105] define hotspot formation as localised overheating on PV modules causing a rapid increase in degradation and irreversible damage. Hotspot heating in Si PV modules predominantly occurs under partial shading conditions, where one or more cells generate less current due to partial coverage of the PV module. Since PV cells are connected in series to form a module, the underperforming cell limits the current flow for the entire module. This mismatch forces the shaded cell into reverse bias, resulting in the dissipation of the voltage drop as heat loss [106], [107].

Simon et al. [108] provided a comprehensive study using IR thermography techniques to identify the root causes of hotspots in multi crystalline cells. Their findings strongly correlated localised hotspot formation with damage to the cell material in the actual solar cell directly correlates with hotspot heating. The damage to the cell material create shunt paths that lead to reverse biasing and localised heating, ultimately causing irreversible structural damage. In contrast, Numan et al. [109] emphasised the role of partial shading in inducing hotspots, employing IR imaging and I-V curve analysis under varying shading conditions. Their experimental results demonstrated that under increasing shading conditions, both the I_{sc} and maximum current I_{mpp} significantly declined, from 7.89 A and 7.1 A with no shading to 6.88 A and 5.88 A under full shading, resulting in a drop in output power from 107.92 W to 50.87 W. Additionally, shading induced substantial thermal variation, with the temperature difference between cells peaking at

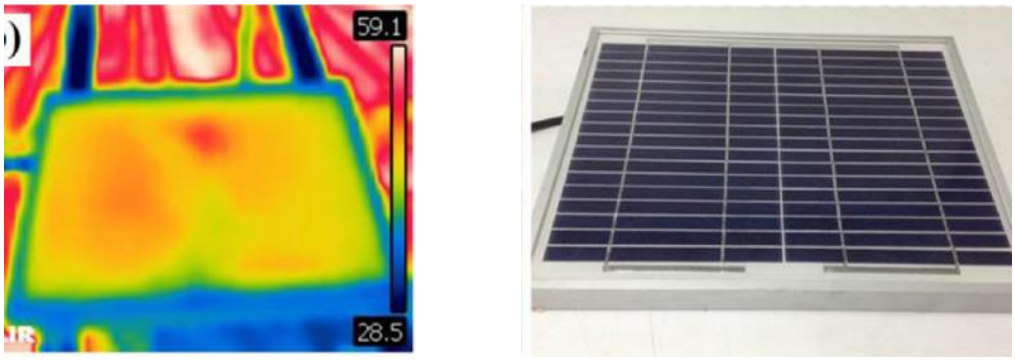
49.3 °C under 75% shading, indicating severe localised heating and increased hotspot risk. While Simon and Meyer focused on intrinsic material defects as the primary cause of hotspots, Numan et al. also highlighted operational and environmental factors like object shading as additional contributing causes [109]. A commonality between [108] and [109] is the use of IR thermograph to identify hotspot development on PV sources with Human et al. [109] concluding that thermographic camera is a key tool for quick hotspot identification.

Clement [110] observed that as little as eight minutes of partial shading on a solar cell is sufficient enough to trigger steady hotspot formation with minimal fluctuations. This phenomenon can occur unnoticed in a short period but leads to a prolonged linear degradation, contributing to 49% of all faults in PV modules [108]. To address these challenges, researchers have focused on developing efficient hotspot detection methods. To exemplify, Itako et al. [111] proposed an artificial intelligence (AI) based software solution as an alternative to traditional IR imaging. Their approach achieved 82.25% accuracy using only two parameters: string current and string voltage. This method eliminates the need for physical proximity to the PV system, enabling detection through PV plant monitoring software and reducing reliance on IR sensors and other hardware devices. Furthermore, AI based solutions are adaptable and can improve hotspot detection accuracy through deep learning techniques while lowering dependence on costly hardware components. Such advancements are particularly beneficial for large, remote power plants that are difficult to access. In contrast, Simon et al. [108] employed a conventional thermographic technique, providing a quick and effective means of locating hotspots. The technique reveals hotspots as distinct yellow regions, indicating abnormal heating patterns. Their findings highlighted that the I-V slope of a cell in reverse bias leads to power dissipation caused by localised breakdowns, resulting in hotspots. However, while the study successfully identified hotspots, it lacked detailed information on the type and characteristics of shading affecting the solar cells, limiting its applicability to real-world scenarios.

Pramana et al. [112] compared manual thermographic camera inspections by technicians to drone-based imaging systems. The drone algorithm scanned 126,000 modules in significantly less time than manual IR detection. However, while the drone technique demonstrated efficiency, its accuracy was not thoroughly validated. To enhance

reliability, future studies should incorporate cross-validation of drone-acquired thermal data with ground-truth measurements, such as on-site I–V curve tracing or localised thermographic inspections. Additionally, integrating ML algorithms trained on annotated datasets could improve hotspot classification accuracy and reduce false positives. Standardising flight parameters (e.g., altitude, angle, irradiance thresholds) could also help ensure consistency and comparability across different inspection campaigns. Enhancements, such as using a fisheye lens, allowed for quicker hotspot localisation. Despite these advancements, the study by Pramana et al. [112] emphasised the need for an algorithm that is both efficient and capable of detecting hotspots caused by nearby shading, yet can do so in a timely and accurate manner. Although many conditions for effective detection are met individually, few studies combine these methods into a validated solution for full-scale PV systems. Moreover, a complementary approach was proposed by Salazar et al. [21], who developed a hotspot detection technique based on IR thermography and k-means clustering implemented in MATLAB as seen in Figure 3.5. Their method successfully identified and quantified hotspots, including their average temperature and relative area, caused by cracks, junction boxes, and shading. The study demonstrated that detailed image analysis, particularly when using colour space conversion and clustering algorithms, can enhance fault detection accuracy and help isolate subtle thermal anomalies.

Together, these findings highlight the need for scalable yet precise hybrid inspection systems combining automated drone imaging with robust image processing and localised verification strategies.



(a) **(b)**

Figure 3.5. Example of a hotspot formation indicated **(a)** by a red spot on a **(b)** 10 W PV Module (right image) [21].

Proactively minimising shading and foreign object on PV modules prevents irreversible damage to solar cells, reduces power losses, and enhances system efficiency and longevity. Accurate shadow quantification is thus critical not only as a corrective measure but also as a vital design consideration.

3.3.2 Bypass Diodes

Bypass diodes optimise solar panel performance by connecting solar cells in an anti-parallel configuration between a string's positive and negative terminals. Nowadays, standard PV modules, having 60 or 120 cells, are divided into three submodules of 20 for the 60 cell PV modules and four submodules of 30 for the 120 cell PV module. When shading causes a cell to enter reverse bias, the diode redirects current to the adjacent substring. As shading moves past the PV module's edge, the diode returns to its forward bias state, ensuring normal operation as visualised in Figure 3.6.

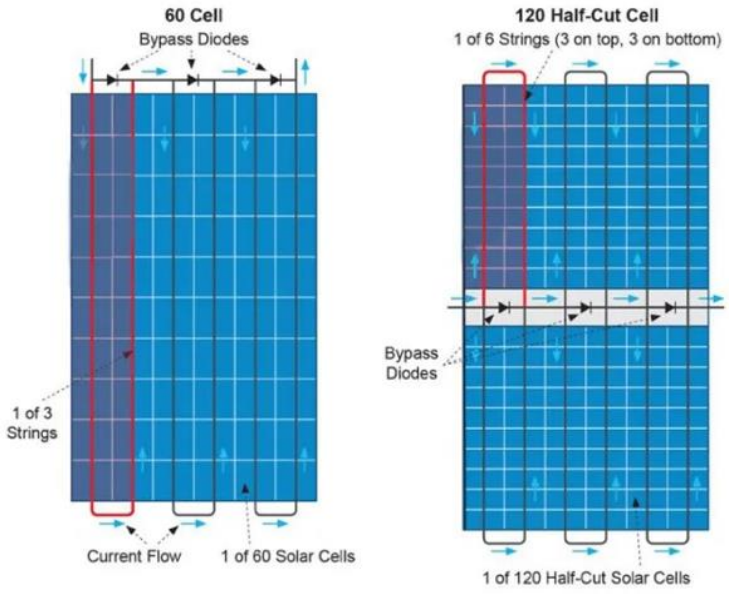


Figure 3.6. The difference between the two most commercially available bypass diode design on PV modules [113].

A study by Teo et al. [114] demonstrated that shading on a PV module leads to an unavoidable voltage drop across the entire string in a PV system, causing localised heating and a subsequent reduction in power output. Viera et al. [115] further validated that the use of bypass diodes significantly reduces power losses due to excessive heating

compared to scenarios without bypass diodes. However, the extent of this reduction depends heavily on the shadow's shape and position. Despite their advantages, bypass diodes also present certain drawbacks. Daniel et al. [116] observed that when a bypass diode is activated, the apparent MPP can increase, leading to a shortening of the active cell string and causing power mismatches within individual cells. This mismatch can negatively impact the performance of the entire module string. Additionally, studies by [58] and [115] corroborate the findings of [116], highlighting that the presence of multiple localised MPPs introduces significant challenges for MPPT systems in inverters. These challenges complicate the pursuit of the global MPP, ultimately exacerbating power losses under shading conditions.

Further research by Deline [118] demonstrated that bypass diodes are triggered when partial shading covers approximately 24% of the PV cell. However, it was noted that bypass diodes could ideally be more sensitive to such shading coverage, as shading in the range of 0-24% can still significantly reduce the PV module power output. These observations highlight the complex interplay of factors, such as temperature, in bypass diode operation. While bypass diodes are often associated with reducing shading losses, their primary role is to protect PV modules from hotspot damage and extend their lifespan.

Bypass diodes remain one of the most extensively researched hotspot and shading mitigation strategies, with most aspects of their design and functionality already well-explored, leading to the cost-effective integration of these components in modern PV modules [119], [120], [121]. However, for experimentation purposes, it is crucial to understand the specific bypass diode configuration within a module to ensure methodological transparency, as the raw effect of PV behaviour excludes the influence of bypass diodes.

3.3.3 Maximum Power Point Tracking (MPPT)

Bypass diodes provide initial shading mitigation at PV module level. Present inverters have evolved beyond simple DC-to-AC conversion to include advanced features such as global power peak tracking through multiple MPPT inputs. Researchers such as Lee and Yun [122] and Fri et al, [123] are focusing on improving inverter MPPT algorithms

to enhance system performance while minimising the number of components in a PV system. While both studies aim to enhance MPPT performance under varying conditions, Fri et al.'s [123] method targets centralized, grid-connected systems using improved voltage-current sampling to reduce error during irradiance shifts, whereas Lee and Yun [122] focus on distributed MPPT with an adaptive dual-step algorithm tailored for module-level power electronics. Simulation results from Fri et al [123]. showed near-zero tracking error and stable DC bus voltage under rapidly changing irradiance, while experimental validation by Lee and Yun [122] demonstrated superior tracking efficiency, faster variation response, and reduced oscillations compared to traditional and adaptive MPPT methods. These outcomes highlight that while both approaches improve MPPT effectiveness, Lee and Yun's solution offers better scalability and precision for modular PV architectures. Moreover, this shift to software based mitigation measures reduces hardware dependency and emphasises software-based solutions, aligning with Lusser's law, which states, "The reliability of a series of components is equal to the product of the individual reliabilities of the components" [124].

As stated in Section 3.3.2, bypass diodes create multiple local MPPs and therefore algorithms encounter difficulties in optimally establishing a global MPP as visualised in Figure 3.7. In the figure one can note that the MPP at unshaded conditions at the apex of the curve indicated in black has been diminished to two local MPPs indicated in the red curve of Figure 3.7. Li et al. [125] concluded that in order to avoid the MPP from falling into the local power points (small peaks of the red curve in Figure 3.7) , a jump out method must be created using segmented mathematical modelling under partial shading conditions. Guerriero et al. [126] underscore that MPPT algorithms can also be tested using a simple PV bench setup comprising of a PV source, a load section, and a data acquisition system which is used by most researches to test their prototype algorithm before field experimentation. In this manner, researchers have a faster way of testing out the rapidness of the algorithm in question to effectively track the global power peak in a fast and timely manner without having to setup complex setups. Eltamaly et al. [127] managed to reduce the time from a conventional MPPT algorithm of 8 seconds down to 3 seconds. This was achieved by updating the memorised global peak (GP) by forcing the PV system to work at the duty ratio of the current GP rather than the duty ratio of the highest sensed GP which increased the output energy and

efficiency of PV systems. Similarly, in their respective research, Eltamaly et al. [127] and Shankar et al. [128] both use PSO (Particle Swarm Optimization), a metaheuristic swarm technique widely adopted for MPPT under partial shading conditions. Shankar et al. implemented an enhanced PSO in conjunction with various PV array configurations to optimise the power extraction, while Eltamaly et al. [127] benchmarked PSO against their proposed bat algorithm, utilizing PSO's swarm dynamics to track the global peak amidst dynamically changing shading patterns. Moreover, the authors of [128] suggested the inclusion of PID (Proportional Integral Derivative) controller to enhance MPPT tracking. Adaptive tracking has gained popularity and demonstrates superior performance in navigating these complex Power-Voltage (P-V) characteristics. Having said that, one needs to delve deep into the addition of such the PID controller and produce a cost benefit analyse to see its feasibility and practicality.

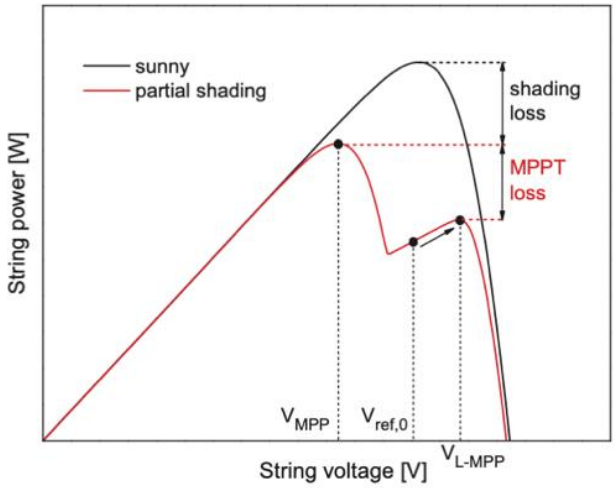


Figure 3.7. A P-V Curve of a PV system under partial shading conditions showing a power loss due to MPPT failure [125].

The literature on various MPPT algorithms has predominantly been targeted towards improving power generation on the general partial shading conditions. However, specific algorithms targeted towards thin object shading is relatively limited. Thin object shading is inherently less predictable due to its simultaneous impact on multiple solar cells and module substrings, leading to significant performance variations. As a result, MPPT algorithms must incorporate sophisticated real-time analysis and rapid response mechanisms to maintain system efficiency. Therefore, over reliance on software

algorithms for compensation can reduce overall system effectiveness, particularly when these algorithms are not perfectly optimised to handle specific shading scenarios.

3.4 Experimental Impact of Partial and Thin Object Shading

The current state of the art on partial and thin object shading explores various methodologies for assessing detrimental effects under different scenarios. This section categorizes the literature into outdoor experiments, laboratory tests, and simulation predictions in order to elicit the existing gaps that shall thus guide the subsequent chapters in this study .

3.4.1 Outdoor Experimental Studies on PV shading

Outdoor experimentation is a popular approach to quantify the effect of partial shading as it provides a real-life setting. However, the lack of standardised experimental methodologies makes comparing research on partial shading challenging [129]. Variability in approaches, such as the use of different sized PV modules often leads to inconsistent results and limits the comparative aspect. Additionally, shadow formation quantification is frequently secondary to the primary focus on mitigation techniques, such as reconfiguration and hotspot prevention.

Numan et al. [100] conducted a comprehensive shading analysis on a small scale PV module consisting of 36 series connected solar cells to simulate the impact of shadowing under controlled conditions. The study utilised opaque cardboard cutouts, proportionate to the desired shading percentage, to replicate shading effects across the module. MATLAB was employed for initial modelling, enabling the exploration of different shading configurations. Results from outdoor experiments revealed that 100% shading condition is considered the power decreases by 99.36 %, 43.7 % and 41.15% for horizontal, single cell, and vertical respectively, as seen in Figure 3.8a, Figure 3.8b and Figure 3.8c respectively, compared with their initial value at no shading condition. This showed that horizontally shading the whole PV module would affect the whole PV module resulting in a cascading effect. These findings provide evidence that horizontal

shading, observed in Figure 3.8a, has the most significant negative impact on power generation compared to other shading configurations [100] such those in Figure 3.8b and Figure 3.8c.

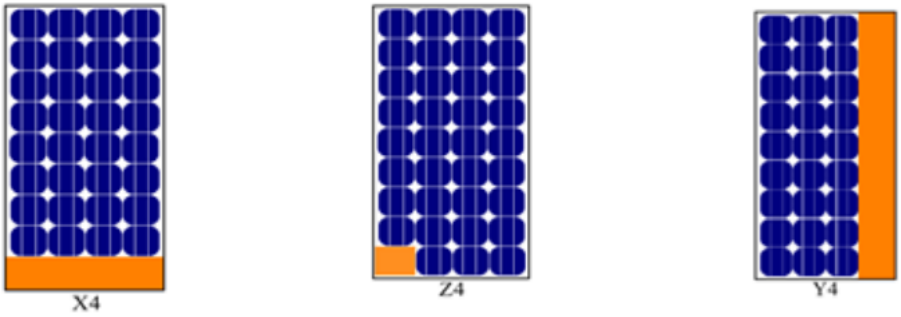


Figure 3.8. A visualisation of the shading case scenarios studied by Numen et al. [100] where **(a)** represents the horizontal shading **(b)** singe cell shading **(c)** vertical shading.

Notably, the horizontal shading results obtained by Numan et al. [100] closely aligned with those reported in the works of Dolara et al. [24]. Based on their findings, both authors concluded that a full-sized PV module has non-linear characteristics when portions of the PV module are shaded. However, the study's approach did not account for the dynamic nature of shadows in realistic scenarios. Real world shadows are rarely opaque, uniform and situated directly atop of the PV source; they often involve variable factors such as ground reflection and diffused radiation. These factors all contribute to a change in shadow formation on the PV module, namely varying between the shadow being dark or light in nature in contrast to the complete coverage of portions of the PV module using the carboard setup visualised in Figure 3.9.



Figure 3.9. Percentage shading a single row of cells using a physical experimental methodology [24].

Rather than conducting outdoor experimentation on a full-sized PV module, Luo et al. [130] focused on shading on a single solar cell within the PV module. In this case shading percentages were calculated relative to the individual cell rather than the entire module, as illustrated in Figure 3.10. Under clear-sky conditions, the module's power output, initially 275 W in the absence of shading, plummeted to 25 W when one single cell was shaded. This is observed in the graph of Figure 3.10. Interestingly, the orientation of shading (vertical or horizontal) on the solar cell caused similar levels of power loss.

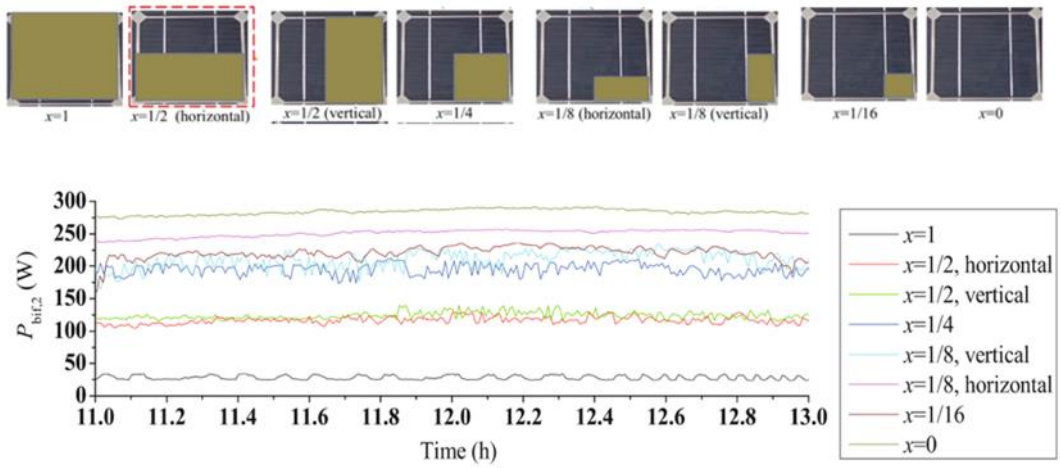


Figure 3.10. The power output of the whole PV module under the shading scenarios depicted on the right side legend, corresponding to the shading scenario in the upper portion of this figure [130].

In contrast to the non-linear shading impact observed when shading a full-sized PV module, horizontally and vertically, as previously outlined by Numan et al. [100] and Dolara et al. [24], Luo et al [130] demonstrate that shading of individual solar cells exhibited a more linear relationship between shaded area and power loss. For example, shading 50% of the single solar cell resulted in approximately a 50% power reduction, while shading one-quarter or one-eighth of the cell led to proportionally smaller reductions. These observations underscore the fundamentally different shading behaviours between individual solar cells and and complete PV modules. However, it is important to note that while these results were obtained under realistic conditions, they do not account for typical shading scenarios involving varying shadow intensity levels. Instead, they are primarily applicable to near total hard obstacle shadows, such as those caused by buildings and walls, since the solar cell or module are shaded by covering the source with an opaque object. Furthermore, neither study distinguished between the

varying gradient of shadowing such as the differences between umbra and penumbra shadows as the proper shadow formed on the PV source as previously described in Chapter 2 Section 2.3.

Among the limited number of research studies addressing thin object shading, Sinapis et al. [131] conducted experiments simulating pole shading by covering 1% to 2% of the PV module surface to assess performance under partial shading conditions. A significant 30-50% reduction in energy generation was observed when a vertical pole of 146 cm in height and 12.5 cm in width was located at a distance of 69 cm from the PV module. In the same research, the authors endeavour to categorise the weather condition as clearness index to gauge the sky conditions. The clearness index denoted by the authors as (Kt) is defined as the ratio of the measured global horizontal irradiance at site conducting experimentation and the extra-terrestrial irradiance just outside the earth's atmosphere. The value of Kt below 0.3 represents overcast days or low irradiance, while days with a Kt between 0.3 and 0.6 are considered mixed weather days of cloud coverage and sun. For days with a Kt above 0.6, the weather is classified as sunny [131]. Furthermore, the author comments that on days with overcast weather, where the largest part of light consists of diffuse irradiance, the pole had a negligible shadow effect on the power ratio. This result was observed when the PV system incorporated a traditional string inverter, power optimisers as well as micro inverter system. Similarly, Dolara et al. [10] observed significant power fluctuations caused by a medium voltage (MV) overhead line (electricity cable) shading a large PV plant as seen in Figure 3.11. This experiment allowed Dolara et al. [10] to consider relocating the position of the MV line to minimise the shading impacts over the PV system's operational lifetime and to simulate the MV line in a small-scale experimentation such as seen in Figure 3.12. Notably, in the latter work, the authors classified shading into umbra and penumbra, despite no correlation between distance and shadow intensity being investigated. Therefore, a lack of empirical evidence demonstrating how power loss varies at various distances (not just at fixed single value distances) from poles and MV wires is noted by both Dolara et al. [10] and previously by Sinapis et al. [131].



Figure 3.11. The PV plant Dolara et al. [10] used to analyse the overhead line shading.



Figure 3.12. The structure built by the Dolara et al. [132] to simulate the MV line shading.

In a similar study using a vertical 10 metre pole, Feng et al. [133] found that the initial power loss of 9.21% was significantly reduced to between 2% and 5% when the pole was moved further away, however, the author did not specify the exact distance at which the pole was moved further away. This reduction occurred because increasing the distance, lessened the shadow's intensity, thereby minimising its impact on the PV system's power generation. While there is substantial theoretical understanding of how shadow formation is categorised as umbra and penumbra, as was also presented in Chapter 2, very few researchers have undertaken the initiative to differentiate between these two shading formations, especially in the context of PV and thin object shading. An exception, however, has to be made for Teneta et al. [23] who explored the effect of thin vertical object shading whilst also categorising the shadows into the respective shadow formation of umbra and penumbra. Teneta et al. [23] replicated a realistic thin-

object shading scenario on a standard full-size PV module composed of three substrings, each containing 20 solar cells. Unlike earlier studies by Numan et al. [100] and Luo et al. [130] that used partial cardboard coverage on solar cells, this study simulated a narrow vertical shadow using a more representative thin object. The three shading scenarios are visually depicted in Figure 3.13. Scenario 1 (Figure 3.13a) resulted in a power loss of 1.40%, while scenarios 2 and 3 (Figure 3.13b and Figure 3.13c respectively) led to losses of 6.17% and 5.60%, respectively. These losses are notably lower than those reported in previous studies on vertical shading such as in [130] and [24], highlighting that shading introduced at a fixed distance of 36 cm, can produce significantly different shadow patterns. This underlines the importance of further research into realistic thin-object shading configurations. Additionally, Teneta et al. [23] only examined a fixed object distance (36 cm) and diameter (18 mm); future studies could explore variations in distance and object thickness to better understand their influence on power loss.



(a) **(b)** **(c)**

Figure 3.13. A visualised figure of the three thin object shading cases outlined by Teneta et al. [23] where **(a)** represents shading scenario 1, **(b)** shading scenario 2 and **(c)** shading scenario 3.

Moreover, in a comparative study on PV modules using half-cell (75 × 156.0 mm) and full-cell (156 × 156.0 mm) configurations, Tobar et al. [134] found that under chimney-induced shading, the half-cell technology significantly improved power output by 11.3% to 20.7%. This increase is attributed to the improved ability of half-cell designs in mitigating shading impacts across multiple substrings effectively, incorporated in the

PV module effectively. The observation of increase in overall power output attributed to half-cell technology was also observed by Mittag et al. [135] where an evaluation of the performance using SmartCalc.CTM and the economic impact of half-cell solar module designs using Scost tools were produced. By simulating different module configurations under standard and varied irradiance conditions, the researchers found that optimised half-cell designs can increase module power by up to 3.6%. and reduce specific costs (€/Wp) by up to 1%. These results further validate the adoption of half-cell technology as a commercial standard, attributed to its improved power output and lower module costs [135].

3.4.2 Laboratory Experimental Studies on PV shading

Whilst reviewing the state-of-the-art, only a limited number of research laboratories were deemed suitable and equipped to simulate shading conditions in a laboratory, whilst replicating STC conditions. The most commonly used equipment for this purpose is an I-V solar simulator with the light source corresponding to the one exemplified in Chapter 2 Section 2.1. The light source of the solar simulator is designed to generate direct beam irradiance of 1000 W/m² on a solar cell or an entire PV module. However, Plag [136] reports that even when using a spectrally matched light source and a calibrated reference cell, there remains an uncertainty level of 1.85–2% relative to STC values. While using the calibrated solar simulator is one of the most consistent and comparable for laboratory simulations [136], it still cannot achieve 100% accuracy. The precision of the results is heavily influenced by the procedures and calibration techniques employed by the researcher.

Utilising a laboratory setting guided by the IEC 60904 standard [137] to maintain controlled conditions, Kumari et al. [138] show that when shading the solar cell by 20%, the power loss observed was 11.6% in a laboratory environment and 15% outdoors as illustrated in Table 3.1. This trend continued on the 40%, 60% and 80% respectively where Table 3.1 demonstrated that an outdoor environment always produces more power loss than when compared to a laboratory environment.

Table 3.1. The comparative results by Kumari et al. between laboratory and outdoor experimentation on a full sized PV module with percentage solar cell shading [138].

Monocrystalline PERC PV Module	P_{max}		Power loss (%)		Efficiency (η)	
Shading percentage	Indoor	Outdoor	Indoor	Outdoor	Indoor	Outdoor
20	322.317	295.86	11.6	15.00	16.42	15.1
40	253.555	210.5	30.4	39.52	12.89	13.5
60	232.474	201.89	36.27	42.00	11.84	12.6
80	232.825	202.78	36.18	41.75	11.83	11.3
100	231.884	237.08	36.43	31.89	11.79	11.9

In his research study, Mamun et al. [139] analysed shading effects through laboratory experimentation under irradiance levels below 1000 W/m². The results demonstrate that when the solar irradiation increased by 100 W/m², the PV module's output power increased by 3.89 W under no shading, 3.37 W under 25% shading, 2.27 W under 50% shading, and 2.02 W under 75% shading. This indicates that while additional sunlight always increases power output, the amount of gain diminishes as shading on the module becomes more severe. Moreover, the short-circuit current and maximum power current increased with higher irradiance but decreased significantly with increased shading, whereas open-circuit voltage and maximum power voltage remained relatively stable.

Both studies by Kumari et al. [138] and Mamun et al. [139] demonstrate the nonlinear relationship between covering a portion of the PV module to replicate shading effects and PV systems, with [138] emphasising the importance of accounting for environmental conditions and diffuse light in outdoor settings. Moreover Mamun et al. [139] highlight the diminishing effect of shading impact as the coverage of shadow portion decreases. Collectively, these findings stress the need for adaptive PV designs that can mitigate shading effects and optimise performance across varied conditions.

Similar to outdoor experimentation, most studies utilising a laboratory environment focusing on shading, maintain the same approach of using hard shading to cover portions of a PV module. To the best of the author's knowledge, no studies have specifically investigated the effects of varying shadow intensities on PV modules or solar cells. Shadow intensity refers to the darkness of the shadow being applied, the units vary according to the methodology opted for by the researcher. Researchers often rely on non-realistic methods to simulate shading such as placing cardboard directly on top of the PV module, leaving this area underexplored. A study on general shadow properties

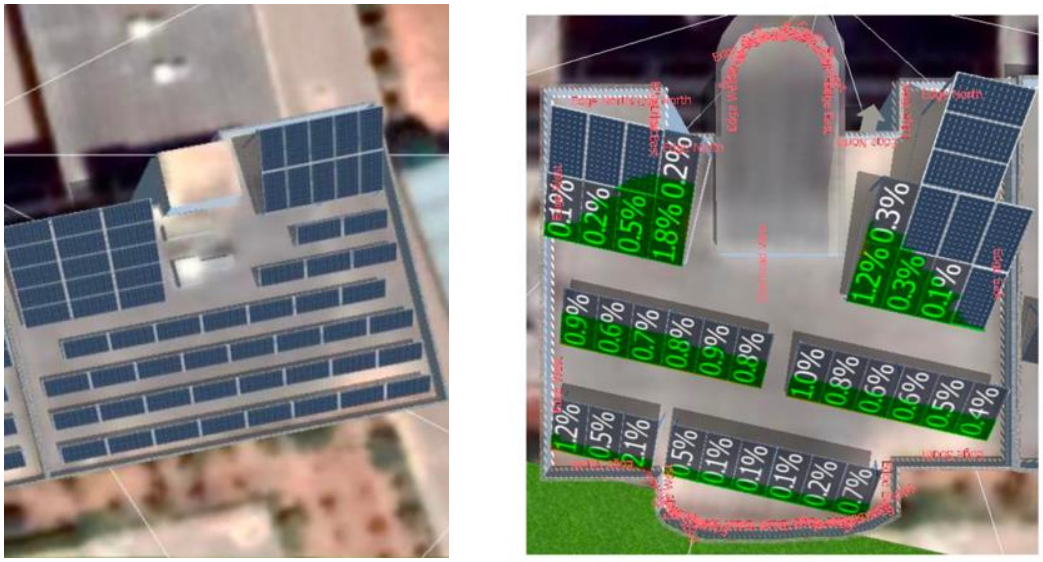
by Demouth et al. [140] demonstrates that as the height of an opaque object increases relative to a flat plane, the penumbra shadow becomes lighter but expands in overall size. While this observation aligns with the principles of optical physics [141], its implications for shading on PV sources remain unclear. Specifically, it is not well understood whether the increase in shadow size caused by the object moving further from the PV source compensates for the reduced shadow intensity in terms of the resultant power loss. In this context, the key predictors of power loss from shadows cast by thin objects near PV sources can be classified into two categories: the object's size, which has been studied more extensively, and its distance from the PV source, which primarily affects shadow intensity. This disparity highlights a critical gap in the current research on shading effects in PV system.

3.4.3 Shadow Modelling using Simulation Tools

Simulation tools are critical for understanding and mitigating the impact of shadows on PV systems. These tools enable researchers to model various shading scenarios, from simple geometric shadows to complex real-world conditions, and evaluate their effects on a predetermined PV system setup.

Nebojsa [142] emphasises on the importance of choosing the right simulation tool especially in complex PV plants where a dense urban setting is found. One such setting is avid in the Maltese islands and their landscape, which consists of significant surface shadowing from vertical third-party facades and building services equipment [143]. PV system modelling tools can be categorized into two main types. The first category includes general PV design tools like PVsyst, MATLAB and PVSOL; which were used in the studies of Grover et al. [144], Chedid et al. [145] and Ramadan et al. [16] respectively to study the effect of partial shading and special visualisation under varying conditions. As outlined from these three studies, the modelling tools employed are user-friendly, making them suitable for the vast majority of basic pre-determined PV design. Such tools often include predesigned PV module parameters, allowing users to quickly select and configure a full PV system and visualise shadows as they move according to time of day and day of the year. These tools offer a representation of a basic shading

effect as seen in Figure 3.14a and an illustrative shading effect value given to each module due to nearby shading in Figure 3.14b.



(a) **(b)**

Figure 3.14. PV shadow modelling using PVSOL for partial shading analysis where **(a)** represents the PV with simulated shadows at a given time of day and **(b)** illustrating the value of direct radiation lost due to array shading [16].

The second category includes advanced simulation tools such as MATLAB and PVSyst, which are widely used by engineers and researchers seeking a more detailed PV system design and analysis. Various system aspects can be simulated, including PV array configurations, integration of different MPPT algorithms, and the incorporation of bypass diodes in specified quantities [146],[147],[148]. One key advantage of computer simulation is the ability to evaluate multiple scenarios quickly and efficiently [149]. For projects involving diverse physical PV sources and combinational designs of PV equipment, starting directly with outdoor experimentation can be both time consuming and resource intensive. Instead, a best-practice approach often adopted in research is to first simulate various PV design configurations using tools like MATLAB and finally validate these design configurations in an outdoor setting. For case, the study by Tenata et al. [23] abided by this approach by first simulating multiple configurations in MATLAB and subsequently testing the best-performing design in real-world conditions. Furthermore, Silva et al. [150] were able to derive a shading factor calculation using small time steps of shadow modelling using MATLAB 'PV_LIB'.

Singh et al. [151] showcase MATLAB simulations' capability to adjust irradiance values by applying three different irradiance levels to three separate PV modules. However,

while reducing irradiance can effectively simulate hard shadows, Hernán [62] and Demouth [140] highlight other forms of partial shading, particularly emphasizing the distinct shadow formation of soft shadows created by thin objects. Therefore, one cannot just apply the same methodology for each partial shading scenarios especially to objects transposing different shadow formation than hard shadows from buildings.

Using MATLAB to model a PV module connected to an MPPT controller, Sameeullah et al. [152] reported that shading on even just one cell can cause up to 40% to 50% power loss. Sameeullah et al. [152] demonstrate the ability to easily vary the irradiance using predefined MATLAB functions, measuring and logging the time taken for these changes to occur. This enabled a comparison of how quickly the MPPT controller detects partial shading. Moreover, Sameeullah et al. [152] are one of the few researchers who verify the experimentation MATLAB simulation with a physical experimentation under artificial lighting. The results compared very well together with just minor discrepancies. This solidifies that when used in an appropriate manner, simulation tools especially MATLAB can be an effective tool to analyse basic shading scenarios on a PV system, without the need for actual physical implementation.

In the early stages of PV development in 1963, Rauschenbach et al. [153] mathematically simulated series resistance to identify shading in PV cells. Today, advanced simulation tools with interactive GUIs, such as PVsyst, used by Ajithgopi et al. [154] and visualised in Figure 3.15 are capable of modelling both domestic and commercial buildings, particularly to create a realistic scenario of the site and attain the estimate power output of the PV system over the span of the desired lifetime.

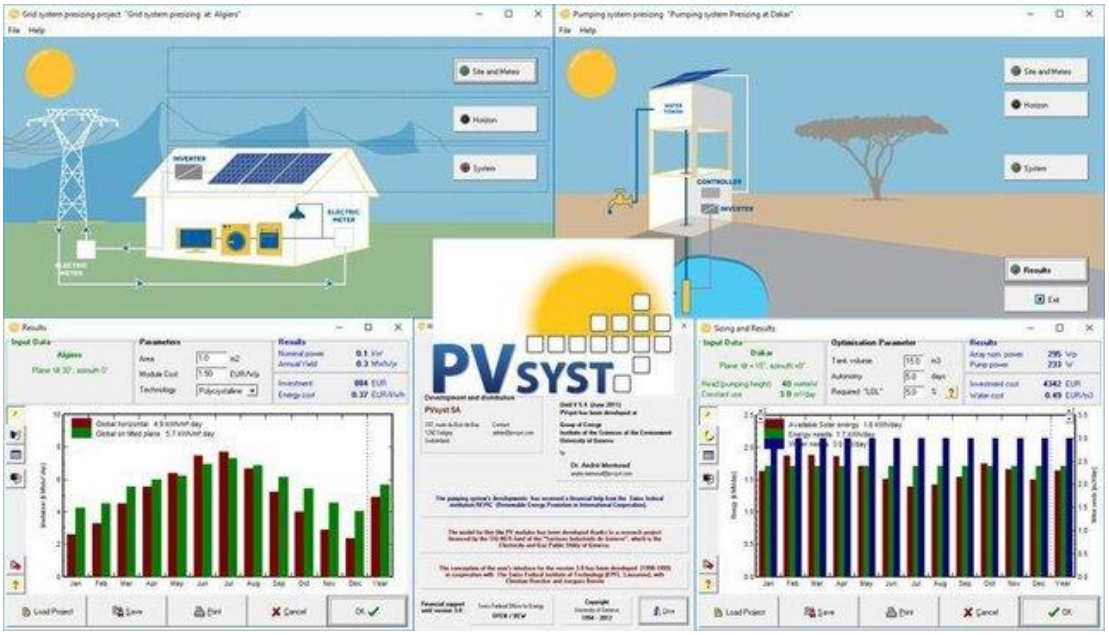


Figure 3.15. A screenshot of the interactive GUI created by PVsyst [154].

Despite the advantageous attributes, an increasing reliance on simulation tools, pre-defined models and datasets, may give rise to concerns during research. Ensuring that simulation parameters accurately reflect real-world conditions is critical, especially when validating results through outdoor or laboratory experiments. Wolk et al. [155] highlight that solar analysis tools are often overly optimistic, ignoring surrounding obstructions, or are too computationally intensive for timely urban-scale decision-making. To counteract Wolk et al. [155]'s claim, a study by Deline [118], models not only the building in question but also considers a portion of the nearby obstructions of pole shading to mimic potential neighbouring obstructions as well. Moreover, while the limited availability of resources is understandable, the current financial affordability of PV modules and the relative ease of measuring PV performance using low-cost pyranometers or reference cells; suggest that outdoor verification is increasingly feasible, even with limited resources [156], [154]. In the study by Axopoulos et al. [157], six PV simulation software packages were analysed, namely TRNSYS, Archelios, Polysun, PVSyst, PVSOL, and PVGIS. These were assessed for their accuracy in estimating energy output and solar irradiation using real data from a 19.8 kWp installation in Greece. Climatic data were input according to each software's capabilities, and results were evaluated using RMSE (Root Mean Square Error), MAD (Mean Absolute Deviation), MAPE (Mean Absolute Percentage Error), and model

efficiency [157]. TRNSYS showed the highest accuracy due to its use of detailed irradiance data. Among commercial tools, the software package Archelios, provided the best energy estimates but overestimated irradiation using Plane of Array (POA), while Polysun showed the most consistent overall performance. PVSOL accurately estimated irradiation but underestimated energy output. The main source of error was found to be the PV cell modelling rather than irradiation input, indicating that future improvements should target improvements in this aspect of the simulation models

One critical limitation of simulation tools is their limited approach to modelling partial shading. As discussed previously, a substantial amount of researchers simply replicate partial shading by reducing irradiance on a portion of the PV module [139], [158] and while this approach provides an acceptable approximation in some cases, it does not comprehensively represent the complexities of real-world shading conditions. Although lowering the irradiance on a PV module can mimic partial shading, this method oversimplifies the shading effect, which is inherently varying and context dependent. Dynamic shadows, particularly in urban environments, pose a significant challenge due to their constantly changing nature. In the vast majority of commercially available simulation tools, shadows are often depicted as one-dimensional patterns with sharply defined boundaries, akin to the concept of hard shading. For case, prior work often depicts shading as uniform, with predefined edges. However, this approach overlooks the varying characteristics of shadows, where intensity varies based on the distance between the shading object and the PV surface.

Commercial simulation tools, such as MATLAB and PVsyst, are constrained by their ability to model shadows as single-intensity, one-dimensional phenomena. This limitation primarily stems from the necessity for PV simulation software to ensure broad compatibility across diverse PV module and inverter configurations. Consequently, shading models within these tools are often simplified to maintain computational efficiency and user accessibility, which compromises the ability to simulate complex, localised shading scenarios accurately. For case, Freitas et al. [159] discuss how urban landscapes with complex topographies pose challenges for accurate shading analysis, leading to the adoption of simplified models in PV system design tools. Similarly, Lorenzo et al. [160] highlight the limitations of existing simulation tools in evaluating energy losses due to complex 3D shading scenes, emphasizing the need for more

sophisticated modelling approaches. This limitation underscores the need for more accurate quantification methods that account not only for the surface POA affected by shadows, but also for their intensity and structure. Specifically, the shadow formation involves an understanding of the distinct regions of umbra and penumbra which are critical for accurately model shading impacts.

3.5 Image Analysis Techniques used in PV Shading Studies

Throughout the years, the advancement of image analysis techniques has amassed popularity in identifying anomalies and inconsistencies at a given scenario. Image processing is described by Kour et. al [161, p. 1] as the process of "changing the nature of an image in order to improve its pictorial information for human interpretation, for autonomous machine perception". This approach has also been applied to detect and analyse shading on PVs, enabling more precise and rapid assessments, and thus aiding mitigation strategies [162], [81], [163].

Given that images are becoming increasingly sharp, detailed, and achievable by most available electronic devices, extrapolating partial shading data has become a possibility, leading to better detection of faults, cell hotspots, defects and dust detection amongst other applications [164]. Various methods of shading identification exist. One of the most popular, IR imaging, is used in applications such as the identification of aging in PV systems, as studied by [165]. In an image analysis approach, Salamanca et al. [166] developed a computer vision approach using standard RGB imagery and co-occurrence matrix features to identify solar panels without specialised lighting, enabling effective segmentation for further monitoring. Expanding on this, Henry et al. [167] presented an autonomous drone system equipped with RGB and thermal cameras to detect and localize faults such as hotspots caused by shading or soiling. Their method integrates flight path planning, image registration, and thermal analysis to evaluate PV module conditions at scale, achieving accurate fault localisation in a real-world 1-MW solar plant. Together, these studies highlight the potential of image processing techniques in automating PV defect detection and shading assessment.

3.5.1 Shadow Detection

The detection of shadows is crucial in the design of PV systems, as occasional shading can lower the MPP , resulting in a reduction in energy yield at the optimal MPP [168]. Bognár et al. [169] developed an algorithm called the 'Fit Grey-Box Model,' which establishes a method to identify locally shading periods of PV installations, using only measured AC power, regional irradiance data and basic information about the sites, such as orientation, tilt and power output as input variables. The authors endeavour to train the model, using the Support Vector Machine (SVM), which adapts the data assuming it as if under clear sky conditions. This is presented in the flowchart in Figure 3.16. The combination of the Fit Grey-Box Model and the SVM results in an algorithm capable of predicting local shading. The primary advantage of Bognár et al.'s algorithm [169] is its ability to forecast shading losses throughout the entire lifecycle of the system, whereas traditional inverters rely on real-time data to detect shading. However, a key limitation of this algorithm is that shadow interpretation must be performed manually by the user, making the process inefficient and time-consuming.

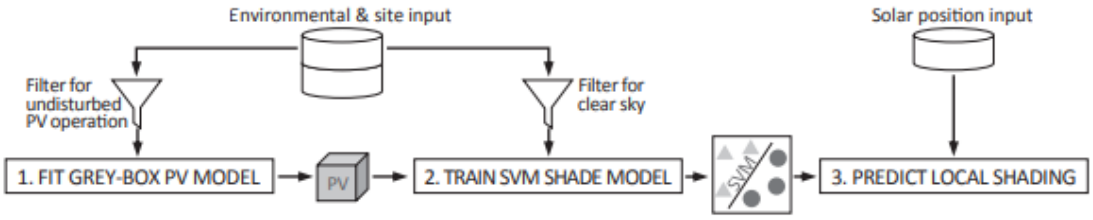


Figure 3.16. Flowchart of the three of the shade detection method by Bognár et al. [169]

Unlike Bognár et al.'s model [169], the model proposed by Sinapis et al. [170] can extract X, Y, and Z coordinates from a 3D representation of the roof and transpose them into a precise shading boundary image to better illustrate the shadow dynamics, as shown in Figure 3.17. The figure consists of the 3 PV modules inclined at 30^{o} from the horizontal surface marked and indicated in red where the pole shading was simulated at 09:00 am, 13:00 and 15:00 respectively for each PV module. Moreover, the intensity score on each cell is written in each of the boxes representing the solar cells of each PV module. Such an intensity score provided the authors a quantifiable measure of where the vertical pole shadow is transposing shadow on the PV modules. Additionally,

Sinapis et al. [170] simulated a typical I-V curve to validate the model. The monitored power output was then compared to the same parameters for unshaded conditions, with power conversion analysis incorporating plane global irradiance and module temperatures. This experimental approach would benefit from further validation against real-world data to substantiate the effectiveness of the point cloud method.

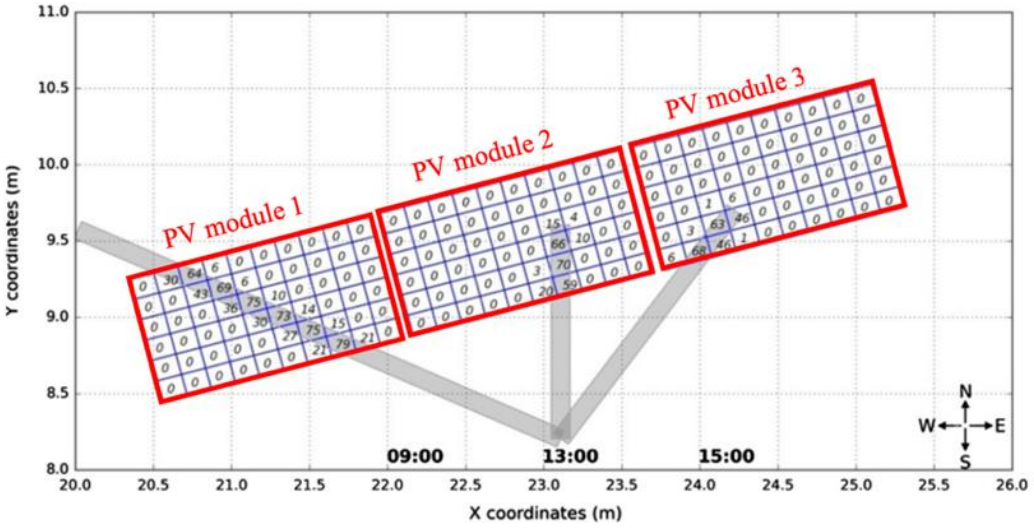


Figure 3.17. Graphic representation of a simple pole shading on 3 PV modules (plan view) [170].

Galeano's [171] research employed a methodology similar to that of Sinapis et al. [170], utilizing an image processing tool to analyse shading ratios, where 0 represented no shading and the value of 100 represents the case when the solar cell is fully shaded. This provided the author with a metric to identify and quantify the shadow coverage. In contrast to Bognár's [169] research, where shading was classified as either present or absent, Galeano's [171] study transposed images to greyscale, allowing shading to be detected at varying intensities. Consequently, similar to the study by Tian et al. [172], the greyscale image shown in Figure 3.18a was converted into binary small pixels as seen in Figure 3.18b, representing the shadow in a simpler form. The author applied a Tricolour Attenuation Model (TAM), which establishes the relationship between shadows and their non-shadow backgrounds across three RGB colour channels.



(a) (b)

Figure 3.18. (a) represents the captured RGB Image, (b) represents the left hand side image translated into binary, specifically focusing on the extracted shading portion [172].

In the study by Tian et al. [172], the authors developed a shadow detection approach that leverages the varying degrees of attenuation across the RGB colour channels. Their TAM quantifies how shadows reduce pixel intensity differently in each channel, enabling the distinction between shadowed and non-shadowed regions. To enhance accuracy and reduce reliance on multiple thresholds, they combined this colour-based attenuation with greyscale intensity information. By linearly blending the TAM image with the intensity image using an adaptive weight, the method produces a single composite image from which shadows can be segmented more robustly, using just one optimised threshold value. Compared to Tian's [172] method, the method requires extensive expertise in image processing, as it applies complex RGB formulae, contrasting with Galeano's [171] approach which offers a simpler yet effective alternative. Although Galeano's [171] method relies on greyscale imaging, its accuracy in detecting shading is comparable to Tian's, [172] with both yielding similar results. However, while the images are segmented into black-and-white representations of shading, it can be argued that shadows may still be difficult to detect, particularly in penumbra regions where shadow intensity is low [171]. Furthermore, the application of the TAM method alone may lead to false shadow detection due to the smoothing effect of computer-generated imagery.

Another effective approach for the automatic detection of shading in PV systems, as reported by Zbeeb [173], where multiple voltage sensors were positioned at the terminals of each PV module, resulting in effectively detecting partial shading conditions. In this method, the authors utilised a principle where as soon as the voltage of the PV module drops by 1V, the partial shading controller is alerted. Interestingly,

J.Ma [174] improved on Zbeeb's [173] study by adopting only one voltage sensor for an array of PV modules, introducing an automatic switching matrix and a controller to measure the voltages across each panel as illustrated in Figure 3.19.

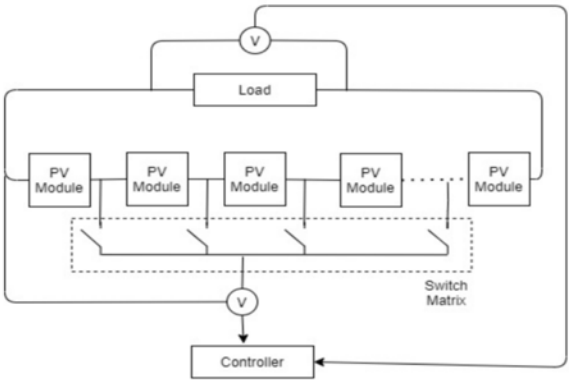


Figure 3.19. Block diagram for the proposed shading detection system first adopted by [175].

Having said that, Al Abri et al. [175], criticised this method as being incredibly expensive and not practical for large array sizes. Therefore, Al Abri et al. [175] employed a binary decision-making process. This enabled a step further from just detection, where the process systematically identifies potential courses of action to mitigate partial shading. Once partial shading is detected, a predefined mitigation procedure is initiated. Al Abri et al. [175] designed this system to be retrofitted onto existing PV installations being affected by partial shading. Furthermore, it would have been interesting if the retrofitting process of Al Abri et al. [175] was somehow integrated with Tian's [172] methodology, combining the voltage sensor system with the TAM model for enhanced shading detection. Additionally, Al Abri et al.'s [175] approach could incorporate the switch matrix and controller directly into the inverter, thereby minimising the need for external devices while maintaining an efficient and reliable partial shading detection system [171], [175].

Numerous shading-detection models, algorithms, and methodologies have been proposed, and several studies such as those conducted by Sinapis et al. [170], Galeano [171], and Al Abri et al. [175] have successfully demonstrated their effectiveness. However, these solutions are seldom integrated with MPPT algorithms or wiring reconfiguration techniques to optimise energy generation under partial shading conditions. Additionally, the complexity of certain detection algorithms, which often require specialised computer programming, limits their practical application for general-

purpose use by technicians and PV installers. To bridge this gap, there is a clear need for a user-friendly shading detection system, one that seamlessly integrates with PV simulators and indicator devices. Such a solution would not only enhance accessibility for practitioners but also improve the overall efficiency and adaptability of PV systems, ensuring more reliable energy output in real-world conditions.

3.6 Shadow Image Segmentation

Image segmentation partitions an image into meaningful regions based on pixel characteristics such as intensity, colour, and texture [176]. Shadows often introduce complexity in image analysis due to their varying shapes, intensities, and interactions with surrounding objects. Effective segmentation techniques help isolate shadow regions, enabling detailed analysis of the shadow [177].

In an early study conducted by Sural et al. [178], the thresholding analysis, used to segment an image to separate the object of interest from the background, was conducted with greyscale image rather than coloured Hue Saturation Value (HSV). The shadow was detected at cell level following a conversion to greyscale, providing the researcher with a number identifier between zero (pure black) and 255 (pure white) and transposed as a matrix. The concept was elaborated upon by Gutiérrez et al. [171] with a methodology that develops a way of identifying at cell level the percentage shadow on each cell on a PV module. This image analysis method enabled the authors to analyse the shading ratio; however, it lacked the ability to quantify the intensity of the shadows or distinguish between light and dark shadows [25]. Contrastingly, Rehman et al. [179] distinguished between light and dark shadows by classifying light shading as a solar radiation level of 500 W/m^2, and dark shadow with a very limited light transition of 100 W/m^2. The commonality among the aforementioned three studies is that, even at solar cell level analysis, none have adequately categorized the shadow into the proper optical shadow formations of umbra and penumbra.

It should be noted that researchers with theoretical background knowledge in shadow formation tend to achieve superior results in various image analysis applications than researchers with limited shadow formation knowledge. This is evident in Sinha et al.'s

study [180] where comprehensive principles of shadow formation, including the classification of umbra and penumbra formations, were applied alongside Otsu Method for thresholding to remove cast shadows from images [180], [181]. Otsu's method is an automatic image thresholding technique that determines the optimal threshold by minimising the intra-class variance (or maximizing inter-class variance) between foreground and background pixel intensities. Additionally, the authors identified various shadow detection methods, including intensity analysis, texture analysis, segmentation, mask construction, colour-based, and edge-based approaches. The study concludes that Otsu's method is more effective for shadow removal, the process of eliminating shadowed areas from an image, than for shadow extraction. Furthermore, Dendrinos [182] extends Sinha et al.'s work [180] by exploring the fuzziness of shadows (a different terminology used by the author for penumbra shadow) and identifying shadow border issues. This is termed the 'theory of fuzzy', encompassing the broad penumbra of shadows [182]. The same fuzzy shadow as cast on a white piece of paper was shown by Huang et al. [183], as seen in Figure 3.20. Moreover, to detect the shadow boundaries of umbra and penumbra, Huang et al. [183] were able to detect and converge towards the region of importance as seen in Figure 3.21a; subsequently plotting the intensity of pixels. This plot resembles a sigmoidal curve function as visualised in Figure 3.21b. The principle is based on Huang et al. 's [183] observation that an umbra shadow maintains consistent intensity, whereas a penumbra shadow contains a multitude of varied intensity levels. As soon as the umbra begins to lose its intensity, it can be classified as a penumbra. By constraining the penumbra shadow, the boundary where the penumbra ends and the background value begins, can be accurately determined. Given that the penumbra cannot maintain consistent intensity like the umbra, these features are crucial for delineating shadow boundaries.



Figure 3.20. Shadow cast on a white paper by building [183].

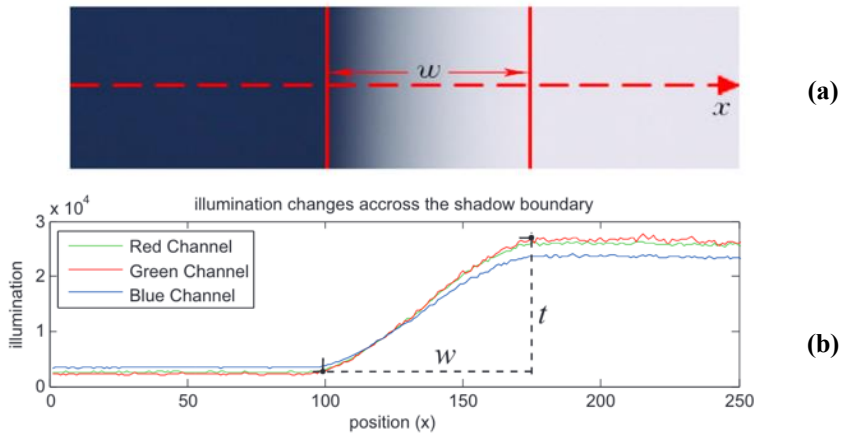


Figure 3.21. (a) depicts the shadow being analysed where w represents the penumbra region and x depicts the distance of pixels, (b) represents the corresponding sigmoidal function for the RGB image [183].

The sigmodal rule was further elaborated by Mirylenka et al. [184], with the given name as 'The Sigmoid Rule Framework' (SRF). The model classifier is a sigmoidal curve, corresponding to varying levels of label noise, enabling the identification and quantification of noise effects. In this framework, performance degradation due to noise follows a predictable sigmoid shape, where the inflection point, the steepest slope on the curve, indicates the region most sensitive to noise. By analysing the curve's minimum and maximum accuracy, slope, and range, the framework allows researchers to pinpoint how much noise a classifier can tolerate before its performance drops significantly. This sigmoidal modelling thus serves as a diagnostic tool, effectively revealing the noise threshold beyond which classifier reliability declines, and helping to distinguish between robust and noise-sensitive models. The points of interests outlined by Mirylenka et al. [184] are visualised in Figure 3.22. The main area of interest for the realm of shading in PV's is Z_* where the authors classify this as the active noise range, the region where performance changes significantly. The positioning of the noise range corresponds with the intersection points of W and t on the sigmoidal curve previously noted by Huang et al. 's [183], visualised previously in Figure 3.21b.

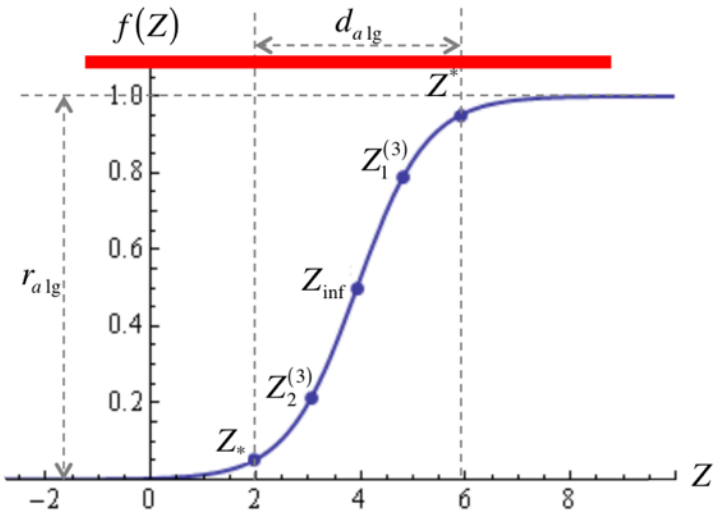


Figure 3.22. Points of interests on the sigmoidal curve, outlined by Mirylenka et al. [184].

3.6.1 Image Enhancement Techniques and Filtering

The basic principle of image enhancement is to modify the information content of an image so that it is more suitable for a specific application [185]. This technique is commonly used by researchers to improve image quality for better interpretation by refining contrast, sharpness, and noise [186]. In most cases, the raw image taken needs to be modified to attenuate certain detail.

Image enhancement has been described as a complicated task because it is not based on a general unified theory [187]. Moreover, image enhancement becomes a more challenging process due to the lack of a quantitative standard of image quality to act as a design criterion [188]. Liu et al. [187] conducted an extensive literature survey where, the authors highlighted the difficulty researchers find to measure and quantify the quality improvement from the original image when image enhancement techniques are applied. The quality of images is attributed not only to the resolution, but also through the colour scheme and sharpness of the subject compared to the background. Techniques such as 'Histogram Equalization' and adaptive contrast enhancement help in highlighting shaded regions of various images by improving the differentiation between illuminated and shadowed areas. These methods enhance image details, making it easier to detect and analyse shading effects similar to the one derived by Aziz et al. [189]. The

authors outline that histogram equalization works by redistributing the intensity values of an image, thereby enhancing global contrast and making hidden details more visible, especially in low-light or low-contrast conditions. The authors discuss its effectiveness across different domains, noting that it is computationally simple and particularly beneficial in scenarios where the visual quality of an image is critical. Despite its strengths, the paper also acknowledges limitations such as over-enhancement or loss of detail in uniformly illuminated regions, which motivates the use of more advanced or adaptive variants. This was further proven by Ramkumar et al. [190] where in their study, a Cumulative Distributive Function (CDF) is used as a form of 'Histogram Equalization'. Histogram equalization enhances image contrast by redistributing pixel intensity values so that their CDF becomes approximately linear. It does this by mapping the original intensity levels to new levels using the normalised CDF, ensuring a more uniform distribution of pixel intensities.

Dubey et al. [191] also proved that Histogram Equalization is considered better for image contrasts as compared to other methods such as Adaptive Histogram Equalization (AHE); where the enhancement is done locally on a specific region rather than globally. Moreover, Huang et al. [192] proposed an adaptive gamma correction using weighted distributions, which can automatically improve image contrast by using a smoothing curve. Moreover, greyscale histograms are commonly used to segment the foreground from the background in digital images and to segment the shadows of PV panels. The histogram can be used to select the threshold more accurately and facilitate segmentation [193], [194]. A greyscale histogram is a function of grey level and describes how often each grey level occurs in an image as seen in Figure 3.23a. The figure demonstrates that the majority of pixels are close to the 250 mark on the x-axis, indicating a light background. Moreover, the subject of the image is evidently shown by the left side subtle increase in the number of pixels. Furthermore, when the shadow is applied as seen in Figure 3.23b, the sudden spike of a darker grey shadow is evidently [81].

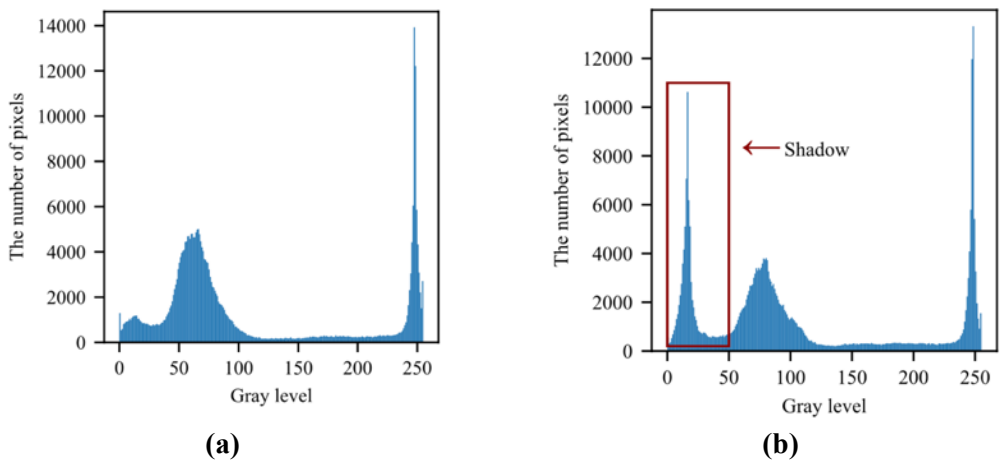


Figure 3.23. The difference between the histogram intensity distribution of an unshaded PV module observed in (a) and when a shadow is applied in (b) [81].

Traditional defect detection methods typically integrate filtering techniques with ML models, such as support vector machines (SVMs), to extract and process defect and external features [195], [196]. An anisotropic diffusion filter has been documented by Anwar et al. [197] for micro-crack detection in solar wafers, demonstrating high efficiency in preserving critical edges of the micro-cracks while smoothing less significant region of the image . Anwar [197] proposed a method for detecting micro-cracks in multi crystalline solar cells using electroluminescence imaging. The approach combines an improved anisotropic diffusion filter with adaptive thresholding to enhance low-intensity, high-gradient micro-crack pixels. Preprocessing removes periodic artifacts, and segmentation is achieved through double thresholding and intensity tracing. Shape classification is performed using Angular Radial Transform (ART) descriptors and SVM. Tested on 600 images, the method achieved 97.7% sensitivity, 80.2% specificity, and 88.6% accuracy [197]. Compared to standard techniques (Otsu, Sobel, Canny, LoG, FIR), the proposed method showed superior segmentation and classification performance. The study demonstrates an effective integration of image processing and machine learning for automated micro-crack detection.

Moreover, image enhancement techniques are also commonly used to remove shadow from images completely as the shadow is considered as noise using gaussian filters with results seen in Figure 3.24. In contrast, recent advancements have seen a shift towards end-to-end approaches, primarily driven by convolutional neural networks (CNNs) [100]. Unlike classical image processing, where filters are manually designed, CNN-

based methods optimise filters using large datasets, enabling direct defect detection from images. This approach has been widely applied to identify microcracks, foreign objects and defects on a PV Plant in conjunction with electroluminescence (EL) and IR images.

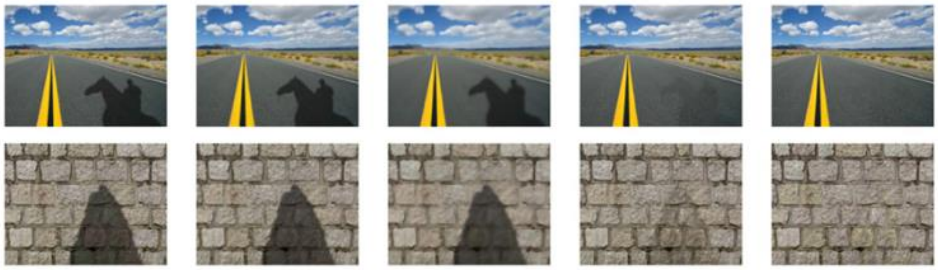


Figure 3.24. Different shadow removal results based on applying gaussian filters where the final two images on the right are the removal result using proposed filtering method in [196].

The study presented by Ju et al. [198] introduces a novel adaptive direction-tracking (ADT) filter for shadow boundary detection, significantly improving the efficiency and accuracy of feature extraction. This approach adapts to changes in the direction of object boundaries, extracting optical and statistical shadow features more effectively than traditional methods. The proposed ADT filter, coupled with a ML based classifier, achieved an accuracy of 84.63%, outperforming the methods of Huang et al. [183] and Lalonde's [199] approach, based on a traditional physical model of shadows, computes shadow characteristics like width, shape, and colour of the penumbra and extracts features such as shadow sharpness and dark-to-bright ratios. These features are then used in an SVM classifier, but the accuracy achieved is only 62.52%. Having said that, Huang [183] is one of the only researchers who opts to isolate the penumbra portion of the shadow from the main attributing shadow during the filtering process. However, the gradient of the penumbra intensity was also not classified. This could lead to an unfavourable result compared to the ADT filtering method used by Ju et al. [198]. On the other hand, Lalonde's [199] method employs a decision tree classifier with a CRF-based optimisation to improve pixel-wise shadow detection by ensuring more coherent contours and isolating weak edges. Despite this, Landone's [199] method performs the least well, with an accuracy of just 52.67%. The superior performance of the ADT filter method in the study Ju et al. [198] lies in its ability to adaptively track boundary directions, offering a more precise and efficient solution for shadow detection in terms of both feature extraction and classification accuracy.

3.7 Machine Learning and Statistical Approaches in Predicting Shading

Predicting the presences of shadows is challenging due to their varying nature, influenced by weather conditions and geographical location. Traditional shading prediction relies on modelling the PV system site and estimating shadows at specific times. However, with the growing adoption of Machine Learning (ML), shadows can now be detected and approximately quantified, driving significant research interest. Studies such as Latoui et al. [163] et al. and Kappler et al. [200] have explored various ML models, ranging from traditional regression to advanced ensemble and deep learning techniques, enhancing shading detection and power forecasting accuracy.

The study by Kappler et al. [201] focuses on ML based short-term power forecasting and shading detection. It demonstrates how large shading effects can be recognized and corrected using artificial neural networks (ANNs) and support vector regression (SVR). The use of kernel functions in SVR enables the transformation of non-linearly separable data into a higher-dimensional space, thereby improving forecasting accuracy. Commonly used ML methods for extracting the data from a PV system such as temperature, series or parallel configuration, voltage, current, power and shadow percentage, were evaluated to determine their correlation with each other by Olivares et al. [202]. Furthermore, the author evaluates five regression models consisting of linear regression, ridge regression, lasso regression, Random Forest regression, and XGBoost regression to predict the overall shading percentages on PV panels. The findings indicate that ensemble methods, a class of machine learning techniques that combine the predictions of multiple models to improve overall performance, particularly Random Forest and XGBoost, outperform linear models due to their ability to capture complex non-linear relationships. This is depicted by the performance metric evaluation in Figure 3.25, which shows the MAE and RMSE value on the primary y-axis, R^2 score on the secondary y-axis over the 5 types of regression model used by Olivares et al. [202]. This reinforces the notion that non-linear models are more suitable for predicting shading effects in PV systems, with the 5 variables previously outlined.

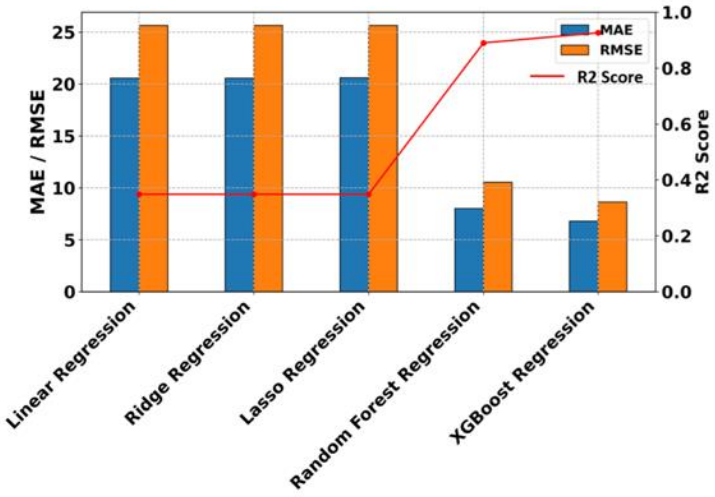


Figure 3.25. A comparative model performance using MAE, RMSE, and R^2 Score metrics [202].

Furthermore, the work of Gaboitaolelwe et al. [203] aligns with these findings by affirming that Random Forest was the best model for PV power forecasting compared the SVR, gradient boost and XGBoost, lasso regression, and multi-layer perceptron (MLP) neural networks. The affirmation was based on the author validating the performance of Random Forest and XGBoost by optimizing their hyperparameters and assessing their accuracy through 10 fold cross-validation. Both models were evaluated on multiple datasets, and their predictions were compared using standard performance metrics such as RMSE, MAE, and R^2. Therefore, one cannot just generalise identifying shadows, but it depends on the type of data chosen and the accuracy of the data. However, while the authors [203] successfully identify the overall shadow using the ML techniques above, they fail to quantify the shadow in terms of its fundamental properties of umbra and penumbra, as outlined in Chapter 2.2 of this thesis.

Beyond shading prediction, detecting and diagnosing partial shading remain a significant research focus. The study by Mustafa et al. [204] introduces a scalable Random Forest-based framework for detecting and locating partial shading in PV systems. Unlike previous works that merely differentiate between shading and other faults [205], [206] the Random Forest based framework method effectively estimates the number of shaded modules and the shading factor. Compared to deep learning techniques, which require extensive datasets and computational resources, Random Forest demonstrates superior efficiency and reliability in practical scenarios. This aligns with findings from studies by Olivares et al. [202] and Gaboitaolelwe et al. [203], where

ensemble models such as Random Forest outperform neural networks, especially in cases with limited training data.

However, as identified by Mustafa [204], while Random Forest and other ensemble models effectively diagnose partial shading, they do not directly detect the shadow itself. Rather, Random Forest and other ensemble models detect the presence of partial shading from the data. Moreover, both Kappler et al. [201] and Olivares et al. [202] use a Pearson correlation coefficient matrix to gauge the impact of independent variables on power output of a PV source affected by shading. Figure 3.26 presents a heatmap of the Pearson correlation matrix [201], where colour intensity is used to represent the strength of correlations between variables. However, including the actual correlation coefficient values at each intersection of the x and y-axis, rather than relying solely on colour would have enhanced the scientific rigor and clarity of the analysis.

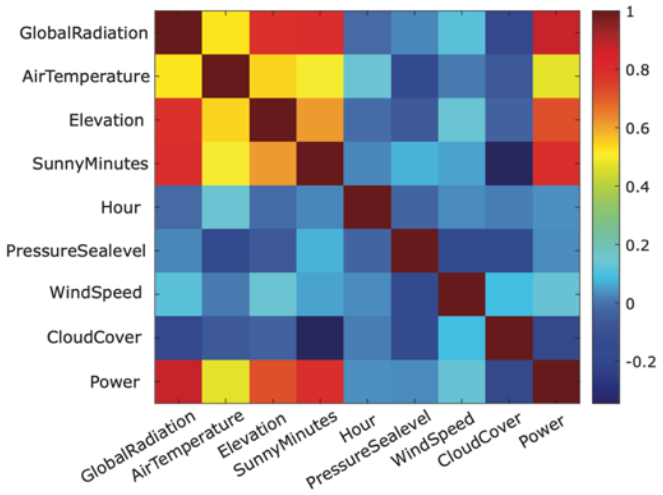


Figure 3.26. An example of a Pearson correlation matrix used in the realm of PV's [201].

Moreover, while ML models, ANNs and CNNs, offer higher accuracy in certain cases, their computational complexity and need for extensive datasets limit their practical deployment when compared to traditional ML approaches like Random Forest and XGBoost. The latter possess less reliance on extensive hyperparameter tuning (settings not learned by the model using training, but defined before the learning process begins) [207].

A crucial avenue for future research lies in the integration of hybrid models that combine the strengths of different ML algorithms and image analysis techniques. For

case, combining ML models such as Random Forest with image analysis tools would allow for more than just identification of shading, detection and forecasting , but also be able to quantify certain shadow aspects. Using a combination could lead to an innovative and novel way of analysing a shadow in depth. Additionally, efforts should focus on improving reproducibility by making algorithms open-access, as suggested in [207]. This would facilitate collaborative advancements and promote standardization in ML based PV shading detection and quantification, addressing the current trend in which researchers often start from scratch rather than build upon prior developments in a cumulative, iterative manner. Establishing shared frameworks, datasets could accelerate progress, reduce redundancy, and shift the field toward more development-oriented research that builds on collective knowledge and tested methodologies.

3.8 Current Challenges and Gaps in the Literature Identified Gaps in Literature, Aims and Objectives of this Study

The state-of-the-art review comprised a variety of crucial topics in the field of object shading. The review has revealed that while significant research has been conducted on hard shading in PVs, thin-object shading remains largely unexplored. Unlike hard shading, which creates well-defined and predictable shadows, thin-object shading introduces varying intensity and irregular patterns that can significantly impact PV performance, as was encountered by [132], [23], [170]. Despite the relevance of the current body of knowledge, research has yet to fully address the complexities of thin object shading, highlighting the need for further investigation. This leads to a number of gaps that were identified through the literature and shall be at the core of this research work. Amongst the gaps identified, the main ones are:

3.8.1 Main Research Gaps Identified from the State of the art

Lack of Comparative Analysis Between Laboratory and Outdoor Shading Conditions:

Existing studies lack a systematic comparison of the general shading effects on PV sources between controlled laboratory environments and outdoor conditions. To the best

of the author's knowledge, no research has specifically analysed the impact of thin object shading in laboratory conditions using a solar simulator. Consequently, it remains unclear whether the shading effects of thin objects on PV sources can be accurately replicated in a laboratory environment, given the complexities of shadow formation. While atmospheric conditions may significantly influence shadow characteristics, the current body of literature does not address a comparative analysis of thin-object shadow formation in laboratory versus outdoor environments. Chapter 4 will aim to address this gap.

RQ.1 What are the discrepancies in power output and shadow characteristics caused by thin object shading on a conventional (156 x 156.0 mm) solar cell under controlled laboratory conditions versus outdoor environments?

Absence of a Method to Quantify Umbra and Penumbra in Thin-Object Shading:

A significant research gap remains regarding the development of a reliable method to quantify and distinguish between umbra and penumbra regions in thin object shading scenarios. Furthermore, the interaction between shadow intensity, shadow size, and power loss under thin-object shading conditions is not well understood. Most existing studies [100], [24], [130] assume static shading conditions; however, real-world shadows vary in shadow intensity. Additionally, current correlation models are predominantly simulation-based and often lack experimental validation, highlighting the need for further empirical research. No existing PV tool can accurately quantify and categorize shadows based on their formation properties, particularly in distinguishing between umbra and penumbra. This study aims to extend beyond mere shadow edge detection to develop a tool capable of quantifying the size and intensity of umbra and penumbra regions while predicting power loss at a given case scenario. This research question (RQ.2) will be addressed in Chapter 5.

RQ.2 How do variations in thin object shading characteristics such as shadow size and intensity based on distance and object thickness correlate with power loss on PV modules, and can these parameters be used to effectively predict power output using image-based analysis?

The simplified constant-intensity representation of the penumbra shadow:

A substantial body of research in the field of shading has either neglected partial shading altogether or simplified the penumbra by representing it as a region of constant intensity. It remains unclear whether this simplification, substituting the inherently varying-intensity penumbra with a constant-intensity, serves purely illustrative purposes or if it also influences scientific interpretation and analysis. To address this gap in the literature, Chapter 6 introduces a novel methodology specifically designed to account for the complexities of the varying nature of the penumbra.

RQ.3 In the absence of an umbra shadow, can the impact of a penumbra shadow on a PV module be replicated by using the mean constant-intensity value of the corresponding varying-intensity penumbra shadow?

The subsequent section outlines the specific aims and objectives that this study seeks to achieve in response to the gaps identified in this section.

3.8.2 Aims and Objectives

While partial shading is a well-established topic, the challenges posed by shading from thin objects have received less attention in the state-of-the-art. The literature review revealed numerous studies on laboratory partial shading, but the differences in light behaviour principles between laboratory and outdoor environments create ambiguity, particularly as the shadow becomes more dynamic due to the factor of distance coming into play. Additionally, the lack of a reliable method for approximating shadow size and intensity contributes to uncertainty about shadow boundaries. Furthermore, although the general characteristics of shadows have been extensively studied, research on the isolated effects of penumbra-only shadows is limited. Consequently, this study aims to close these aforementioned gaps by conducting a comparative analysis between laboratory and outdoor shadow formation. Moreover, this study aims to derive a methodology capable of quantifying the size and intensity of the umbra and penumbra regions while exploring their correlation with worst power loss case scenario on PVs as a benchmark quantifiable measure. Additionally, this aims to isolate the effect of the

penumbra shadow and assess its isolated power loss on PVs under a comparative state of varying-intensity penumbra and a replicated constant shading condition.

To accomplish the above aims, the following objectives were derived:

O.1 Analyse how the size and intensity of horizontal thin object shadows influence the power loss when observed at incremental distances in both outdoor and laboratory experimental settings.

O.2 Develop an innovative image analysis tool capable of quantifying the approximate size of umbra and penumbra shadows in thin object shading scenarios, measuring shadow intensity in terms of pixel darkness value and using a predictive model to estimate the worst-case scenario power loss based on changing parameters in horizontal thin object shading.

O.3 Validate the innovative image analysis tool by creating realistic scenarios with various thin objects and verifying that predicted power loss aligns within acceptable limits with actual measured values.

O.4 Replicate the varying intensity behaviour of penumbra-only shadows using a constant average intensity approximation, and evaluate whether the proposed innovative methodology or the constant intensity approximation is scientifically valid.

As a summary of the multiple experimentation conducted in the subsequent chapters of the thesis, Table 3.2 below has been compiled for ease of reference.

Table 3.2. An overview of the PV source, environmental condition, date and time each experimentation in the subsequent chapters was conducted.

Description of experiment	Chapter No.	PV Source	Environmental condition	Date	Time
Preliminary experiment to determine the statistical significance of different colour coatings (Absorbent black vs Reflective Silver) on the effect of the power output on a PV source.	4.3.1.1	Solar Cell	Laboratory	12th December 2023	08:45 – 09:30
Preliminary experiment to determine the difference of orienting the thin object (Horizontal vs Vertical) on the effect of the power output on a PV source.	4.3.1.2	Solar Cell	Laboratory	12th December 2023	09:30 – 10:15
Determining the power loss of multiple thin object shading conditions for a variety of difference thin object size at varying distance from the source.	4.3.3	Solar Cell	Laboratory	18th December 2023	14:00 – 15:30
Determining the power loss of multiple thin object shading conditions for a variety of difference thin object size at varying distance from the source.	4.3.3	Solar Cell	Outdoor	23rd May 2024	12:30 - 13:30
Quantifying the effect of various thin object shading on a PV module	5.3.1	PV Module	Outdoor	8th June - 10th June 2024	12:00 - 14:00
Validating the performance of ThinShadePV tool	5.3.4	PV Module	Outdoor	8th May 2025	12:30 - 13:00
Preliminary experimentation to determine the effect of elevating the ND filter from the PV module	6.3.1.1	PV Module	Outdoor	4th July 2024	12:30 – 12:45

Determining the intensity value of a range of ND filters	6.3.1.2	PV Module	Outdoor	4th July 2024	12:30 – 13:30
Analysis of the intensities between varying-intensity penumbra-shadow and a constant-intensity shadow	6.3.2	PV Module	Outdoor	5th July 2024	13:00 – 13:30
Comparative analysis of the size of a varying-Intensity penumbra-only shadow and a constant-Intensity shadow	6.3.3	PV Module	Outdoor	10th July 2024	12:30 – 13:30

This thesis will hereon address the research questions in sequential order, starting from RQ.1 outlined in the subsequent Chapter 4.

Chapter 4 Outdoor vs Laboratory Environmental Conditions

4.1 Introduction

This chapter endeavours to answer the first research question presented in Chapter 3 Section 3.8.1, focusing on the discrepancy range in power output and shadow formation caused by thin object shading under controlled laboratory conditions, when compared to outdoor environmental conditions. Given the complexities of shadow formation, a direct comparison between laboratory and outdoor environments is conducted, maintaining identical shading object thickness and distance from the solar cell. By scientifically analysing the characteristics of shadows in both environments, this study aims to uncover discrepancies in shadow behaviour and their effects on performance of a solar cell. Part of the methodology and some of the main results discussed in this chapter were published in the peer-reviewed Multidisciplinary Digital Publishing Institute (MDPI) journal 'Energies' [208]. This chapter presents an in-depth methodology that encompasses the work in [208].

This chapter examines three key attributing variables influencing PV performance: firstly, the distance between the thin object and the solar cell (hereafter referred to as 'distance'), secondly, the diameter of the thin object (hereafter referred to as 'thickness'), and thirdly the resulting power loss. The power output of a control monocrystalline solar cell connected to a fixed load is evaluated in comparison to an identical solar cell which is partially shaded by the thin object. Power output measurements are obtained at the fixed load point. This means the solar cell output performance is assessed while operating under a constant and predefined maximum load condition, ensuring consistency in the measurement process. Further details on this measurement setup are provided in Section 4.2.2. Moreover, the experimentations in this chapter will be conducted on a four busbar monocrystalline solar cell shown in Figure 4.1 of which electrical specifications will be derived in Section 4.3.2, under both laboratory and outdoor environmental conditions under STC conditions. Such a single unencapsulated solar cell (as depicted in Figure 4.1) was chosen to isolate the impact of thin object

shading, ensuring that the influence of any external factors present in a traditional PV module, on power output was mitigated as much as possible.

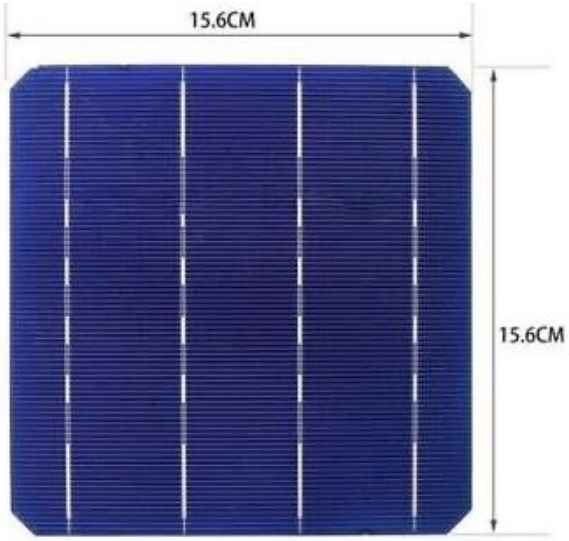


Figure 4.1. The 4-busbar monocrystalline solar cell used in this study.

4.2 Methodology

The methodology in this chapter is applied in two distinct environmental conditions; outdoor and laboratory; followed by a comparative analysis of the two. Firstly, outdoor experimental data was collected to emulate real-world conditions as further investigated in Section 4.2.2. A laboratory-based solar simulator was consequently used to conduct controlled experiments as shall be discussed in Section 4.2.3. Moreover, Section 4.2.4 and Section 4.2.5 finally elaborate on the quantification and analysis of the shadow formation in these two environmental conditions. This approach aimed to comprehensively investigate the thin object shading effects on a solar cell under different conditions, thus providing a well-rounded analysis to be able to answer the research question RQ.1 introduced in Section 3.8.1. It should be noted that, the experimentation setups for both environmental scenarios were designed to provide testing under the same experimental conditions with only the environment as the differentiating factor.

4.2.1 Experimentation Biases and Assumptions

Assumption 1: It is assumed that the resistive load connected to the system remains constant throughout the experimentation. Furthermore, all voltage and current readings in the outdoor environment are directly measured according to the resistive load sized appropriately used in the setup.

Bias 1 - The thin object casting the shadow on the solar cell has been painted black to minimise light reflections in both environments. To assess the significant impact of colour coating on reflection bias, a preliminary experiment was conducted in Section 4.3.1.1, comparing an absorptive black coating with a reflective silver surface.

Black and silver were selected to represent the two extremes of surface reflectivity within the albedo spectrum. Black surfaces exhibit very low reflectivity, typically below 0.2, effectively absorbing incident radiation, whereas silver surfaces have high reflectivity, with albedo values around 0.9, thereby reflecting the majority of incident light [209], [210]. The purpose of analysing the difference in power output of colour coating on thin objects was to assess whether the reflectivity of the thin object's surface plays a significant role in power loss and whether it influences the PV cell's performance under thin shading conditions. Such an influence could potentially lead to variations in light redirection, that may partially mitigate the impact of the power loss result [211]. Therefore, the following hypothesis statements were compiled:

Null Hypothesis (H_0): The colour coating of the object (black vs. silver) has no significant effect on the reflection bias on the solar cell in either environment.

Alternative Hypothesis (H_1): The colour coating of the object (black vs. silver) has a significant effect on the reflection bias on the solar cell in at least one environment.

Bias 2 - The shadow was positioned horizontally across the solar cell during experimentation. However, it is assumed that the results will be applicable regardless of the orientation of the shadow on the solar cell. To validate this assumption, an experimental bias test was conducted to confirm that the findings are also applicable to

vertically transposed shading given the same overall shadow size. The results of the preliminary experiment will be conducted in Section 4.3.1.2.

The purpose of analysing the effect of thin object orientation on power output was to assess whether the orientation of a thin object's shadow, that is, either horizontally or vertically, plays a significant role in power loss and influences the PV cell's performance. This evaluation is crucial for determining whether subsequent experiments can be generalised across different shadow orientations given the same shadow coverage. Similar to Bias 1, a preliminary test was conducted to identify whether there is a significant difference between the shadow of a thin object being positioned horizontally across the solar cell as opposed to vertically, aiming to answer which of the below hypothesis can be accepted.

Null Hypothesis (H_0): The orientation of the shadow (horizontal vs. vertical) has no significant impact on the solar cell's performance, assuming the same overall shadow size.

Alternative Hypothesis (H_1): The orientation of the shadow (horizontal vs. vertical) significantly affects the solar cell's performance, even with the same overall shadow size.

Given the identification of these two biases, it was of paramount importance to conduct preliminary testing to ensure that colour and orientation do not introduce statistically significant effects. The laboratory environment was deliberately selected to evaluate these two biases, ensuring a controlled and stable setting and minimising external influences that could otherwise affect the results. In contrast, outdoor conditions introduce significant variability due to fluctuating weather parameters, particularly changes in global horizontal irradiance and ambient temperature, which may obscure minor differences in the performance of these biases. Moreover the uncertainty analysis exemplified in Appendix B.2 for the laboratory experimentation setup, provided a lower uncertainty result compared to the outdoor setup shown in Appendix B.1, further elaborated in their respective results section in Section 4.2.2 and Section 4.2.3. Therefore, similar to [212] and [138], a laboratory environment was chosen to assess the impact of both Bias 1 and Bias 2. A consolidated range of object thicknesses

comprising of ⌀2.0 mm, ⌀6.0 mm, ⌀10.0 mm, ⌀14.0 mm and ⌀20.0 mm, was opted for as these object thicknesses provide a significant spectrum of thin objects. This aimed to answer which hypothesis statement for both bias 1 and 2 can be accepted respectively. The results of both bias experimentations are outlined in Section 4.3.1.

4.2.2 Outdoor Experimentation Method and Setup

To establish an authentic outdoor environment, the experimentation was conducted outdoors at the premises of the University of Malta Institute for Sustainable Energy situated in Marsaxlokk, Malta, which is situated at latitude 35º50′03.42″N and longitude 14º32′36″E. These experiments aimed to quantify the impact of shading from thin objects of various sizes and positioned at different distances from the solar cell. The experiments were conducted on the 23rd of May, 2024 between 12:30 and 13:30, in favourable weather conditions comprising clear skies with no partial shading from clouds. Moreover, this research acknowledges the varying nature of solar positioning and its consequential impact on shadow projection. Since the sun's position changes continuously throughout the day and influences the size of shadows cast, an approach to address this variability in the experimentation was employed. Initially, a 3D visual conceptualisation of the experimental setup was produced in Figure 4.2 to establish its orientation in relation to the sun path.

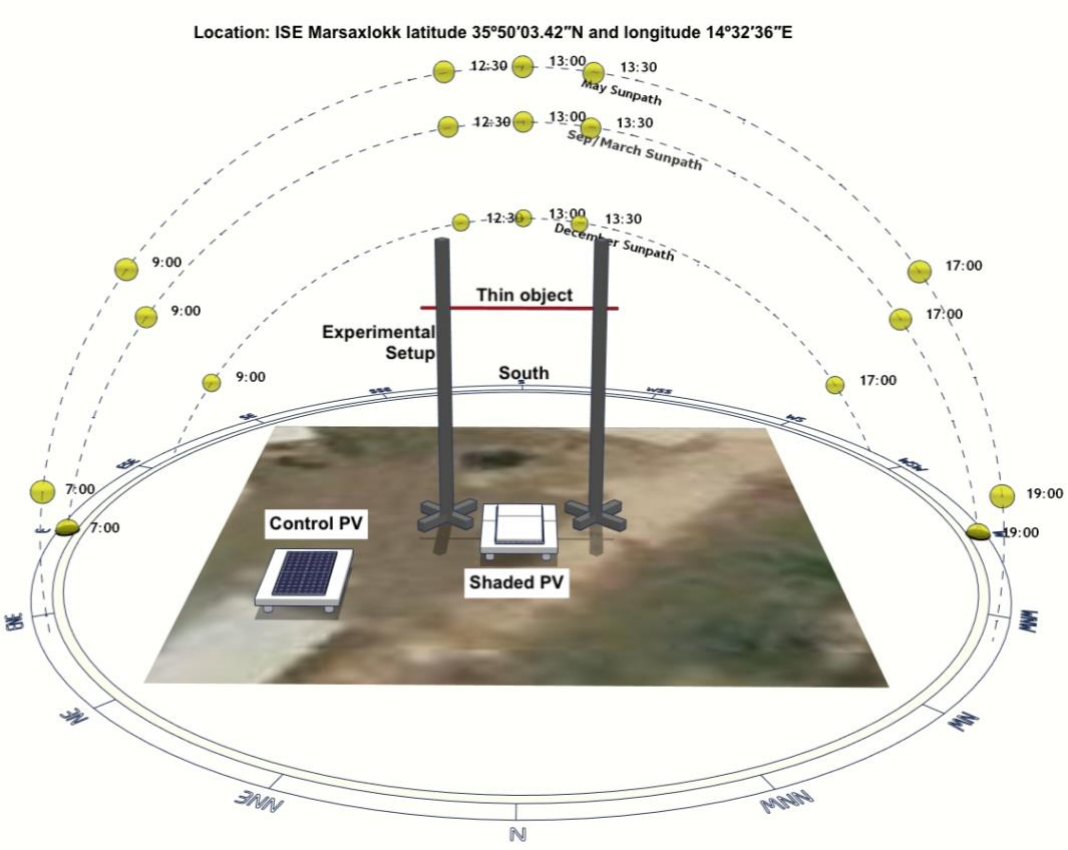


Figure 4.2. A conceptual 3D visual of the outdoor experimental setup including the yearly sun paths.

Altitudes were recorded at 15-minute intervals throughout the study, and trigonometric principles were employed to derive the apparent shadow projections at various times of day. As an exemplary representation, three sun positions have been visualised to illustrate the shadow being cast on the surface of the PV source. Sun position 1 is represented by Figure 4.3 illustrating the instance when the sun is positioned at 12:30 (30 minutes before solar noon), sun position 2 is represented by Figure 4.4 visualising the sun position at solar noon, while sun position 3 is represented by Figure 4.5 illustrating the sun position 30 minutes after solar noon at 13:30, on the 23rd of May 2024 when the experimentation was conducted. Variations in observed shadow lengths due to changes in solar altitude were corrected using a correction factor to ensure consistency and comparability across different solar positions.

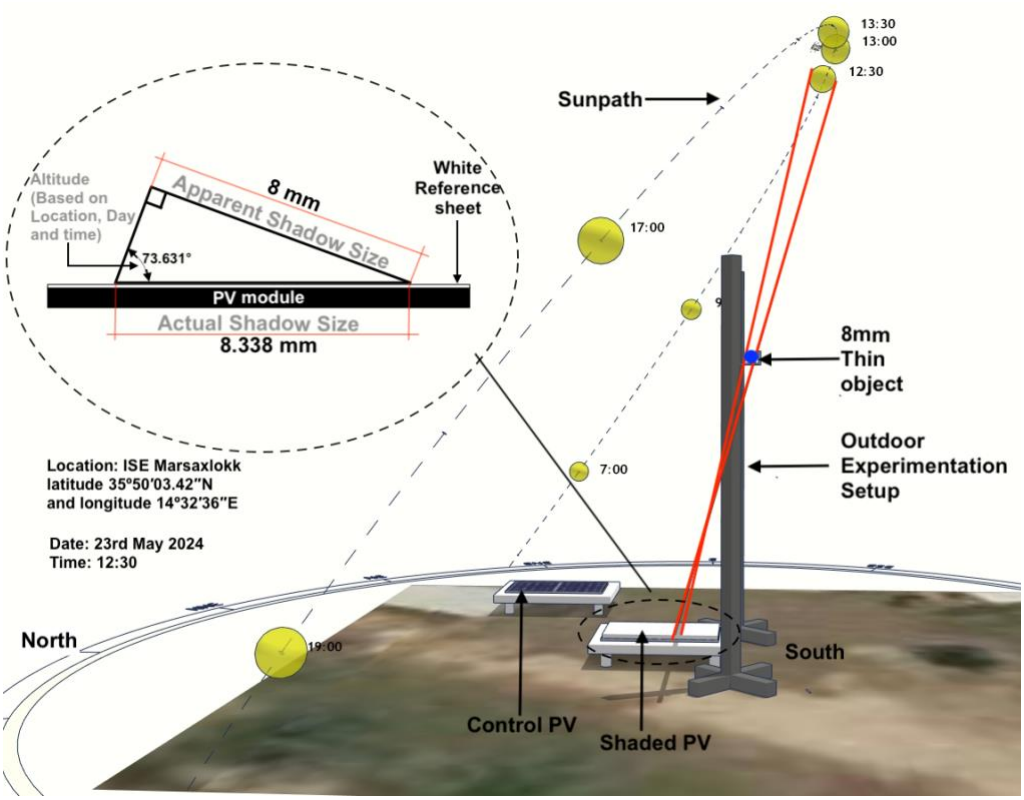


Figure 4.3. Sun position 1: A 3D model of the geometrical sun position model based on the location of ISE Marsaxlokk at 12:30 on the 23rd of May 2024.

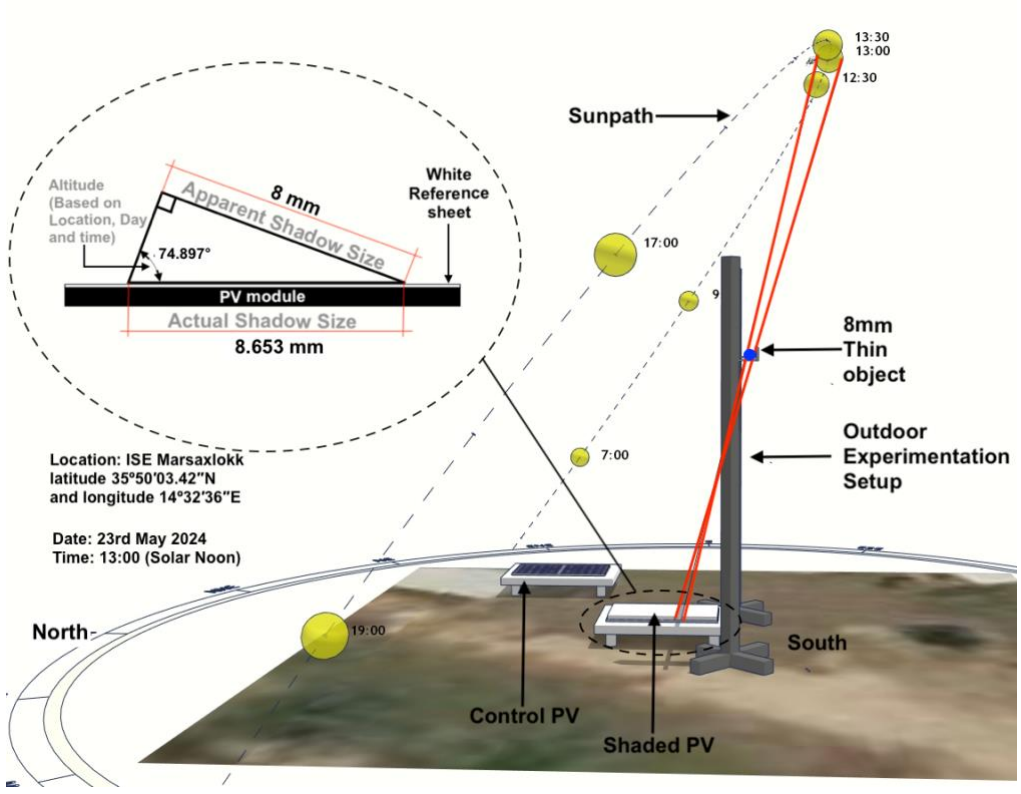


Figure 4.4. Sun position 2: A 3D model of the geometrical sun position model based on the location of ISE Marsaxlokk at 13:00 (Solar Noon) on the 23rd of May 2024.

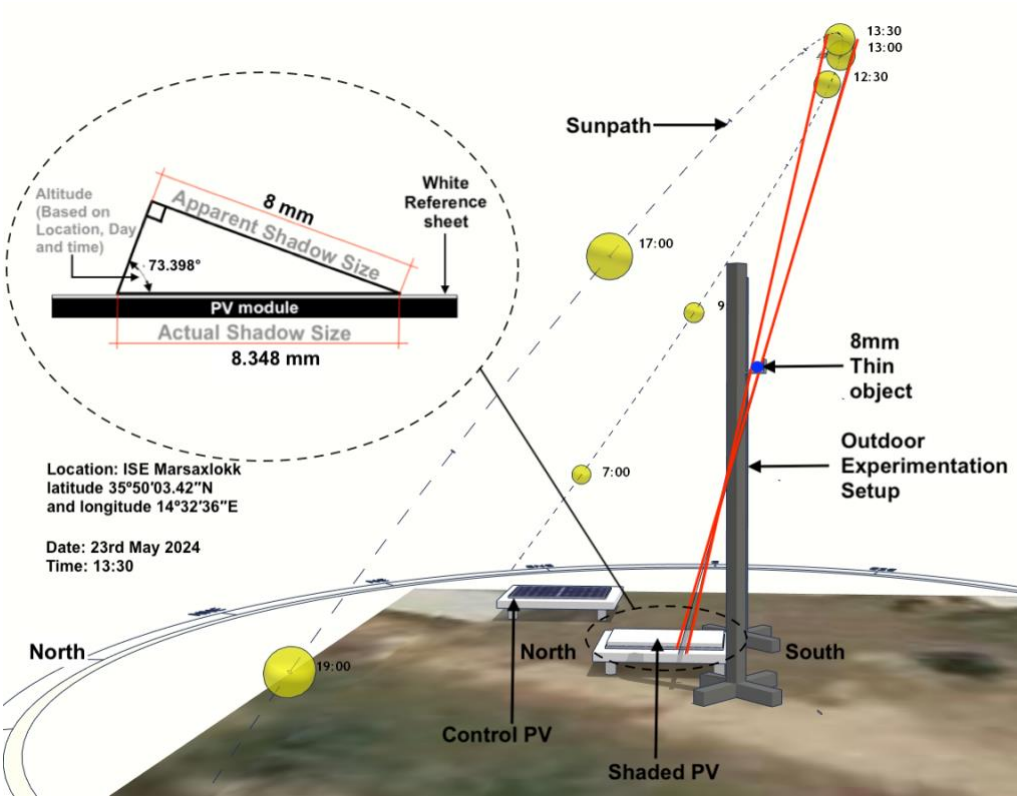


Figure 4.5. Sun position 3: A 3D model of the geometrical sun position model based on the location of ISE Marsaxlokk at 13:30 on the 23rd of May 2024.

As an explanation to the three figures above, Table 4.1 presents a representative example demonstrating how date and time determine solar altitude. Sun position 1 (Figure 4.3) will hereon be used as an example case scenario where the data corresponded to the 23rd of May 2024 at 12:30 pm, resulting in an altitude of 73.631 through the python script in the first exemplified tab in Appendix H. In this scenario, an apparent example of shadow thickness of ⌀8.0 mm, associated with a thin object, was calculated using trigonometric derivations depicted within the top left side circle in Figure 4.3. Consequently, the actual physical thickness, accounting for the sun's position, was determined to be 8.338 mm. The corresponding correction factor, derived as the ratio of the apparent to actual thickness (8 / 8.338), was calculated as 0.959. This correction factor was then applied to adjust the apparent power loss of 18.89%, resulting in a corrected value of 18.12% for Sun position 1.

Table 4.1. Examples of the sun position correction factor workings for the three sun positions.

	Unit	Sun Position 1	Sun Position 2	Sun Position 3
Date	dd/mm/yyyy	23/05/2024	23/05/2024	23/05/2024
Time	hh/mm	12:30	13:00	13:30
Altitude	Degrees (º)	73.631	74.878	73.398
Apparent Shading Size	mm	8	8	8
Actual Shading Size	mm	8.338	8.653	8.348
Apparent Power Loss	%	18.89	18.89	18.89
Correction Factor		0.959	0.965	0.958
Corrected Power Loss	%	18.12	18.23	18.10

This methodology was applied consistently across all sun positions based on the corresponding solar altitudes at each experimental time point. By incorporating these adjustments, the outdoor experiments ensure standardised evaluation and contribute to a more accurate understanding of the interplay between solar position, shadow projection, and resulting power loss.

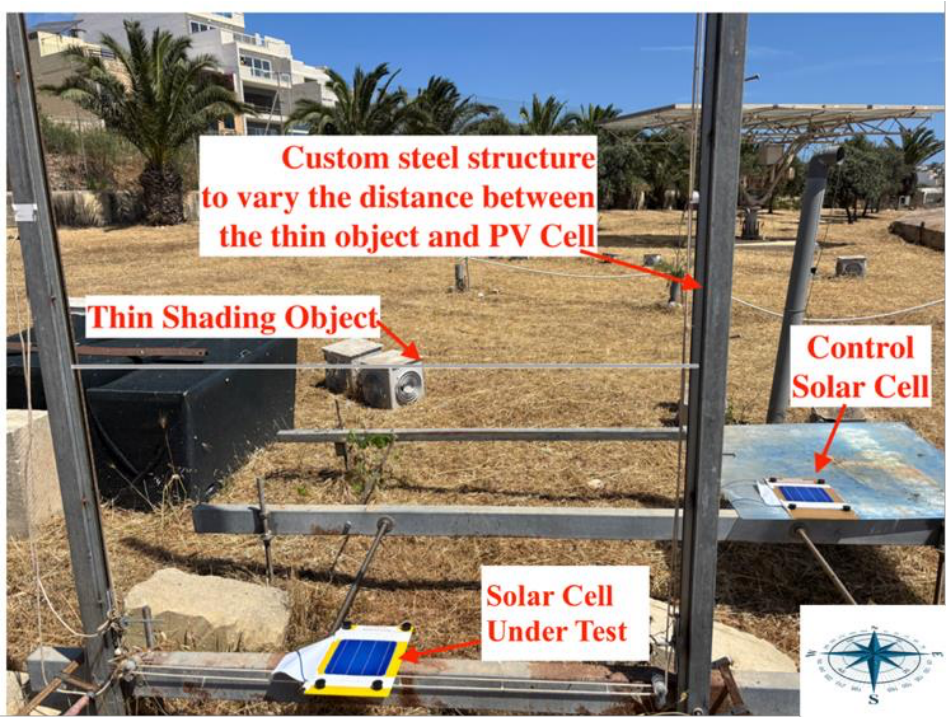


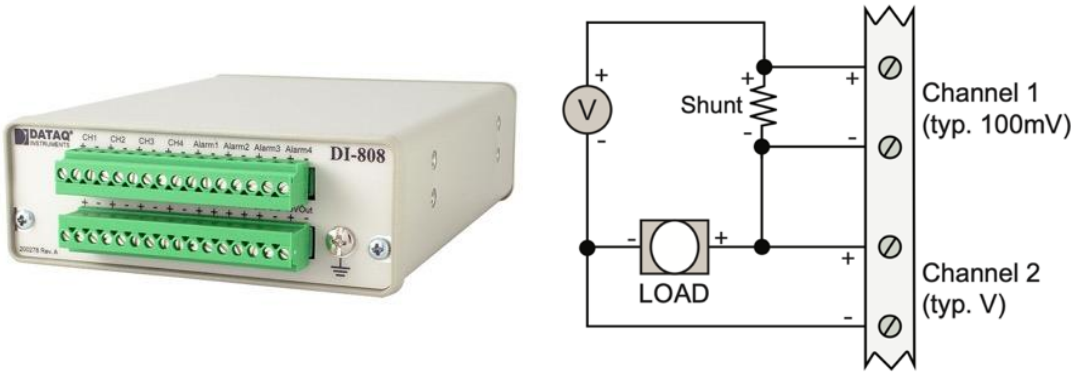
Figure 4.6. Physical outdoor experimental setup for the solar cell, taken facing the North direction.

To simulate various thin object shading scenarios, both distance and object thickness were incrementally and independently varied. A custom steel structure was constructed to adjust the distance between the shaded solar cell and the thin object casting the shadow, as previously illustrated in Figure 4.6. This structure allowed the distance to be varied from 10 cm to 40 cm, in 10 cm increments. These measurements were determined to match the constraints of the solar simulator used in laboratory experimentation, as outlined in the methodology section of the laboratory environment setup in Section 4.2.3. To capture a wide range of shading effects for a more comprehensive power loss analysis, thin objects consisting of horizontally aligned rods, were placed above the solar cell. These rods had diameters corresponding to those in Table 4.2 and were selected to emulate real-life thin objects such as electrical wires, telecommunication lines and passive air clothes drying lines which are usually of about those thicknesses and which usually obstruct light on PV sources.

Table 4.2. The range of thin object thicknesses used in both laboratory and outdoor experimentation.

The diameter of the thin objects (⌀ in mm)													
2.0	2.3	2.8	3.2	4.4	4.6	6.0	6.4	7.2	8.0	10.0	12.0	14.0	20.0

To obtain the required power measurement from the solar cell under experimentation, a custom-built circuit board was wired according to the specifications of the data logger DATAQ Instruments Model DI-808 as seen in the reference image of the logger in Figure 4.7a and the schematic in Figure 4.7b. This device was chosen for its compatibility with the low voltage levels typical of small-scale solar setups, the detailed specifications are provided in Appendix C. The single solar cell used in the experiments operates within a voltage range of approximately 0.5 - 1 V, while it is also capable of measuring the small-scale PV module that produces output up to around 20 V, subsequently used in Chapter 5. These values fall well within the input range and resolution capacity of the DI-808, making it a suitable data logger for accurate data acquisition with accuracy of (±0.05% of span + 10 μV). Compared to field-grade loggers commonly used for large-scale PV systems with multiple interconnected strings, which are designed for higher voltage and current levels, the DATAQ DI-808 offers lower measurement uncertainty and better resolution for small-output devices.



(a) **(b)**

Figure 4.7. (a) A reference image of the datalogger DATAQ DI-808, **(b)** Custom circuit wiring diagram for the operation of the DATAQ DI-808.

To obtain the voltage measurement across the circuit shown in Figure 4.7. A fixed load resistor was sized based on the MPP potential of the solar cell to capture its voltage output. However, since the data logger could not directly measure current, a full I-V curve could not be derived. Instead, current was calculated using Ohm's law by measuring the voltage drop across a high-quality aluminium wire-wound shunt resistor as shown in Figure 4.7. Both resistors were mounted on an aluminium heat sink to dissipate heat and minimise thermal errors. This setup allowed the experimental circuit box to measure both voltage and current at a fixed resistive load. It is important to note that the measured power (V × I) does not represent the MPP, as achieving MPP would require a variable resistive load to adjust dynamically for each shading scenario. However, to maintain consistency, power measurements were taken along the fixed load line as sized using Equation (11). Even though theoretically, the resistive load required was calculated at 0.066 Ω, such a precise resistive load could not be sourced nor specifically ordered, posing an initial limitation. However, an 0.05Ω and a 0.01 Ω resistor were sourced and wired in series to create a 0.06 Ω fixed resistor, the specifications of which can be referred to in Appendix C. This resistive load value was the closest available combination to the theoretical calculated 0.06 Ω. Furthermore, the difference in power output between the control and shaded solar cell was determined using Equation (12). To ensure repeatability and accuracy, each experimental condition

subject to 50 readings (a measurement every 0.25 seconds), and the power loss values were averaged into a single value.

$$R_{LOAD} = \frac{V_{MPP}}{I_{MPP}} = \frac{0.526}{7.897} = 0.066 \text{ ohms} \quad (11)$$

The current and voltage measurements were extrapolated from the x and y axis measurements of Figure 4.8.

where:

R_{LOAD} is the resistive load being sized

V_{MPP} and I_{MPP} are the Voltage and Current outputs of the solar cell respectively at MPP used only for sizing the fixed load resistor.

$$\text{Percentage Power Loss} = \frac{\text{P}_{\text{Load Control}} - \text{P}_{\text{Load Shaded}}}{\text{P}_{\text{Load Control}}} \quad (12)$$

where:

Percentage power loss is the difference between the power output of the control solar cell and the solar cell under thin object shading conditions

$P_{Load\ Control}$ is the output power measured at the fixed load resistance for the control solar cell

$P_{Load\ Shaded}$ is the output power measured at the fixed load resistance for the solar cell under thin object shading conditions

The control and shaded solar cells are identical in terms of manufacturer, physical dimensions and efficiency. This ensures consistency across all relevant parameters. Their I-V characteristics, represented by the blue curve in Figure 4.8, were obtained using I-V measurements taken with the solar simulator and I-V tester described in the laboratory experimental methodology in Section 4.2.3. Nonetheless, an outdoor

calibration process was conducted to verify performance. The shaded solar cell was calibrated based on the control solar cell power output by recording voltage and current measurements for both solar cells every second for 15 minutes to derive a mismatch factor, ensuring both cells started with identical electrical outputs.

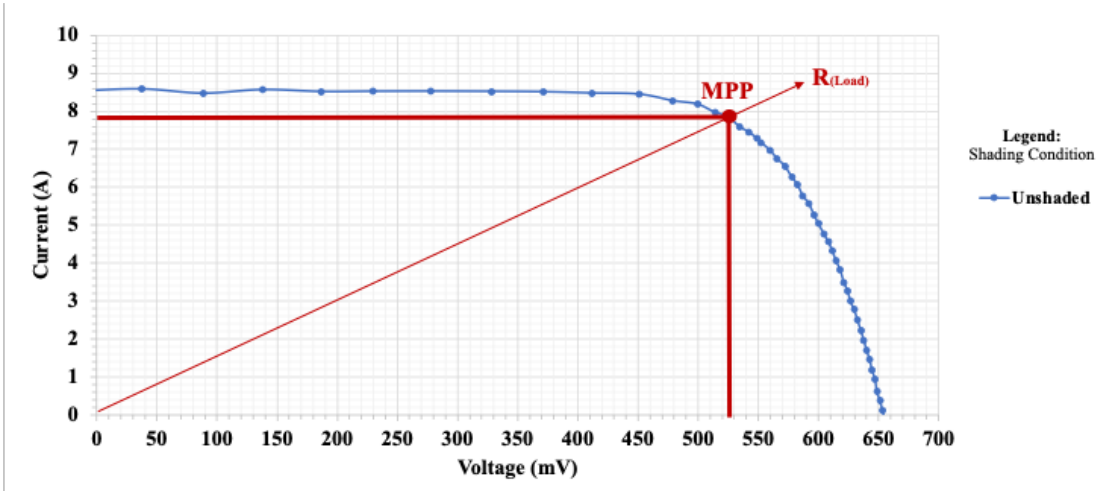


Figure 4.8. I-V curve electrical characteristic for the chosen solar cell.

It is important to note that although there was no partial shading from external objects or clouds whilst conducting the outdoor experimentation on a sunny day with clear skies, the nature of the light source cannot be solely attributed to Direct Normal Irradiance (DNI) [213]. Therefore, the experimentation assumes a blend of both DNI and Diffuse Horizontal Irradiance (DHI) for a collective Global Horizontal Irradiance (GHI) measurement as illustrated in Table 4.3. Ground reflection is assumed negligible given that both the control and shaded solar cells were set at a direct orientation toward the sky of 0° tilt angle [44]. To ensure that the irradiance levels closely matched STC measurements were obtained from a nearby weather station located in close proximity to the experimental setup; the corresponding data are also available online using [214] and downloadable upon request. Solar radiation from the weather station was logged at 10-minute intervals, and it is assumed to remain constant over each interval. This assumption applies throughout the thesis unless stated otherwise. Moreover, the temperature of the solar cell was measured using an IR thermometer UNI-T UT302+ series to ensure the solar cell is operating at a temperature of 25°C ±1.5°C. A

comprehensive account of the operating conditions for outdoor experimentation is delineated in Table 4.3.

Table 4.3. Operating conditions of outdoor environmental experimentation.

	Unit	Outdoor Single solar cell
Date	Dd/mm/yy	23/05/2024
Time UTC+1	hh:mm	12:30 – 13:30
Light Source	N/A	Sunlight
Range of DNI	W/m^2	822 - 843
Range of DHI	W/m^2	121 - 123
Range of GHI	W/m^2	946 – 1007*
Temperature	^{o}C	25 (±1.5)

**The GHI was corrected to STC conditions at 1000W/m^2 using the following method*

The experimentation conducted in this chapter and also when using the similar setup in Chapters 5 and 6 utilise the standard procedure applied in IEC 60904-1:2020 [137] and IEC 60891:2021 [215], consisting of correction parameters of the PV module for current and voltage under STC, which are listed as Equations (13) and (14) respectively.

$$I_2 = I_1[1 + \alpha_{rel}(T_2 - T_1)]\frac{G_2}{G_1} \tag{13}$$

$$V_2 = V_1 + V_{oc}\,[\beta_{rel}\,(T_2 - T_1) + a\ln\left(\frac{G_2}{G_1}\right)] - R'_s(I_2 - I_1) - K'I_2(T_2 - T_1) \tag{14}$$

where:

- I_1 and V_1 refer to current and voltage measured at operating conditions (OPC);
- I_2 and V_2 refer to current and voltage measured at STC conditions;
- G_1 is the irradiance measured at OPC conditions;
- G_2 is the standard irradiance (1000 W/m^2);
- T_1 is the cell temperature measured at OPC conditions;
- T_2 is the standard cell temperature (25 °C);
- V_{oc1} is the open circuit voltage at OPC;
- α_{rel} and β_{rel} are, namely, the current and voltage temperature coefficients of the test specimen measured at 1000 W/m^2;
- a is the irradiance correction factor for the open circuit voltage;
- R_s' is the internal series resistance of the test specimen; and
- k' is the temperature coefficient of the internal series resistance R_s' [216].

4.2.3 Laboratory Experimentation Method and Setup

In the second segment of the methodology, laboratory experimentation served the purpose of establishing a controlled environment for measuring the power output of the unencapsulated solar cell which was also used in the outdoor experimentation, under various shading scenarios. The STC conditions for the solar cell were replicated using the solar simulator Photo Emission Tech., Inc. (Moorpark, CA, USA) (SS150AAA–EM) [217], situated at the solar research laboratory at the Institute for Sustainable Energy, University of Malta and depicted in Figure 4.9. Additionally, the solar simulator provides a guaranteed uniform illumination area of 156 mm × 156 mm, matching the standard dimensions of the solar cells tested in this chapter and ensuring accurate and representative performance measurements. The solar simulator interfaces with an I-V tester measurement system 'Advance CC Series Model' and is used to measure parameters such as P_{max}, V_{mpp}, I_{mpp}, V_{oc}, I_{sc}, and cell efficiency. For data acquisition in this research, the focus was directed towards the full I-V curve points, V_{mpp}, I_{mpp}, and P_{max} of the unencapsulated solar cell. The procedure and measurement requisites in this section adhere to the standard IEC 60904-1:2020, specifically in line with Section 4.2 of the aforementioned standard [137].

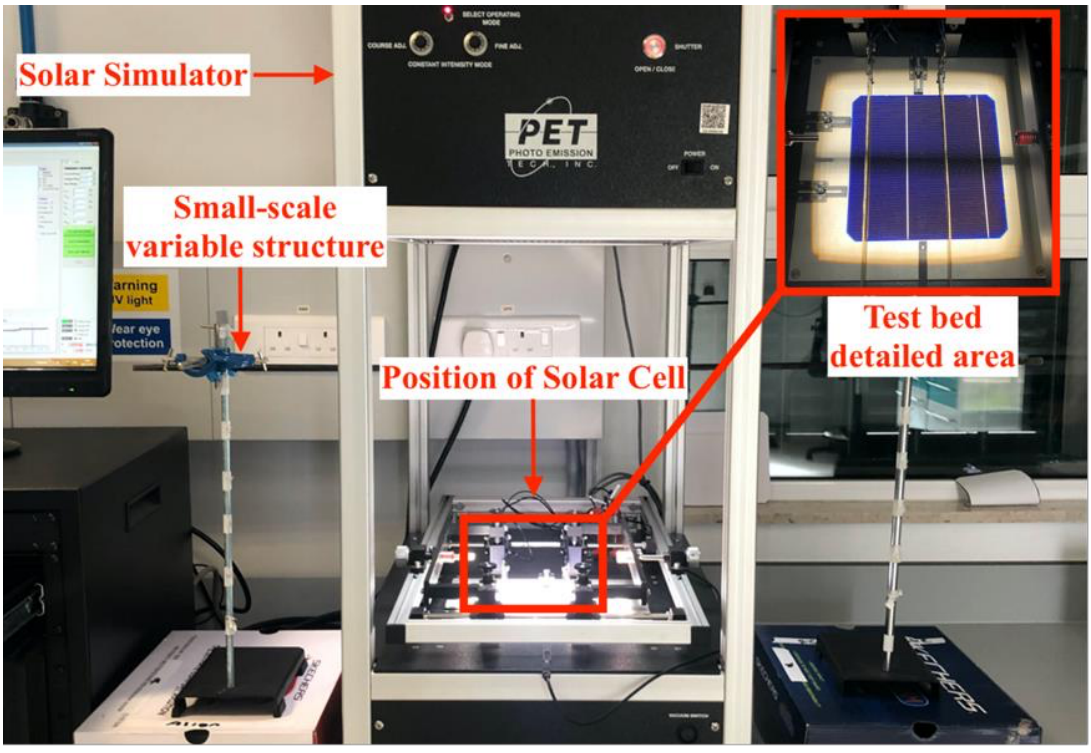


Figure 4.9. The laboratory experimentation setup.

To achieve the same dataset of distance and thickness values previously mentioned in Section 4.2.2, a small-scale variable structure was custom-built to manipulate the positioning of thin objects, as illustrated in Figure 4.9 . Under the solar simulator's radiant illumination, the various-sized thin objects were methodically positioned individually until every possible combination of distance and thicknesses was covered. The methodology, however, encountered a limitation with a capped distance of 40 cm between the individual PV cell and the light source due to the physical constraints of the solar simulator.

Moreover, all thin objects from the outdoor experimentation were retained. However, the only exception was the shaded solar cell power reading was compared systematically with the control power reading recorded at the beginning of the experimentation round rather than instantaneously due to experimental setup limitations. To ensure the reliability and accuracy of the data, each laboratory dataset reading was repeated three times for every combination of distance and thickness. The obtained values were then averaged to minimise potential minor variations and produce more repeatable results. The complete results for the three measured values in each experimental round, along with the calculated averages and corresponding percentage power losses, are presented in Appendix D and visually illustrated in the results shown in Section 4.3.3.

In contrast to the outdoor experiments where a fixed load was applied, the I-V tester used in the laboratory setup is capable of generating a full I-V curve, including identification of the MPP, by varying the resistive load to track the MPP. To ensure a fair comparison between the laboratory and outdoor results, the same power point measured during the outdoor experiments was extrapolated from the laboratory I-V curve explained subsequently.

Building on the I-V curve shown previously in Figure 4.8, Figure 4.10 was created to further investigate the measured power point corresponding to the outdoor measurement, previously referred to as P_{load}. The blue I-V curve represents the control condition of the solar cell. The MPP, marked in red, is extrapolated to the x- and y-axes to determine the current and voltage values used to calculate the resistive load necessary for the solar cell to match the P_{load} observed in outdoor testing. This resistive load is illustrated in Figure 4.10 by a diagonal line labelled R_{load}, consistent with the theoretical

representation firstly introduced earlier in Chapter 2 Section 2.2 by [50]. The point where this fixed resistance line intersects each shaded I-V curve, shown in four different colours as indicated in the legend, corresponds to the power point measured under shaded conditions during the outdoor experiments. Accordingly, the comparative analysis will be based on P_{load}. The percentage power loss is calculated as the difference between the P_{load} of the shaded solar cell and that of the control solar cell, which, under ideal conditions, closely approximates the cell's maximum power output at MPP.

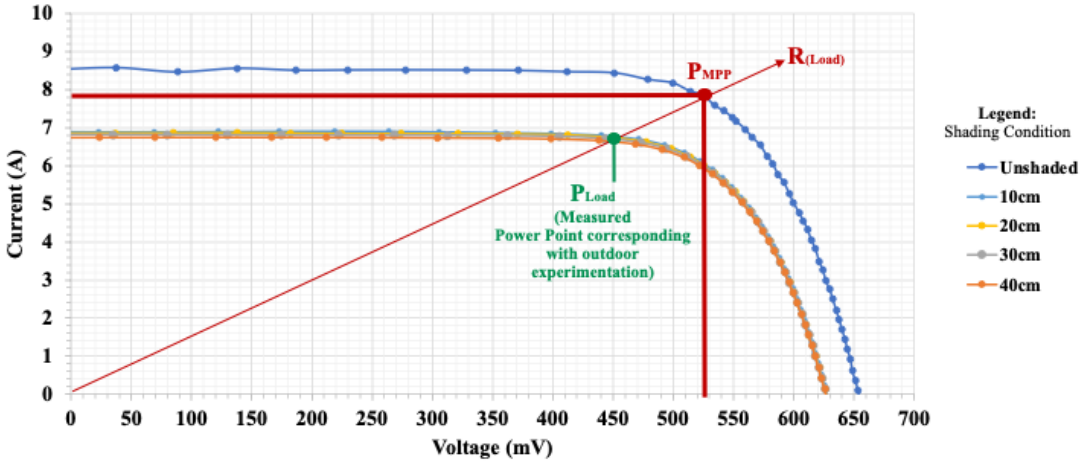


Figure 4.10. An I-V curve generated for a laboratory environmental setting depicting the MPP at control conditions and the measured power point corresponding with the outdoor experimentation for a ⌀20.0 mm thin object shading scenario between 10 cm and 40 cm distance from the solar cell.

Before initiating any readings, the solar simulator underwent calibration using the reference cell Model 60623 PET Serial RC-1160 (Moorpark, CA, USA) visualised in Figure 4.11. A constant irradiance value of 1000 W/m^2 ± 1% was maintained. Additionally, a Peltier cell temperature control device was employed to maintain a consistent temperature of 25 °C (± 1°C) for the solar cell being tested. These standardised experimental configurations allowed for baseline results at STC conditions.



Figure 4.11. The reference silicon solar cell used as reference for the calibration process of the solar simulator.

4.2.4 Image Capture and Quantification Methodology

An integral aspect of the experimental methodology involved the systematic capture of images for each combination of rod thickness and distance for both laboratory and outdoor conditions. This documentation serves a dual purpose: First, to interpret specific discrepancies between outdoor and laboratory experimentation, providing visual insights into the effects of shading under varying environmental conditions. Second, the images serve as crucial visual aids in illustrating the changes in shadow formations resulting from different distances and object thicknesses. The images were captured across all relevant configurations of distance and thickness using a single-lens reflex (SLR) camera, the Canon EOS 6D Digital SLR. Complete specifications are provided in Appendix C, while the principal camera settings are detailed at the end of this sub-section.

This study aims to capture images in both a laboratory and outdoor setting to capture the shadow transposed on a white background. Therefore, it is imperative that the same camera settings are utilised for both scenarios to obtain a direct comparative analysis later for Section 4.3.2. From literature reviewed in Chapter 3, no research work has definitively provided the ideal camera settings in such a scenario for either outdoor or laboratory environment. This is due to different scenarios having different ideal camera settings to capture the subject perfectly. However, a research paper by Rangelov et.al [218] outlines the best balance for high quality 3D reconstruction images of various two-

dimensional scenes. This provides detailed and precise digital representations for various applications. The author exemplifies the crucial importance of this in fields such as engineering. However, the study is specific to a laboratory controlled environment and are not directly applicable to more complex environments in an outdoor setting. Having said that as previously stated, it is important the same camera settings are utilised for laboratory and outdoor environment to capture the shading scenario. Therefore, this study will endeavour to use the same camera settings outlined by Rangelov et al. [218] and also apply them for the outdoor environment so as to have a direct comparison between the shading images. Although laboratory and outdoor lighting conditions typically require different camera settings, in this study the same settings were maintained to ensure methodological consistency and direct comparability between the captured shading scenarios. The outlined camera settings parameters manage light interacting with the camera sensor and the detail in the images, thus impacting clarity, brightness, and overall quality of the 3D model.

- **ISO:** ISO determines how sensitive the camera sensor is to light. Increasing the ISO can help capture images in darker settings, though it may also lead to more image noise. The results from Rangelov et al. [218] indicate that an ISO of 200 provides the best balance for high quality image capture.

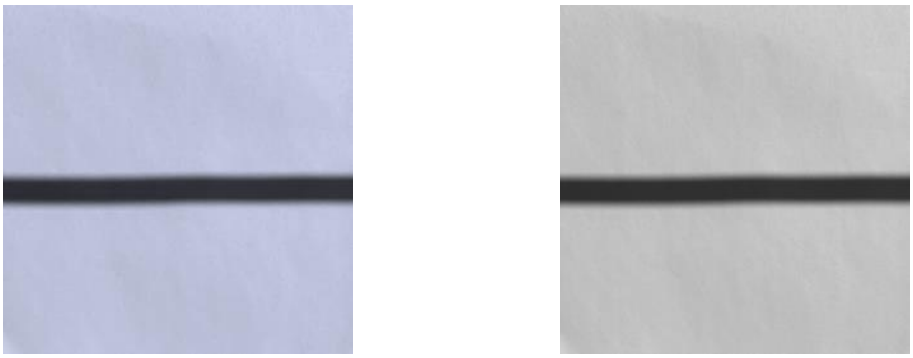
- **Shutter Speed:** Shutter speed indicates the duration the camera's shutter stays open to expose the sensor to light. A fast shutter speed can capture moving subjects sharply by minimising blur, whereas a slower shutter speed lets in more light but may result in motion blur. The findings from Rangelov et al. [218] indicate that a shutter speed of 1/60s is ideal.

- **Aperture:** The aperture is the part of the lens that controls how much light reaches the camera sensor. A large aperture (represented by a smaller f-number) allows more light in and creates a shallow depth of field, whereas a small aperture (larger f-number) increases depth of field but limits the amount of light entering the camera. The findings from Rangelov et al. [218] indicate that a an aperture of f/3.5 is the best for high quality image capture.

Therefore, the camera settings for any image analysis in this chapter will be taken using an ISO of 200, shutter speed of 1/60 s and an aperture of f/3.5 for both laboratory and outdoor environment, ensuring baseline consistency and minimising variability in image acquisition.

4.2.5 Combined Shadow Factor (CSF)

During the analysis of results, it was deemed necessary to produce an initial quantifiable measure, termed Combined Shadow Factor (CSF), that incorporated both the intensity of the shadow and the size of the shadow to attain a better understanding of the discrepancy between outdoor and laboratory environment shadow formation. Initially, the first methodology employed, attempted to quantify the overall size of the shadow by placing a white piece of carboard directly on top of the PV solar cell and using a measuring tape, to manually measure the overall size of the shadow. However, it was soon determined that the shadow dissipates into the white background very subtly, hence the ambiguity of considering which portion can be considered as shadow or not. Therefore, size and intensity of shadow were identified as the influential factors of a shadow during the state-of-the-art outlined in Chapter 3. The CSF was derived for each case of object thickness and distance combination previously outlined in Section 4.2.2 with the methodological calculation derived below referenced to a typical analysed image as shown in Figure 4.12a and b.



(a) **(b)**

Figure 4.12. Typical captured image of a ⌀10.0 mm thin object shading at 40 cm distance from the solar cell on a white background under laboratory environmental conditions. **(a)** RGB, **(b)** Converted to greyscale.

The CSF calculations were carried out using a tailor-made Python script outlined in Appendix F. As a preliminary step, the script converts the input raw RGB image into a greyscale format using the *OpenCV library (cv2)* as seen in the typical conversion example in Figure 4.12. This is achieved via the *cv2.cvtColor()* function, which transforms the colour image into a single-channel image where each pixel represents an intensity value [73]. Once in greyscale, each pixel is mapped to an 8-bit intensity value, meaning it is represented by an integer between 0 (black) and 255 (white). This 8-bit representation allows for 256 different shades of grey, which is standard for image processing applications and ensures sufficient varying range for visual and computational analysis as seen by [74] and more specifically in Chapter 2 Section 2.4. The pixel intensities and the quantity of pixel count were extracted from the image as visualised in Figure 4.13 and were be used for the CSF score calculation later in this section.

To improve the interpretability of the greyscale shadow image demonstrated in Figure 4.13 and Figure 4.14a, a corresponding schematic representation in pixel format is visualised in Figure 4.14b.

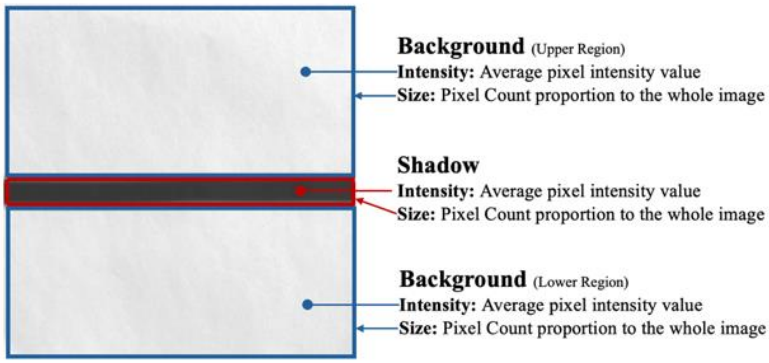
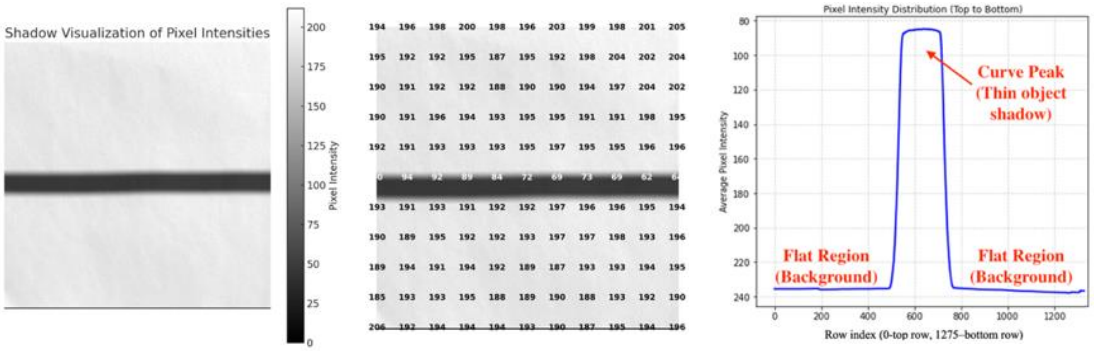


Figure 4.13. Visual representation of the shadow and background intensity and size capture indicated.



(a) **(b)** **(c)**

Figure 4.14. (a) representation of the pixel intensity darkness range, **(b)** a scaled down version of each pixel intensity value of the image, **(c)** the average column pixel intensity distribution resembling a histogram.

This schematic displays the exact same image content, but each pixel is annotated with its greyscale intensity value ranging from 0 to 255 corresponding to studies outlined in the state of the art by Sural et al. [178], Huang et al. [183] and Giraud-Carrier et al. [219]. This numerical format allows the image to be quantitatively analysed, as each value directly corresponds to a level of brightness: 0 represents pure black, 255 represents pure white, and values in between denote varying shades of grey represented in Figure 4.14b. Moreover, a histogram of the intensity distribution commonly found in the state of the art in Chapter 3, particularly by [81], [193] and [194] was compiled using a custom Python script referred to in Appendix H as a visual representation of the pixel intensity distribution visualised in Figure 4.14c. The method used to translate Figure 4.14b to Figure 4.14c is attributed to averaging the pixel values in each row from left to right and plotted from top to bottom, resulting in an averaged pixel intensity column then transposed to a histogram. The x-axis of Figure 4.14c denotes the row index, with the topmost rows of the image appearing first, while the y-axis represents the average greyscale intensity of pixels in each row. The relatively flat regions at the bottom indicate uniform intensity areas, representing the white background. The peak in the curve represents the shadow corresponding with the thin object shadow. After this peak, the intensity returns to baseline, indicating a transition back to a more uniform region.

The first step comprises of estimating the background intensity of the image to distinguish the non-shadowed regions from the shadowed ones as indicated by the blue peripheral indicated in Figure 4.13 and in the flat region labelled in Figure 4.14c. The background intensity is assumed to correspond to the dominant intensity level in the

image, which represents the darker areas in relation to the background values not affected by shadows. The script in Appendix F calculates the 95th percentile of the pixel intensity values across the entire image. Thus, the bottom 5% of the histogram in Figure 4.14c representing the background intensities is eliminated, to focus on the pixel intensity for the shaded region. This approach ensures that the background intensity is robust to resist minor variations in lighting conditions and is not influenced by shadow regions or outliers in the image, allowing for a more reliable detection of shadows in subsequent steps.

Once the background intensity is estimated, the next step consisted of measuring the relative darkness of each pixel compared to the background as indicated by the red perimeter indicators in Figure 4.13. This darkness serves as a proxy for shadow intensity.

For each pixel in the image, the script calculates the darkness as the difference between the background intensity (control) and the intensity of the shaded pixel:

$$D(x,y) = I_{background} - I(x,y) \tag{15}$$

where:

- $D(x,y)$ represents how darker a pixel is compared to the average background intensity.
- $I_{background}$ denotes the background intensity of each pixel in the image, accounting for 95 percent of the pixel distribution used as the estimate of the background intensity level.
- $I(x,y)$ is the intensity of the shaded pixel at coordinates (x,y)(x,y).

Only the shadowed region (pixels darker than the background) contributes to the CSF, denoted as D_{shadow} for the full image (x,y) in equation (16). Therefore, the darkness of the shadow region consists of pixels which are brighter than the established background pixel values. Therefore, the background pixel values do not contribute to the CSF score.

$$D_{shadow}(x,y) = \max(0, D(x,y)) \tag{16}$$

Once the darkness for each pixel is calculated, two factors are derived to quantify the shadow's impact, an Intensity Factor (IF) and a Size Factor (SF).

IF is the average darkness of all shadow pixels. It represents the overall intensity of the shadow shown in equation (17).

$$Intensity\ Factor = \frac{1}{N} \sum_{(x,y)} D_{shadow}(x, y) \tag{17}$$

Where N represents the total number of pixels.

SF is the proportion of shadow pixels relative to the total number of pixels in the image. It represents the size of the shadow relative to the entire image area with the derivation denoted by Equation (18)

$$Size\ Factor = \frac{Number\ of\ shadow\ pixels}{N} \tag{18}$$

The CSF is a product of the IF and the SF, which combines the intensity and size of the shadow having an equal weighting of 1 into a single score. The CSF is then multiplied by 100 to make it easier to interpret as seen in equation (19):

$$CSF\ =\ 100\ (IF\ \times\ SF) \tag{19}$$

A higher CSF indicates that both the shadow intensity and its coverage are significant, whereas a lower CSF suggests a weak and smaller shadow formation.

Whilst the formation of shadow comprising of umbra and penumbra has been established in the fundamentals section of this thesis in Chapter 2 Section 2.3. Moreover, the CSF calculations in this chapter do not make a distinction between umbra and penumbra shadow and shall thus use the average shadow intensity as a metric. Nonetheless, Chapter 5 addresses this limitation by distinguishing between umbra and penumbra in shadow image analysis.

4.3 Results and Discussion

The comparative differences in power output of the same solar cell under laboratory versus outdoor conditions will be outlined in this chapter. This will be followed by a detailed comparison of performance under thin-object shading scenarios, all within the same environmental conditions as previously described. Additionally, the results will be cross-referenced with shadow formation discrepancies identified through the image analysis approach, providing an understanding of the reason behind the difference in performance on a solar cell in both laboratory and outdoor conditions.

4.3.1 Analysing the Significance of Experimental Bias 1 and Bias 2

4.3.1.1 Bias 1 - Analysing the Significance of Colour Coating on Thin Objects on Power Loss: A Comparison of Black (Absorbent) and Silver (Reflective) Finishes

The distance between the solar cell and the thin object was varied in increments of 5 cm for each object thickness interchanging between black and silver painted thin objects and the power loss between the control and shaded solar cells was recorded. Figure 4.15 illustrates these effects, comparing the power loss associated with absorbent black-coloured thin objects (represented by solid lines) and reflective silver objects (depicted by dashed lines). The uncertainty associated with each power loss value was derived from Appendix B.2. While the uncertainty of the solar simulator I-V testing unit was calculated to be 0.042%, a more conservative approach was adopted to account for the variability of the laboratory testing environment. Specifically, a 95% confidence interval was applied, with the remaining 5% outside this interval taken as the assumed uncertainty level. This value is reflected in the error bars presented in Figure 4.15 and subsequently in Figure 4.16. Notably, the uncertainties corresponding to the 5% outside the confidence interval were consistently greater than the inherent uncertainty of the I-V testing unit, thus justifying the use of this more conservative method.

The results demonstrate that the percentage power loss remains relatively consistent across different object thicknesses, with minor variation between absorbent and reflective surfaces. This finding suggests that the primary influence of power loss is the shadow formation itself, rather than secondary effects associated with surface reflectivity.

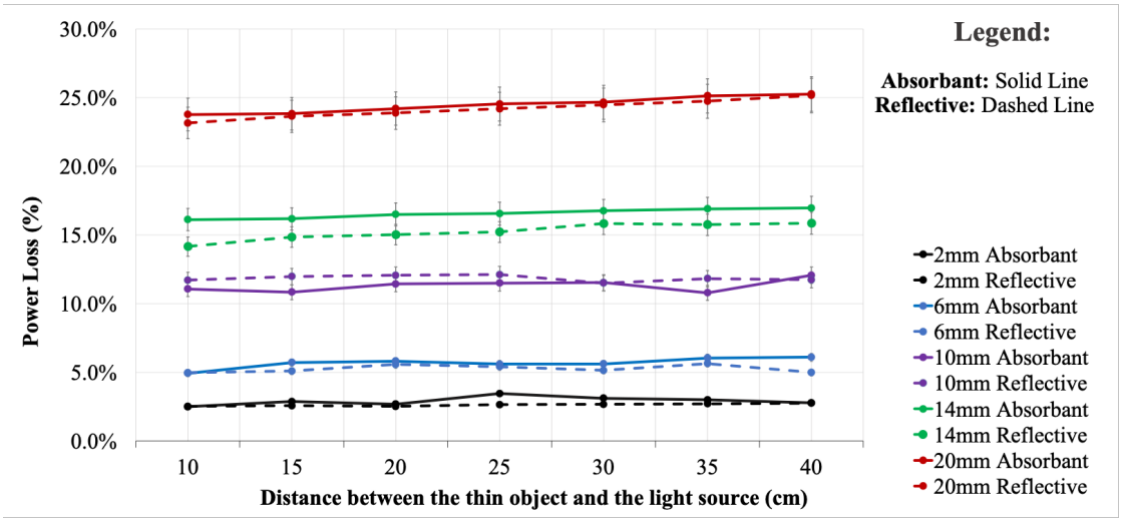


Figure 4.15. A comparative difference between black absorbent (solid lines) and silver reflective (dashed) coated thin objects in a laboratory environment.

To evaluate the statistical significance of these observations, a one-way Analysis of Variance (ANOVA) was conducted to determine whether the any significant effect on power loss was observed by absorbent black and reflective silver thin objects. The ANOVA results yielded an F-statistic of 0.0489 and a p-value of 0.8257, indicating no statistically significant difference, as the p-value exceeds the standard 0.05 threshold.

For the thinnest objects (⌀2.0 mm and ⌀6.0 mm), both absorbent and reflective materials exhibited nearly identical power loss trends, reinforcing that the reduction in output is primarily due to the obstruction of active cell areas rather than variations in surface reflectivity. As object thickness increased (⌀10.0 mm, ⌀14.0 mm, and ⌀20.0 mm), power loss increased proportionally, yet the difference between absorbent and reflective coatings remained below the statistical significance level of $p < 0.05$ using the significance measurement threshold highlighted by [220]. If reflectivity had a significant impact, greater differences in power loss would be expected, particularly for thicker objects with larger surfaces for light redirection. While minor variations due to

diffuse reflection may occur, their overall effect is negligible and statistically insignificant for the presented experimentation setup and methodology presented on the specified solar cell.

Therefore for Bias 1, the null hypothesis (H_0), that the colour coating of the object (black vs. silver) has no significant effect on the reflection bias on the solar cell in either environment is accepted, while the alternative hypothesis (H_1), that the colour coating has a significant effect in at least one environment, is not supported by the data. Since no statistically significant difference was observed, it can be inferred that the same thin objects may be appropriately used in both laboratory and outdoor environments without affecting the reflection bias on the solar cell.

4.3.1.2 Bias 2 - Analysing the Significance of the Orientation of Thin objects on Power Loss: A Comparison between Horizontal and Vertically Oriented Thin Objects

The results of this section aim to determine how sensitive the solar cell is to shadow placement and whether power loss remains consistent across different orientations.

To observe these trends, Figure 4.16 visualises the power loss impact for the same selective thin object thicknesses and distances from the solar cell, with horizontally transposed thin shadows (indicated by solid lines) and vertically transposed shadows (depicted by dashed lines). The results demonstrate that the percentage of power loss due to thin object shading is fairly similar between the two orientations, with only slight variations. This suggests that, similar to the comparison between absorbent and reflective thin objects, the primary contributing factor to power loss is the shadow itself rather than its orientation on the solar cell. This trend remains consistent even as the diameter of the thin object and its distance from the solar cell increase.

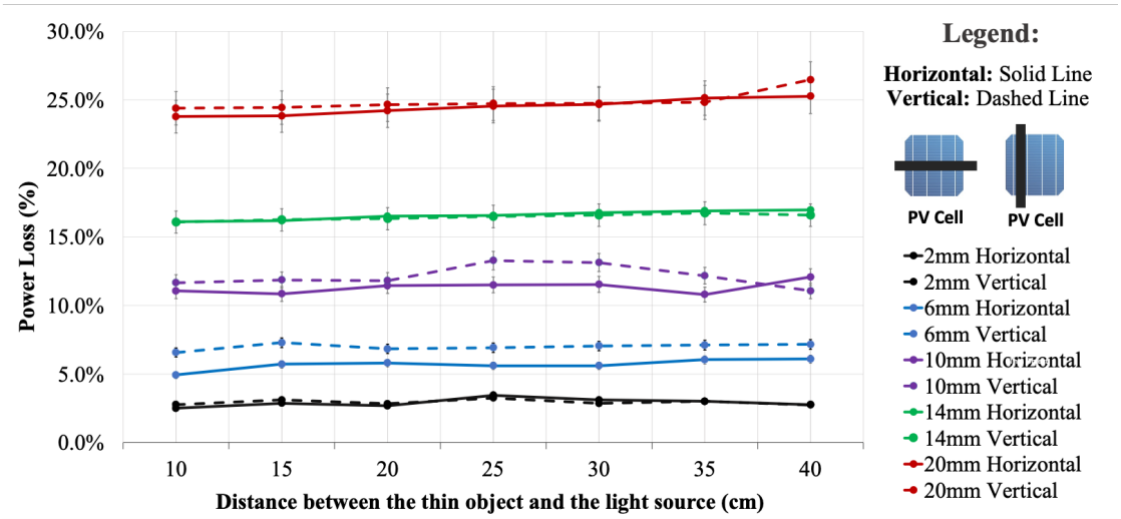
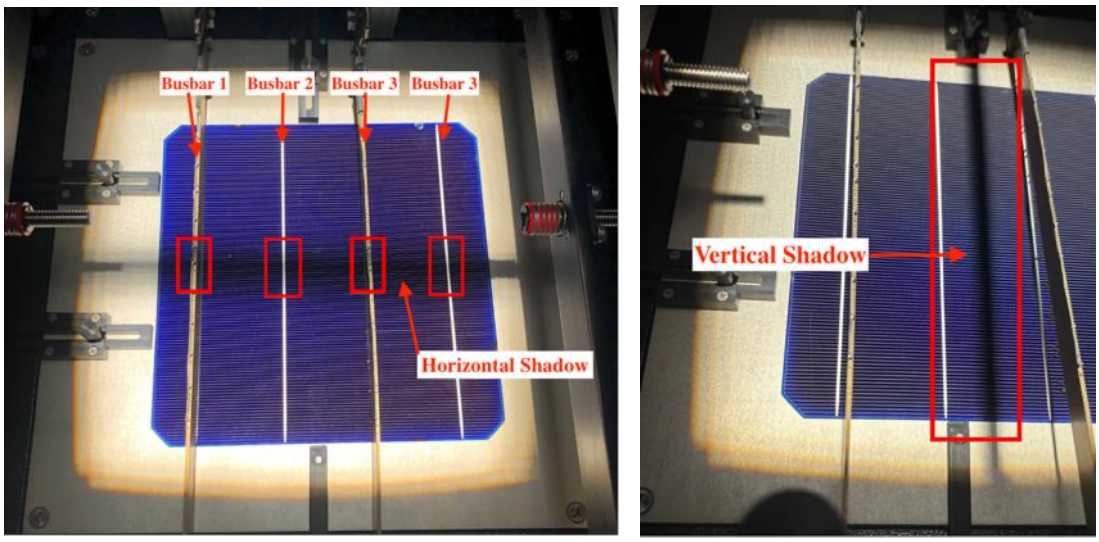


Figure 4.16. A comparative difference between horizontal (solid lines) and vertical (dashed) aligned thin object shadow on the solar cell in a laboratory environment.

A potential contributing factor to the slight discrepancy observed in the results is the increased likelihood of horizontal shadows overlapping with the PV cell's busbars as seen in Figure 4.17a as opposed to the no overlapping shadow on the busbars visualised in Figure 4.17b. The busbars play a crucial role in collecting and transporting the generated electrical current. In this experiment, a four-busbar solar cell was used. When the shadow was transposed horizontally as shown in Figure 4.17a, an intersection of the shadow with the busbars was noted at four points. Therefore, the effective shadow coverage was reduced by a total area corresponding to the thickness of the shadow multiplied by the width of the busbars at those intersections as seen in Figure 4.17a. Conversely, when the shadow was transposed vertically, it fell between the solar cell's busbars as seen in Figure 4.17b, theoretically leading to a slightly less shadowed surface area on the active cell regions.



(a) **(b)**

Figure 4.17. A comparative understanding between the **(a)** Horizontal transposed shadow on the busbars contacts **(b)** Vertical transposed shading on the busbars.

To assess whether this minor variation had any statistical significance, a one-way ANOVA test was conducted to compare the impact of horizontally and vertically transposed shadows on the PV cell. The test resulted in a p-value of 0.849, indicating no statistically significant difference. Therefore, the null hypothesis (H_0) that the orientation of the shadow (horizontal vs. vertical) has no significant impact on the solar cell's performance, is retained, while the alternative hypothesis (H_1), that shadow orientation significantly affects performance even when overall shadow size remains constant, is not supported by the data. Consequently, the minor shadow losses caused by busbar interactions do not significantly impact the overall efficiency of the solar cell, and experimental results can be assumed to be statistically applicable across both shadow orientations on the solar cell.

The solar simulator is set up and calibrated to deliver irradiance under STC. One of the primary discrepancies examined in this study was the difference in solar radiation characteristics between the controlled laboratory simulator environment and natural outdoor sunlight, and how this difference impacts the shading effect. This study acknowledges that, in outdoor environments, the global horizontal irradiance includes a proportion of diffuse horizontal irradiance even in clear sky conditions, whereas the solar simulator emits mostly all direct normal irradiance with just minor diffusion occurring. However, the difference in power output of the solar cell under control conditions between the two environments is an inherent part of this discrepancy as will

be elaborated in Section 4.3.2. This difference reflects variations in spectral distribution, as well as the presence or absence of diffuse light. Importantly, this baseline difference is not treated as a separate correction factor; instead, it is considered an inherent part of the comparative analysis between laboratory and outdoor conditions. By acknowledging this distinction, the study ensures that the observed shading effects are accurately compared between the two environments.

With the assumptions and hypothesis outcomes of the preliminary experimentation established, the investigation now proceeds to the experimental evaluation of solar cell performance under controlled laboratory and outdoor conditions.

4.3.2 Comparative Baseline Analysis at Control Conditions between Laboratory and Outdoor conditions

Prior to the introduction of shadows on the solar cells, a comparative analysis was conducted to assess the electrical performance of the solar cells under two distinct lighting conditions. These consist of the full spectrum of light emitted by the Xenon lamp within the solar simulator and the full solar spectrum under outdoor conditions previously outlined under Section 2.1 in Chapter 2, bearing electromagnetic spectrum discrepancy as seen in Figure 2.2 of the same section. The results, presented in Figure 4.18, were obtained under corrected STC conditions, ensuring a controlled comparison between laboratory and outdoor environments. The full I-V curve shown in blue is a replication of the previously outlined curve in Section 4.2.3 Figure 4.10 demonstrating the performance of the solar cell under the solar simulator. Moreover, the red point on the graph indicated by the red point marker is the MPP for the outdoor conditions with extrapolated voltage and current readings on the x-axis and y-axis respectively. The comparative difference can be analysed by the difference in the red and blue point marker on the graph demonstrating the power output of the identical solar cell at control conditions.

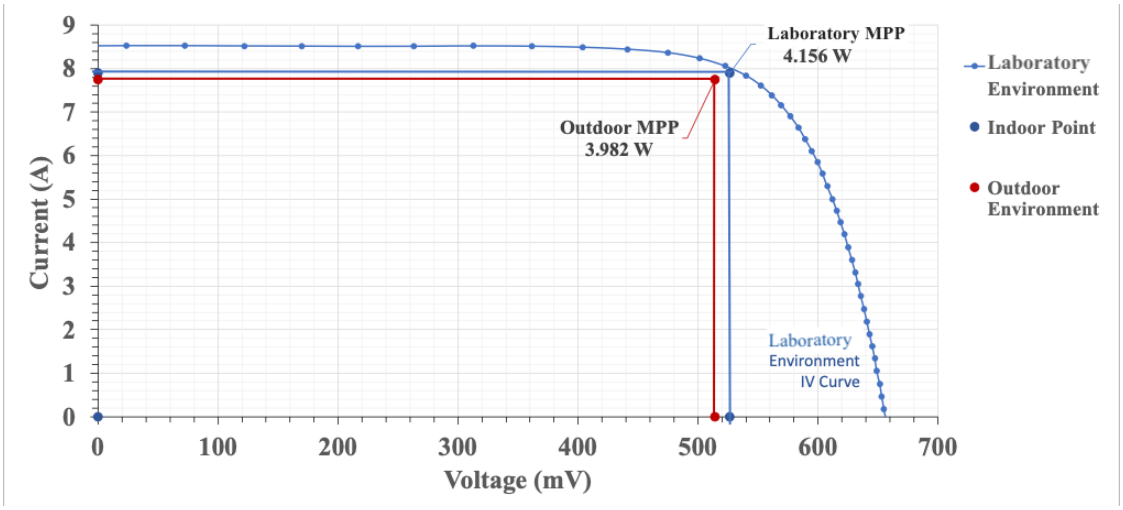


Figure 4.18. Comparative control conditions between outdoor (red point) and laboratory environment (blue point and curve) using identical PV solar cells.

While the laboratory setup was designed to closely replicate solar irradiation, spectral differences between the Xenon lamp and natural sunlight, particularly in the IR and UV regions, may introduce slight variations in the solar cell's response. The solar cell operating in the outdoor environment exhibited an output power of 3.982 W, whereas the laboratory environment yielded a slightly higher output of 4.156 W, representing a 4.37% increase.

The observed discrepancy in power output can be attributed to multiple factors. One possible explanation lies in slight variations in the measurement conditions. In the outdoor setup, the solar cell's busbars were manually soldered, whereas in the laboratory setup, gold-plated contacts were precisely aligned with the busbars, potentially allowing for more consistent electrical contact. While these differences in setup may introduce minor variations, every effort was made to ensure the highest level of accuracy within the constraints of the available resources. However, the primary contributing factor to the lower power output observed during outdoor testing compared to laboratory testing is the difference in the spectral and directional composition of sunlight. Sunlight consists of a combination of direct and diffuse radiation [44, p. 53],[213, p. 21],[14], with a significant portion of its energy concentrated in the infrared region. In contrast, laboratory testing was conducted under controlled artificial illumination that simulates only the beam component of sunlight and emphasises the UV and visible spectra wavelengths that are more effective in exciting electrons within photovoltaic materials. Since infrared radiation primarily generates heat rather than promoting electron

excitation, it contributes less to the photoelectric conversion process. Consequently, under natural sunlight, where diffuse and infrared components are prevalent, the effective photon energy available for electron excitation and current generation is reduced, resulting in lower power outputs compared to the idealised laboratory environmental conditions.

Additionally, environmental factors such as humidity, wind speed, the presence of airborne particles and atmospheric scattering conditions could contribute to variations in power output between the two settings. Given that these differences are inherent to the experimental conditions, the observed discrepancy will not be adjusted in subsequent data analysis, as it represents a natural variation in power output rather than an experimental limitation. This approach aligns with one of the rare case where previous studies have reported laboratory versus outdoor PV performance discrepancies previously outlined in the state of the art in Chapter 3 by Kumari et al. [138]. Having said that, Kumari et al. [138] places the shadow coverage object atop of the PV source rather than a realistic thin object shading scenario.

4.3.3 Comparative Difference between Laboratory and Outdoor Environment at Thin Object Shading Conditions

The purpose of analysing the power loss relative to the control solar cell is to determine the range of discrepancies, from the minimum to the maximum power output differences, caused by the thin object shading scenarios outlined in Section 4.3.2. This comparison between laboratory and outdoor environments directly addresses RQ.1.

Figure 4.19 has been compiled to visualise the respective outdoor environmental experimentation, where the power loss is given for thin objects of various thicknesses and distances from the solar cell. Likewise, Figure 4.20 presents a similar bar chart, for the laboratory environmental experimentation.

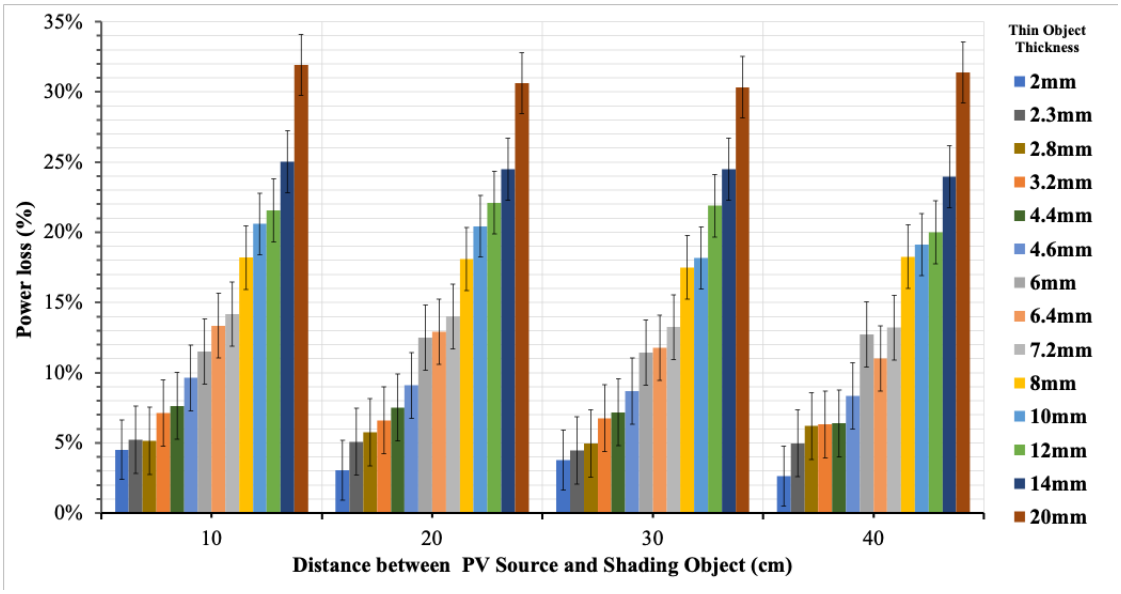


Figure 4.19. A visual bar graph representing the power loss due to thin object shading scenarios in an **outdoor** environment.

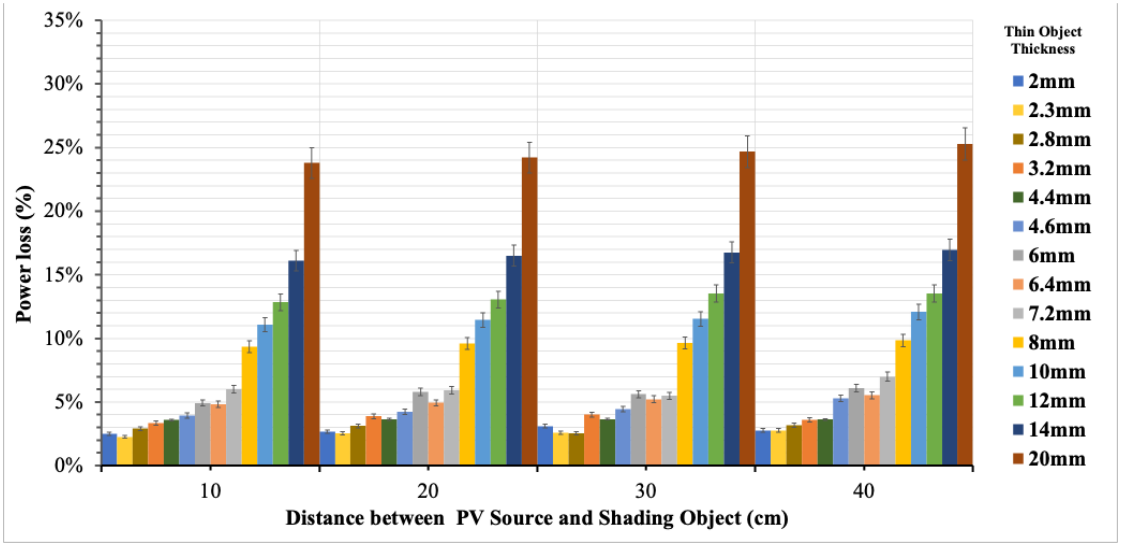


Figure 4.20. A visual bar graph representing the power loss due to thin object shading scenarios in a **laboratory** environment.

The initial clear observation is that in an outdoor environment, the power loss due to any thin object shading is always higher than that of a laboratory environment. This aligns with the findings of Kumari et al. [138], who reported that shading a portion of a PV solar cell led to a greater percentage of power loss in outdoor conditions. Therefore, this entails that the solar cell placed in an outdoor environment will always produce less power under thin object shading scenario at any distance or object thickness. Apart from the discrepancy in the light spectrum initially observed in Section 2.1 Figure 2.2 as a differentiating factor between the two environments, the reason for this initial

observation cannot be derived from either figures and therefore a more in-depth analysis of the variation of shadow is required. Apart from difference in the overall loss in power between both environments, similar trends between the power loss and the thickness of the object have been observed for all the distance and thickness parameters analysed.

A key observation is how power loss progresses as the distance between the shading object and the solar cell increases. In both outdoor and laboratory environment, power loss remains relatively consistent across distances, with a gradual rise for thicker objects. This suggests that as distance increases, even though the shadow softens due to ambient light diffusion, the impact on the solar cell is retained up to 40 cm distance apart. Furthermore, when the thin object is positioned at a distance of 40 cm from the PV source, one can notice that the power loss trends in Figure 4.19 and Figure 4.20 is similar to that of the thin object being at a distance of 10 cm to the PV. This implies that even though the shadow may lose a portion of its intensity due to the ambient light diffusion as distance increases, the corresponding increase in shadow size compensates for this intensity loss. This relationship between distance from the PV source, thickness of the object and the resulting power loss shall be investigated in more depth in Chapter 5, in order to answer RQ.2.

The overall trend shows that as expected, as the thickness of the thin shading object increases, the power loss increases in both environments. This is due to a larger shadow being projected on the solar cell and therefore more resistance on the solar cell. However, the rate at which the power loss increases is slightly different between the two environments as visualised for the case of distance of 10 cm shown in Figure 4.21. Evidently, the red trend line representing the outdoor environment, demonstrates a steeper rate of power loss compared to the laboratory environment. Moreover, this is confirmed by the higher gradient of 0.0181 observed for the outdoor trendline compared to the gradient of the laboratory environment at 0.0110 than that compared to a laboratory environment. The same trend is also observed in all the other distances between 15 cm and 40 cm from the solar cell.

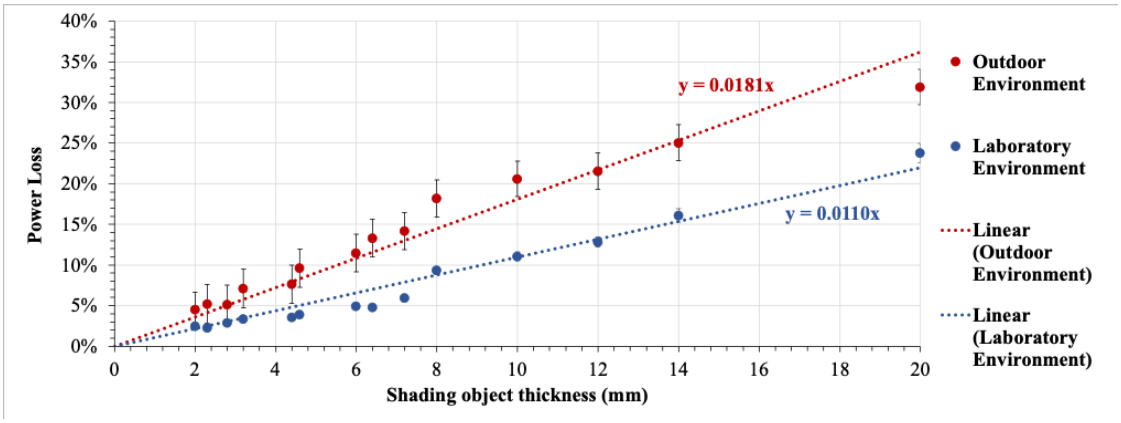


Figure 4.21. A comparative visual representation between the rate of power loss in outdoor environment shown in blue and laboratory environment shown in red at 10 cm distance from the solar cell.

To answer the first part of RQ.1, Figure 4.22 outlines a heatmap produced specifically to visualise the power output difference in Watts (W), between both environments for all the combinations of distance and thickness. It is important to understand that the laboratory environment produces more power output than the outdoor environment on the solar cell, therefore the values in Figure 4.22 illustrate the power output the laboratory environment generates more than the outdoor environment. The thickness and distance combinations visualised in blue indicate the lower difference in power output between the laboratory and outdoor environment. Contrastingly, the red visualised instances denote higher power difference.

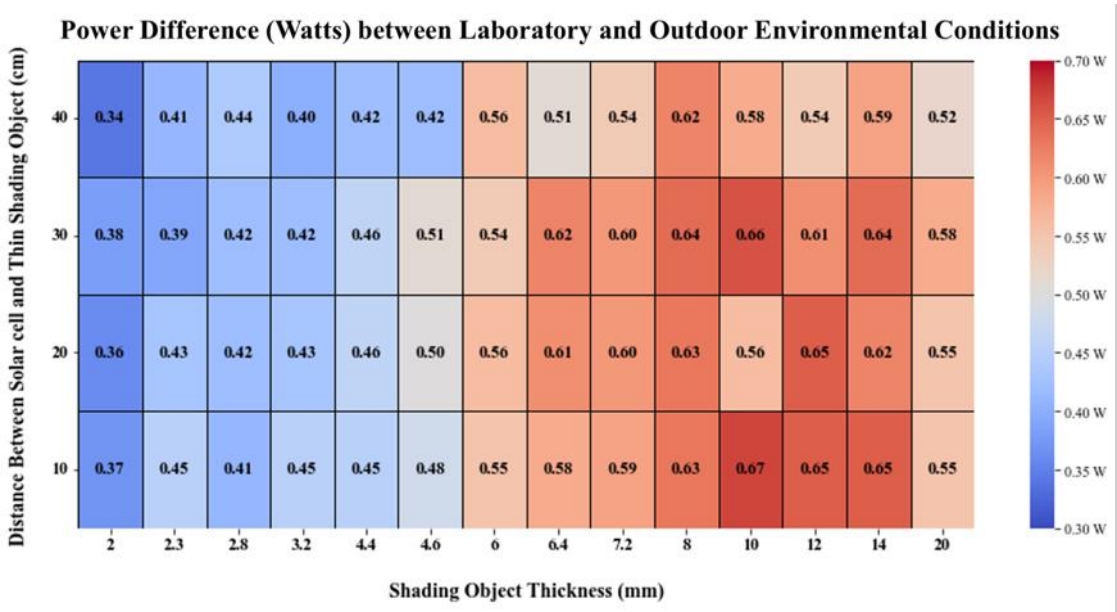


Figure 4.22. A heat map visualising the area where the highest discrepancy in power output between outdoor and laboratory environment is observed.

Although percentage power loss was utilised as a metric to compare both environments in previous sections, the heatmap in Figure 4.22 is designed to analyse the actual power output difference, thereby providing a more comprehensive assessment of the discrepancy. The left portion of the heatmap indicates a smaller power output difference compared to the right portion, suggesting that as thin objects increase in size, their shading effect on the solar cell becomes more pronounced, leading to an amplified loss in power output. However, the power output difference is not directly proportional to the size of the shadow. For case, to double the observed power difference of 0.37 W for a ⌀2.0 mm thickness at a ⌀10 cm distance, the object thickness would need to be more than ten times larger than ⌀2.0 mm, as a ⌀20.0 mm thickness at the same distance results in a similar power difference of 0.55 W. This indicates that doubling the object thickness does not result in a doubling of the power difference; instead, the trend is more gradual. Notably, beyond a thickness of ⌀10.0 mm, the power difference stabilises, suggesting a saturation range where additional thickness does not significantly exacerbate the discrepancy.

Therefore, to answer the first part of RQ.1, the discrepancy range in power output between outdoor and laboratory experimentation for the conventional monocrystalline 156 x 156.0 mm solar cell would be between 0.34 W and 0.67 W. It should be noted that these values reflect the given methodology and the distance and thickness boundaries considered in the experimental setup outlined in Section 4.2. The significance of this discrepancy becomes more pronounced when multiple solar cells are integrated into a PV module, and even more so when multiple PV modules are connected in series to form a full panel string as seen previously in Section 2.2. For future studies, this unprecedented comparison specifically for thin-object shading, can serve as a reference for researchers examining thin object shading in both laboratory and outdoor environments. Moreover, although the discrepancy range was determined, this study aims to also take into account shadow formation discrepancies. This shall be carried out by analysing images captured during experimentation to identify any anomalies and trends in shadow formation in Section 4.3.4. As a sample to the image dataset, visual representation of the shadow is seen in Figure 4.23, where the images taken in outdoor and laboratory environment are compared for a fixed object thickness of ⌀10.0 mm and distances at 10 cm increments. However, the interpretation of these

images is subject to researcher bias, and thus a more objective analysis was conducted using the CSF methodology previously mentioned in Section 4.2.5.

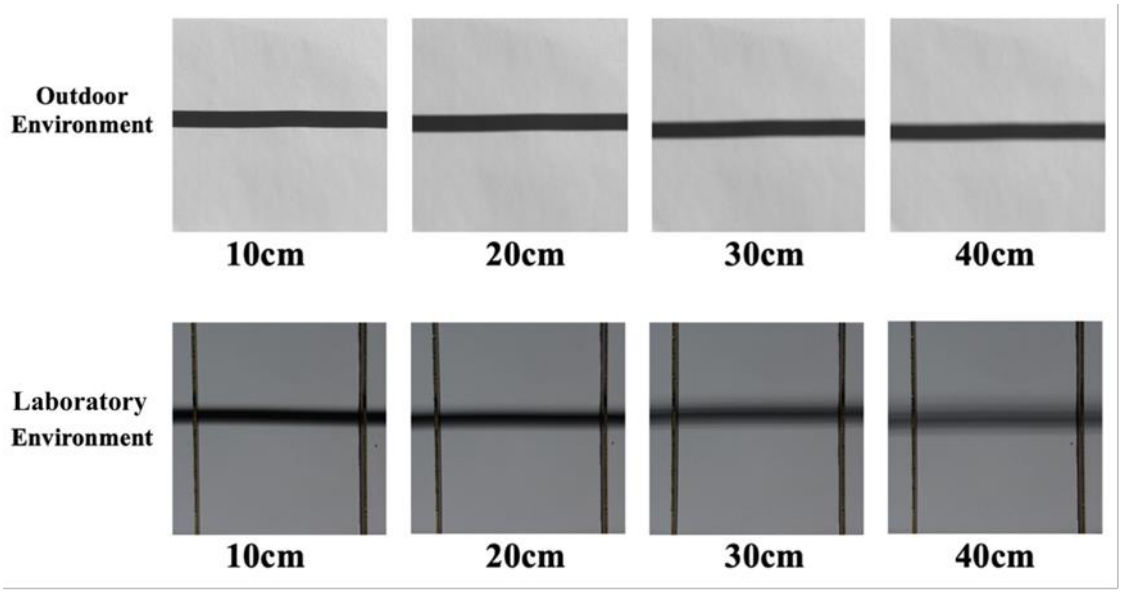


Figure 4.23. Comparative interpretation of the ⌀10.0 mm thickness thin objects between outdoor and laboratory environment.

In the analysis of shadow impacts on solar cells, it is crucial not only to consider the shadow's presence but also its intensity. The CSF reflects both the size and intensity of the shadow, as both factors contribute significantly to the overall impact on the solar cell's power output. To automate the calculation of the CSF, a custom Python script was implemented using the code in Appendix F, offering a method for analysing the digital images with a white background, which represents the solar cell surface, and the horizontal shadow in the middle similar to the exemplary image in Figure 4.12b shown previously in Section 4.2.5 . Moreover, the resulting CSF score for each image for a distance up to 40 cm at 10 cm increments, and the consolidated object thickness range introduced at the end of Section 4.2.1 was computed in Table 4.4 with the relative difference and average values illustrated in Table 4.5. Figure 4.24 provides a comparative analysis of the CSF factor for outdoor and laboratory environments across varying consolidated object thicknesses and distance from the solar cell.

Table 4.4. Comparing the CSF score between outdoor and laboratory environment shadows between 10 – 40 cm distance from solar cell at the consolidated thin object thickness range.

	⌀2.0 mm		**⌀6.0 mm**		**⌀10.0 mm**		**⌀14.0 mm**		**⌀20.0 mm**	
	Lab	Outdoor	Lab	Outdoor	Lab	Outdoor	Lab	Outdoor	Lab	Outdoor
Dist. 10 cm	2.20	5.23	3.63	5.76	5.21	7.29	6.27	8.88	8.56	11.92
Dist. 20 cm	2.31	5.26	3.68	5.35	5.20	7.18	6.44	9.20	8.46	12.18
Dist. 30 cm	2.38	5.42	3.70	5.95	4.86	7.42	6.26	8.91	8.50	11.61
Dist. 40 cm	2.35	5.09	3.52	5.40	4.84	6.93	6.39	9.09	8.28	12.31

Table 4.5. The difference and average value of the CSF score between outdoor and laboratory environment shadows between 10 – 40 cm distance from solar cell at the consolidated thin object thickness range.

	⌀2.0 mm	**⌀6.0 mm**	**⌀10.0 mm**	**⌀14.0 mm**	**⌀20.0 mm**
Dist. 10 cm	3.03	2.13	2.08	2.61	3.36
Dist. 20 cm	2.95	1.67	1.98	2.76	3.72
Dist. 30 cm	3.04	2.25	2.56	2.65	3.11
Dist. 40 cm	2.74	1.88	2.09	2.7	4.03
Average CSF Score	**2.94**	**1.98**	**2.18**	**2.68**	**3.56**

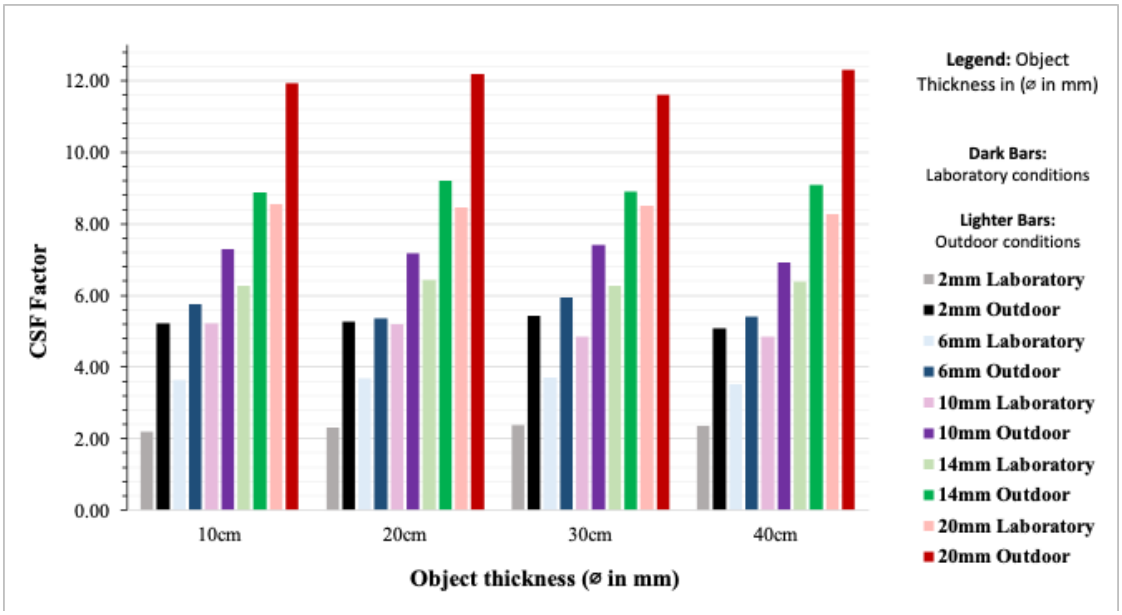


Figure 4.24. Comparative visual representation of the CSF factor between outdoor and laboratory environment.

The results demonstrate that the outdoor environment consistently yields higher CSF scores, reinforcing the observation that outdoor conditions produce stronger and more

pronounced shadow effects. This results corresponds to the result previously observed in this section where the outdoor environment produced higher power losses than in a laboratory environment. This trend is evident across all tested thicknesses, with the most significant difference occurring at the thickest object (20 mm) at a distance of 40 cm, which is also where the outdoor CSF values reached their highest levels as seen in Figure 4.24. Conversely, laboratory conditions yield substantially lower CSF values, indicating that shadows formed in a laboratory environment are not only weaker in intensity but also less impactful in terms of overall shading effects. Furthermore, whilst the absolute size of the shadow may not always be larger in an outdoor setting, the increased shadow intensity plays a crucial role in elevating the CSF factor, reinforcing that shadow intensity is a contributor to CSF rather than shadow size alone. For case, while thinner objects (⌀2.0 mm and ⌀6.0 mm) generate smaller shadows, their CSF values under outdoor conditions remain consistently higher than their laboratory counterparts, reinforcing the idea that intensity amplifies shading effects. Additionally, as object thickness increases, it is apparent that CSF values widen (2.2 at ⌀2.0 mm up to 12.31 at ⌀20.0 mm). This is also true when analysing the average relative difference between the laboratory and outdoor CSF score for the anomaly of the ⌀2.0 mm object, the average CSF score difference increases from 1.98 at ⌀6.0 mm up to 3.56 for the ⌀20.0 mm thin object as seen in the average values denoted in the last row of Table 4.5. When investigating the anomaly for the ⌀2.0 mm thin object average score, it was found that since the shadow was predominantly very light in intensity, there was a significant amount of fringes created in laboratory environment which resulted in having a distributed image as will be further investigated in Section 4.3.4. Nevertheless, thicker objects, when exposed to outdoor conditions, create more intense shading effects, which in turn contribute to greater power loss, as previously discussed in this section.

Although CSF effectively quantifies the overall shading effect by incorporating both size and intensity, a key limitation of this metric is its inability to differentiate between the distinct formations of umbra and penumbra shadows. This distinction is particularly significant given that variations in shadow characteristics influence power loss differently. As identified in Chapter 2, understanding the role of umbra (fully shaded regions) and penumbra (partially shaded regions) is essential for a more precise assessment of shading impacts on monocrystalline solar cells. To address this gap, Chapter 5 will introduce a refined approach that separately quantifies umbra and

penumbra contributions, thereby enhancing the accuracy of shading analysis and its correlation with power loss in PV systems. The classification of umbra and penumbra shadow formation and the correlation with the variable factors is a unique identifier of this research study which will be further exemplified in Chapter 5.

4.3.4 Outdoor and Laboratory Comparative Shadow Formation Analysis

The previously discussed comparative results highlight a clear discrepancy in power output between outdoor and laboratory experimentation, despite maintaining consistency in key variables such as the solar cell, object thickness, and distance from the solar cell's surface in both experiments. This suggests the presence of additional external factors influencing the observed variations. As outlined in the methodology Section 4.2.4, images were captured for each thin object shading case to facilitate a more detailed quantitative assessment of the shadows cast on the 156.0 mm × 156.0 mm solar cell.

To conduct a more focused analysis, a ⌀10.0 mm thin object was selected as a representative case for shadow formation. The images captured were subsequently cropped to a refined scale to better visualise the thin object shadow in detail, allowing for a more detailed examination of shadow characteristics, as visualised in Figure 4.25. One of the most immediately apparent discrepancies is the variation in background colour between laboratory and outdoor settings. Under outdoor conditions, illuminated by natural light, the captured images exhibit a visibly light background with a slight shift toward grey tones, despite the use of consistent camera settings. Conversely, during laboratory experimentation, the background was intentionally darkened to attenuate the light source of the solar simulator, thereby reducing the current required to operate the bulb and maintain STC. In contrast, outdoor experimentation resulted in significantly higher background brightness.

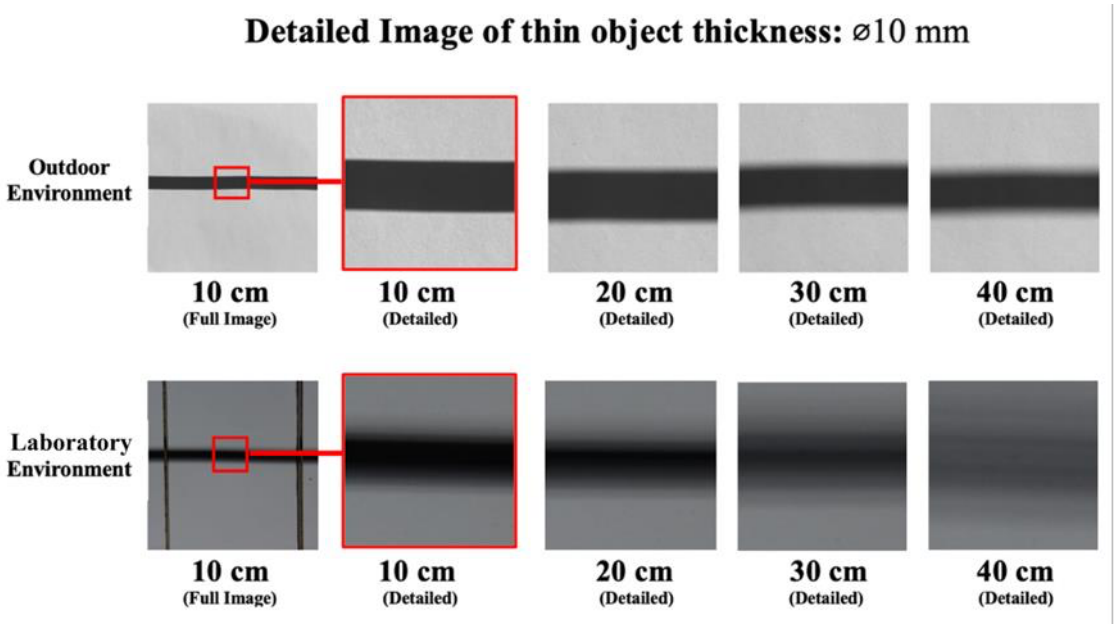
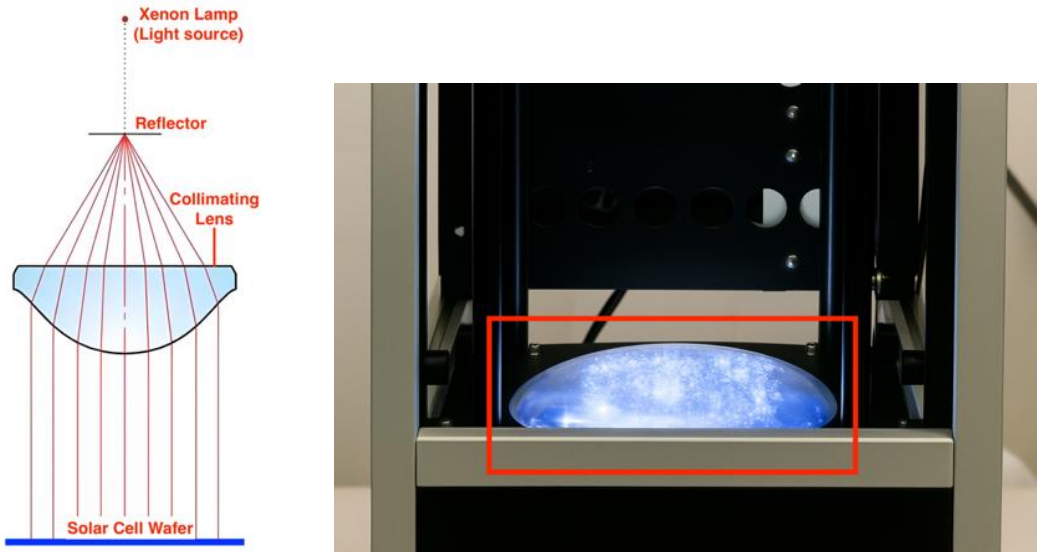


Figure 4.25. A Comparative analysis of detailed images for a ⌀10.0 mm thin object at each distance range.

At a 10 cm distance from the solar cell, the properties of both outdoor and laboratory shadow formation mostly comprise a dark portion similar to the umbra shadow fundamentally seen in Chapter 2 Section 2.3. Gradually, as the distance between the thin object and the solar cell increases up to 40 cm, the shadow becomes lighter in nature. Moreover, it is evident that at 40 cm distance the outdoor setting still maintains most of the umbra shadow and only a small portion is attributed to penumbra shadow. In contrast, in a laboratory environment and at 40 cm distance, the ⌀10.0 mm thin object shadow is much lighter and fragmented into straight parallel horizontal lines. The lines observed are similar to the ones observed by Sinzinger which are called interference fringes [221]. These fringes are a measure of the curvature of the wave which is formed through the interaction of the light waves with the thin object in their path, equivalent to the scenario observed in the laboratory environment. In contrast, as the distance between the thin object and the solar cell decreases, the fringes are not as apparent and display a resembling comparative shadow to outdoor experimentation at the same distance. This optical principle starts to shed light on the reason why the power loss results in Figure 4.19 and Figure 4.20 emerged distinctively different from each other.

Referring to the theoretical principles of light introduced in Chapter 2, the sun, located approximately 150 million kilometres away from Earth, acts as a quasi-point source at infinity [222, p. 12]. As a result, its rays arrive at Earth as nearly parallel beams

producing highly collimated light [223]. Due to this reason, the outdoor experimentation yielded sharp and well-defined umbra and penumbra shadow for all the thin object thicknesses with negligible diffraction noted. The combination of the high collimation and the inherently large distance between the sun and the earth prevent the visible formation of diffraction fringes in shadows observed in the outdoor experimentation. In contrast, in laboratory experimentation, unlike the sun, a Xenon arc lamp point source emits inherently divergent light and requires an optical collimation system which is incorporated in the solar simulator used in this research, consisting of a convex collimating lens to approximate the parallelism of sunlight. This is seen schematically in Figure 4.26a and realistically in Figure 4.26b.



(a) **(b)**

Figure 4.26. (a) Schematic diagram of the laboratory I-V solar simulator, **(b)** The collimating lens inside the I-V solar Simulator.

Upon incidence on the thin object rod, the light waves undergo diffraction, bending around the edges of the obstacle causing Fresnel light diffraction fringes. These fringes are similar to the phenomena studied by Claude et al. [224], also resembling the effect seen in laboratory environment. These fringes can also be observed at the edge of the light hitting the shutter opening window and being transposed on the surface of the experimental bed as seen in Figure 4.27, where the parallel light beam hits the slit of the solar simulator creating fringes caused by the diffraction of light. Having said that, the fringe formation observed did not interfere with the light incident on the solar cell, as

the simulator's specifications guarantee a full illumination area of 156 mm × 156 mm, accommodating a standard full-sized solar cell [225].

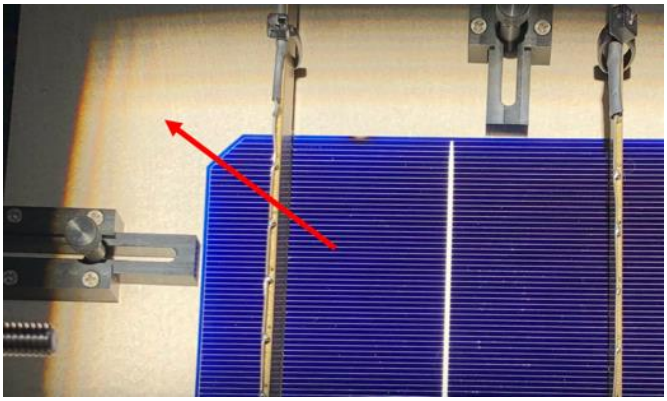


Figure 4.27. Fringes evidently transposed from the slit of the solar simulator.

Given the relatively short propagation distance, the resulting diffraction pattern falls within the Fresnel regime, characterised by complex wavefront curvature and varying phase relationships. According to Huygen's principle [226], every point on a wavefront can be considered a secondary source of spherical wavelets, and the new wavefront is formed by the superposition of these secondary wavelets. When the incident wavefront encounters the edges of the circular object, the wavelets originating from the object's edges interfere with one another, creating a structured intensity distribution on the observation plane beneath the object.

The diffraction pattern consists of concentric fringes surrounding the geometric shadow of the circular object, with alternating regions of high and low intensity resulting from the interference of these secondary wavelets. As the wavefront bends around the edges of the object, the transition from light to dark is not abrupt but rather exhibits a gradual intensity variation, a result of near-field diffraction effects [227]. Additionally, edge diffraction at the periphery of the circular object further modifies the light distribution, contributing to additional interference effects and influencing the overall contrast and spacing of the fringes [228]. The final observed pattern is highly dependent on the wavelength composition of the Xenon light source, with polychromatic illumination leading to a superposition of wavelength-dependent fringe structures. This phenomenon provides a direct visualisation of wave-optical effects and demonstrates the principles of near-object diffraction and Huygen's principle in the context of wave optics. Moreover, Luo et al. [229] also noted that altering the distance between the thin object

and the surface (solar cell) results in different fringe formation as evidently seen in Figure 4.28a. This corresponds to the results of this experimentation visualised by the rotated thin shading object images in Figure 4.28b [229].

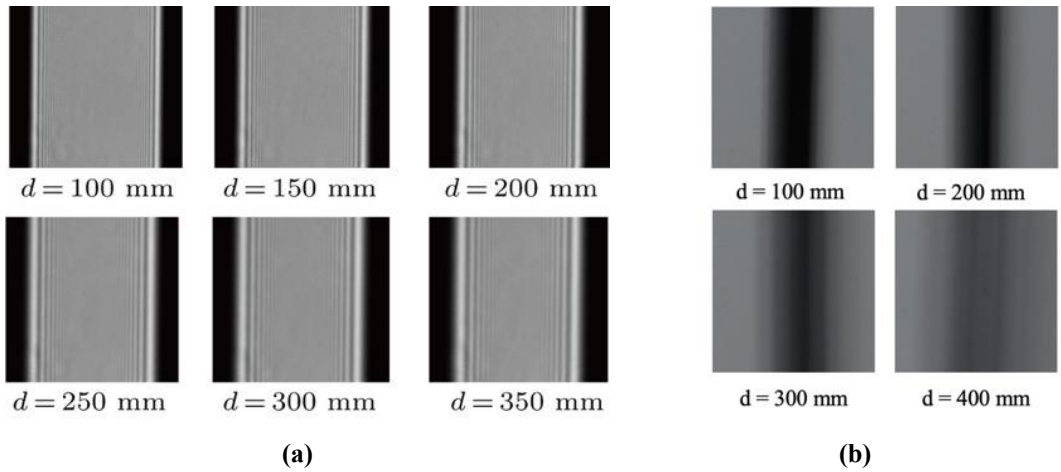


Figure 4.28. (a) Diffraction patterns of a slit noted by Luo et al. [229] **(b)** Rotated images from the image dataset, captured in the laboratory environment of this study, are presented. These images show the same slit diffraction pattern observed using objects of different sizes, demonstrating similar diffraction behaviour at comparable distances from the source.

To better observe Fresnel light diffraction and incident waves on the surface of the solar cell , ⌀2.0 mm and ⌀20.0 mm thin objects embodying the extreme ends of the thin-object spectrum, were analysed at a distance of 40 cm. This distance ensures that the Fresnel fringes are the most attenuated. Figure 4.29 and Figure 4.30 illustrate the results for the ⌀2.0 mm and ⌀20.0 mm respectively, for both outdoor and laboratory conditions. Additionally, both figures encompass histogram analysis using the methodology outlined in Section 4.2.5. The histogram distribution for the ⌀2.0 mm object at outdoor conditions demonstrates a single, prominent peak, indicating a clear and cohesive shadow, while the ⌀20.0 mm object presents a broader shadow with a stable intensity plateau owing to its thickness. In contrast, the laboratory environment introduces additional interference effects, leading to more complex fringe patterns and non-uniform intensity variations. The ⌀2.0 mm object at laboratory conditions displays multiple peaks and valleys in its histogram, suggesting uneven intensity distribution. Meanwhile, the ⌀20.0 mm object in the laboratory setting exhibits less pronounced fringes, with its histogram still showing some fluctuations but appearing more stable compared to the thinner object. Overall, the results indicate that thicker objects produce broader and more stable shadow regions, while thinner objects are more susceptible to Fresnel diffraction variations. Additionally, the outdoor environment provides clearer and more

consistent diffraction patterns, whereas the laboratory setting leads to increased intensity fluctuations and irregular fringe formations.

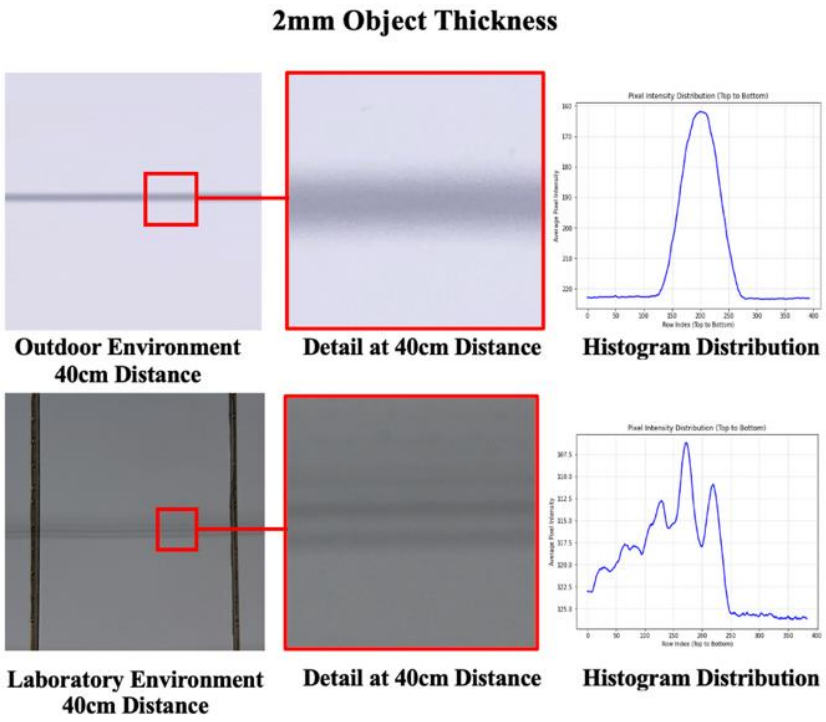


Figure 4.29. A comparative detail between outdoor and laboratory setting for a ⌀2.0 mm thick object at ⌀40 cm distance from the solar cell.

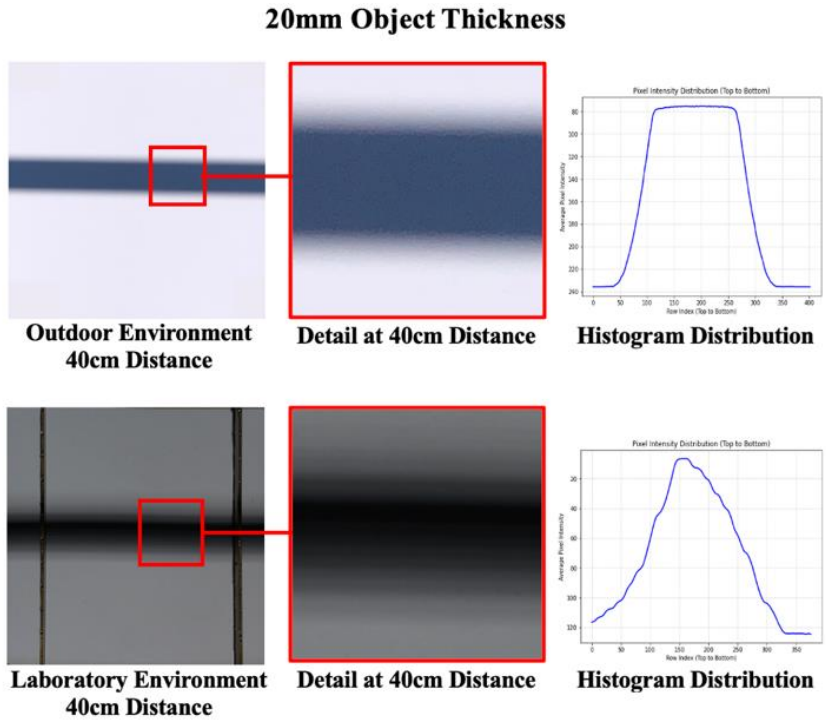


Figure 4.30. A comparative detail between outdoor and laboratory setting for a ⌀20.0 mm thick object at 40 cm distance from the solar cell.

4.4 Conclusion

The purpose of the chapter was to answer RQ.1 outlined below:

RQ.1 What are the discrepancies in power output and shadow characteristics caused by thin object shading on a conventional (156 x 156.0 mm) solar cell under controlled laboratory conditions versus outdoor environments?

RQ.1 was addressed across the relevant sections, beginning with Section 4.3.1, which found no statistically significant difference in power loss based on whether the thin object casting the shadow had a reflective or absorptive surface coating. Similarly, no significant difference was observed when the shading orientation of the thin object was varied between horizontal and vertical across a single solar cell. These preliminary experiments were designed to eliminate potential biases in the subsequent main investigations.

Furthermore, Section 4.3.3 examined the power output discrepancies relevant to RQ.1, identifying a variation range of 0.34 W to 0.67 W, equivalent to 8.18% to 16.13% respectively, across a conventional 156 × 156.0 mm solar cell. The findings indicated that outdoor conditions are more susceptible to power losses from thin-object shading. This effect was evident for objects with thicknesses ranging from ⌀2.0 mm to ⌀20.0 mm and positioned at distances between 10 cm and 40 cm from the solar cell.

Moreover, the second part focused on shadow formation characteristic differences was answered through Section 4.3.4 by first introducing a quantifiable metric that combines shadow intensity and size, referred to as the Combined Shadow Factor, given the acronym as ‘CSF’. Significantly lower CSF values under laboratory conditions indicate that shadows in this environment are both weaker and less impactful. As detailed in Section 4.3.4, image analysis revealed that light diffraction, explained by Fresnel theory, produced fringe patterns that reduced shadow intensity, especially when the thin object was placed 40 cm from the solar cell in a laboratory environment. These interference phenomena weakened the shadows, resulting in reduced CSF values and diminished impact on power output. In contrast, shadows observed in outdoor environments were

sharper and more intense, leading to higher CSF values and correspondingly greater power losses.

While RQ.1 has been addressed, outdoor experiments offer a more realistic representation of shadow patterns, as demonstrated in Section 4.3.4. To develop a predictive image model for thin-object shading, it is essential to move beyond the general CSF score and adopt a more refined metric that distinguishes the shadow into the proper formation regions of umbra and penumbra. This refined approach aims to improve the accuracy of power loss estimation and will be further explored in Chapter 5 through RQ.2.

Chapter 5 Shadow Quantification using Image-based Analysis

5.1 Introduction

This chapter aims to build on the quantified shadow formations introduced in Chapter 4, narrowing to the umbra and penumbra shadow formation, defined in Chapter 2. The literature review in Chapter 3 highlights that research on image analysis in the field of PVs is often solely confined to shadow edge detection, without fully quantifying both shadow formation types. This represents a research gap. Additionally, there is limited understanding of the quantification of the correlation between the umbra and penumbra when factors such as shadow size and intensity variation are considered. Consequently, the primary objective of this chapter is to use image analysis to quantify umbra and penumbra shadow formations and explore their correlation with power loss on the chosen PV source, scalable to full-scale PV modules. Image analysis will therefore be used to develop 'ThinShadePV', a predictive tool that estimates power loss based on shadow size and intensity. This approach has been explored in depth in a peer reviewed journal article published in EPJ Photovoltaics [230] and which was presented during the 41st edition of the European Photovoltaic Solar Energy Conference and Exhibition (EU PVSEC) in 2024 [231].

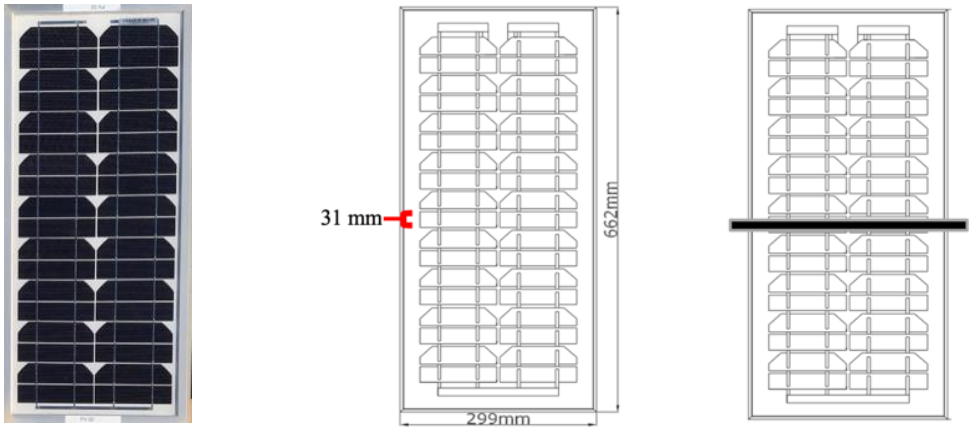
5.2 Methodology

5.2.1 Outdoor Experimentation Setup for Thin Object Shading on a Small-scale PV Module

In addition to the terminology of 'thin object shading' already established in prior chapters, this chapter shall adopt a more detailed definition of the term. The latter shall thereon refer to any opaque object casting a shadow on a surface of PV source, given that the shadow's width (including both umbra and penumbra) does not exceed the width of an individual solar cell within a PV module. The objective of this section is to quantifiably compare the difference in power loss between a control unshaded small-

scale PV module and an identical PV module under various thin object shading conditions. Moreover, a similar methodology to that used in Chapter 4 Section 4.2.2 will be subsequently used in this chapter. A fixed resistive load shall aim to serve as a benchmark to keep the load constant while the distance between the PV module and the shading object and the thickness of the thin object are interchanged independently.

The PV sources utilised for the duration of this chapter are two identical small-scale PV modules (Model No. ET M53620) with a manufacturer maximum rated power output of 20 W, as seen in the datasheet in Appendix C. The chosen PV modules consist of 36 quarter-cut solar cells connected in series, with each solar cell measuring 31 x 125 mm, as shown in Figure 5.1a, and overall dimensions of 299 mm in width and 662 mm in length, as shown in Figure 5.1b. The particular model of the PV module was chosen due to its solar cells having no bypass diode, allowing for a more focused analysis on the effect of thin object shading rather than that on other attributing features in the PV module. Typically, a PV module of this size would have solar cells cut into even smaller sections, making it difficult to observe the effects of thin object shadows. The module consists of multiple individual solar cells, each measuring 31.0 mm in width shown in the schematic diagram of Figure 5.1b. Therefore, given that 'thin object shadow' represents the shadow in which the total width of umbra and penumbra together does not exceed the width of the solar cell, in this case the width is therefore that of 31.0 mm. The shadow cast by the thin objects was intentionally transposed horizontally on the PV module as illustrated in Figure 5.1c and centred directly on two adjacent quarter cut cells.



(a) **(b)** **(c)**

Figure 5.1. (a) Plan view of the small-scale PV module, **(b)** A schematic of the dimensions of the PV module **(c)** A visual representation of the horizontal position of the thin object shadow on the PV module.

To better visualise the power loss measured in this study, the I-V curve in Figure 5.2 provides a scientific understanding of partial shading conditions from thin object shading on the small-scale PV module chosen. The explanation is based under the thin object shading conditions exhibited in Figure 5.1c and which are further elaborated below. The explanation shall follow Kirchoff's voltage and current laws as the fundamental principles for analysing the electrical circuits and the research studies of Seyedmahmoudian et al. [232] and Mahmoud et al. [233]. Moreover, Lappalainen et al. [234, p. 2] denote that "In a series connection of PV cells, the same current flows through all the cells and the total voltage of the series connection is the sum of the individual cell voltages" which will serve as the basis of understanding the below relationship.

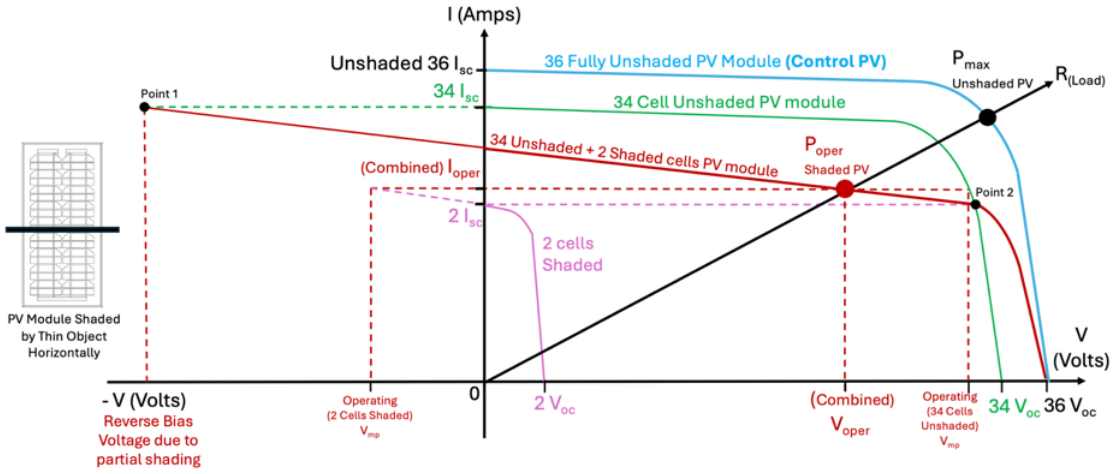


Figure 5.2. Solar cell level operation under thin object shading conditions on the small-scale PV module consisting of 36 quarter cut solar cells.

The blue I-V curve corresponds to the ideal case of a fully unshaded PV module with the maximum power at the rated load resistance denoted as 'P_{max} unshaded PV'. As a conceptual understanding the diagram denoted the short circuit current as 36 I_{sc}, representing the I_{sc} of the combined 36 cells in series. Likewise, 36 V_{oc} represents the combination of the 36 solar cells in open-circuit voltage for the control PV module. Moreover, the full 36 solar cells can be split into the individual characteristic of 34 combined control solar cells which are represented by a green I-V curve. This curve shows a reduction in both the current and voltage due to the presence of fewer solar cells in series. Conversely, the magenta coloured I-V curve represents the remaining 2 solar cells (as per set up of Figure 5.1c) at shaded conditions with a significant reduction in current and voltage levels.

To visualise the operation of the small-scale PV module under thin object shading conditions, the red curve illustrates the space combined case of the green and magenta I-V curve, where the module is now operating with 34 unshaded cells and two shaded cells at a given distance and object thickness where the full shadow is not exceeding the width of one solar cell. In this case, the current drops more significantly due to the shading-induced mismatch. The maximum voltage at which the module can operate is also noticeably lower due to the lack of operation contribution from the 2 shaded solar cells. Notably, when the unshaded cells are connected in series with the two partially shaded ones, the shaded solar cells are forced into reverse bias operation, where they start consuming power instead of generating power. This is due to the full current being generated by the remaining 34 solar cells. As noted in Chapter 3, authors such as Simon et al. [108] and Gallon [235], note how reverse bias occurs when the shaded cells experience a negative voltage due to the unshaded cells forcing current through them and dissipating the power in the form of heat, even though they are not generating power. The reverse bias voltage extends into the negative side of the voltage axis in Figure 5.2, demonstrating how the shaded cells introduce a reverse voltage in the overall module [234]. Moreover, the furthest reverse bias point on the left side denoted as Point 1 in Figure 5.2 is extended towards the point at which the operating I-V curve of the 34 unshaded (visualised in green) and I_{sc} of the 2 shaded solar cells intersect as denoted by Point 2 in Figure 5.2. The R_{Load} (resistive load) connected in series, is drawn as a diagonal to the maximum power of the control I-V curve P_{max} of the control PV, the I_{oper} (operating current) and V_{oper} (operating voltage) of the shaded PV module and is representative of the power point that the forthcoming experimentation endeavours to quantify (P_{oper}).

Moreover, the power loss expressed as a percentage will be the difference between P_{oper} of the shaded PV module and the P_{max} of the control PV module previously explained in Chapter 4 Section 4.2.2, Equation (12). Both PV modules were tested at the solar research laboratory in Marsaxlokk, Malta to verify an acceptable electrical output under the same conditions documented in Table 5.1. The calibration process enabled both PV modules to output equal power under corrected STC, essential for accurate and reliable analysis in subsequent experiments. The calibration process was conducted under clear

skies, ensuring no partial shading, and both PV modules were thoroughly cleaned beforehand to remove dust accumulation, which can lead to shading and light scattering effects that diminish the amount of solar radiation reaching the PV cells and consequently lower their performance. Each module's power output was recorded every second for a duration of 15 minutes, allowing for the identification of any mismatch between the modules. A correction factor of 0.23% was then applied to the control PV module in order to ensure that the experimentation began on even grounds for accurate benchmarking. Furthermore, the fixed resistive load was crucial to determine the difference in P_{oper} of each thin object shading scenario. P_{oper} shall be taken at different points across the diagonal of the R_{Load} shown by Figure 5.2 in accordance with the loss in current corresponding to the severity of shading governed by the umbra and penumbra size and intensity.

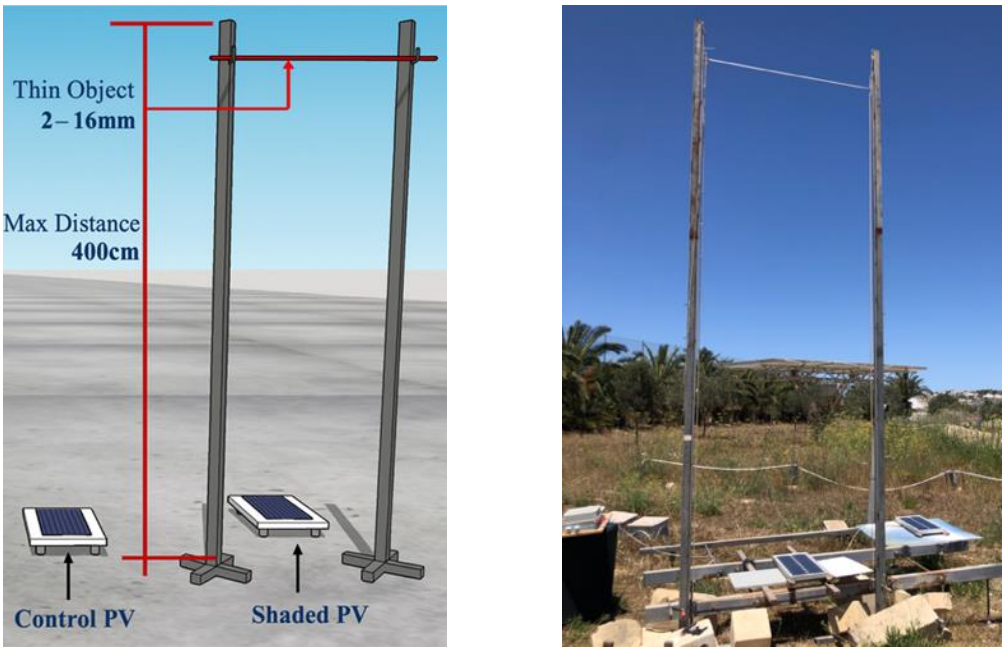
Table 5.1. Electrical characteristics of the PV module used in the power loss experimentation, extracted from the manufacturer datasheet in Appendix C.

Datasheet Information	**Symbol**	**Manufacturer datasheet**
Type of Cell Technology		Monocrystalline
Power Rating	P	20 W
Short circuit current	I_{SC}	1.27 A
Open circuit voltage	V_{OC}	21.96 V
MPP current	I_{MPP}	1.14 A
MPP voltage	V_{MPP}	17.82 V

Moreover, the same procedure used in Chapter 4 Section 4.2.2 to geometrically correct the sun's position was also applied in this methodology using Equations (13) and (14) respectively. These techniques are applied to correct power loss by considering the time of day and the shadow size, which is determined by the altitude at the time of experimentation. Furthermore, the same STC correction was conducted based on the method outlined at the end of Section 4.2.2.

For this study, the power loss experimentation was conducted between 12:00 and 14:00 from June 8th to June 10th 2024, with solar noon occurring at 13:00. During these times, the sun was at its highest point in the sky for the day and near its peak position for the

year. The weather data retrieved from the pyranometer in the weather station was recorded as an average of every 10-minute increments. Similarly, the temperature of the PV module was measured at the same 10-minute intervals using a digital IR thermometer aimed directly at the PV module. This experimental approach enabled the assessment of power loss caused by a single rod thickness across a range of distances from the PV module, provided that the resulting shadow does not exceed the width of an individual solar cell. The outdoor setup for the power loss experimentation can be conceptualised in Figure 5.3a and was realistically implemented in Figure 5.3b.



(a) **(b)**

Figure 5.3. (a) Conceptual visual of the outdoor methodology, (b) In-situ outdoor experimentation setup.

Moreover, the thicknesses of the objects casting the thin object shadow have been purposely sized by following the below criteria:

- The object used to cast shadows should be as thin as feasibly possible. This ensures that when the shadow is scaled up for validation on a full-scale PV module consisting of a full-sized solar cell (156.0 mm x 156.0 mm), it still qualifies as relatively thin, maintaining consistency with the original shadow classification.

- The incremental object thickness range must reflect a variety of thin objects, and where possible maintain a relative consistent increment so as to obtain intermediary points effectively.
- The thin object of minimum thickness must be stiff enough to constitute a manageable size to cast at least a horizontal shadow on top of the quarter cut solar cell of the PV module.
- The thin object of maximum thickness must, on the other hand, be of a reasonable size such that the shadow cast (both umbra and penumbra shadow) does not exceed the width of the solar cell .

From the above considerations, the individual thin objects which were sourced are illustrated in Table 5.2**.** Moreover, since this study endeavours to analyse a significant diverse range of thin object thicknesses, these were classified into two categories. Small thin objects (⌀2.8– ⌀8.0 mm), typically exhibit material flexibility representing that of wires, cables and passive air clothes drying lines, Large thin objects (⌀10–⌀16.0 mm) are more rigid in their composition, closely representing that of thin objects such as horizontal fall protection safety railings and horizontal safety lines. Therefore, the chosen thicknesses should cover the majority of the common types of thin object shadows addressed in Chapter 1 Section 1.2.

Table 5.2. Shading object thicknesses as categorized for the purpose of correlation in this work.

Category 1 – Small Thin Objects Cross sectional thickness (mm)				**Category 2 –** Large Thin objects Cross sectional thickness (mm)			
⌀2.8	⌀3.2	⌀6	⌀8	⌀10	⌀12	⌀14	⌀16

Furthermore, the structure setup also includes the capability of varying the distance between the PV source and the shading object from 25 cm up to 400 cm at increments of 25 cm as illustrated in Figure 5.3a for both categories of thin objects. However, the condition that the overall size of the shadow at the given distance does not exceed the surface area of a quarter cut solar cell on the small-scale PV module.

During the experimentation, the control PV module and the shaded PV module were situated in close proximity to each other to maintain an equal exposure to outdoor conditions. The thin object positioned directly on the PV module (at a distance of 0 cm between the PV module and the thin object) was excluded from the range, as this setup is both unrealistic for representing typical thin-object shading scenarios as well as problematic for capturing shadow images, since the object itself obstructs the view of the shadow cast on the module.

The aforementioned methodology will henceforth be applied to determine power loss data for each combination of distance and thickness. Percentage power loss, denoted as the difference in PV output under shaded and control conditions expressed as a percentage, will serve as the primary dependent variable for the image analysis tool ThinShadePV. Additionally, the specified equipment may be substituted, provided all other parameters outlined in this study remain unchanged. Furthermore, it is important to emphasise that the quantification of power loss addressed in this section, specifically addresses conditions under which shadows have the most significant impact. Therefore, cases involving reduced shadow intensity due to partial cloud coverage or lower irradiance periods within the day have been excluded from this investigation. Nevertheless, researchers may adapt the described methodology to explore power loss under alternative shading scenarios or at different times of the day.

5.2.1.1 Image Capture Setup

The image capturing setup was designed to obtain reliable and geometrically consistent images of the thin shadows cast onto a controlled white reference surface placed on top of the small-scale PV module. Since these images serve as the basis for quantifying both the size and shape of the thin object, it was essential that all images were captured under identical conditions and that no distortion or foreign objects were present. A documented image of the setup is shown in Figure 5.4 and is explained in detail in the following section.

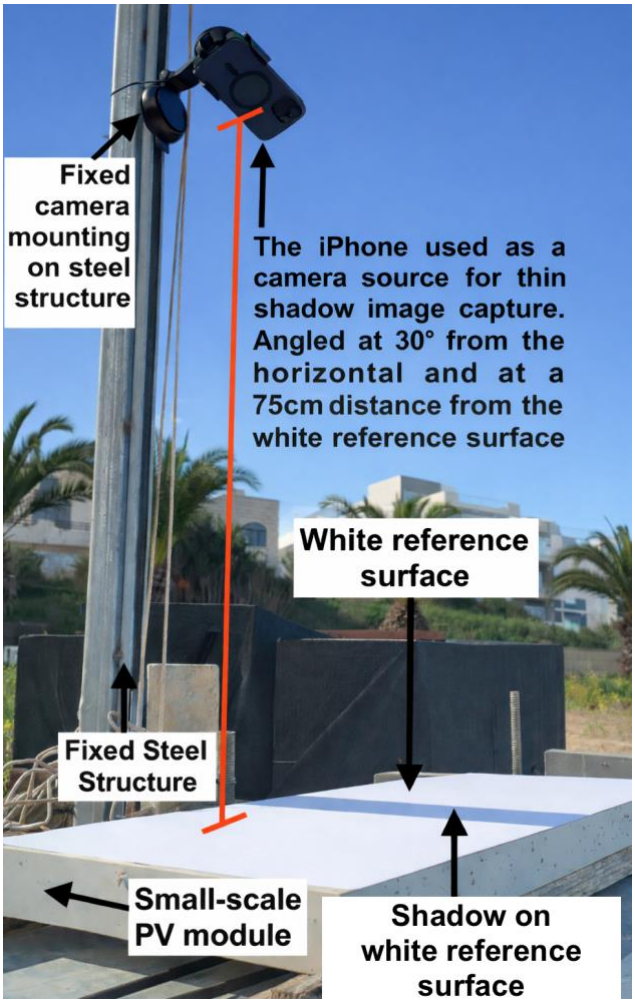


Figure 5.4. The image capture setup showing the fixed mounted device as well as the shadow cast by the thin object higher than the camera setup.

The same fixed steel structure shown on the left-hand side of Figure 5.4, which was used to vary the distance of the thin object, also served as the mounting frame for the imaging device, an iPhone 15 integrated camera with a 48 mega pixel sensor. An adjustable smartphone holder was secured to this structure, allowing stable and repeatable positioning of the phone, which was used as the camera. The mounting frame and camera were situated as close to the steel structure as possible and ensured that the protruding length of the cantilever did not cast a shadow on the white reference surface underneath. Moreover, rather than being positioned directly overhead, the camera was oriented at an inclination of 30° from the horizontal and maintained at a fixed distance of 75 cm from the white reference surface beneath the PV module. Although, in an ideal configuration, the camera would have been positioned directly overhead and perpendicular to the reference surface, this arrangement was not feasible in the present setup. Positioning the image capturing device vertically above the PV module would

have caused the camera and potentially the mounting arm to cast distinct shadows onto the module and reference surface, thereby introducing foreign shadows in addition to the thin-object shadow of interest. The chosen angled configuration therefore represented the most practical and non-intrusive solution, avoiding unwanted shadowing while maintaining full visibility of the shadow region.

To compensate for the geometric distortions introduced by the angled camera orientation, all captured images underwent post-acquisition perspective correction. This step follows established methods reported in previous studies by Heck [236], Wang et al. [237] and Bedrich [238], which similarly apply post-acquisition four-point perspective correction to accurately capture a known planar surface as the primary subject of the image. Several tools are available to perform such corrections; for this thesis, the perspective correction tool provided by ImageOnline.io [239] was selected due to its four-point adjustment capability. By identifying the boundaries of the reference surface within the software, the images were rectified to counteract angular distortion, resulting in a corrected planar view suitable for subsequent quantitative image analysis.

The white reference surface onto which the shadow was cast, played a crucial role in the experimental setup. Its matte finish and uniform texture provided a contrast against the shadows cast by the thin objects. Furthermore, maintaining a fixed relative distance of 75 cm between the PV module and the reference plane ensured that observed variations in shadow geometry arose solely from changes in the thin object, as successive thicknesses were introduced at controlled distances from the PV module. This positional stability was particularly important given the outdoor conditions under which the data and images were collected.

Although the experimental constraints prevented the use of an ideal overhead imaging arrangement, the implemented setup provided a reliable image capture solution. By combining controlled oblique imaging with geometric perspective correction, the configuration enabled the acquisition of high-quality shadow images suitable for thin-object shadow analysis.

5.2.2 Operation of ThinShadePV (Image Analysis Tool)

From the literature reviewed in Chapter 3, particularly in Section 3.5, image analysis has emerged as an innovative and effective approach for analysing visual imagery. Accordingly, this study aims to leverage existing features available within open-source Python libraries to analyse shadow images at different combinations of distance and thickness. Employing this analytical approach is crucial in addressing RQ.2, which seeks to determine how the variation of factors affecting shading from thin objects, correlates with PV power loss. Additionally, this chapter investigates whether the relationships identified between the variable shadow factors of umbra and penumbra size and intensity can effectively predict power loss. The result of this relationship led to the development of a predictive model hereafter referred to as ThinShadePV, developed using Python version 3.12.7 within the Anaconda Distribution (release 2024.10-1). The full script for ThinShadePV can be referred to in Appendix G and as a digital script link in the same section. Furthermore, the shadow images used to generate the ThinShadePV training dataset were captured using the 48 Megapixel built-in camera of an Apple iPhone 15. This portable device was selected over the Canon EOS 6D SLR camera employed in Chapter 4 (specifically Section 4.2.4), based on the practical requirements of ThinShadePV for on-site image acquisition. Since most potential users of ThinShadePV are more likely to own a smartphone than a professional-grade SLR camera, the use of a mobile device was deemed more representative and accessible.

This choice also facilitates consistency in the validation process described later in Section 5.2.3, where image capture under realistic shading conditions will again be conducted using a portable device. Unlike the Canon EOS 6D, the iPhone 15's built-in camera does not allow manual adjustment of ISO or shutter speed by default, and its aperture is fixed due to hardware limitations. However, these constraints were addressed using Halide, a third-party application available on the iOS App Store. Halide enables manual control of camera settings by interfacing with Apple's AVFoundation framework, thereby allowing the replication of the camera parameters used in Chapter 4, specifically, an ISO of 200 and a shutter speed of 1/60s. Although the iPhone 15's aperture is fixed at approximately f/1.6 and cannot be modified, the same image capture parameters (ISO 200, shutter speed 1/60s, aperture f/1.6) will be consistently applied throughout both the training dataset acquisition and the validation stages detailed in the

methodology in Section 5.2.3 and results in Section 5.3.4. This ensures high-quality image capture and consistency across all experiments.

The aim of using an image analysis approach is to facilitate the quantification of percentage umbra and penumbra shadows from horizontally transposed thin object shadow cases. The shadow quantification process explained in this section was derived specifically for quantifying a spectrum of shadow sizes for thin object shading when transposed on a white background. The method being used in this chapter revolves around the varying-intensity pixel values as seen in Figure 5.5. The varying-intensity pixel range in digital images spans from 0 (black) to 255 (white). Each pixel value represents an intensity level, with 0 being no light and 255 being maximum light. Values between these extremes represent shades of grey, allowing for 256 distinct intensity levels. This range enables a detailed representation of visual information in greyscale images, simplifying analysis by focusing on light and dark variations.

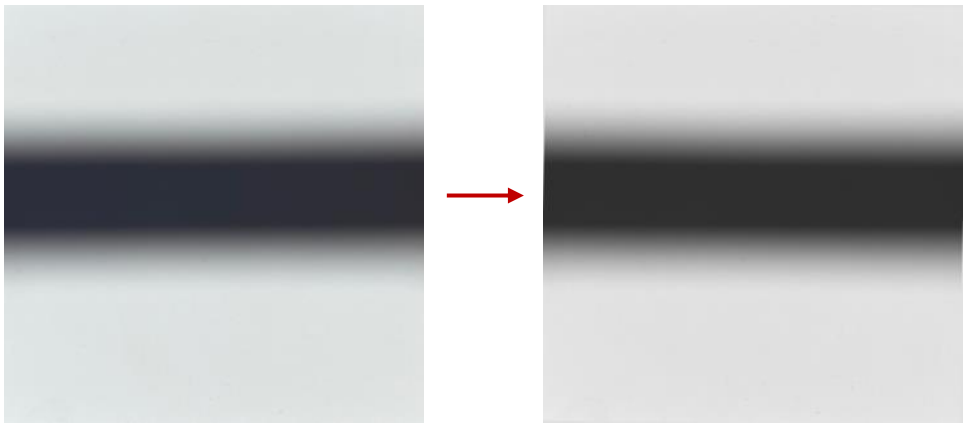


Figure 5.5. Varying-intensity range of greyscale pixels.

In this study, the background pixel intensity from each of the 104 thin object shading cases was used as a reference baseline for image analysis. This value was obtained by calculating the average pixel intensity of a uniform white plane surface in each image, explicitly excluding the shadowed regions. The variation in these background values across all cases was minimal, confined within a range of ±2 intensity units, which is taken as the accuracy margin for the baseline reference. Establishing this baseline helps to account for minor fluctuations in lighting conditions and potential inconsistencies introduced by the portable imaging device across different captures. As a result, any variations in pixel intensity observed within the experimental umbra and penumbra regions are more likely to reflect actual differences in shadow intensity, rather than an experimental limitation in the imaging setup.

The image analysis process begins with the user loading an image similar to the one visualised in Figure 5.6a into ThinShadePV. Once the image is loaded, it is converted

from an RGB image to a greyscale format to facilitate the computational efficiency of shadow detection without compromising accuracy as seen in Figure 5.6b. This was achieved using the img.convert('L') in Python, simplifying the analysis by focusing exclusively on the intensity values. Although greyscale conversion removes chromatic information, the approach used in this chapter is focused on luminance-based shadow detection by using Pythons's *Pil* (Pillow) library, which is inherently robust to the absence of colour data. Shadows primarily manifest as intensity gradients rather than chromatic shifts, particularly in outdoor environments where lighting conditions are the dominant factor in shadow formation. While intensity gradients refer to changes in brightness across an image, chromatic shifts involve changes in colour hue or saturation, independent of brightness. Prior research by Chandran and Kumar et al. [240], [73] has demonstrated that intensity-based methods perform comparably in both greyscale and RGB contexts, especially when shadow boundaries are defined by luminance differences. Therefore, the greyscale conversion did not impede the algorithm's ability to accurately detect shadows in the presence of complex shadows on a white surface without any background texture.



(a) **(b)**

Figure 5.6. (a) A typical thin object shadow case transposed on a white background in RGB colour format, **(b)** The same image converted to greyscale.

To determine the peripheral points of umbra and penumbra respectively for the example greyscale image capture in Figure 5.6b, the forthcoming method will be adopted. Table 5.3 as the complimentary nomenclature of Figure 5.7 serving as a visual aid for the remainder of this subchapter. Figure 5.7 is an important visual that extrapolates key points from the image to a dual sigmoidal curve, deriving the important quantifiable points of the shadow formation for each thin object shading case. Section 5.2.2.1 will

be used to determine the intensity of umbra and penumbra and Section 5.2.2.2 for determining the size of umbra and penumbra of thin object shadow formation.

Table 5.3. Summary nomenclature for Figure 5.7.

Acronym	Description
Point A	Start of Penumbra Upper Region
Point B	End of Penumbra Lower Region
Point B -1 pixel value	Start of Umbra Region
Point C -1 pixel value	End of Umbra Region
Point C	End of Penumbra Upper Region
Point D	Start of Penumbra Lower Region
DV	Darkest Pixel Value
UI	Umbra Intensity
$\underline{UI}_{Total}$	Total Umbra Intensity
PI_1	Penumbra intensity Upper region
PI_2	Penumbra intensity Lower region
PI_{Total}	Total Penumbra Intensity
US	Umbra Size
PS_1	Penumbra Size Upper region
PS_2	Penumbra Size Lower region
PS_{Total}	Total Penumbra Size

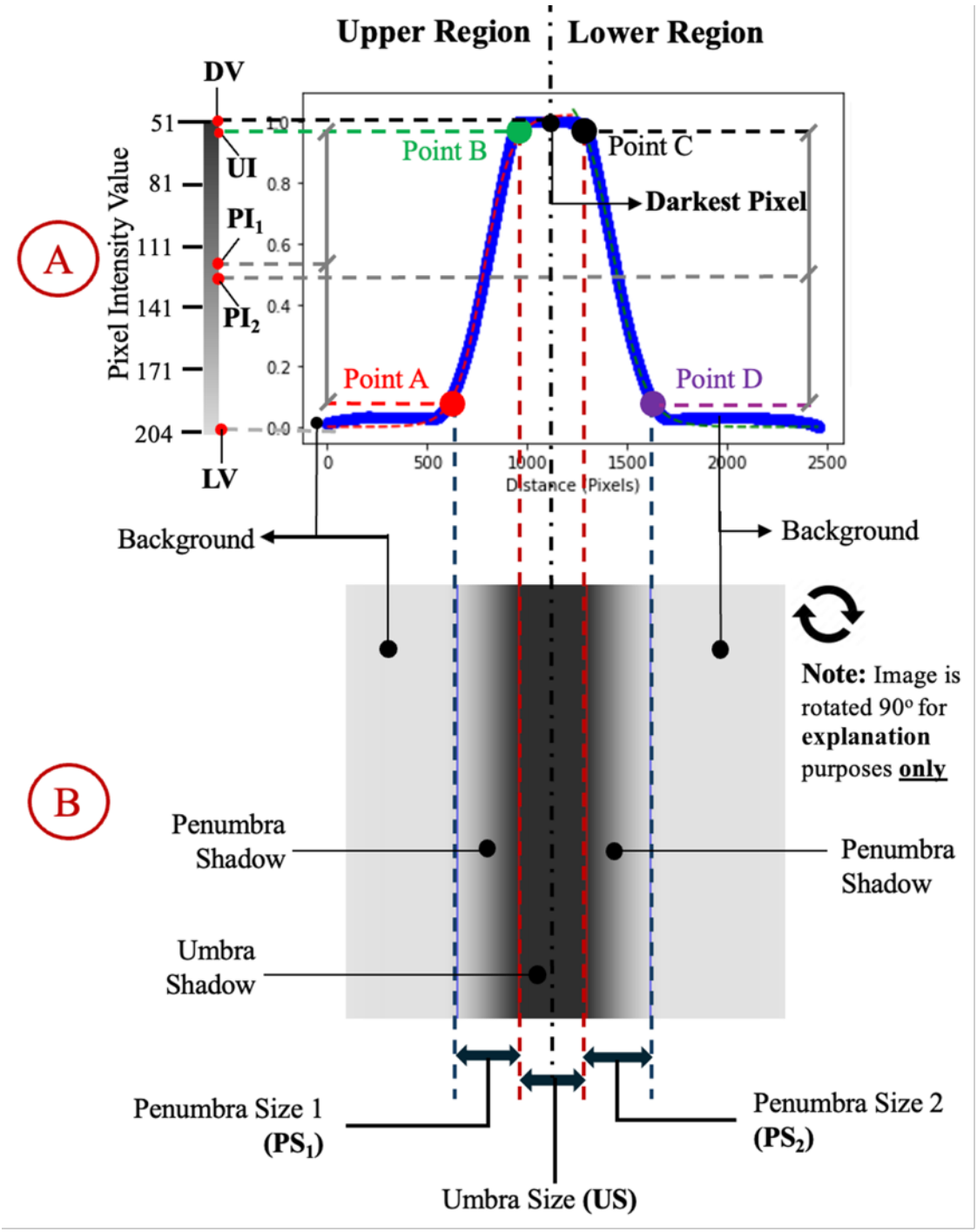


Figure 5.7. Visual representation of the dual sigmoidal curve (Section A) extrapolated from a sample image (Section B) which shows thin object shading.

To determine the start and end points of umbra and penumbra respectively, this study uses an adapted version used by Mirylenka et al. [184] where the active noise range induces a measurable change in the performance at the two curvature cases of a sigmoidal curve. Therefore, within the remit of this work, the noise level is equivalent

to the penumbra shadow, since using the applied criteria, it is the only shadow formation that has a varying change in shadow intensity. On the other hand, umbra shadow has a constant intensity throughout since no light passes through the opaque thin object.

Due to the practical limitations of capturing images with portable devices, shadows are not always perfectly symmetrical. These discrepancies typically arise when the sun, the thin object casting the shadow, and the white background surface are not perfectly aligned along a vertical axis, an alignment that is nearly impossible to achieve in real-world conditions. Consequently, symmetry between the upper and lower regions of the shadow cannot be assumed. To address this limitation, ThinShadePV employs a dual sigmoidal curve approach denoted in Section A in Figure 5.7. The dual sigmoidal curve consists of two mirrored sigmoidal curves, with the left side curve representing the upper shadow region consisting of the two noise points of A (red) and B (green), while the right side curve representing the lower region consisting of the two remaining points C (black) and point D (purple). Therefore, due to the practical limitation identified previously, the two opposing sigmoidal curves in Figure 5.7 may exhibit slight variations in shape. The boundary between the upper and lower regions of the image corresponding to the left and right hand side sigmoidal curves are indicated by the dashed-dot line in the middle of Figure 5.7, defined by the location of the darkest pixel in the image. This pixel typically lies at the centre of the shadow as the darkest point and corresponds to the apex of the dual sigmoidal curve as indicated in Figure 5.7.

ThinShadePV translates pixel intensity values from the standard 8-bit greyscale range (0–255) into normalised values between ‘0’ and ‘1’, where a value of ‘0’ corresponds to the brightest pixel intensity of the image, and a value of ‘1’ corresponds to the darkest pixel intensity. This procedure was done to effectively rescale the intensity values between these two extremes. Equation (20) was adopted, where x denotes the pixel number.

$$x' = 1 - \frac{x - \min(x)}{\max(x) - min\ (x)} \tag{20}$$

This normalisation is implemented to simplify computational processing and to ensure that the y-axis scale of the curve in Figure 5.7 Section A remains visually consistent and manageable within ThinShadePV. Importantly, the normalised y-axis adapts to the specific image being analysed. The lightest pixel value, LV, typically representing the background of the image, corresponds to the lower end of the y-axis. On the other hand, the darkest pixel value, denoted as DV, is positioned at the upper end of the y-axis, corresponding to the region of highest shadow intensity.

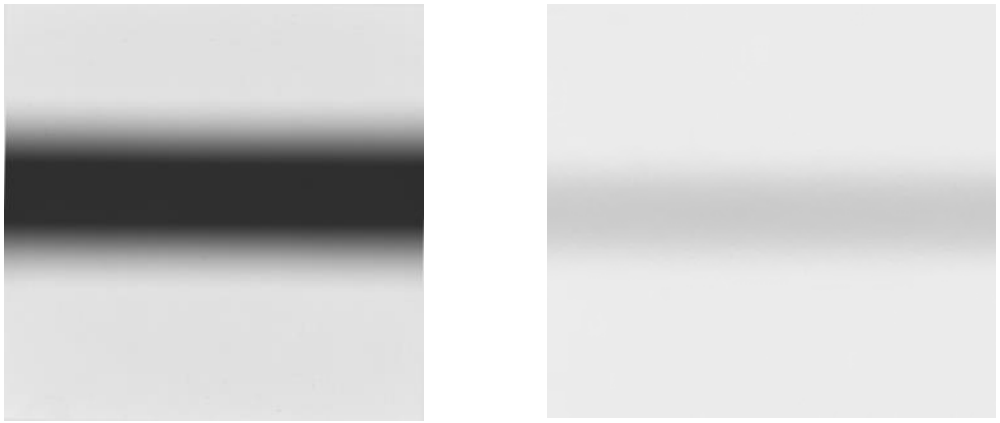
5.2.2.1 Quantifying the Intensity of Umbra and Penumbra Regions

The section continues to refer to Figure 5.7 as a visual aid. The determination of total umbra intensity, $UI_{Total,}$ for the captured horizontal shadow image is based on principles outlined in Huang et al. [183], which establish that the umbra region is characterised by a region of constant intensity. Theoretically, this means that the darkest pixel in the image could represent the umbra intensity. However, in practical applications, slight variations in pixel intensity are often observed within the umbra region. To account for this, the dual sigmoidal curve shown in Section A of Figure 5.7 is used to extrapolate the total umbra intensity. When an umbra is present, the pixel intensity between DV and Point B–1 defines the umbra intensity for the upper region, while the intensity between DV and Point C-1 represents the lower region. These values are interpolated along the x-axis of the dual sigmoidal curve in Figure 5.7. The subtraction of one pixel from Point B, hence referred to as Point B-1 and the addition of one pixel to Point C (thus becoming Point C-1), ensured that Points B and C exclusively represent the penumbra boundary rather than having a duplicate function. In this way, Points B and C are not counted twice, but are rather classified only as either part of US or PS_{Total}. UI_{Total} is then calculated as the average of the umbra intensity values from both the upper and lower regions.

The penumbra shadow is subdivided into two regions in Figure 5.7, the upper region (PS_1) and the lower region (PS_2). PS_1 spans from Point A to Point B, and the pixel count within this range represents the upper penumbra. PS_2, on the other hand, covers the area from Point C to Point D, representing the lower penumbra.

Determining the total penumbra intensity, $PI_{Total,}$ is inherently more complex due to the nature of the penumbra region. As outlined in Chapter 2, Section 2.3, a penumbra does not exhibit a fixed intensity value; instead, it spans a gradient of intensities. Consequently, for computational purposes, and to account for the varying nature of penumbral shading, ThinShadePV estimates the average intensity across defined segments of the captured image. Specifically, the average pixel intensity between Points A and B (upper penumbra region) and between Points C and D (lower penumbra region) is calculated, with the average intensity values denoted as PI_1 and PI_2, respectively, and illustrated in Figure 5.7. PI_{Total} is then derived by averaging PI_1 and PI_2, resulting in a single representative value in the standard 0–255 pixel intensity range.

The derivation of PI_{Total}, up until this point has always focused on cases where both umbra and penumbra shadows are present as seen in the example scenario image in Figure 5.8a. However, in the case where the thin object is situated at a significant distance from the PV source, the shadow is much lighter in nature and creates a shadow similar to the one shown in Figure 5.8b, which from this point onwards will be classified as ‘penumbra-only’ shadow.



(a) **(b)**

Figure 5.8. A typical image case classified as **(a)** umbra and penumbra case, **(b)** penumbra-only shadow case.

A scenario is defined as ‘Penumbra only’ if the difference between the darkest pixel and either Point B or Point C is less than or equal to a 3-pixel value, indicating a minimal or no umbra presence. The 3-pixel threshold was determined through an extensive analysis of all combinations of distance and thickness images for the cases outlined in Section 5.2.1. A difference of 1 or 2 pixels was resulting in a large amount of detections of false penumbra-only, instead of also accounting for umbra cases. However, a difference of 3

pixel values maintained a consistent true penumbra-only classification using the manual verification conducted. However, at higher pixel differences such as 4 and 5 pixel value difference, an overestimate of the penumbra-only region was observed. Hence, it was thus inferred that a difference of 3 pixel values would classify the image as detected penumbra-only shadow. Consequentially, the PI_{Total} remains the sole intensity output provided by ThinShadePV for this shading scenario, as no umbra shadow is detected. Therefore, UI is not applicable in this case and a value of N/A is given to the UI.

5.2.2.2 Quantifying the Size of Umbra and Penumbra Regions

The determination of the umbra and penumbra shadow sizes was achieved through sigmoidal point extrapolation along the x-axis, where the cross-sectional width of the image was interpolated, as illustrated previously in Figure 5.7. The size of the umbra shadow, US, was determined by calculating the number of pixels between Point B – 1 and Point C + 1 and divided by the total pixel count of the cross sectional width of the image expressed as a percentage. Furthermore, the total size of the penumbra shadow ($PS_{Total)}$ is then computed by summing the pixel counts of PS_1 and PS_2. Therefore PS_{Total} is the penumbra size represented as a percentage of the total pixel count of the cross sectional width of the image as visualised in an illustrative example in Figure 5.9.

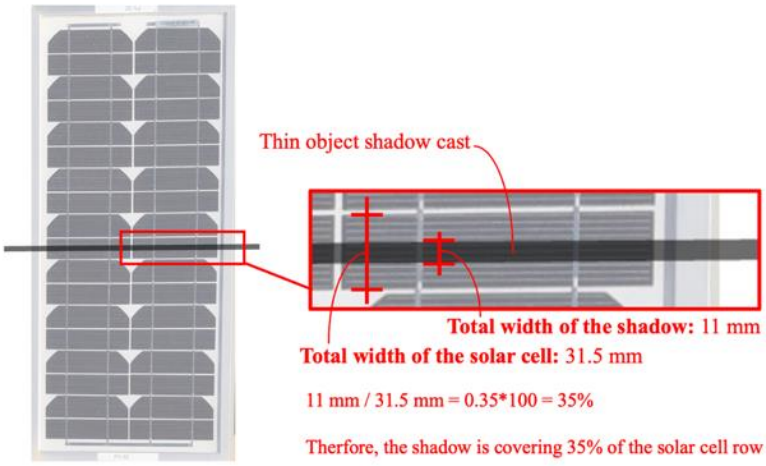
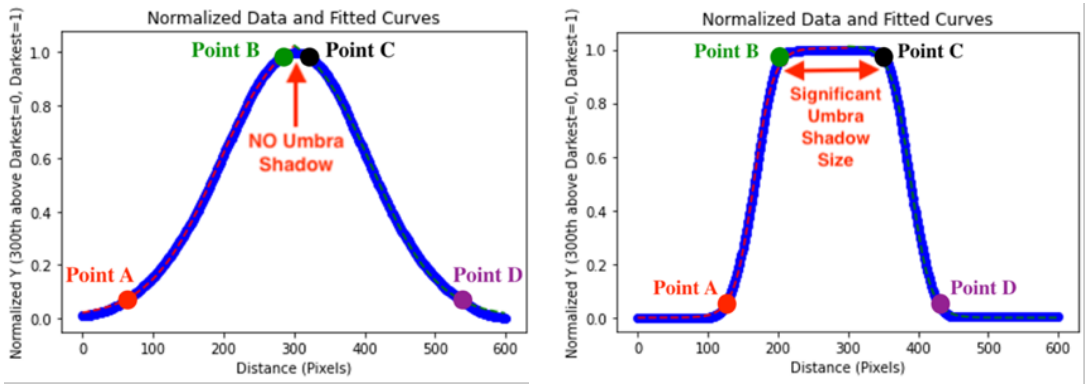


Figure 5.9. An illustrative example of the methodology utilised to quantify the shadow size.

In cases where ThinShadePV detects a penumbra-only shadow, as shown in Figure 5.10a, the algorithm follows the previously outlined methodology to quantify the shadow characteristics of Section 5.2.2.1. This typically occurs when Point B and Point C, Figure 5.10a, are positioned close to each other due to the absence of an umbra. This scenario contrasts with that of Figure 5.10b, where the presence of an umbra is evident through the plateau at the top of the intensity profile, indicating a region of constant intensity.

In the penumbra-only scenario, ThinShadePV calculates the total penumbra shadow by measuring the number of pixels between Point A and Point D divided by the total pixel count of the cross sectional width of the image expressed as a percentage. This completes the quantification of penumbra shadow in the absence of a distinct umbra region, typically observed when thin objects are positioned far away from the PV source.



(a) **(b)**

Figure 5.10. (a) Shadow case indicated no umbra shadow due to the presence of the peak (no plateau), (b) Shadow case indicating a significant amount of umbra shadow due to plateau.

While the complete methodology for deriving the size and intensity of both the umbra and penumbra was outlined in detail in Section 5.2.2.1 and this section, the process is further summarized in the flowchart shown in Figure 5.11. This flowchart represents the full image analysis process, which is based on the ThinShadePV Python code provided in Appendix G. The flowchart is designed to be transparent, replicable, and easily repeatable, ensuring consistency in the analysis across all the different combinations of distance and thickness outlined previously.

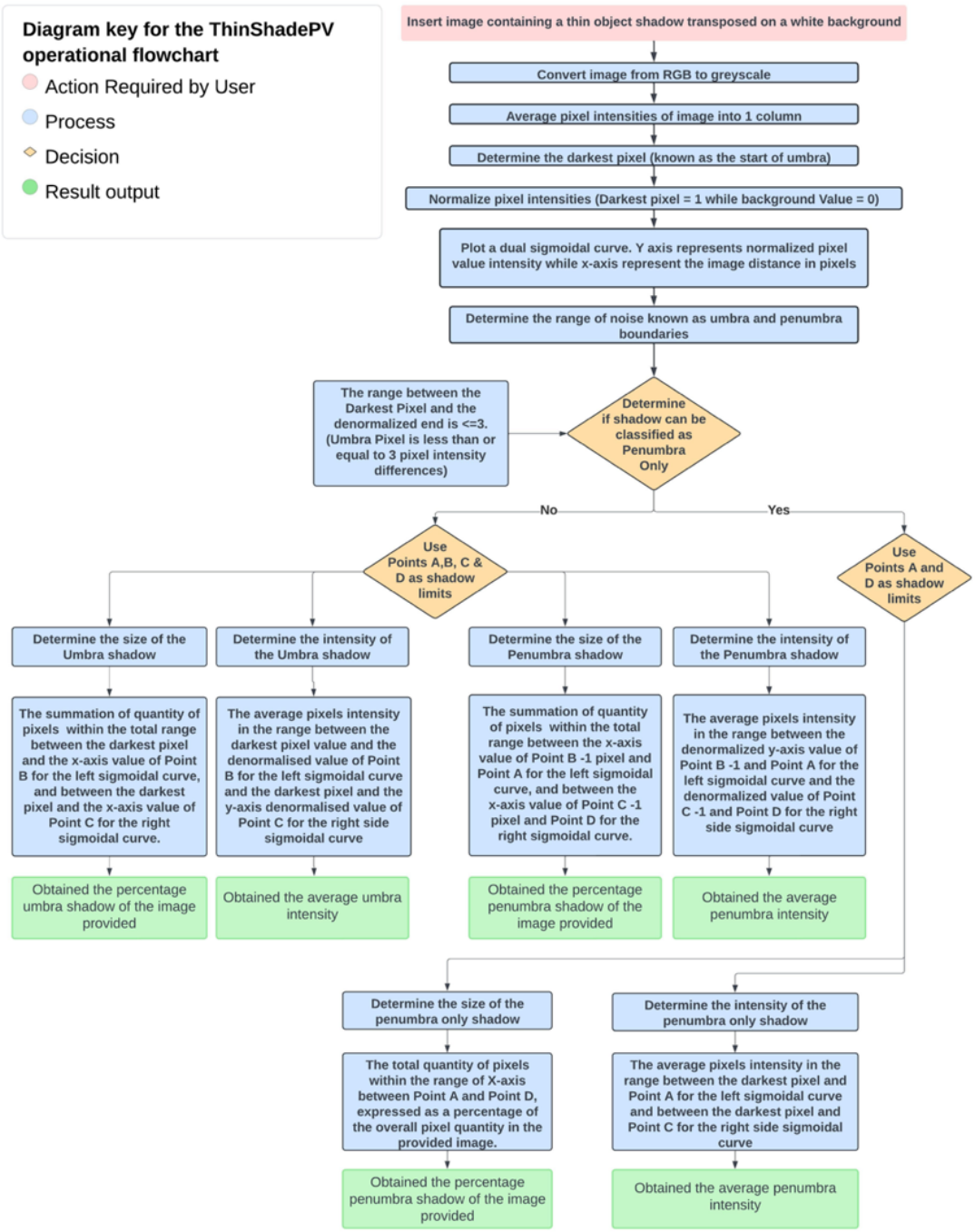


Figure 5.11. The shadow quantification algorithm based on key literature aspects by Huang et al. 's [183] and Mirylenka et al. [184] identified in Chapter 3 and methodologically outlined in this chapter, and Section 5.2.2.1.

5.2.2.3 Determining the Correlation amongst Factors affecting Power loss

This section shall examine the relationships between power loss and attributing variables, namely of the size of the umbra, the size of the penumbra, the intensity of the umbra and the intensity of the penumbra, in pursuit of answering RQ.2. These relationships shall then be explored through a Spearman correlation matrix, owing to this matrix being an effective approach for understanding how each variable factor influences power loss under thin object shading conditions. Authors such as Kappler et al. [201] and Olivares et al. [202] have also employed this method.

Spearman correlation, a non-parametric measure, evaluates the strength and direction of relationships between variables [241], [242]. It was chosen over Pearson correlation due to its robustness against outliers and its suitability for non-normal data distributions, making it more appropriate for analysing complex interactions in the data [243]. The primary focus is on the correlation between power loss and the four attributing variable factors. However, the general correlation between power loss and the parent attributing factors of the shadow formation, that is, object thickness and distance, shall also be analysed.

As previously denoted in Section 5.2.1, the thicknesses of the object analysed were split into two categories, small and large thin objects. The correlation will abide by this segregation by producing two respective Spearman correlation matrices, with power loss being the primary dependent variable of interest. Box matrices were generated using a second custom script written specifically for the study's dataset as denoted in Appendix H. This script utilised the Python libraries Pandas, for reading and handling the Excel dataset, and scipy.stats.spearmanr, for computing the Spearman rank correlation coefficients.

Subsequently, *Easygui* was used to provide a user-friendly graphical interface for file selection. For visualisation of results, *seaborn* and *matplotlib.pyplot* were employed to create heatmaps that clearly display the correlation matrices for both small and large thin object variable dataset.

Additionally, this study employs the correlation coefficient metric as outlined by Hair et al. [244] to systematically measure the strength and direction of the relationships

between the identified factors. This statistical approach allows for a quantitative assessment of how closely the variables are related, providing clarity on whether the associations are positive, negative, or negligible. Furthermore, prior to the results in Section 5.3.3, Table 5.4 tabulates the correlation introduced by Hair et al. [244] with the interpretation of the metric used evaluate the correlation coefficient between the factors effecting the power loss for thin object shading cases.

Table 5.4. Correlation coefficient metric [244].

Correlation Metric	Interpretation of Correlation Metric
0.91 to 1.00 / -0.91 to -1.0	Very Strong
0.71 to 0.90 / -0.71 to -0.90	High
0.41 to 0.70 / -0.41 to -0.70	Moderate
0.21 to 0.40 / -0.21 to -0.40	Weak
0.20 to 0.01 / -0.20 to -0.01	Very Weak

5.2.2.4 Development of a Training Model to Predict Power Loss

Originally, ThinShadePV was developed with the sole purpose of attaining a quantifiable measure of umbra and penumbra shadow size and intensity extracted directly from images. This provided a more objective approach in comparison to current literature. This was first introduced in Chapter 3 Section 3.6 and Section 3.7 and furthered through the image capturing data methodology of the outdoor experimentation outlined in Sections 5.2.2.1 and Section 5.2.2.3. Shadow size and intensity were selected because they represent the geometric and optical features of shadows, which are correlated with the extent of power loss in PVs. Moreover, using the upcoming methodology outlined in this section, ThinShadePV aims to contribute further to the body of research by building upon the approaches of Salazar et al. [164], which focused on detecting faults and hotspots, and Salamanca et al. [166], which addressed general partial shading detection. By integrating elements from these methods along with the machine learning approach utilised by Kappler [201] to detect shading conditions on PV systems, ThinShadePV adopts a novel approach to predict power loss at a given case based on data extracted from image capture. The improvement of ThinShadePV into a comprehensive predictive tool is primarily intended to answer the second portion of

RQ.2 while simultaneously making a meaningful contribution to the broader research community working on partial shading issues.

The initial outdoor experiments were performed with intervals of 25 cm for distances and with specific object thicknesses determined by available resources as outlined in Section 5.2.1. In the preliminary stages of the tool's conceptualisation, the model encountered limitations when users tried to import an image that provides shading data not exactly matching with the umbra and penumbra intensities and size figures in the database. For example, the existing dataset does not include intermediate object thicknesses (e.g., ⌀10.5 mm, ⌀11 mm), which could potentially be the thickness of rooftop obstructions to PVs. Similarly, distance values such as 26 cm, 32 cm, or 38 cm, falling between the tested intervals, remain unaddressed by the original model. Unlike linear interpolation, which estimates values based on a mathematical function between known points, the ThinShadePV prediction tool uses a Random Forest model to generate predictions for these intermediate values. The model does not perform explicit interpolation; instead, it provides data-driven estimates based on patterns learned from nearby training points, effectively filling the gaps in the dataset. Any realistic combination of object thicknesses and distances within the predefined thickness boundaries of ⌀2.0 mm - ⌀16.0 mm and distances up to 400 cm, was accommodated, provided that the width of the solar cell is not exceeded by the shading region. By adopting a more analytical approach, the predictive model will identify and utilise inherent trends, relationships, and correlations between shading parameters and ensure better predictions of power loss resulting from thin object shading, significantly improving its applicability and value to researchers and practitioners in the field.

Two effective machine learning models traditionally used for computation of image analysis data were identified by Olivares et al. [203], Gaboitaolelwe et al. [202] and Mustafa et al. [245] in the literature review of Chapter 3, Random Forest and XGBoost. Random Forest inherently provides clear interpretability and direct insight into feature importance without requiring complex hyperparameter optimisation or extensive tuning. Given the physical context of predicting power loss from the shadow formation of thin object shading, this inherent interpretability is crucial. This allows for a direct understanding of the physical relationship between shadow features (umbra and penumbra size and intensity) and resulting PV power loss, facilitating a straightforward

evaluation of the model's predictive behaviour. Moreover, both XGBoost and Random Forest models are highly robust to noise and variability within input data [246], which is particularly beneficial given that image-derived measurements of umbra and penumbra intensity and size may inherently contain measurement uncertainties due to lighting conditions. Random Forest reduces susceptibility to potential measurement errors or outliers through averaging predictions across independently constructed decision trees [247].

On the other hand, XGBoost provides faster training and improved computational efficiency by processing data in parallel and optimising memory and feature handling. These improvements make it particularly advantageous for large-scale applications or situations where the predictive model must be retrained frequently and quickly, without sacrificing accuracy [248], [249]. Additionally, Random Forest requires less extensive hyperparameter tuning than XGBoost, which typically demands careful optimisation of numerous parameters, including learning rate, tree depth, and regularization terms, to prevent overfitting. This reduced complexity simplifies the model development process, accelerates training and validation, and quickly provides practical insights into how umbra and penumbra characteristics relate to power loss.

Based on the outlined characteristics, strengths and weaknesses, the Random Forest algorithm is deemed more suitable for the ThinShadePV application, as also supported by Gaboitaolelwe et al. [203] in the state-of-the-art review. Random Forest was chosen for the ThinShadePV model because it aligns well with the structure of the dataset having multiple attributing variables (umbra and penumbra, shadow size and intensity) and a single output of power loss. Therefore, the methodology employed was to build multiple decision trees, each trained on slightly different subsets of the shadow features, and then averaging their outputs. This makes the model less sensitive to noise and allows the model to handle the missing intermediate thickness and distance values by drawing on patterns learned across the full range of training examples. Compared with boosting methods such as XGBoost, Random Forest provides clearer information about which shadow features drive the predictions using an integrated sensitivity analysis. Overall, the ability of random forest to generalise from limited experimental intervals make it a practical and reliable choice for estimating power loss in the ThinShadePV tool.

Within the developed Python-based model appended in Appendix G, specifically in code lines 21-64, the Random Forest regression model was trained by initially loading a comprehensive dataset, which included measurements of *'Total_umbra_percentage'*, *'Total_penumbra_percentage', 'Umbra_Intensity',* and *'Penumbra_Intensity',* as well as corresponding unknown outputs of power loss. The dataset was then split into training and testing subsets, with 80% of the data utilised for training and the remaining 20% reserved for validation purposes. Similar to the procedure adopted by Basaran et al. [250], the model was trained using standard hyperparameters (100 estimators), ensuring stable performance without extensive parameter tuning.

Upon training, the final Random Forest prediction is obtained by averaging the predictions from each decision tree. Mathematically, the final prediction $\hat{y}$ of the Random Forest regression model is expressed as Equation (21), where T is the total number of decision trees in the forest, and $f_t(x)$ represents the predicted value of the input feature vector x from the t^{th} decision tree.

$$Random\ Forest\ (\hat{y}) = \frac{1}{T}\sum_{t=1}^{T} f_t(x) \tag{21}$$

To evaluate the result of the prediction, this study endeavours to use the standard performance metrics, including the coefficient of determination (R^2) described and used by Olivares et al. "to estimate the regression model's ability to match the prediction with the actual values" [202, p. 4]. The Root Mean Square Error (RMSE) was used to "give more weight to large deviations due to the squaring of the deviations" [200, p. 3]. The Mean Absolute Error (MAE) was used as a metric to measure the average magnitude of the difference between the actual training data and predictions without considering its direction [251]. The below symbols shall be used throughout the equations thereafter in Equations (22) to (24).

$\bar{y}$ is the mean of the observed values, y_i is the observed value for sample i, and $\hat{y}_i$ is the predicted value for sample i. These metrics were calculated using Python's widely adopted *scikit-learn library*, specifically leveraging its *metrics* module. The functions

employed were *r2_score()* for calculating R^2, *mean_squared_error()* with its square root computed manually using *NumPy (numpy.sqrt())* for RMSE, and *mean_absolute_error()* for MAE.

The Coefficient of determination (R^2) can be calculated as:

$$R^2 = 1 - \frac{\sum_{i=1}^{n}(y_i - \hat{y}_i)^2}{\sum_{i=1}^{n}(y_i - \bar{y})^2} \tag{22}$$

Where an R^2 close to 1 means that the model's prediction matches perfectly with the outdoor experimentation data outlined in Section 5.3.1. Whilst on the other hand, R^2 close to 0 means that the model is unable to explain any variations in the thin object outdoor experimentation dataset.

The Root Mean Square Error (RMSE) can be determined as:

$$RMSE = \sqrt{\frac{1}{n}\sum_{i=1}^{n}(y_i - \hat{y}_i)^2} \tag{23}$$

Since RMSE quantifies the square root of the average of the squared differences between predicted and observed values, effectively measuring the model's prediction accuracy in the same units such as the dependent variable power loss expressed as a percentage. Moreover, a lower RMSE value indicates reduced residual variance, whereas a higher RMSE value reflects lower model prediction precision [252].

Mean Absolute Error (MAE):

$$MAE = \frac{1}{n}\sum_{i=1}^{n}|y_i - \hat{y}_i| \tag{24}$$

Whilst RMSE is sensitive to large errors, MAE provides a balanced view of overall errors by treating all errors equally regardless of their magnitude. Similarly, lower MAE values indicate higher model accuracy with respect to the thin object outdoor experimentation dataset [253]. Moreover, for the power loss prediction, the unit of MAE corresponds to the output predictive value, in this case power loss expressed as a percentage (%).

Utilizing these established performance metric functions ensured accurate and standardised evaluations, facilitating clear comparisons and interpretations of the ThinShadePV model's predictive capabilities.

5.2.2.5 Different Functionalities of the ThinShadePV Tool

To further advance the contribution to knowledge and improve the practical application of ThinShadePV, this study endeavours to introduce two functionalities in the prediction tool of ThinShadePV. The first function of ThinShadePV focuses on a case where a PV module is already installed on the roof and the second function is to be used at the design stage of the PV system. These functions both share the same training Random Forest model. Whilst the scientific methodology of quantifying umbra and penumbra shadow remains the same to both functionalities, it was decided that ThinShadePV will cater for both pre-installation cases and existing PV modules already installed on the roof. Figure 5.12 visualises the main menu of ThinShadePV where the user must choose between either Function 1 or Function 2 based on the required scenario.

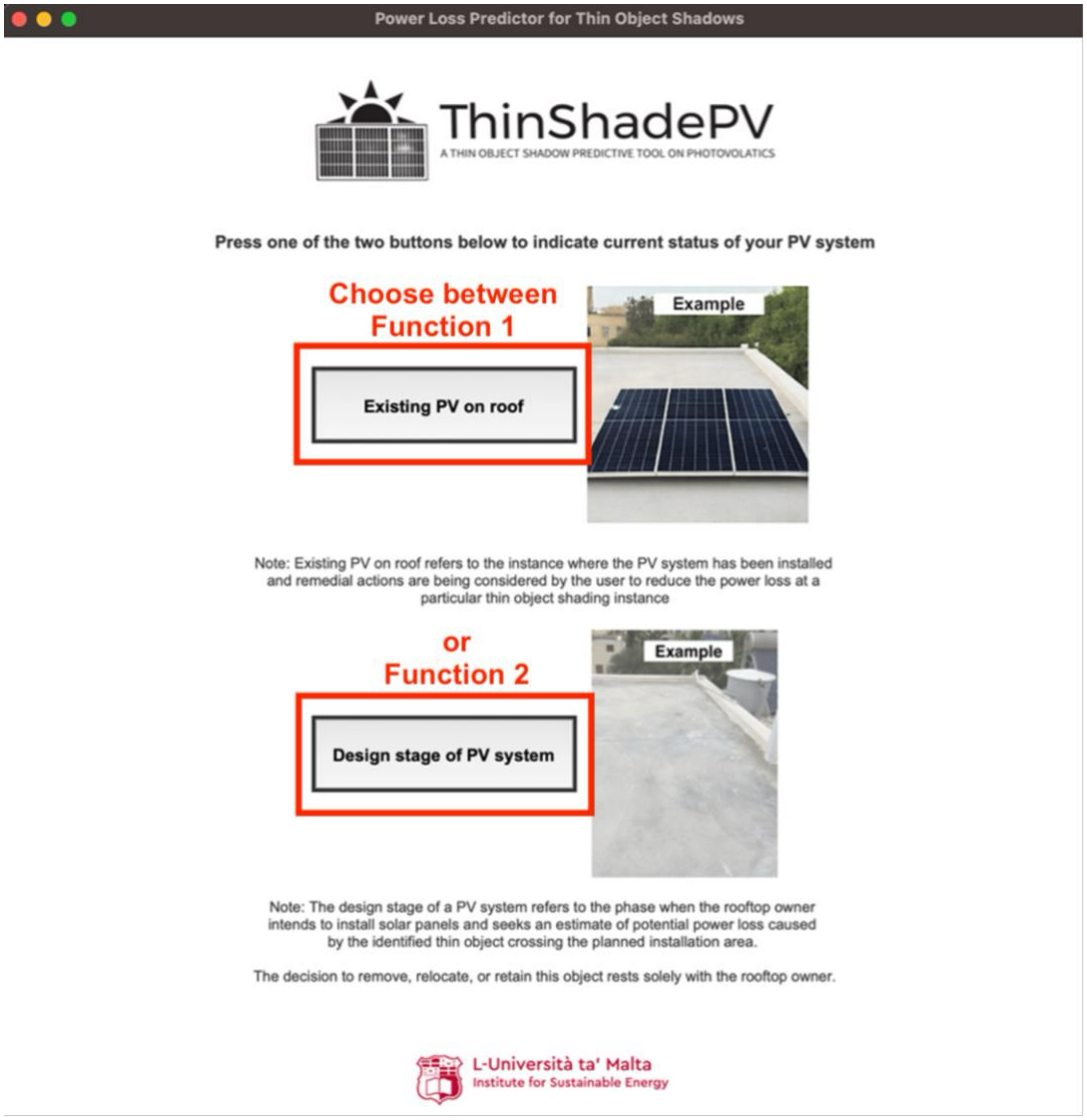


Figure 5.12. Initial main window prompt of ThinShadePV. To move to the subsequent section, either function 1 or function 2 buttons must be selected according to the shading case scenario.

5.2.2.6 Function 1: Existing PV on Roof

The selection of this function is prompted in the main window of ThinShadePV's GUI as visualised in the results section of this methodology in Section 5.3.4.

This function enables ThinShadePV users to quantify the power loss caused by shading from thin objects positioned in front of an already installed PV module, as illustrated in a conceptual example case image in Figure 5.13.



Figure 5.13. A conceptual scenario where a PV module is already installed on the roof with a horizontal thin object casting a shadow on the PV module. The photo of the rooftop was taken facing south as indicated by the cardinal compass direction indicator.

To utilise this function, users must capture an image of the shadow cast on the module and upload it to ThinShadePV when prompted. Users should start by preparing a reference surface using white paper, white cardboard or white PVC ensuring it is non-reflective and has a matte surface. The size of the reference surface must correspond to the same size of one single solar cell of the PV module connected in series and installed on the roof as outlined by the schematic diagram on Figure 5.14. This reference surface is then placed directly onto the PV module, carefully positioned so the shadow aligns precisely over a single solar cell which is being covered by the thin object shadow across.

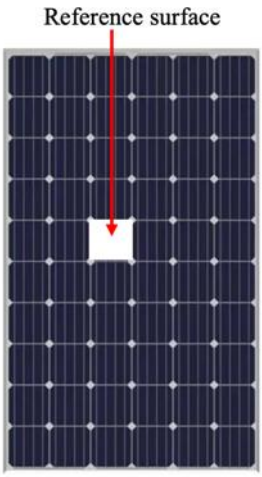


Figure 5.14. Reference surface placed on a single solar cell of the PV module.

Users must first capture an image of the entire reference surface, ensuring that the thin-object shadow is positioned at the centre of the white reference area. Any extraneous background visible in the image should be cropped so that only the reference surface remains. Moreover, although a perpendicular image capture would be ideal, this is not practical because the camera would cast its own shadow onto the reference surface. To avoid this, images must be taken from a slightly oblique angle. For consistency across the dataset, all training images were captured under identical conditions were the camera was inclined at 30^{o} relative to the reference cell and positioned at a distance of 75 cm. Future improvements to ThinShadePV may enable image captured even when the camera's inclination and distance deviate from the conditions represented in the training dataset. However, in the current version presented in this thesis, users must maintain the same camera angle and distance used during training to ensure proper performance.

Before importing images into ThinShadePV, the captured images must be corrected to an orthographic (perpendicular) perspective. This step follows established methods used in previous studies [236], [237], [238] as already outlined in Section 5.2.1.1. While future versions of ThinShadePV may include built-in perspective correction, the version described in this thesis relies on this external third-party tool as a pre-processing requisite, and users are encouraged to apply the same methodology. This approach ensures that the corrected image preserves the true geometric relationships of the scene, allowing measured shadow dimensions to reflect the real spatial configuration.

In terms of handling characteristics, ThinShadePV was trained exclusively on images captured at a fixed distance of 75 cm between the camera and the reference surface, ensuring that all training inputs were directly comparable. The current version of ThinShadePV does not correct for variations in camera distance, and it must therefore be emphasised that only images taken at this fixed 75 cm distance are suitable for processing. Moreover, to minimise distortions and ensure stable image capture, images in the training dataset were taken using a supporting arm mounted to the steel structure as previously explained in the detailed image capture methodology in Section 5.2.1.1, effectively eliminating camera shake; accordingly, images intended for use in ThinShadePV should also be free from noticeable motion blur. This means that it is not recommended that the image capture of the thin object shadow reference surface is taken with a handheld camera, but a fix mounted device at 75 cm away is mandatory.

The version of ThinShadePV presented in this thesis, as well as in Appendix G, is currently limited to cases in which a thin shadow intersects all solar cells along the horizontal axis of a PV module, assuming the module is positioned vertically. Under this condition, all bypass-diode subcircuits within the module are uniformly affected. As a result, the current implementation does not include an input parameter for specifying the number of cells per module. Instead, ThinShadePV can provide a reliable power loss prediction as long as the thin-object shadow crosses every cell within a horizontal row, consistent with the structure and assumptions of the training dataset.

Regarding image-capture characteristics, ThinShadePV has been intentionally designed to operate independently of the specific camera hardware used. The system does not require sensor metadata, optical calibration parameters, or internal camera specifications; instead, it relies solely on the pixel content of the captured image. Provided that the image is clear, in focus, and taken at a resolution sufficient to identify the thin-object shadow on the reference surface, ThinShadePV can perform reliably. Variables such as sensor type, zoom level, or focal length do not influence the processing pipeline, so long as the geometric information supplied by the user accurately reflects the capture conditions. Having said that, zoomed in images and images taken with a low quality image capturing devices will result in an image with less pixel density, meaning the quantification of the shadow pixels to determine the size of the shadow can be less accurate.

A further limitation concerns the specific PV module used during model training. The training dataset was generated using a small-scale PV module with an efficiency of 15.6%, and ThinShadePV currently lacks the capability to adjust its predictions based on different module efficiencies. As a result, all estimated power losses inherently reflect the characteristics of the training module. For the tool to be scalable and applicable to a wider range of photovoltaic technologies, future versions would need to incorporate support for multiple module types and efficiency values, allowing the model to adapt its predictions accordingly. This development would also require modifications to the graphical user interface, including the introduction of an input field enabling users to specify the efficiency of the module under analysis.

Following the conditions outlined above and the limitations of ThinShadePV identified, the prepared image can be uploaded into ThinShadePV's Function 1 GUI as indicated by Step 1 of Figure 5.15 and the *'Process & Predict'* button is clicked to initialise the prediction, as seen in Step 2 of the same figure. The integrated algorithm calculates the percentage umbra and penumbra size and shadow intensity, and provides a prediction of the power loss based on the trained Random Forest model associated with the shading in the image input by the user. Subsequently, Section 5.2.2.7 will further detail the second functionality as prompted in the main window of ThinShadePV's GUI, highlighting another essential feature and function.

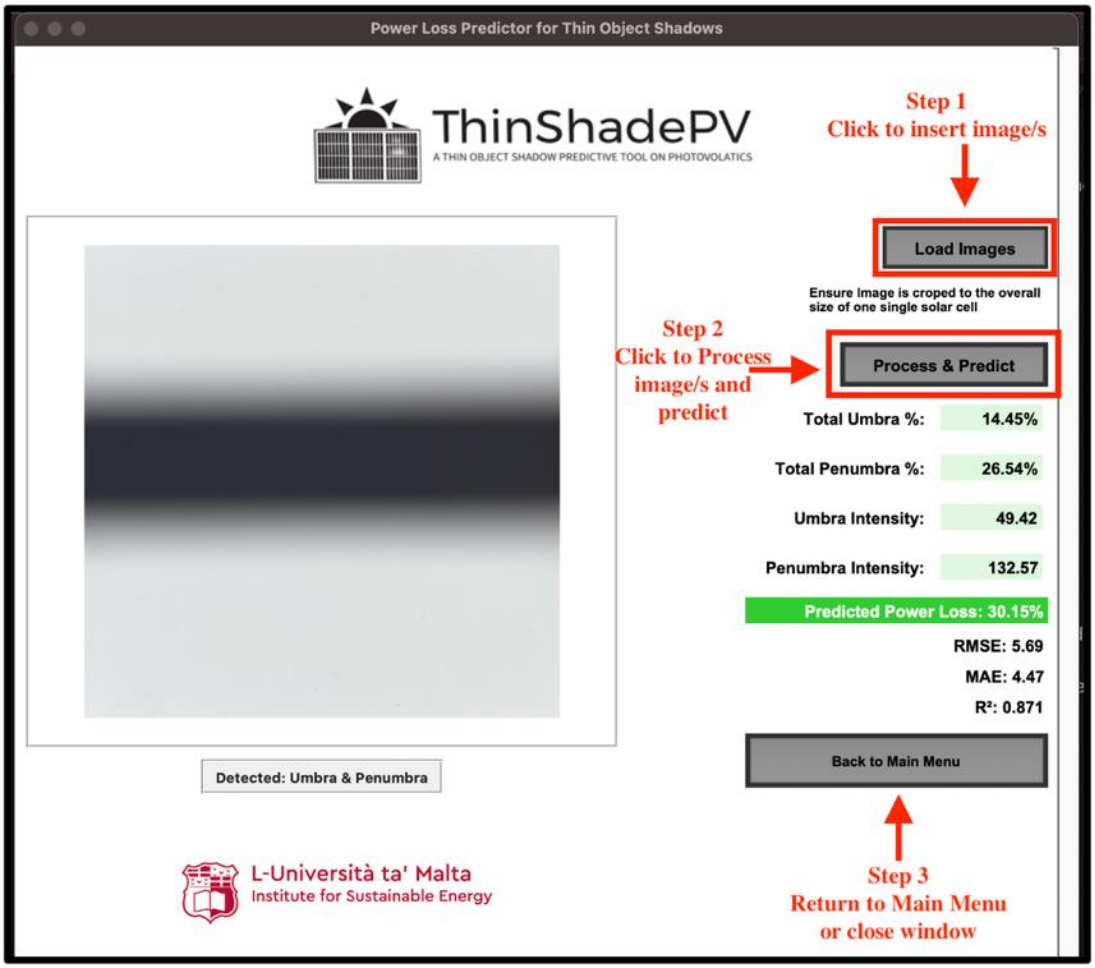


Figure 5.15. The window prompt upon selecting the Function 1 in the main menu. Insert image of the shading case and press the '*Process & Predict'* button to predict the power loss.

5.2.2.7 Function 2: Design Stage of PV System Function

Contrary to Section 5.2.2.6, the second function of ThinShadePV is predictive and thus forecasting potential power losses caused by thin objects, during the design stage and prior to the installation of any PV modules. A scenario of such an unoccupied roof is illustrated in Figure 5.16.

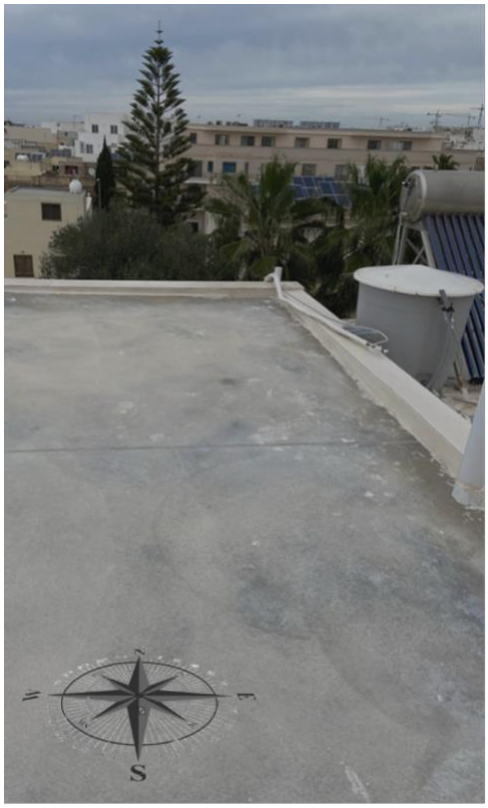


Figure 5.16. A typical scenario involves a roof that is currently unoccupied by any PV modules but is intended to accommodate a PV system in the future. The photo of the rooftop was taken facing south as indicated by the cardinal compass direction indicator.

This function becomes applicable when a user identifies a thin object that could potentially obstruct the light path to the proposed PV module placement on a roof surface. Once function 2 has been selected and its criteria satisfied, the user must manually measure both the distance between the obstructing object and the planned PV module location (indicated as the blue measurement), as well as the object's thickness (indicated as the green measurement) in Figure 5.17.

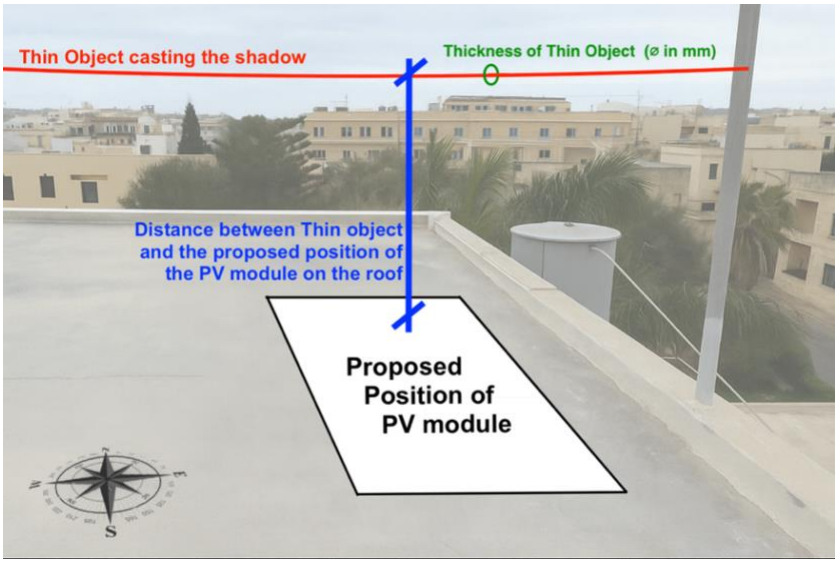


Figure 5.17. An indicative conceptual diagram of measurements required to be logged by the user of ThinShadePV, applicable to the case when a PV module is under design planning stage. The photo was taken from the south side of the roof.

Moreover, the user must know the dimensions of an individual solar cell within the PV module intended for installation. These specifications can be found in the module's datasheet. The length and width of the solar cell are required inputs in ThinShadePV to accurately calculate each cell's surface area. Once the distance, object thickness, and solar cell size are obtained, the input requirements for Function 2 of ThinShadePV are met. The user can then enter these values into their respective input fields in the GUI, as shown in Figure 5.18. After completing the three input fields, the varying visualisation on the left side updates automatically, illustrating the corresponding thin object shading scenario. Next, the user clicks the *'Predicted Factors'* button to generate values for umbra size, umbra intensity, penumbra size, and penumbra intensity using the pre-trained Random Forest model. Finally, by clicking the '*Predicted Power Loss*' button, the expected power loss, expressed as a percentage, is calculated and displayed in the green box of Figure 5.18.

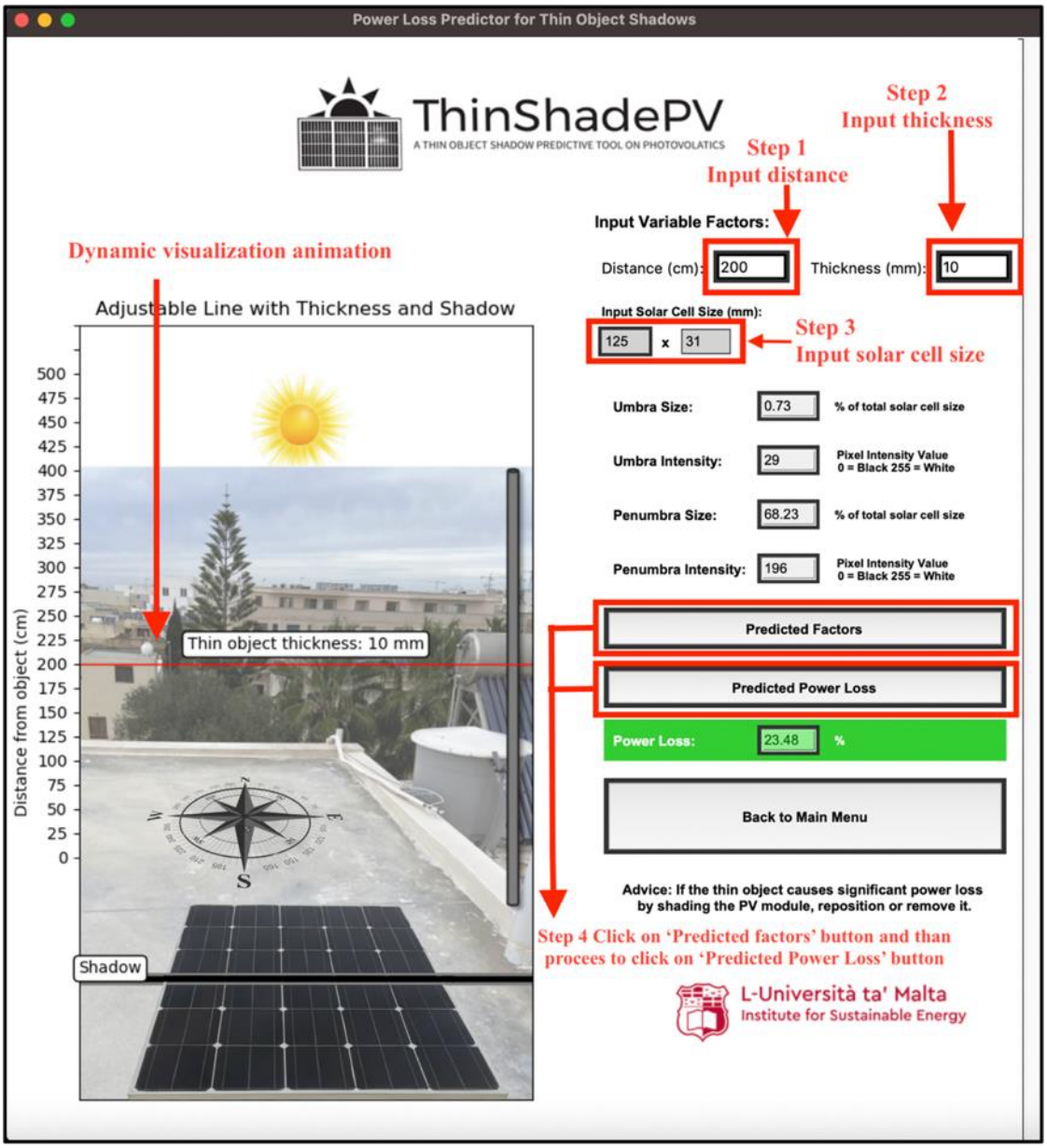


Figure 5.18. A snapshot of function 2 in ThinShadePV demonstrating the capabilities of predicting power loss based on distance and thickness measurements when the PV system is at design stage.

The integrated Random Forest model based on methodologies described in Section 5.2.2 and used by ThinShadePV, estimates the size and intensity of the umbra and penumbra cast by the simulated thin object. It then cross-references this information with a dataset of power loss values based on the trained Random Forest model, derived in Section 5.2.2.4, to predict power loss under the specific scenario. Furthermore, ThinShadePV is an open-source tool, enabling researchers to input their own power loss data, provided they follow the same methodology. This allows for contributions involving varying PV

module sizes and technologies, thereby broadening the dataset and enhancing the tool's applicability across occupied and unoccupied roofs.

5.2.3 Setup and Procedure for Validating ThinShadePV

ThinShadePV was specifically developed using thin object shading images and associated power loss data obtained from the outdoor experimentation methodology outlined in Section 5.2.1. Consequently, this section outlines a methodology to validate the accuracy of ThinShadePV predictions under realistic thin object shading conditions. Validation is conducted by comparing the power loss values predicted by ThinShadePV to empirical measurements obtained under fixed resistive load conditions defined in prior sections. In this process, multiple realistic thin object shading scenarios are replicated experimentally on a full-scale PV module, and the resulting power is recorded. The difference in output power between the control and shaded states is used to calculate the actual power loss, which is then directly compared to the ThinShadePV's predicted value. This comparison enables a quantitative assessment of the model's ability to simulate real-world shading effects on PV performance. Moreover, the accuracy of ThinShadePV will be validated based on two main factors:

- How closely the predicted power loss under fixed load conditions matches the actual power loss measured on a full-scale PV module. This shall be done when the module is exposed to a proportional amount of shading across the area of the solar cell, as would occur in a realistic thin shading scenario.

- Whether ThinShadePV can predict power loss for thin object thickness-distance combinations not explicitly tested in Section 5.2.1, such as intermediary values of cases such as ⌀11.0 mm thickness at 168 cm distance. This shall still be validated using the performance metrics provided in Section 5.2.2.4, which assess the effectiveness of the Random Forest model's training.

To evaluate these two criteria effectively, a realistic thin object shading scenario was carefully designed to serve as the basis for validating the predictions generated by ThinShadePV. This scenario was intended to replicate typical real-world conditions in

order to compare predicted and measured power loss values under various thin object shading conditions.

The validation was conducted on the 8th of May 2025 between 12:30 and 13:00 on the roof of a private residence located in Ħaż-Żebbuġ , Malta (35.876653, 14.417278). This site was selected primarily due to the building being south-facing and matching the exact orientation used in the experimentation described in Section 5.2.1 used as training data for ThinShadePV. Additionally, the roof offered substantial vacant space as indicated by the red perimeter marked in Figure 5.19, with neighbouring buildings situated at roughly the same height of the selected roof. This ensures that hard shading from adjacent walls is avoided. Furthermore, the rooftop featured multiple thin object shading scenarios commonly encountered in practical applications, such as passive air clothes drying lines and horizontal electrical and telecommunication cables. These characteristics allowed for realistic and relevant validation conditions. Therefore, despite the difference in location from the training dataset utilised in Section 5.2.1, it was ensured that consistency in the PV module setup was maintained to ensure a fair validation process.



Figure 5.19. The vacant roof area used for validation of ThinShadePV consisting of full sun exposure without any hard shading from nearby walls. The photo was taken from the north side of the roof.

A limitation that should be acknowledged for the setup shown in the figure above is that, unlike the Marsaxlokk site, which had no adjacent buildings, the Żebbuġ site has some nearby third-party walls. While these walls do not cause direct shading on the test area, they may produce minor variations in the local radiation due to reflecting radiation from

the walls. Having said that the irradiance was measured adjacent to the PV module which limits the previously outline setup discrepancy with the Marsaxlokk site. In addition, the diffuse irradiance component could not be measured separately, as the weather station for such measurements remained installed at the Marsaxlokk location. Consequently, only total irradiance values were available, which were used by the Seaward PV200 to correct the measurements to STC conditions.

Another factor to consider is the placement of the PV module. For this validation section, the module was positioned directly on the roof, whereas at Marsaxlokk, where the training data were collected, the module was slightly elevated from the ground. This provided slightly better airflow at Marsaxlokk. To mitigate this difference, the PV module at Żebbuġ was initially kept in the shade to prevent preheating before the experiment. The module was then placed on the roof at the time of testing. Furthermore, measurements from both the Marsaxlokk and Żebbuġ sites were corrected to 25 °C using STC conditions, ensuring that any minor differences in thermal environment is corrected.

The PV module chosen for the validation setup consisted of a full-scale PV module which is visualised in Figure 5.20a the overall dimensions of which are indicated in Figure 5.20b. The full-scale PV module has a 255 W maximum output power at STC and comprises 60 solar cells connected in series with three bypass diodes according to the diagram shown in Figure 5.20c. Although the full-scale PV module incorporates three bypass diodes, they did not affect the results, as the thin-object shading extended uniformly across all three sections of the module and was insufficient to activate the diodes. The electrical characteristics are delineated in Table 5.5 and further supported by the datasheet provided in Appendix C. This module was chosen due to its size corresponding to a traditional roof mounted PV system such as the ones observed in [138] and [25], thus providing a PV source closer to real life conditions. Moreover, testing the functionality of ThinShadePV on a full scale PV module allows other researchers to adapt ThinShadePV to other particular PV module brands and manufacturers currently on the market. The adaptation must follow the same principles used to derive the ThinShadePV training dataset. Specifically, each solar cell must have an overall size of 156.0 mm × 156.0 mm, the PV module must be positioned at a 0-degree inclination, and a horizontal thin shading object must be placed above the module

so that its transposed shadow covers the entire horizontal span of the PV module. This ensures that all 6 cells, and therefore the entire series-connected PV module, are uniformly affected by the thin-object shading.

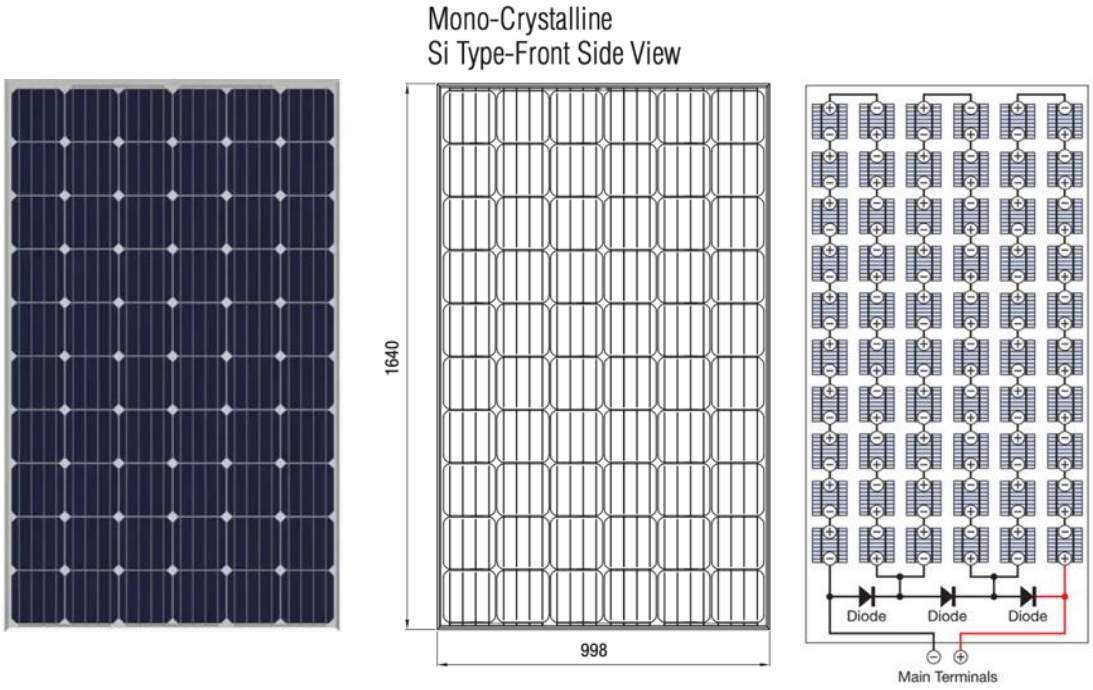


Figure 5.20. (a) The front elevation of the full-scale monocrystalline PV module, **(b)** Schematic diagram of the same full-scale PV module, **(c)** Wiring diagram of the three diodes located in the full-scale PV module used for ThinShadePV validation.

Table 5.5. Electrical characteristics of the full size PV module used to validate ThinShadePV.

Datasheet Information	Symbol	Manufacturer datasheet at STC	Tested Outdoors and calibrated at STC
Type of Cell Technology		Monocrystalline	Monocrystalline
Power Rating	P	255 W	237 W
Short circuit current	I_{SC}	8.8 A	9 A
Open circuit voltage	V_{OC}	37.7 V	37.1 V
MPP current	I_{MPP}	8.3 A	8.3 A
MPP voltage	V_{MPP}	30.8 V	28.7 V

Throughout the validation process, it was ensured that the position of the thin shadow matched that used in the small-scale PV module which was used to train ThinShadePV (Section 5.2.1). This was achieved by placing the thin objects horizontally across the width of the full-scale PV module as visualised in Figure 5.21. Although only the 6

solar cells were directly shaded, the resulting electrical behaviour influenced the performance of the entire string of 60 series-connected cells. In this manner, the complete shadow of the thin object, encompassing both umbra and penumbra shadow, was aligned with the central active region of the PV cells on the module, as depicted in Figure 5.21. Otherwise, shading on one solar cell will affect the current flow through all 60 cells in a similar manner, mirroring conditions experienced with the small-scale PV module outlined previously in Section 5.2.1.

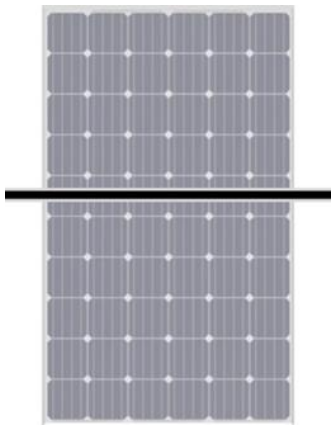


Figure 5.21. The position of the horizontal thin object shadow on the PV module.

To validate the percentage power loss prediction (output result of ThinShadePV) based on a real case scenario, a method was required to ensure that shadows cast during validation experiments on full-scale PV modules were proportional to those used during the training phase conducted on the small-scale PV module in Section 5.2.1. This method, explained in more detail in this section, was required since a full-scale solar cell (156.0 mm width) is much larger when compared to the solar cell used in the training dataset of ThinShadePV. The solar cell used in the training set was 31.0 mm wide.

As a purely illustrative example, Figure 5.22 visualises an example scenario on the small-scale PV module previously utilised for training data. The shadow cast by a thin object shading case, results in a 4.5 mm umbra translating to 14% of the solar cell's width and a 9.0 mm penumbra representing 28% penumbra shadow of the solar cell's width.

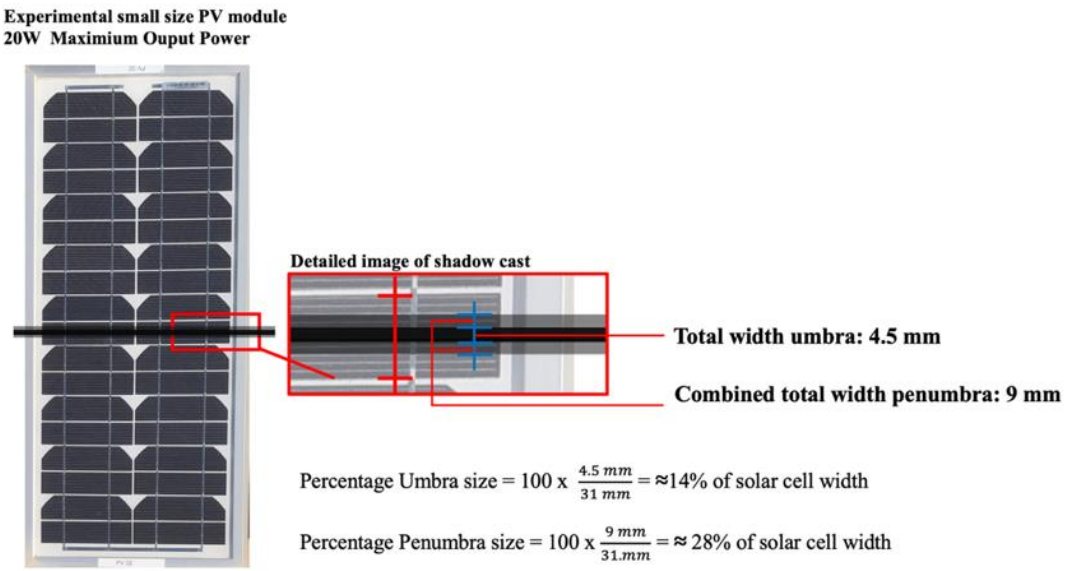


Figure 5.22. A visual explanation of the percentage shadow cast on the small-scale PV module.

To maintain the same percentage of umbra and penumbra coverage as observed in the small-scale PV module, the width of the shadow must increase in proportion to the larger width of the full-scale solar cell. In other words, because the denominator (the total solar cell width) becomes larger, the numerator (the corresponding umbra or penumbra width) must also increase to preserve the same percentage shadow coverage. This is illustrated in Figure 5.23, where an umbra width of 22.0 mm is required to achieve the same 14% umbra that corresponds to the 4.5 mm umbra on the small-scale module. Similarly, a penumbra width of 44.0 mm is needed to obtain a 28% penumbra coverage.

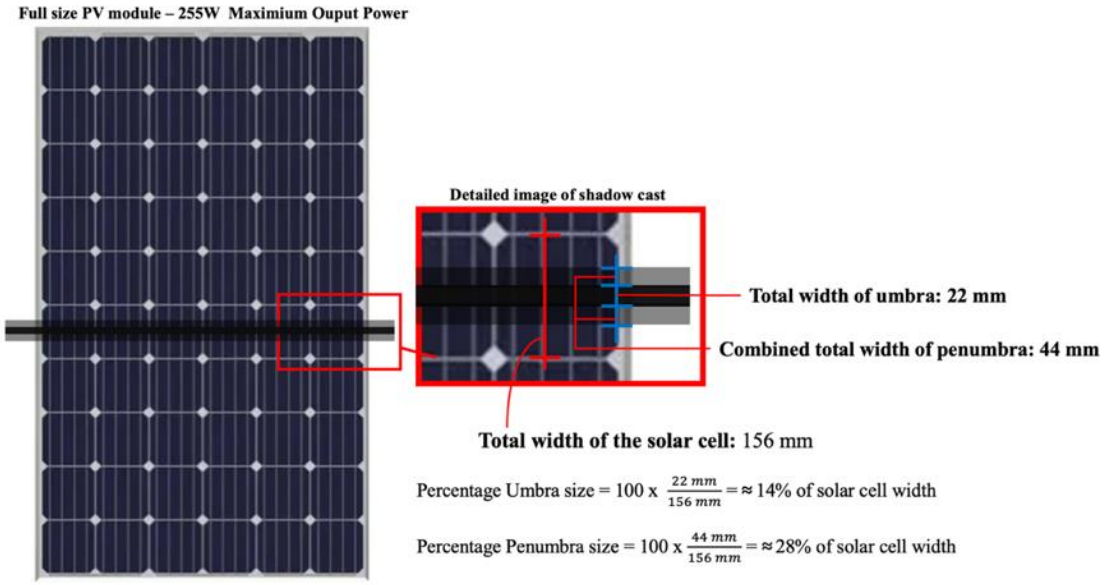


Figure 5.23. A visual explanation of the percentage shadow cast on the full-scale PV module used in the validation process.

It is essential to clarify that the proportionality applied in this study is used exclusively to preserve the relative shadow characteristics, namely the percentage of umbra and penumbra coverage for the small to the large PV module. The intent is not to compare the absolute dimensions of the thin objects casting the shadows, but rather to ensure that the resulting shadow coverage on the solar cell remains equivalent across different module sizes. Equation (25) provides the general formulation for determining umbra and penumbra widths and is applied uniformly to both small and the large-scale PV module. By ensuring that the numerator (total shadow width) increases in accordance with changes in the denominator (measured solar cell width), the same proportional shadow conditions are maintained. Retaining the same relative shadow size is critical for establishing a fair and directly comparable shading scenario across modules of varying dimensions, ensuring consistency in testing conditions and strengthening the validity and generalisability of the results.

$$\text{Umbra / penumbra size (\%)} = 100 \text{ x } \frac{\text{measured shadow width (in pixel qty)}}{\text{total shadow width (in pixel qty)}} \quad (25)$$

A data partitioning approach was used to validate the effectiveness of ThinShadePV in accurately predicting the power loss. This approach involves selecting a percentage of the 104 training cases (outlined in Section 5.2.1) to be used as a validation dataset. 15% of the total training comprising 104 cases of thin object shading was selected for validation purposes. This approach is informed by several recent studies: one study suggested using 10% of the dataset for validation [254], while two others employed a 15% split to validate model performance effectively [255], [256]. A 15% validation dataset will help provide a more comprehensive validation of results, resulting in a total of 15 different thin object shading cases as outlined in Table 5.6. These cases were based on the availability of size corresponding with the mathematical extrapolation of the size of the shadow on the PV module.

Table 5.6. A description of the 15 cases selected as the validation dataset. Each case shall be tested on the full-scale PV module.

Case Number	Description
1	A ⌀8.0 mm thick telecommunication line situated at a distance of 40 cm
2	A ⌀8.0 mm thick telecommunication line situated at a distance of 275 cm
3	A ⌀14.0 mm thick electrical cable situated at a distance of 60 cm
4	A ⌀16.0 mm thick drain pipe situated at a distance of 180 cm
5	A ⌀14.0 mm thick drain pipe situated at a distance of 215 cm
6	A ⌀16.0 mm thick electrical conduit pipe situated at a distance of 300 cm
7	A ⌀25.0 mm thick electrical conduit pipe situated at a distance of 215 cm
8	A ⌀25.0 mm thick drain pipe situated at a distance of 225 cm
9	A ⌀16.0 mm thick electrical conduit pipe situated at a distance of 215 cm
10	A ⌀16.0 mm thick drain pipe situated at a distance of 225 cm
11	A ⌀16.0 mm thick electrical conduit pipe situated at a distance of 325 cm
12	A ⌀32.0 mm thick drain pipe situated at a distance of 25 cm
13	A ⌀40.0 mm thick drain pipe situated at a distance of 30 cm
14	A ⌀40.0 mm thick drain pipe situated at a distance of 215 cm
15	A ⌀50.0 mm thick electrical cable situated at a distance of 180 cm

Note: The thickness of the cases named above always refers to the cross sectional diameter of the thin object (⌀) whilst the distance always refers to the distance between the full-scale PV module and the thin object.

Assessing the performance of each of the selected cases will adopt the same power loss metric as described in Section 5.2.1. However, the significantly higher power output of the full-scale PV module would require a large fixed load resistance capable of withstanding 255 W. Given its specifications, such a load was difficult to source for this experimentation. Moreover, the operational power output of the PV module, 255 W, far exceeds the absolute maximum input the DATAQ DI-808 data logger can withstand without damage. As a result, this investigation will utilise the power measurement equipment previously employed in studies [99] and [257], having proven effective in gauging power output in full-scale PV modules. Specifically, the Seaward PV200 I-V tracer, visualised in Figure 5.24a, was used. This device is intended for precise testing of full-scale PV systems in compliance with IEC 61829 standards. The I-V curve traced by this equipment provides comprehensive data that facilitates the extrapolation of power loss information. Furthermore, the same principle of determining altitude values based on the specific time and date of the validation experiment, as outlined in Chapter

4 Section 4.2.2, was applied to correct the measured power loss. Subsequently, the sun correction factor was computed using these altitude values to establish a consistent comparative baseline for all thin-object shading cases. Moreover, the Seaward PV200 has a built-in feature that facilities the recorded I-V curve to be corrected to STC conditions based on the manufacturer's coefficients and the external temperature and irradiance sensor (Seaward Survey 200R) as visualised in Figure 5.24b. This correction feature will be utilised to aid the power output values to be corrected at STC conditions without having to adopt the calculation corrections previously described in Chapter 4 Section 5.2.1 Equations (13) and (14) . To visualise the experimentation setup and the positioning of the equipment mentioned, Figure 5.25 was compiled.

It is noteworthy that even though the Seaward PV200 provided I-V curves for both shaded and control scenarios, the P_{load} was still chosen as a metric of the shaded case in order to correspond with the power output percentage difference (power loss) results for the experimentations conducted in Section 5.2.1, the same metric used as input data for ThinShadePV.



(a) **(b)**

Figure 5.24. (a) The Seaward PV 200 tester and I-V tracer, (b) The Seaward Survey 200R multi-function irradiance meter with suction mount on the full-scale PV module.

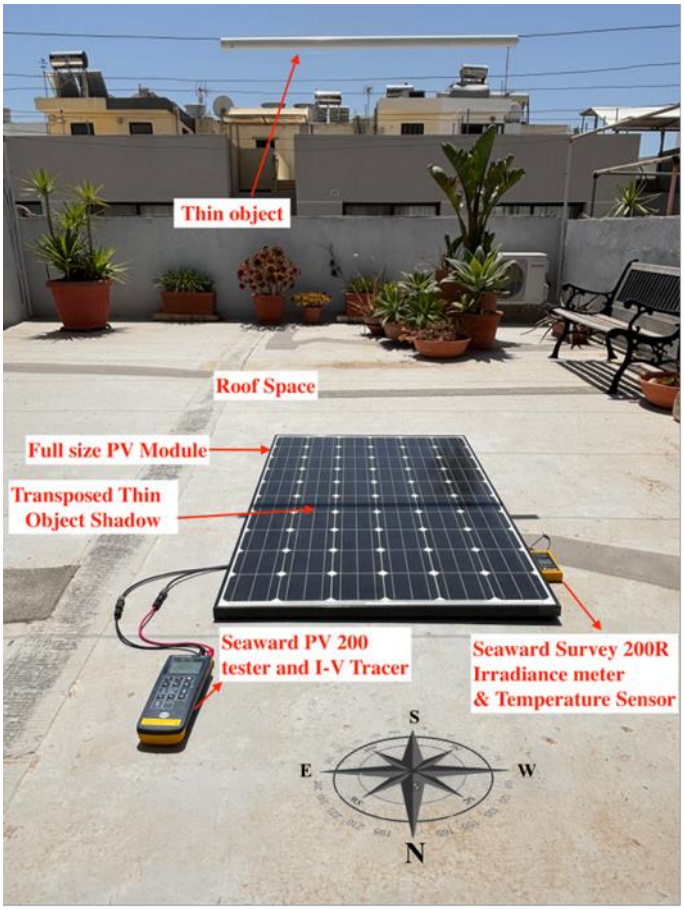


Figure 5.25. The outdoor validation experimentation setup of ThinShadePV at a real thin object shading scenario.

Furthermore, to capture the image reference prior to importing into the ThinShadePV tool and determining the predicted power loss, a square piece of matte white PVC sheet measuring 156.0 mm by 156.0 mm was positioned centrally on top of the full-scale PV module as visualised in Figure 5.26. This size corresponds to the size of a single solar cell of the full-scale PV module, following the requirements of operation of ThinShadePV outlined in Section 5.2.2. Images were captured using the same device and camera settings outlined in Section 5.2.2 using the built-in camera of an Apple iPhone 15 bearing camera settings of ISO 200, shutter speed 1/60s, aperture f/1.6 for each thin object shading scenario listed. The choice of the portable device was chosen with intent, to emulate a realistic scenario where the potential users of ThinShadePV would not need an SLR camera but a portable device like a smartphone would be sufficient. Each captured image was precisely cropped to the dimensions of the white PVC sheet, ensuring the horizontal shadow remained the central focus.

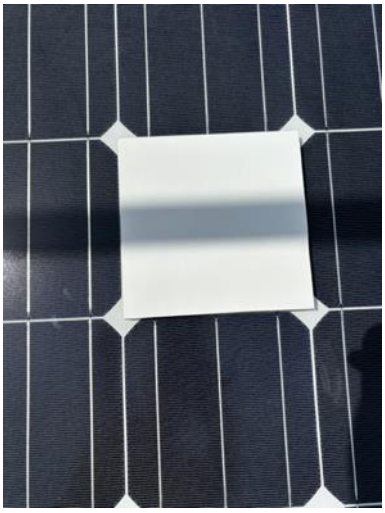


Figure 5.26. The matte white PVC sheet covering a single shaded solar cell of the full scale PV module as image capture for the ThinShadePV prediction.

The cropped images were then imported into the ThinShadePV software under the 'Existing PV on Roof' function, as seen in Figure 5.15 Section 5.2.2.6, as the scenarios being investigated met the necessary conditions stipulated by this software's function. ThinShadePV processed each image to determine the size and intensity of the umbra and penumbra regions. This led to a data-based prediction of the estimated percentage power loss under fixed load conditions. Consequently, the predicted values were compared to the percentage difference between the MPP (P_{max}) of the control condition of the full-scale PV module scenario and the corresponding load power (P_{Load}) obtained under thin object shading conditions from the I-V curve generated by the Seward PV200 analyser. To clarify, the calculation of percentage power loss consistently utilises data from the same PV source under unshaded control conditions.

A step-by-step insight into the method used to analyse the performance of ThinShadePV given the measured full-scale PV module is summarised below.

1. A full-scale PV module was positioned horizontally with a tilt angle of 0°, directly on a flat roof surface, simulating optimal irradiance conditions.
2. A thin object of suitable material and dimensions was selected to simulate a thin object shading case.
3. The shadow cast by the thin object was aligned and placed at a predetermined distance on top of the full-scale PV module to create a controlled shading scenario.

4. The Seaward PV200 tester and I-V tracer were connected to the PV module via MC4-compatible red and black test leads, ensuring correct polarity with the module's male and female terminals.
5. The Seaward Survey 200R irradiance meter and temperature sensor was wirelessly paired with the PV200 device to enable real-time environmental monitoring during testing.
6. The PV200 device was configured to a voltage range of 250 V, the most appropriate for single-module testing, and set to Mode 2 to capture the I-V curve. The "Auto" function was initiated to begin the measurement.
7. The I-V curve data was logged and imported into SolarCert Elements software, where it was corrected to STC conditions using the corresponding irradiance and temperature values obtained during measurement.
8. The I-V curve of the control full-scale PV module was plotted alongside the STC-corrected I-V curve of the shaded condition to enable direct comparison.
9. A diagonal line, shown in red illustrated in Figure 5.27 representing a constant resistive load R_{Load} was drawn from the origin (0 V, 0 A) to the MPP P_{max} of the control curve.

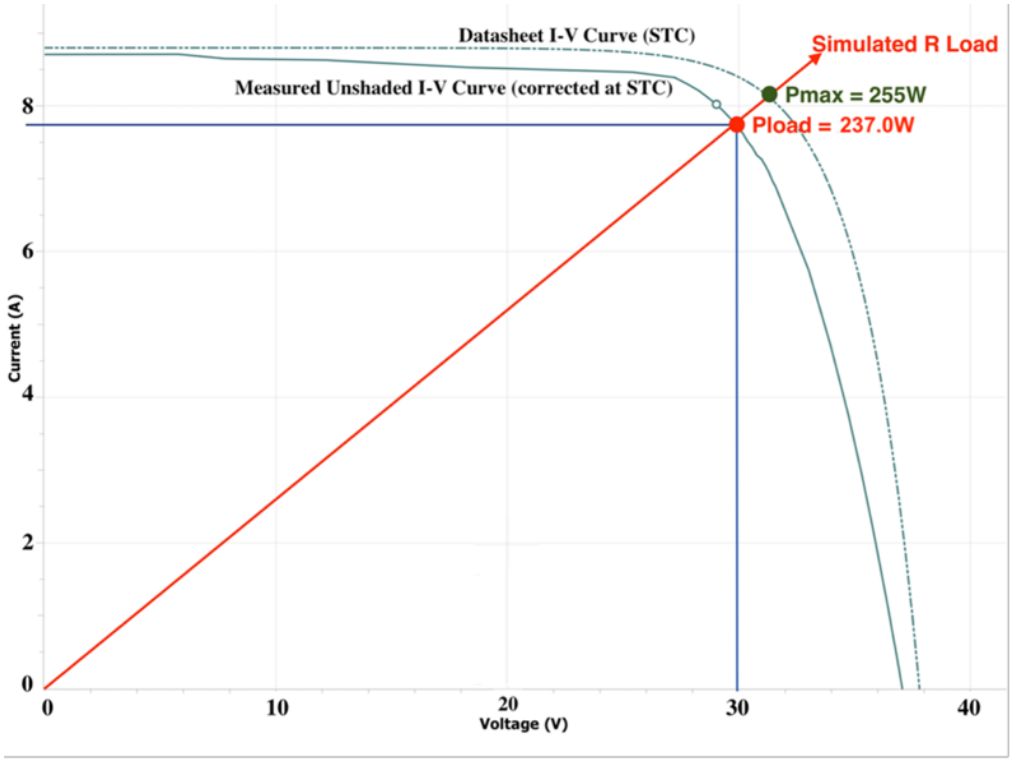


Figure 5.27. The measured points used for validation indicated as P_{load} by the red point marker where the measured I-V curve intersects with the simulated diagonal fixed load denoted as R_{load}.

10. The intersection point of the shaded I-V curve and the R_{load} diagonal line was determined, representing the operating point under load P_{load}, and compared to the control P_{max}.
11. The power loss due to shading was quantified by comparing the control P_{max} to the STC corrected power output of the shaded scenario.
12. An image from the experiment, featuring a white background and matching the dimensions of a standard solar cell (156.0 mm × 156.0 mm), was uploaded into the 'Existing PV on Roof' function of the ThinShadePV software. The 'Process and Predict' button was selected to initiate analysis.
13. ThinShadePV analysed the image and identified whether the shading case consisted of umbra and penumbra, or penumbra only.
14. The software provided key shading characteristics, including the percentage area of umbra and penumbra, the intensity of the umbra, the average penumbra intensity, and the predicted power loss.
15. Finally, the predicted power loss (from ThinShadePV) and the experimentally measured power loss (from step 12) were compiled into a comparative results table to assess the accuracy and reliability of the ThinShadePV predictions.

When comparing the measured power loss on the full-scale PV module to the ThinShadePV predictive percentage power loss, it is important to note that the absolute power output will increase due to the increased power output of the PV module. However, the relative percentage of power loss under conditions of thin object shading remains unchanged, provided that all other operational variables are constant and a relative shadow is transposed. This approach ensures a standardised comparison of percentage power loss attributable to thin object shading conditions. The results of this section shall be elaborated further in Section 5.3.4.

5.3 Results and Discussion

This chapter presents and discusses the results obtained from using the methodology highlighted in Section 5.2.1. The outdoor experimentation setup used to train ThinShadePV, built around the small-scale PV modules, was designed to determine the

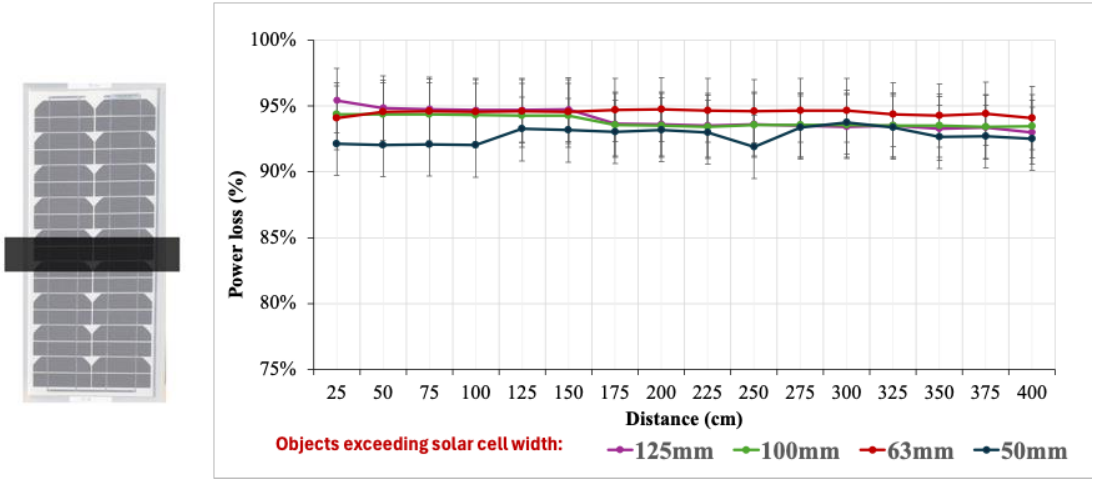
power loss under thin object shading conditions to develop a training dataset. This shall be the prediction output for ThinShadePV using the Random Forest model. Additionally, power loss data from a full-scale PV module subjected to realistic thin object shading conditions was employed to validate these predictions and attempt to answer RQ.2. The results of these investigations are presented and discussed in the following sections.

5.3.1 The Quantifiable Effect of Various Sized Thin Object Shading on a Small-Scale PV Module (ThinShadePV Training)

This section shall focus on the results obtained following the methodology introduced in Section 5.2.1, which established an experimental procedure to evaluate the influence of both distance and object thickness independently, such that a training dataset can be developed. Prior to commencement of the thin object shading quantification experiments, it must be noted that despite designing a setup capable of evaluating the distance between the small-scale PV module and the thin object up to 400 cm, power loss was not consistently recorded across the full distance range (25 – 400 cm). This limitation arose due to the combined shadow (comprising both umbra and penumbra) often exceeding the 31.0 mm width of a single solar cell of the small-scale PV module. As a result, the penumbra spilled over onto the cells adjacent to the targeted row. This scenario led to additional shadows falling on neighbouring solar cells, which, although still within the active area of the PV module, had their influence overshadowed by the dominant thin shadow on the selected solar cell row. This effect can be attributed to the theoretical principle observed in literature, whereby in PV modules with cells connected in series, the output current, which is heavily influenced by shading, is dictated by the solar cell experiencing the lowest current output [47, p. 17]. Therefore, the impact of the shadow on the top and bottom solar cells is dominated by the current output from the solar cell under the most extensive shadow.

To validate the theory above, prior to the quantification of thin object shadow cases, a preliminary experiment was conducted to validate whether having a fully shaded solar cell on a PV module would affect the power output of the whole PV module, regardless of the excess spill over shading on nearby solar cells. Therefore, a total of 4 large

cylindrical objects having a diameters of ⌀50.0 mm, ⌀63.0 mm, ⌀100.0 mm and ⌀125.0 mm, respectively, were utilised to provide varying levels of overall shading coverage on the PV module. These diameters were chosen because they cast shadows that extend beyond a single row of solar cells as seen in Figure 5.28a.



(a) **(b)**

Figure 5.28. (a) a visual representation of the shadow and PV module setup investigating the impact of large cross sectional diameter object shading, **(b)** The resultant power loss for objects transposing shadows whose thickness exceeds the width of the solar cell on the small-scale PV module.

The visualised line graph in Figure 5.28b, outlines the percentage power loss for each large cross sectional diameter objects at a distance between 25 cm and 400 cm from the PV module. The uncertainty for each power loss value was derived from Appendix B.1 of the appendix and is shown as error bars in Figure 5.28b. The average uncertainty was calculated to be ±2.52% of power loss.

It is clearly evident that a substantial power loss incurred when objects casting shadows exceed the width of a solar cell on the small-scale PV module. Notably, the analysis reveals that the power loss attributable to a ⌀50.0 mm, ⌀63.0 mm, ⌀100.0 mm, and ⌀125.0 mm object consistently surpasses 90% of the potential output power of the solar cell across various distances. This significant reduction indicates that when an entire row of solar cells is shaded, the power output is drastically minimised, irrespective of distance. Interestingly, with the exception of a single case at a 25 cm distance and ⌀125.0 mm thickness, no other case exhibited more than 95% power loss, even when the series connected solar cells were fully shaded. This is attributed to the fact that unless the shading object is placed directly on top of the PV module, even if minimal, some light would still be captured by the PV module, thus the shadow transposed never had an

intensity value of 0 as the darkest pixel. While the data presented in Figure 5.28b exhibits some fluctuations and imperfections, such as the slight variations in power loss percentages across different distances for object size ⌀50.0 mm, these do not fundamentally alter the outcome of this section.

These findings validate results from Numan et al. [100] who claim that the power output of a PV module is heavily dependent on the unobstructed functioning of each row of cells, particularly in configurations where cells are connected in series. Therefore, the experimental results strongly support the theory that for effective analysis of quantifiable effect of thin object shading on a PV module, the total shadow cast by objects must not exceed the total width of the solar cell. It shall thus be enforced that experiments with thin objects will adhere to this guideline and ensure the thin object shading is confined between one single row on the small-scale PV module to ensure a fair experimentation and determine the independent effect of thin object shading. Moreover, this constraint was implemented to retain practical applicability of ThinShadePV later in this chapter for full-scale PV modules comprising multiple solar cells of either 156.0 mm width for a full-scale solar cell or a 75 mm for half cut cell, as exemplified by Tobar et al. [134]. Therefore, an object exceeding this width would not be considered as a ’thin' shading by definition, but rather considered as 'hard' shading.

To analyse the relationship between distance, thickness, and the resulting power loss, a visual representation of the quantified power loss is provided in Figure 5.29, with different point markers used to categorize and distinguish the data. The thin objects are categorised into two groups, the first pertaining to small thin objects (⌀2.8 mm to ⌀8.0 mm) and the second focusing on large thin objects (⌀10.0 mm to ⌀16.0 mm), as previously explained in Section 5.2.1. The uncertainty for each power loss value was derived from Appendix B.1 of the appendix and is shown as error bars in Figure 5.29. As a representative value, the average uncertainty was calculated to be ±2.38% of power loss.

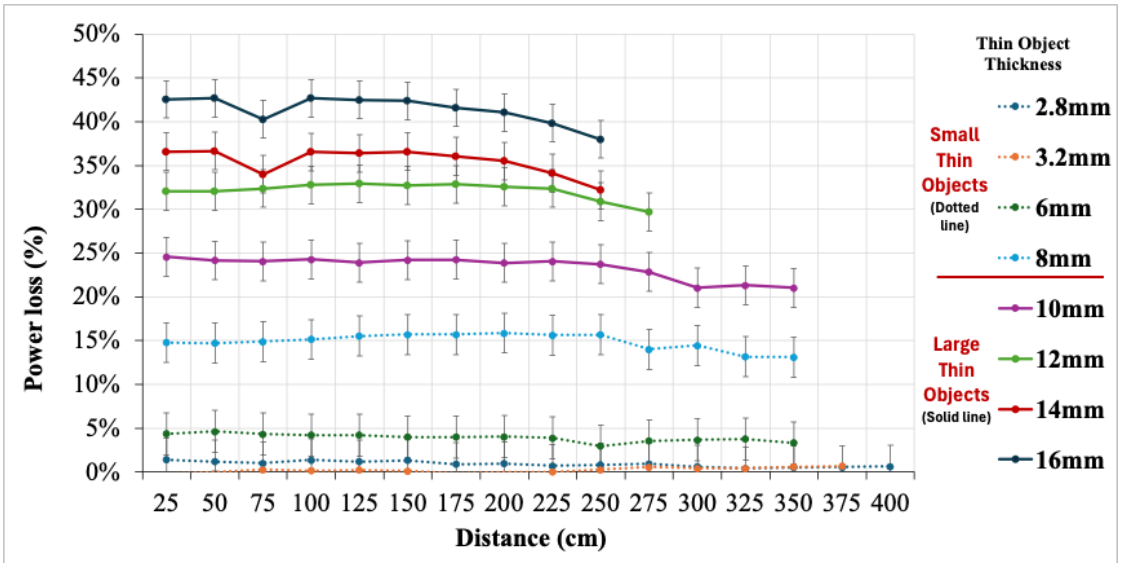


Figure 5.29. Analysing the various power loss levels as the distance between the two categories of thin objects and the small-scale PV module increases.

The analysis of thin object shadows transposed on a single row of solar cells on the small-scale PV module revealed several critical insights. Interestingly, the ⌀2.8 mm thin object is the only thin object that, at 400 cm away from the PV module, still transposes an overall shadow less than the width of the solar cell (31.0 mm). Moreover, for both the ⌀2.8 mm and ⌀3.2 mm object thicknesses, power losses remained within the uncertainty margin or error with less than 1.5% for all distances tested indicating that the shadow produced a negligible impact on the power output. This result is to be expected since the minimal power loss is attributed to the low intensity of the shadows cast by these smaller objects, primarily in a penumbra dominated region as will be outlined further in Section 5.3.2. Moreover, whilst a ⌀6.0 mm thin object still maintains a power loss of less than 5%, a considerable power loss of between 13.12%-14.77% is noted for object thickness of ⌀8.0 mm. Thereafter the rise in power loss is incremental as the thickness of the object increases, reaching up to a 42.53% power loss for the ⌀16.0 mm thin object at a distance of 25 cm where the shadow is at its most intense.

Interestingly, between 25 cm and 150 cm distances, power loss remains relatively constant and linear across all the thin objects. This implies that the intensity lost due to the increase of distance is being compensated by the increase in penumbra shadow. Consequently, when researchers such as Alsayid at al. [158] employ methodologies that involve placing an object directly atop the PV module, ignoring the impact of distance and shadow intensity, their findings are likely valid for distances up to 150 cm from the

PV source and up to 400 cm for small, thin objects measuring ⌀3.2 mm or less. However, beyond 175 cm, large thin objects, more notably the ⌀12.0 mm, ⌀14.0 mm and ⌀16.0 mm thin objects, begin to demonstrate a slight decline in power loss. For the ⌀8.0 mm and ⌀10.0 mm thin objects, this decline is observed much later, at around 275 cm, and for thin objects between ⌀2.8 mm and ⌀6.0 mm the power loss remains relatively constant.

This implies that at these points, the umbra loses a significant amount of its intensity that is not being compensated for by the increase in shadow size. Therefore, the shadow impact will be reduced overall as can be clearly seen in Figure 5.29. Beyond the 275 cm distance mark, the power loss starts to decrease more evidently for large thin objects especially for diameters of 8 mm and 10 mm. Additionally, the linearity indicates that, although the overall shadow intensity decreases with increasing distance, the growing penumbra size compensates for most of the loss in intensity by increasing the overall shadow size. A comparable trend was noted in Chapter 4 Section 4.3.3, where thin objects of different thickness in an outdoor setting exhibited relatively consistent power loss as the distance increased up to 40 cm.

To utilise the data illustrated in Figure 5.29, it was tabulated in a dataset repository comprising column names after each attributing factor of distance, thickness and power loss. However, as outlined in Section 5.2.2.1, the prediction model aims to estimate power loss based on the size and intensity of umbra and penumbra shadows on the PV module. This approach is intended to generalise beyond the specific small-scale PV module, making the model applicable to a range of PV modules. By attributing power loss to specific umbra and penumbra percentages, rather than solely relying on distance and thickness values, the model accounts for the relative scale of the shadow and the solar cell in question. Therefore, the following section will endeavour to derive and analyse the umbra and penumbra size and intensity at both the small and large thin object shading cases outlined in this section.

5.3.2 Analysing the Size and Intensity of Umbra and Penumbra as Distance Increases.

In this section, the size and intensity of the umbra and the penumbra shadow formation at each object thickness and distance will be analysed as determined by the methodology outlined in Section 5.2.2.1. From this point onwards, ThinShadePV will be utilised to evaluate the 104 cases of distance and thickness combinations outlined in Figure 5.29. The size of both umbra and penumbra shadow were calculated as a percentage of the total width of the solar cell as exemplified in the methodology of Section 5.2.3. Values exceeding the 100% threshold suggest that the combined umbra and penumbra shadow extends beyond the width of the solar cell, thus spilling over onto adjacent cells above and below the focal solar cell. However, this study focuses specifically on the effects observed on a single solar cell. Figure 5.30 illustrates an example of the type of the indicative marker lines on the input image generated by ThinShadePV, where the umbra and penumbra boundaries have been determined by the tool as the size is calculated. Furthermore, Figure 5.31 illustrates a similar example with a case where only a penumbra shadow was identified by ThinShadePV. These indicative markings were fully automated by ThinShadePV based on the dual sigmoidal function outlined in Section 5.2.2.2, without any input from the user except for the initial image input, using Function 1.

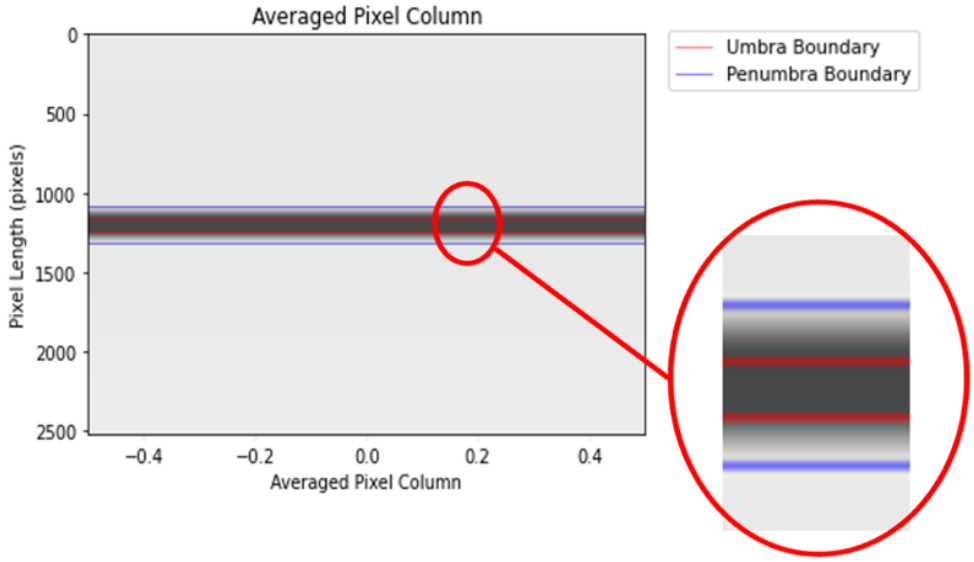


Figure 5.30. The identification of a case where the shadow consists of both umbra and penumbra derived from the dual sigmoidal curve method and generated by ThinShadePV.

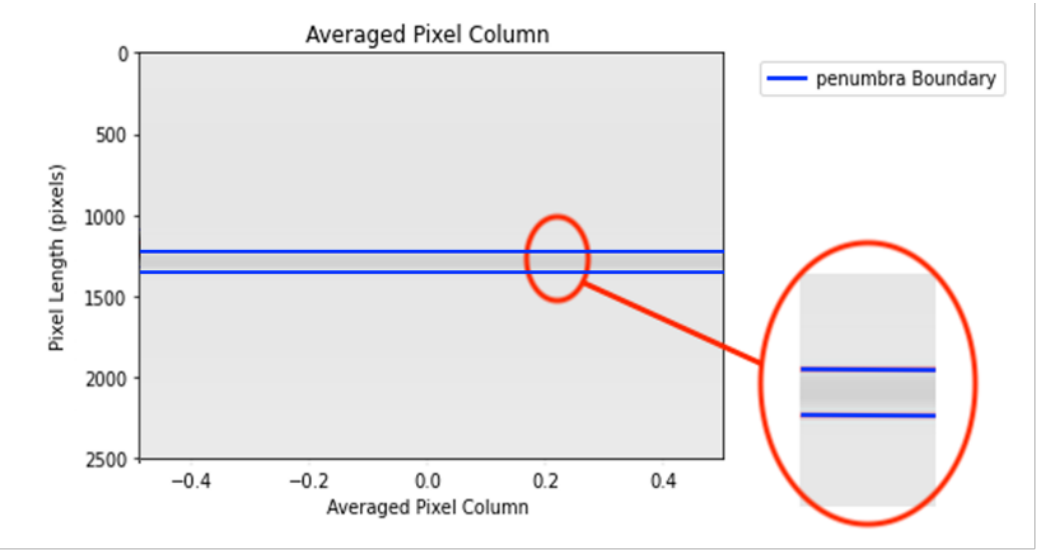


Figure 5.31. The identification of a case where the shadow consists of only penumbra derived from the dual sigmoidal curve method and generated by ThinShadePV.

This study recognises that the intensity of the penumbra shadow exhibits a varying range of pixel values as exhibited in Figure 5.31, in contrast to the relatively uniform intensity observed in the umbra, as illustrated between the blue and red lines in Figure 5.30. Therefore, for computational purposes, the penumbra intensity was quantified by calculating the average pixel value within this range. The same methodology was applied in cases where only the penumbra was present, such as in Figure 5.31, where the penumbra intensity was similarly determined by averaging the pixel values between the blue lines.

The results of the above quantification factors affecting the power loss have been denoted in Figure 5.32 a-d, where the categorical small thin objects between object thicknesses ⌀2.8 mm and ⌀8.0 mm are outlined, whilst the large thin objects between ⌀10.0 mm and ⌀16.0 mm are illustrated in Figure 5.36 later in this section. The black line graph represents the umbra size alongside the percentage shadow to cell width on the primary y-axis and distance on the x-axis, whilst the penumbra size is denoted by a grey line using the same primary axis. Furthermore, in the same line graph, the umbra intensity is represented by the blue line whilst the penumbra intensity is depicted by the green line. A general observation across the four thicknesses analysed in Figure 5.32a-d reveals that, as the distance increases (as shown on the x-axis), the size of the umbra shadow decreases, and its intensity becomes progressively lighter for all small thin objects. Moreover, as the umbra shadow transitions to a penumbra shadow due to the

increase in distance as in [23], the penumbra shadow increases in size but the intensity significantly decreases until it reaches the background intensity value. Prior to this study, the outlined relationship has already been documented in the literature, notably by researchers such as Hernan [62] and Sinha [180]. However, this study aims to provide a more comprehensive analysis on the underlying relationships between umbra and penumbra shadow size and intensity with reference to the power loss results previously seen in Section 5.3.1.

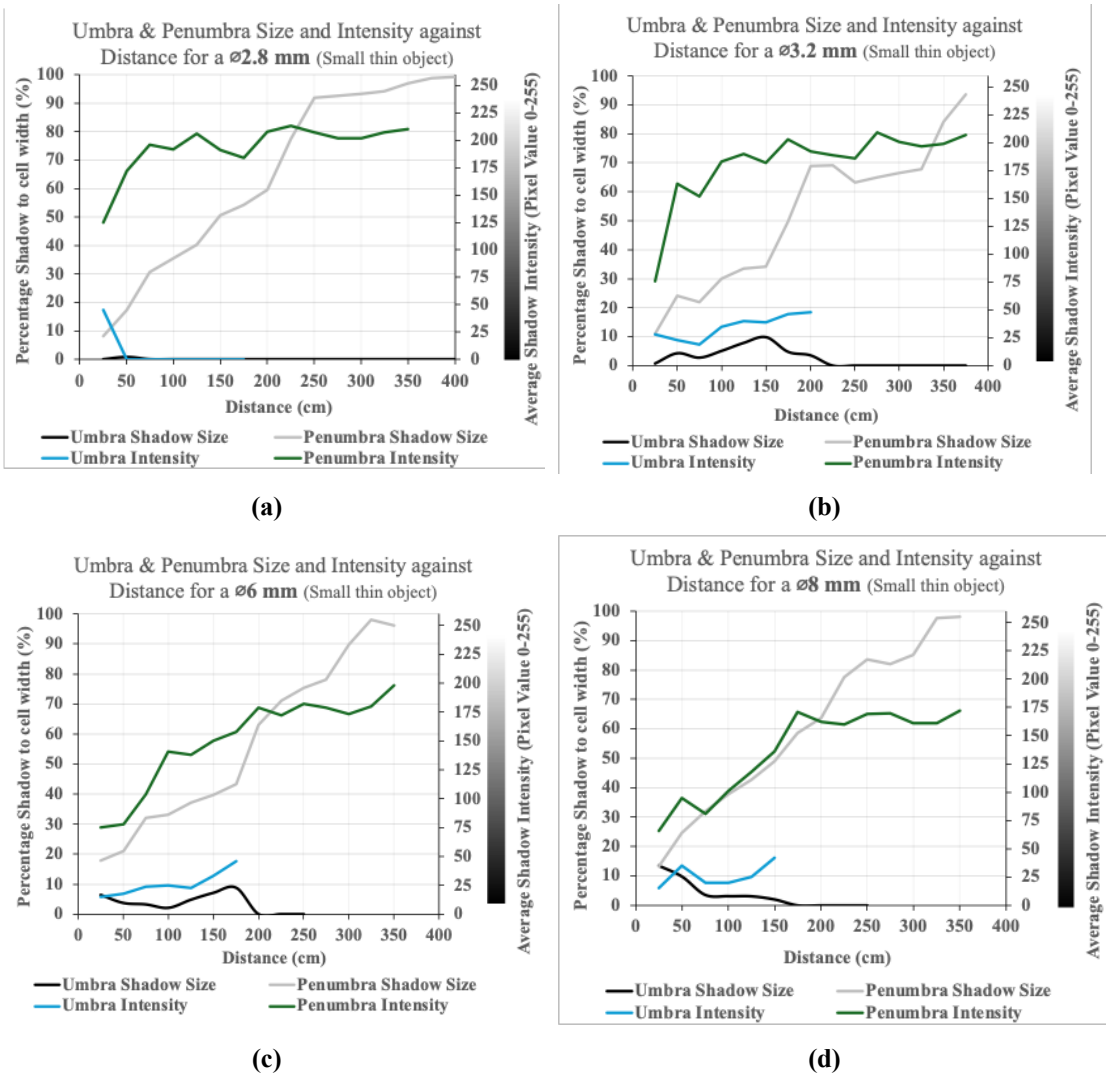


Figure 5.32. An illustration of the umbra and penumbra size and intensity results for the small thin objects. **(a)** ⌀2.8 mm, **(b)** ⌀3.2 mm, **(c)** ⌀6.0 mm, **(d)** ⌀8.0 mm

The shadows cast within the object thickness range of Figure 5.32 a-d predominantly consist of penumbra, with the umbra constituting a smaller fraction of the percentage of the total width of the solar cell. For case, for objects having a thickness of up to ⌀6.0 mm shown in Figure 5.32a-c, the size of the umbra accounts for less than 10% (3.1 mm) of

the width of the solar cell on the small-scale PV module. For an ⌀8.0 mm thick object, the umbra shadow constitutes less than 15% of the width of a single solar cell, corresponding to 4.65 mm. Moreover, at 25 cm distance from the PV module, the ⌀8.0 mm thin object produces a very intense umbra shadow as visualised in Figure 5.33.

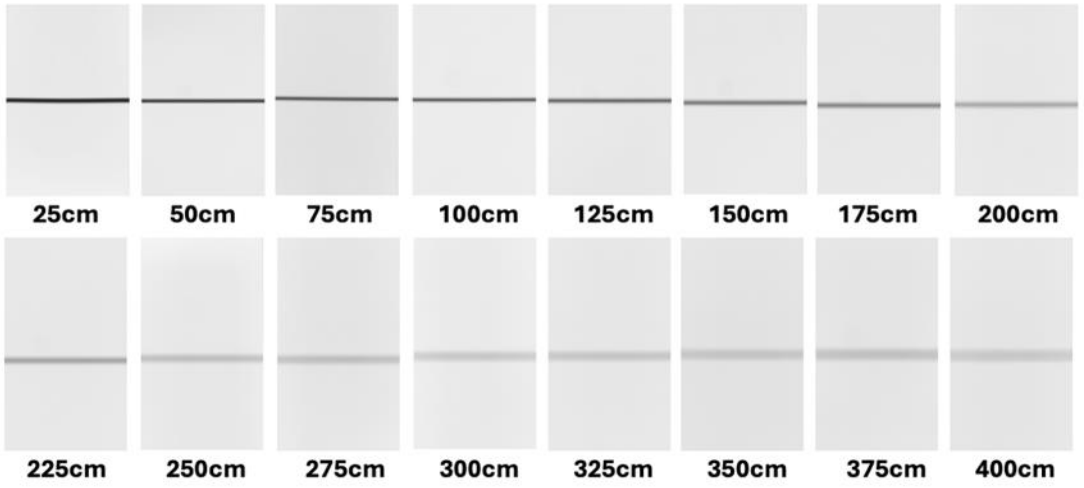


Figure 5.33. Image sample dataset illustrating the transition from umbra and penumbra shadows at a distance of 25 cm, to a penumbra-only shadow at the maximum distance of 400 cm for a small thin object (⌀8.0 mm).

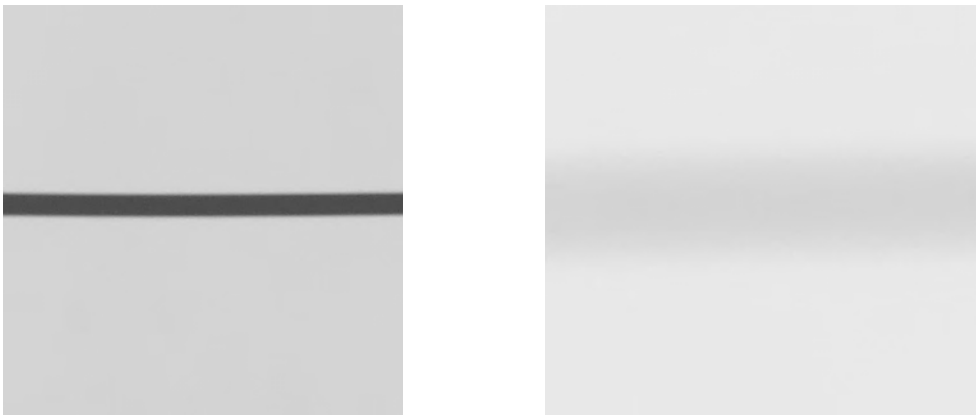
The intensity gradually gets lighter up to 175 cm, after which it is replaced by a predominantly penumbra shadow as seen comparatively between the first and the final images within the same figure. A similar trend is observed for objects thinner than ⌀8.0 mm, such as for a ⌀2.8 mm thin object, where the size of the penumbra-only shadow is seen to be significantly larger than when compared to 25 cm distance. This difference is exhibited in Figure 5.34a and Figure 5.34b. This transition occurs because small thin objects do not significantly obstruct the light path, resulting in a larger area of penumbra when compared to the umbra area. A smaller thin object causes light to spread around the object more extensively, resulting in a shadow with a broad penumbra and a narrow umbra. Since small thin objects offer minimal obstruction, they allow more divergent light rays to bypass the object, amplifying the penumbral area. This effect is intensified by the geometry of light paths, where the umbra is restricted to rays that are completely blocked, which are fewer due to the object's limited thickness [258].



(a) **(b)**

Figure 5.34. A detailed view of the shadow created by a ⌀2.8 mm thin object at **(a)** a distance of 25 cm and **(b)** a distance of 400 cm from the small-scale PV module.

A common characteristic among the small thin objects is the presence of a transitional point at which the umbra-dominated shadow is gradually replaced by the penumbra shadow due to the increase in distance coherent to the geometric representation in Chapter 2 Section 2.3. Concurrently, the size of the penumbra was observed to expand at a relatively proportional rate with increasing distance. For the small thinner objects depicted in Figure 5.32a–b, the penumbra ultimately covered the entire solar cell at distances of approximately 350–400 cm. Therefore, although the shading object (⌀2.8 mm) in Figure 5.32a is nearly three times thinner than the object (⌀8.0 mm) in Figure 5.32d, the rate at which the penumbra expands with increasing distance remains relatively consistent. As a result, the penumbra shadow in both scenarios covers the solar cell at approximately the same distance. In contrast, the intensity of the penumbra varies significantly with the thickness of each small, thin object. For case, the ⌀2.8 mm thin object at 400 cm in Figure 5.34b exhibits a penumbra intensity very close to background intensity on the white surface, resulting in a notably lighter shadow. Conversely, the ⌀8.0 mm at a distance of 375 cm produces a relatively darker penumbra-only shadow as visually comparable between Figure 5.34b and Figure 5.35b. This comparison proves that unlike common practices in literature by Numan et al. [100], Luo et al. [130] and Dolara et al. [24], the intensity of the shadow plays a crucial role in the shadow formation. Furthermore, this work has shown that placing a thin object directly on the PV module (as in prior art) to analyse the repercussions of partial shading, poses scientific shortcomings in the methodology.



(a) **(b)**

Figure 5.35. A detailed view of the shadow created by a ⌀8.0 mm thin object at **(a)** a distance of 25 cm and **(b)** a distance of 375 cm from the small-scale PV module.

This chapter refines the CSF score from Chapter 4, Section 4.2.5 by dividing shadow intensity into umbra and penumbra, for a more precise evaluation of the shadow's impact. Moreover, with reference to the observation noted in Figure 5.29, the power loss remains relatively constant for the small thin objects across the distance range with only a subtle drop in power for the ⌀8.0 mm thin object at 250 cm distance. The observed reduction in power at approximately 250 cm can be explained by Figure 5.32d, which illustrates that at this distance, the ⌀8.0 mm umbra region is replaced by the penumbra. Although the penumbra expands in size beyond this point, its intensity remains relatively constant up to a distance of 400 cm. This suggests that for thin objects measuring ⌀6.0 mm or less, the power loss remains largely unchanged over varying distances.

As the distance increases and the umbra region transitions into a penumbra, the decreasing intensity of the penumbra is nonetheless sufficient enough to compensate for the initial umbra effect observed at a distance of 25 cm. However, at a thickness of ⌀8.0 mm, where the thin object has a substantial size compared to that of ⌀2.8 mm thickness, the transition point between the end of the umbra and the onset of the penumbra marks a noticeable change. Shortly after this transition, a decline in power loss is observed, indicating that the penumbra is no longer effectively compensating for the umbra shadow as initially observed at 25 cm. This suggests that beyond a certain distance, the compensatory effect of the penumbra diminishes, resulting in a reduction in power output and therefore further power loss. Therefore, it is of particular interest to investigate whether this trend persists for larger thin objects to understand if the specific

distance at which the penumbra is no longer compensating for the umbra effectiveness is just an anomaly or a consistent trend. In the case of large thin objects, the shadows have a higher presence of umbra shadow whilst also noting that in Figure 5.29, power loss begins to decrease rather than remain constant throughout all distances.

To assess the behaviour of larger thin objects (⌀10.0 mm to ⌀16.0 mm in thickness), the analytical approach used in Figure 5.32 for smaller thin objects is replicated in Figure 5.36a-d. Moreover, the analysis maintains the interaction between shadow formation and the 31.0 mm wide quarter-cut single solar cell for the small-scale PV module as a reference.

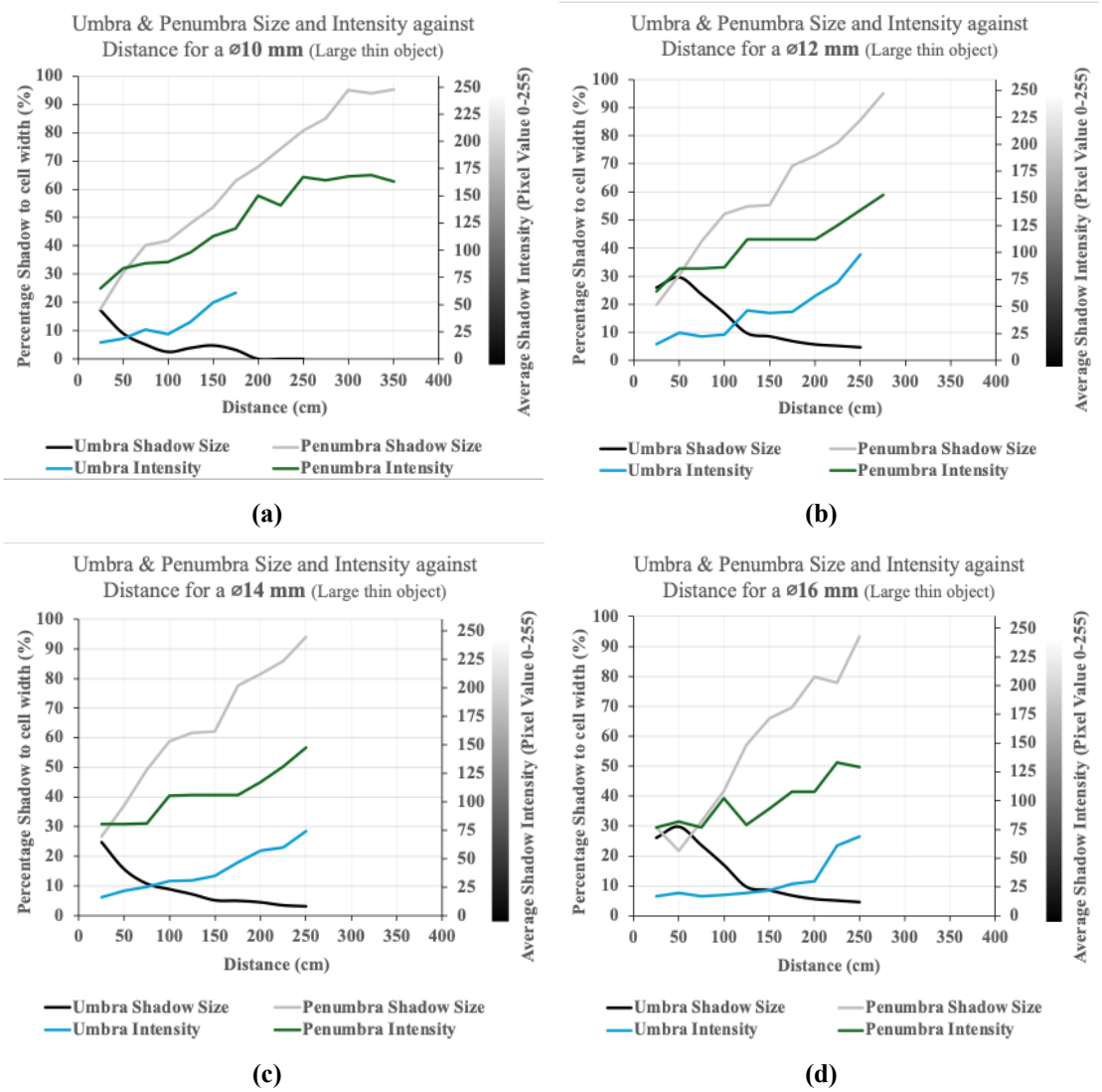


Figure 5.36. An illustration of the umbra and penumbra size and intensity results for the large thin objects. (a) ⌀10.0 mm, (b) ⌀12.0 mm, (c) ⌀14.0 mm, (d) ⌀16.0 mm

Initial observations demonstrated that as the distance increased, the size of the penumbra increased in size exhibiting a similar pattern to that of smaller thin objects, thus confirming the behaviour even across large thin objects. Similarly, the umbra shadow significantly diminished in size and became progressively less prominent with increased distance when umbra shadow is present. Notably, the penumbra shadow intensity demonstrated a gradual decrease in intensity, reaching a stable plateau at 250 cm distance for the ⌀10.0 mm objects shown in Figure 5.36a. However, this plateau effect was not visible in the range between ⌀12.0 mm and ⌀14.0 mm, due to the total shadow size exceeding the solar cell width before a clear umbra to penumbra transition could be observed. Consequently, the ⌀12.0 mm- ⌀16.0 mm range always maintained the presence of the umbra shadow up to the point of exceeding the solar cell's width and no penumbra-only cases were classified after the solar cell width was exceeded. This is evident since for this range of thicknesses (⌀12.0 mm to ⌀16.0 mm) in Figure 5.36b-d, the umbra shadow size still maintained its presence, whilst still retaining the same upward trend in penumbra size as was also the case for small thin objects.

Significant transitions in shadow characteristics occurred predominantly in the distance range up to 250 cm for both umbra and penumbra size and intensity for all the large thin object thicknesses outlined in Figure 5.36a-d. This range corresponds to the decreasing power loss observed in Figure 5.29 Section 5.3.1, where the power loss starts to decline indicating a change in the shadow effect on the PV module. This observation was not seen in the small thin objects as for most of the thicknesses, the power loss was retained throughout all the distances. To investigate further, the substantial power loss for the large thin object thicknesses can be attributed primarily to the high intensity of the umbra shadow, which exerts a significantly stronger effect on power output, despite its smaller size when compared to the penumbra. In this way, large thin objects up to a distance of 250 cm observed a strong presence of the umbra shadow which begin transitioning distinctively into a more diffused penumbra, resulting in a noticeable dip in shadow intensity and associated power output, particularly evident in the ⌀14.0 mm and ⌀16.0 mm as shown in Figure 5.36c and d and illustrated in Figure 5.37 for ⌀16.0 mm. Moreover, in contrast to the case of small, thin objects, where a stable power loss was observed in Figure 5.29 Section 5.3.1 and the increase in penumbra size effectively compensated for the reduction in intensity, this relationship does not hold for large, thin objects. In these cases, the decrease in umbra intensity and size diminishes the overall

power loss, and the corresponding increase of the penumbra region is insufficient to offset the sustained power loss at greater distances.

The strong presence of the retained penumbra shadow of the ⌀16.0 mm large thin object particularly at about a distance of 225 cm, produced a shadow nearly twice its own width, fully covering the solar cell, thereby leading to a substantial power loss of 39.83% of the original power output at control conditions.

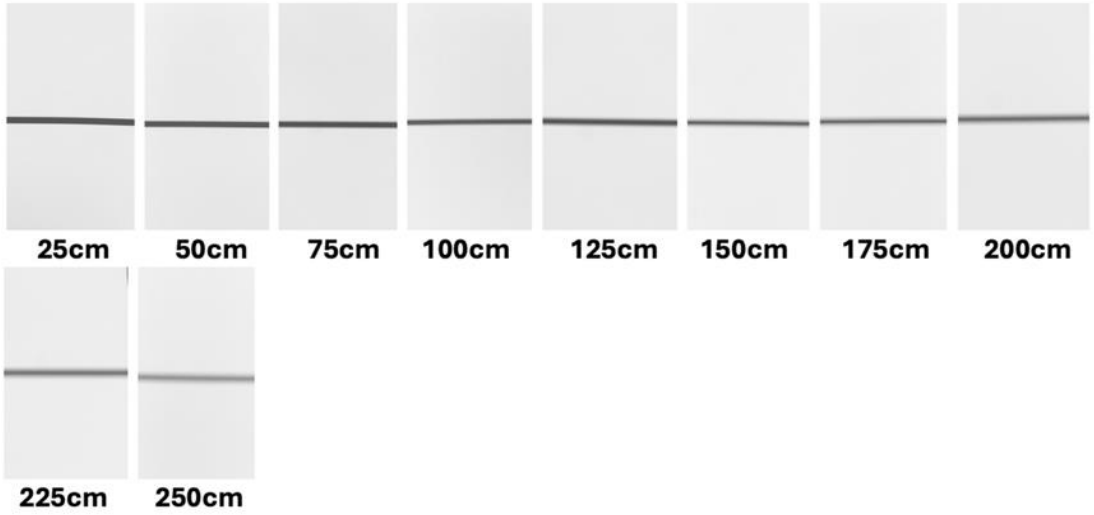


Figure 5.37. Image sample dataset illustrating image analysis performed on a large thin object (⌀16.0 mm)

The quantification data of the four key shadow formation factors that govern the shadow formation and presented in Figure 5.32 and Figure 5.36, exhibit minor trend imperfections in the resulting graphs. These discrepancies can be attributed to minor fluctuations in ambient light conditions, which were captured by the portable smartphone camera during image acquisition. Future improvements to ThinShadePV could incorporate the idealised shading profile model introduced by Teneta et al. [23], where the authors derived a mathematical formula based on geometrical analysis to determine the profile of umbra and penumbra as visualised in Figure 5.38. Although this model cannot be directly comparable with the findings in this section due to the significantly greater observation distances used (1000–4000 cm in [23]), Teneta's model [23] could be adapted to suit the distances used in this section (up to 400 cm). This model could than be incorporated in ThinShadePV to cross reference the detected umbra and penumbra size and intensity with the mathematical model and determine whether

the detection of the attributing shadow characteristics was coherent to the mathematical expectation.

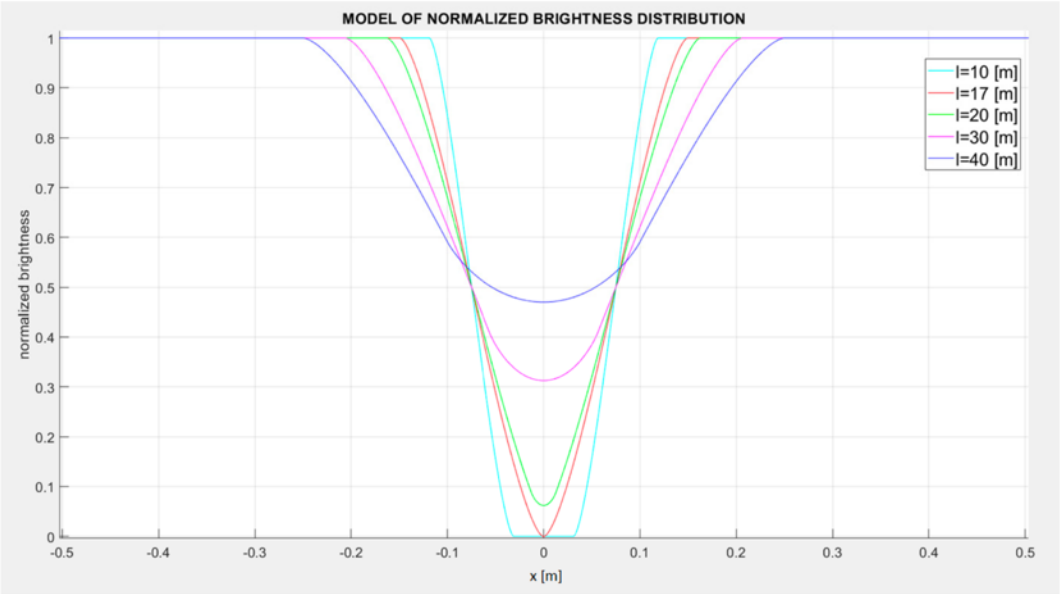


Figure 5.38. The model created by Tenata et al. [23] where the normalised brightness on the y-axis representing the intensity in this study is plotted against the (x) representing the size of the shadow.

Furthermore, while the relationship between the size and intensity of the umbra and penumbra has been well documented in this section, for ThinShadePV to serve as a reliable predictive tool, it is essential to first establish the quantifiable correlations between these factors and the power loss using the dataset outlined in this section and Section 5.3.1. Subsequently, a sensitivity analysis based on the trained Random Forest model will ensure that the prediction model reflects the relationships and dependencies identified in the dataset. Accordingly, the next section explores the quantifiable correlations between the four key shadow formation factors, along with the parent variables, distance and thickness, and their direct impact on power loss relative to an control scenario.

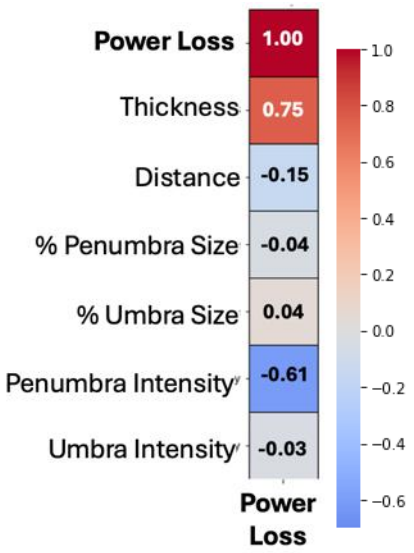
5.3.3 Correlation and Sensitivity Analysis of Factors Affecting Shadow Formation and Resulting Power Loss on the Small-Scale PV Module

This section presents the results of the Spearman correlation and sensitivity analysis based on the data outlined in Section 5.3.1 to explore the relationships between power loss on the small-scale PV module and key influencing variables: distance and thickness as parent variables (Figure 5.29 Section 5.3.1) and umbra size, penumbra size, umbra intensity, and penumbra intensity as attributing variables, influenced by the shading conditions and based on the data outlined in Figure 5.32 and Figure 5.36 in Section 5.3.2. In addition, a sensitivity analysis is carried out for each of the four attributing variables derived from the trained Random Forest regression model of ThinShadePV using the same data of Section 5.3.1 and the correlation analysis which quantifies the relative importance of the same variables in predicting power loss.

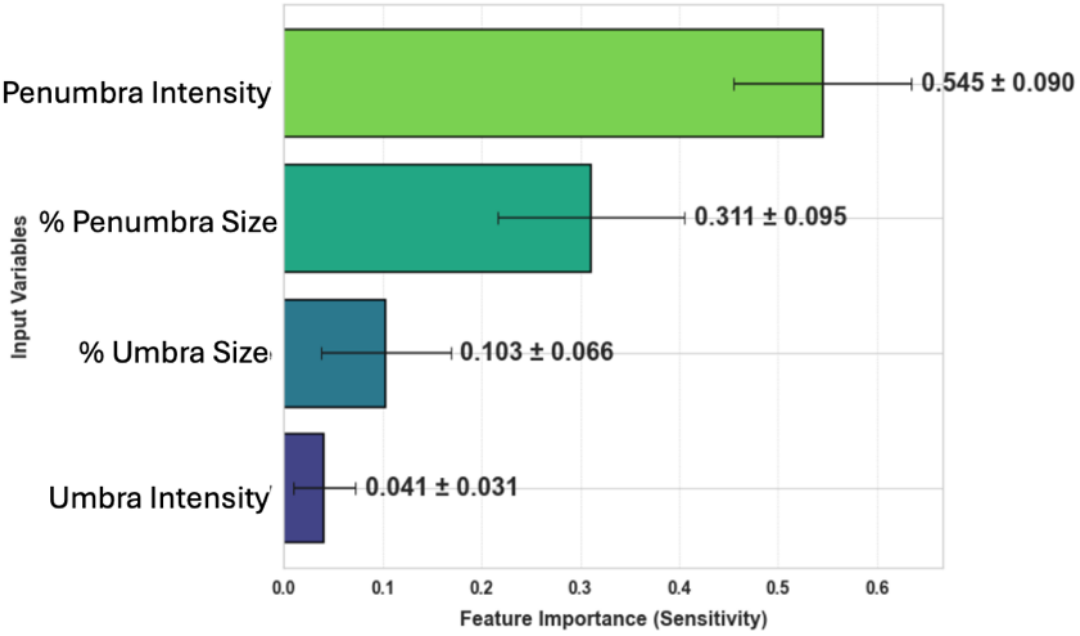
The Random Forest model was implemented and trained using the ThinShadePV script outlined in Appendix G. Specifically, a custom function *(train_random_forest2)* developed to load the experimental dataset of both small (⌀2.8 mm – 8mm) and large thin objects (⌀10.0 mm – ⌀16.0 mm) separately from an Excel database and train the model using the *RandomForestRegressor* class from the *sklearn.ensemble module* [259]. The model was trained using the four attributing variables outlined previously and the dependent variable of power loss. Moreover, the Random Forest model was configured with 100 estimators *(n_estimators=100)* and a fixed random state *(random_state=42)* to ensure result reproducibility as utilised by [260] and [261]. Once trained, this model *(rf_model_2)* was used as the basis for the sensitivity analysis, enabling the quantification of the relative influence of the parent variables on shadow characteristics and the power loss observed on the small-scale PV module. The uncertainty for each sensitivity feature importance value was derived from Appendix B.3 of the appendix and shown as error bars in Figure 5.29b and Figure 5.40b respectively.

The Spearman correlation analysis was carried out for small thin objects, producing the heatmap shown in Figure 5.39a. This revealed that thickness exhibits the strongest positive correlation with power loss, with a coefficient of 0.75. According to the interpretation metrics previously presented in Section 5.2.2.3 Table 5.4, this falls within

the ‘high correlation’ category, indicating a strong positive relationship. This entails that as object thickness increases, the power loss increases significantly which corresponds to the results presented previously in Figure 5.29 where the incremental increase in object thickness resulted in the constant increase in power loss. Penumbra intensity demonstrated a moderate negative correlation with power loss (-0.61), suggesting that higher penumbra intensity is associated with a reduction in power loss. Conversely, variables such as distance (-0.15), percentage penumbra size (-0.04), percentage umbra size (0.04), and umbra intensity (-0.03) all exhibited very weak correlations. Moreover, such low correlation values indicate that these factors have minimal correlation on the resulting power loss.



(a)



(b)

Figure 5.39. (a) Spearman correlation matrix heatmap **(b)** Sensitivity Analysis based on the Random forest model created for small thin objects (⌀2.8 mm – ⌀8.0 mm).

To complement the Spearman correlation, a model-based sensitivity analysis was performed using a Random Forest regressor, the results of which are shown in Figure 5.39b. Notably, similar to the Spearman correlation heatmap, the penumbra intensity emerged as the most influential parameter, with a feature importance score of 0.544. This aligns well with its moderate correlation, confirming its key role in the dependent variable of power loss. This is to expected since predominantly small thin objects have a high percentage of penumbra shadow due to the light being diffused

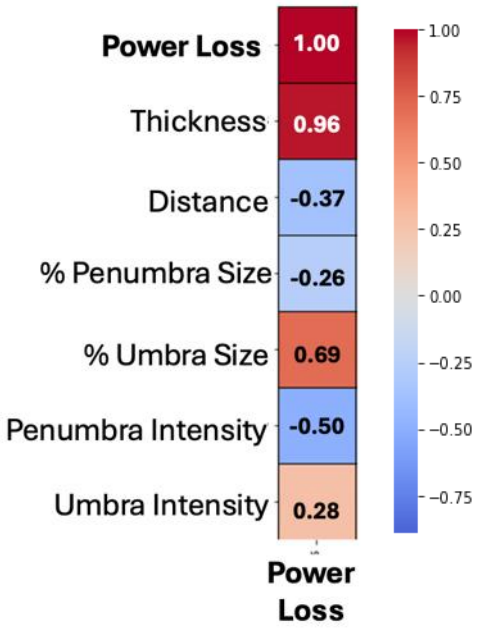
around the shading object. This aligns with the findings of the previous section, specifically in Figure 5.32.

Furthermore, percentage penumbra size was the second most important input, with a sensitivity score of 0.311. Interestingly, this parameter had shown only a very weak correlation in the Spearman analysis, suggesting that its influence is likely non-linear and thus not adequately captured by correlation alone. Percentage umbra size and umbra intensity were found to have lower sensitivity scores (0.103 and 0.041, respectively), indicating relatively minor influence on power loss corresponding with the correlation and image analysis previously denoted in the analysis conducted in Section 5.3.2, where the presence of umbra is limited for small thin objects.

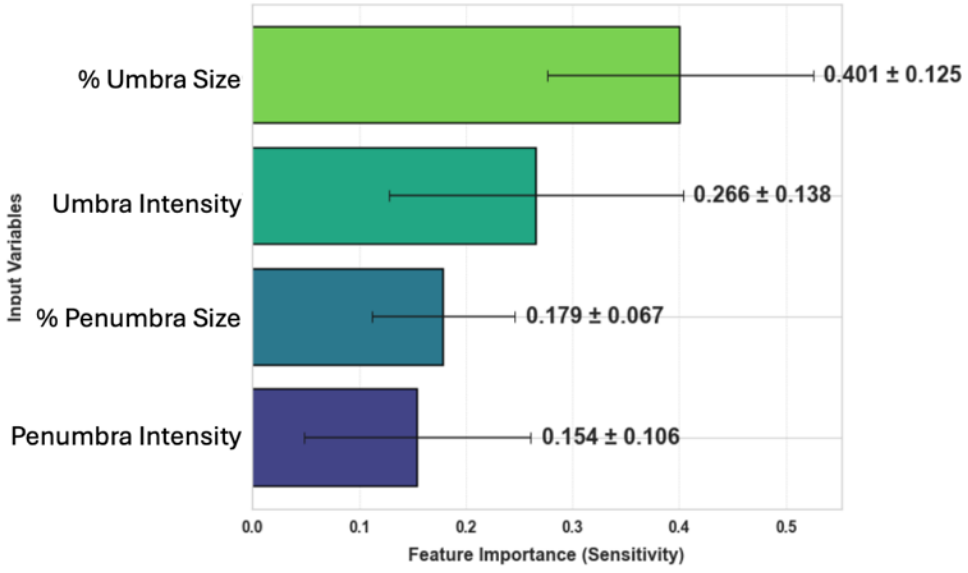
While the correlation analysis evidently demonstrates that the thickness of the thin object is the strongest parent variable, thickness and distance were not included in the sensitivity analysis of Figure 5.39b. This is due to the trained Random Forest not considering thickness as a variable factor but rather focusing on the varying effect of the shadow, a novelty of this research study. On the other hand, penumbra intensity was consistently identified as a dominant factor across both analytical methods, making it a critical variable for optimisation efforts. Moreover, the apparent weak correlation and relatively high sensitivity of percentage penumbra size highlights the limitations of relying solely on correlation measures, particularly in complex, non-linear interactions similar to the data outlined in Section 5.3.2.

A similar analysis to the one conducted for small thin objects was also repeated for the large thin object dataset compiled in Figure 5.29 Section 5.3.1 and Figure 5.36 in Section 5.3.2. The Spearman correlation results illustrated in Figure 5.40a reveal that thickness has a very strong positive relationship with power loss (0.96), similar to that shown for the small thin objects in Figure 5.39a. This result indicates that as the object becomes thicker, power loss increases substantially in a consistent manner. Another variable demonstrating a strong association is percentage umbra size (0.69), which falls into the moderate to high correlation range, implying that higher umbra coverage generally leads to increased power loss. This is to be expected and was also previously noted in Section 5.3.2 since the larger thin objects predominantly have a much higher umbra size percentage than smaller thin objects. On the other hand, penumbra intensity shows a moderate negative correlation with power loss (-

0.50), suggesting that higher penumbra intensity contributes to higher power loss. Variables such as distance (-0.37), percentage penumbra size (-0.26) and umbra intensity (0.28) showed weak negative correlations, indicating minimal influence on power loss.



(a)



(b)

Figure 5.40. (**a)** Spearman correlation matrix heatmap **(b)** Sensitivity Analysis based on the Random forest model created for large thin objects (⌀10.0 mm – ⌀16.0 mm).

The outcome of the sensitivity analysis based on the Random Forest training model illustrated in Figure 5.40b, offers complementary insights into the true predictive influence of each attributing variable. Unlike the small thin object scenario, where penumbra intensity dominated, the most influential variable for larger thin objects is percentage umbra size, with a feature importance score of 0.401. This confirms that umbra coverage has a significant non-linear influence on power loss in larger thicknesses. Umbra intensity also emerges as an impactful variable (0.266), which contrasts its relatively low correlation value, again highlighting the presence of non-linear effects not captured by correlation alone. This is similar to the behaviour of penumbra size in smaller thin objects. Moreover, percentage penumbra size and penumbra intensity have lower importance scores (0.179 and 0.154, respectively), suggesting more moderate contributions to model performance in this context.

The shift in dominant variables between small and large objects is notable. Penumbra intensity, while highly important for small thin objects, becomes less influential for larger thin objects, while percentage umbra size rises in prominence. The findings reinforce the value of combining correlation with sensitivity analysis, especially when seeking to interpret complex physical phenomena involving multiple interacting variables. For optimisation and design purposes, focus should be placed on controlling umbra characteristics, particularly coverage and intensity, when seeking to minimise power loss in large thin objects.

Importantly, the sensitivity analysis closely aligns with the correlation trends observed in the data, indicating that the trained Random Forest model captures the underlying relationships between input variables and power loss, including non-linear effects not evident through correlation alone. This agreement between the data and model behaviour supports the reliability of the model and justifies its use in predictive applications. However, to properly evaluate how closely ThinShadePV predicts power loss to real case thin object shading scenarios based on the trained Random Forest model, a validation process is required to assess the model's generalisability and performance on unseen data. Unseen data is data comprising intermediary thicknesses and distances lying between the object thickness and distance combinations that were not specifically measured. Nonetheless, through the combinational Random Forest

model of small and large thin objects, ThinShadePV is capable of predicting power losses with the performance metrics outlined subsequently in Section 5.3.4.

5.3.4 Validating the Performance of ThinShadePV in Real Case Scenarios.

The validation of ThinShadePV begins with assessing the performance metrics of the Random Forest training dataset to ensure the model has achieved an acceptable level of accuracy. Following this, the power loss results for 15 cases of thin object shading are compared to highlight variations in performance. Finally, both the improvements made to ThinShadePV and potential future improvements are presented.

5.3.4.1 Performance of the Training Dataset of ThinShadePV

The Random Forest model was trained using a comprehensive approach that combined the parent and attributing variables for both large and small thin objects into a single, unified thin object training set, to generalise different geometries more effectively across a wider range of shadow scenarios. The forthcoming evaluation will focus on utilising the first function of ThinShadePV named *'Existing PV on roof'*, (Figure 5.12). Nonetheless since the same Random Forest model was also utilised in Function 2 *'Design stage of PV system'* the forthcoming validation applies to both functions. The difference is that in Function 2, the user inputs the thickness of the shading object and its distance from the PV module rather than using an image of an existing shading scenario such as required in Function 1. Therefore, in the forthcoming section, the ThinShadePV trained model will be tested under real thin object scenarios.

As outlined in Section 5.2.3, 15 cases of thin object shading scenarios were considered, with each case transposed on the full-scale PV module. The thickness and distance combinations used were purposely chosen to encompass distances at increments of 25 cm and predefined thicknesses utilised in the training data. Furthermore, combinations that did not exactly match the ones used for training the Random Forest model were also

considered. In this way, the validation could also prove that the model also catered for cases which did not exactly match the training data set provided to the model.

To evaluate the performance of ThinShadePV, a Random Forest Regressor was implemented using a supervised learning approach [262], with the dataset split into 80% for training and 20% for testing similar to Osadolor et al. [263]. The model was trained on a dataset comprising the 104 cases of thin object shading scenarios in Section 5.3.1. In this case, the objective was to predict power loss as a percentage when compared to a control PV module setup, based on input features such as total umbra percentage, total penumbra percentage, umbra intensity, and penumbra intensity. Moreover, the metrics outlined in Section 5.2.2.4, R^2, RMSE and MAE are used as the performance metrics of ThinShadePV, with the results presented subsequently.

An RMSE of 5.76, an MAE of 4.53, and an R^2 of 0.862 were achieved, showcasing a relatively high level of predictive accuracy. The RMSE of 5.76 indicates that, on average, the model's predictions deviate from the actual power loss values by approximately 5.76 % power loss. This value will be further analysed in a comparison between the predicted power loss and the actual measured power loss for a series of thin object shading scenarios later in this section. The MAE of 4.53 provides a more interpretable measure of predictive performance, revealing that the model's estimates typically differ from the true values by about 4.53 % points across the training dataset. This low MAE value further reinforces ThinShadePV's training model consistency in predicting the power loss from thin object shading scenarios. Most notably, an R^2 of 0.862 suggests that 86.2% of the changes in the dependant variable (power loss) can be explained by the input features based on the attributing variables. This high R^2 indicates a strong correlation between the four shading characteristics of total umbra and penumbra size and intensity, and the resulting power loss, implying that the model is effectively learning the underlying relationships. However, the moderate error margins and limited sample size suggest that while the model exhibits good performance, its generalisation capability could be improved. Future research must focus on increasing the dataset size as will be further explained in Chapter 7 Section 7.4.

5.3.4.2 Comparative Validation between Power Loss Predicted by ThinShadePV and the Measured Power Loss

The 15 thin object shading cases outlined in Table 5.6 of Section 5.2.3, were recreated on the vacant roof area previously visualised in Figure 5.19 using the full-scale PV module as the PV source and the thin objects as the source of shading. For each case, an image was captured and processed using ThinShadePV to estimate the predicted power loss. The tool also identified the umbra and penumbra regions, with an example of this detection shown for Case 14 (A ⌀40.0 mm thick drain pipe situated at a distance of 215 cm) in Figure 5.41.

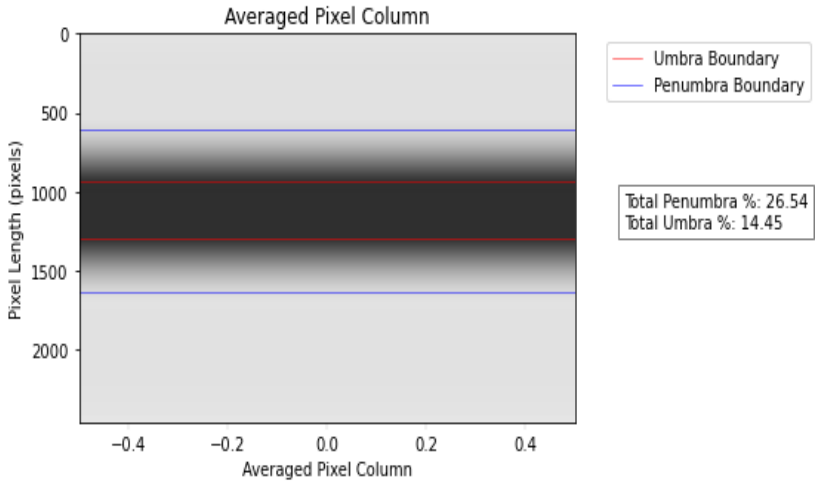


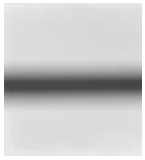
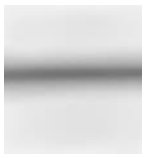
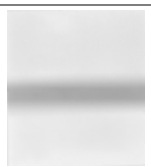
Figure 5.41. Example output from ThinShadePV for Case 14, showing automated detection of umbra and penumbra. The red and blue lines represent the detected shadow boundaries, while the total umbra and penumbra areas are displayed on the right-hand side of the image.

To illustrate the comparative analysis between predicted and measured power loss, Table 5.7 was created. The first column lists the different shading cases, while the second column provides a preview of the corresponding image capture used as reference. Moreover, the four subsequent columns were derived from the predicted Random Forest training model based on the image input of each case. The third and fourth columns illustrate the umbra size and penumbra size which were derived in proportion to the solar cell width. The percentage of umbra and penumbra shadow coverage was calculated based on the total area of the solar cell. In the training model, a 31.0 mm × 125.0 mm cell was used, corresponding to the quarter-cut configuration of the small-scale PV module. For the large-scale PV module, which utilised full-size 156.0 mm × 156.0 mm cells, the same proportional shadow coverage was maintained to ensure consistency in the comparative analysis. Moreover, the umbra and penumbra

intensity, expressed as pixel intensity values between 0-255, was also extracted from the image captured for each case. Furthermore, from the predicted four variable factors extracted from the input image, the predicted power loss (%) is denoted in the red column. This value is comparable to the blue column, where the measured power loss was derived from the actual power loss measured using the Seaward I-V analyser and the R_{load} correction point extrapolated as shown previously in Figure 5.27. The final column of Table 5.7 demonstrates the change in percentage power loss between the predicted and the measured power loss which illustrates the discrepancy observed.

Table 5.7. Validation results between predicted power loss generated by ThinShadePV denoted in red and the measured power loss on the full-scale PV module denoted in blue.

Case Number	Image capture reference	Umbra Size (%) *1	Penumbra Size (%) *1	Umbra Intensity (pixel intensity) *2	Penumbra Intensity (pixel intensity) *2	Predicted Power Loss (%)*3	Measured Power Loss (%)*4	Δ (%)
1		5.07	4.35	140	185	2.42	4.13	**-1.71**
2		0	8.98	N/A*5	201	1.68	1.32	**0.36**
3		2.56	2.28	103	155	7.77	7.93	**-0.16**
4		1.29	20.42	83	146	7.12	7.48	**-0.36**
5		0.89	16.08	138	171	5.32	4.50	**0.82**
6		0	22.56	N/A	200	1.36	0.95	**0.41**

7		2.26	26.41	76	140	13.96	13.94	**0.02**
8		3.30	27.72	71	138	16.67	13.14	**3.53**
9		6.37	25.65	122	181	6.37	7.16	**-0.79**
10		6.40	25.65	122	181	5.44	6.05	**-0.61**
11		0	21.17	N/A	192	1.71	1.31	**0.40**
12		15.73	2.50	46	162	20.25	21.81	**-1.56**
13		28.88	5.46	52	133	31.43	27.95	**3.48**
14		14.45	26.54	49	132	29.69	26.84	**2.85**
15		45.82	25.19	75	155	29.67	29.10	**0.57**

Notes:

*[1] - The umbra and penumbra size was calculated based on the total area of the 156.0 x 156.0 mm solar cell

*[2] – The umbra and penumbra intensity was given a value between 0 – 255 representing the pixel value range. The umbra intensity represents the constant intensity nature and the penumbra intensity is given as the average single intensity of the varying range of pixels in the penumbra shadow.

*3 – The predicted power loss is based on Function 1 of ThinShadePV using the fixed R_{load} correction factor expressed as a percentage difference from the MPP at control conditions.

*4 – The measured power loss corrected to STC by the Seaward PV200 based on a fixed R_{load} at MPP at control conditions. Moreover, the measured power loss is also corrected based on the time, date, altitude using the sun correction factor previously outlined in Chapter 4 Section 4.2.2.

*5 – N/A refers to the cases where no umbra shadow was detected. Therefore, the intensity value of the umbra cannot be given a quantifiable measure.

To visualise the difference between the predicted power loss and the measured power loss, Figure 5.42 was compiled, utilising the same colours opted for in Table 5.7 to represent both scenarios in separate comparative bar graphs. The uncertainty for each power loss value was derived from Appendix B.2 of the appendix and shown as error bars in Figure 5.42. As a value representation, the average uncertainty of all cases was calculated to be ±1.82% for the measured power loss.

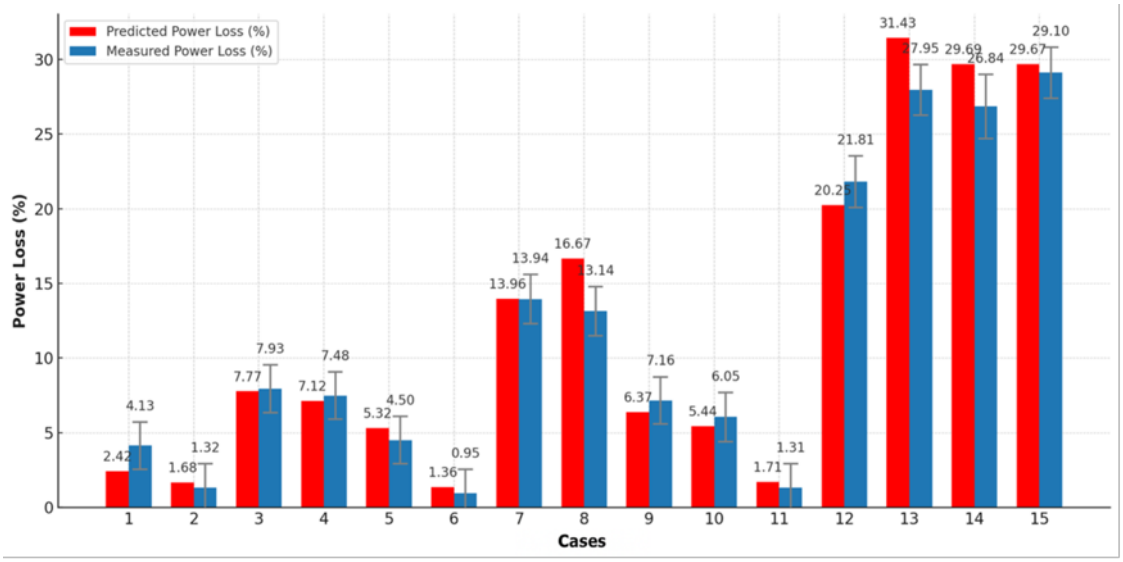


Figure 5.42. A bar graph comparing the predicted percentage power loss visualised in red and the measure percentage power loss visualised in blue.

Visually, for each of the 15 cases, the percentage power power loss between the predicted and the measured method was relatively coherent. No significant anomalies were observed, and the discrepancy between the predicted and measured power loss did

not consistently indicate a systematic overestimation or underestimation by either method. Thin object shading with minimal shading impact, namely those producing a light shadow with impact less than 2% power loss, tended to be more relatively coherent than when the shadows were larger in size. This is because larger objects have more complex shadows being quantified by ThinShadePV.

To evaluate whether there is an agreement between the predicted and measured power loss values, this study employs Bland–Altman analysis. This statsitical analysis facilitates the assessment of any systematic differences and quantifies the range within which most differences between the predicted and measured values lie, thereby offering a comprehensive evaluation of their agreement. The approach is consistent with that used by Shareef et al. [264], who applied this approach to assess the performance of a Random Forest model, as well as Kumar et al. [265], who used the Bland–Altman significance test to compare predicted and measured MPP values from their model. The Bland–Altman method evaluates consistency between two quantitative measurement techniques by plotting the mean of each observation pair against their difference. This visualisation reveals both systematic bias and the degree of error dispersion. The 15 cases analysed are plotted and presented in Figure 5.43.

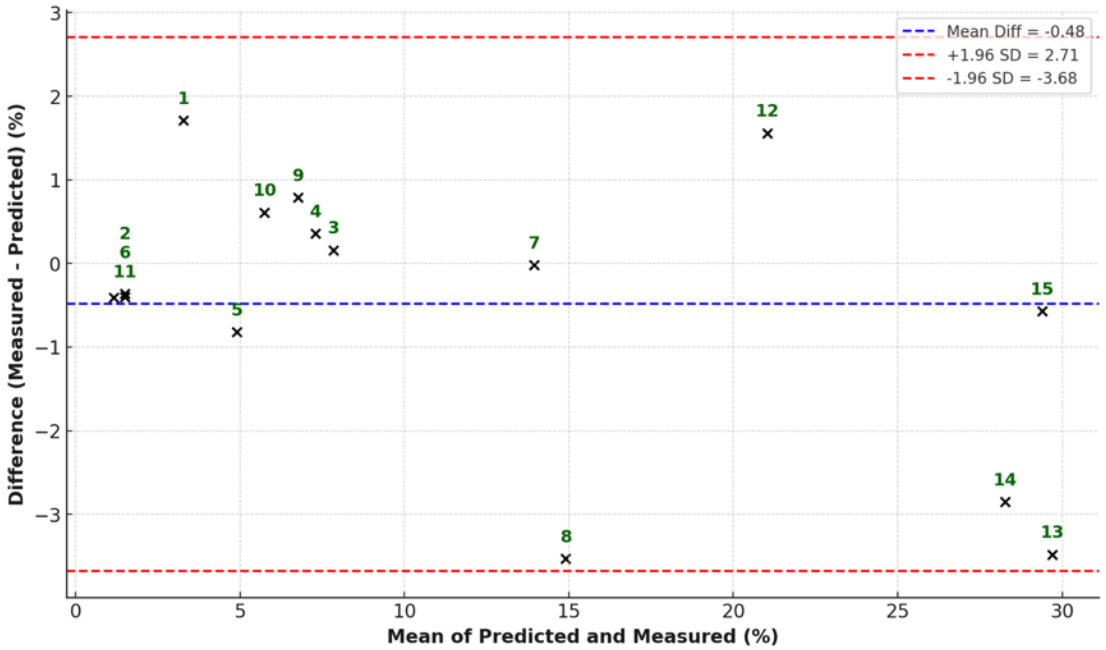


Figure 5.43. Bland–Altman plot showing the agreement between predicted and measured percentage power loss. The x-axis represents the mean of the predicted and measured values, while the y-axis shows their difference (measured minus predicted). Each data point is labelled with an "×" to indicate the corresponding case.

The results of the Bland-Altman analysis visualised in Figure 5.43 demonstrate the mean difference between predicted and measured power losses which was calculated to be -0.48%, indicated by the horizontal blue dashed line in Figure 5.43. Moreover, by using the standard z-score of 1.96 derived by Myles et al. [266] at which 95% of values are expected to fall. The standard deviation of the differences between measured and predicted power loss values was calculated as 1.63%, based on the 15 paired cases. This was obtained by computing the squared deviations of each difference from the mean bias (0.48%), averaging them over (n−1) degrees of freedom, and taking the square root of the result. The resulting limits observed an agreement from −3.68% to +2.71%, as indicated by the horizontal red dashed lines in Figure 5.43 respectively. Interestingly, the deviation range noted between the measured and the predicted power loss is slightly better than the RMSE of 5.76% observed in the training model dataset.

The observed limits encompassed all 15 data points, suggesting that the predictive model (trained on the small-scale PV module using ThinShadePV) maintained an acceptable level of agreement with the actual power loss measurements on the full-scale PV module. Moreover, the Bland-Altman plot revealed greater variability in prediction errors at higher power loss values, confirming the visual observation previously made. This behaviour may be attributed to more complex thin object shadows observed in the input image, where a greater amount of pixel extraction is required to determine the umbra and penumbra shadow size and intensity. This trend indicates an area where further model refinement may be beneficial through the expansion of the dataset of thin objects and also a potential improvement in greyscale conversion such as a 16 bit conversion rather than the 8-bit conversion. Having said that, the Bland-Altman analysis confirms that the ThinShadePV predictive model offers statistically and practically acceptable agreement with the measured data, while also highlighting the importance of model improvements required, especially for complex shading scenarios.

5.3.4.3 Improvements Implemented to ThinShadePV during Application and Validation Process

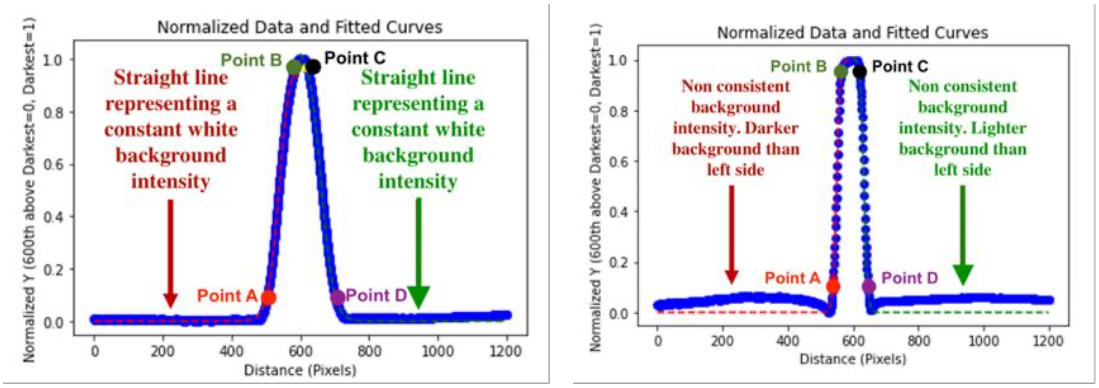
During the initial validation of ThinShadePV, it became evident that, although the background intensity is theoretically assumed to be a uniform white, practical variations such as the angle at which images were captured led to minor inconsistencies in

background whiteness. Through the validation process, it was determined that both the camera angle and the surrounding environment influence the intensity of the background. To illustrate this observation, Figure 5.44 presents a representative example.



Figure 5.44. An example image of the inconsistent upper and lower background intensity

Upon initial visual inspection, differences in brightness values between the upper and lower regions of the image were not immediately apparent. Therefore, the *'Normalised Data and Fitted Curves'* chart generated by ThinShadePV was consulted for further analysis. As a comparative baseline, Figure 5.45a displays an idealised scenario in which the lower horizontal sections of both the left and right sigmoidal curves are flat, indicating a uniformly white background. In contrast, Figure 5.45b reflects a more practical case, showing an uneven curvature in the background region between the two sigmoidal curves. The left bottom horizontal portion of the sigmoidal curve in Figure 5.45b, indicated by the red arrow, exhibits a notably higher curvature compared to the right side, indicated by the green arrow, which remains relatively flat. This disparity clearly suggests that the upper region of the image (corresponding to the left sigmoidal curve) in Figure 5.45b, has a background that is darker than the lower region (represented by the right sigmoidal curve).



(a) **(b)**

Figure 5.45. A comparative visual **(a)** representing the ideal background intensity where the brightness level is consistent for both left and right sigmoidal curves **(b)** representing inconsistent left and right background intensity.

The penumbra start points, denoted as Points A and D, were initially established by defining the first 0.05 of the normalised pixel intensity range as representative of background intensity. However, as observed during the validation phase of Section 5.3.4.2, background intensity was not always uniform. In some cases, the darkest regions of the background were located very close to the penumbra boundary, which while acceptable, raised concerns under conditions of greater intensity variation. Specifically, there was a risk that the darkest background pixels could extend beyond Points A and D, leading to a misclassification of background as penumbra shadow. To address this, and as outlined in Section 5.2.2, the methodology was improved by redefining the 0.05 threshold. Instead of applying it from the lightest pixel of the image, the threshold was revised to be measured from the darkest horizontal background of the sigmoidal curves. This adjustment ensures more accurate isolation of the penumbra region, even in cases where background intensity varies significantly, minimising the risk of background intensity pixels being misclassified as part of the penumbra shadow.

5.3.4.4 Future Improvements to ThinShadePV

While the power loss data was successfully derived, one must note a limitation for this dataset. The power loss data derived in Figure 5.29 for each thin object shading case applies solely to PV sources using monocrystalline technology, chosen to align with prevalent commercially available cell technology and methodologies for studying

partial shading, similar to those in [138] and [25]. The decision to opt for monocrystalline PV modules was taken to ensure the study's applicability to commercially common PV technology, offering findings that are adaptable to other PV modules for broader research applications. While this control ensures the clarity of the data regarding the effects of object thickness and distance, it does not fully capture the variable conditions of real-world settings. Future research could employ the same methodology under different environmental conditions and times of day. This approach would have improved the dataset for ThinShadePV, by providing a broader perspective on how these factors impact PV performance across various shading scenarios.

In Section 5.3.2, reference was made to the rate at which the sizes of the umbra and penumbra, expressed as percentages, change with respect to distance, measured in centimetres. A potential improvement to ThinShadePV could involve determining the curve of best fit for this relationship, thereby enabling the calculation of the rate of change as a percentage of umbra or penumbra per centimetre. This functionality would allow researchers inputting new data into ThinShadePV to more accurately analyse and quantify the rate of change, facilitating a more rigorous and data-driven assessment.

An additional improvement of ThinShadePV lies in increasing the R^2 value, leading to a more accurate model prediction. To do so, it is essential to expand the dataset significantly. The current model was trained on 104 cases, which serves as a solid foundation but is limited in its ability to generalise across a wider range of real-world scenarios. For ThinShadePV to reach a commercially viable level of accuracy and robustness, the dataset must be extended to include a broader variety of distances, material thicknesses, object position on a PV module, and environmental conditions. This will enable the model to better capture the underlying patterns and variability present in thin object shading, leading to more reliable and accurate predictions across diverse use cases. Moreover, by expanding the dataset, one needs to consider also the type of prediction model training used. For this study, Random Forest was proven as an effective prediction ML algorithm given the type and size of dataset outlined in this thesis. However, as the dataset of ThinShadePV is broadened by other researchers, it would be good to simultaneously consider XG Boost as an option to train the data and perform a comparative analysis on the performance of each model. XG Boost provides

faster training speed and computational efficiency through optimised data handling, making it advantageous for large scale application.

ThinShadePV was developed using libraries from available Python packages such as *easygui*, *tkinter*, *matplotlib, cv2 FigureCanvasTKAgg, mpimg* and others that can be found in the first 19 lines of the ThinShadePV code in Appendix G. To further improve ThinShadePV and reach full commercialisation, the current GUI should be upgraded from the basic GUI and visualisation libraries like *easyGUI, tkinter*, and *matplotlib* should be revised to more modern GUI frameworks such as *Ploty and Ploty-Resembler* [267] and *Seaborn, Bokeh, Altair, and ggplot* as demonstrated by Addepallu et al. [268]. These libraries provide interactive dashboards and improve the GUI functionalities. Adding these GUI abilities to the existing ThinShadePV Python code would improve visual appeal, usability, and interactivity, offering sleek, responsive designs, and advanced features like drag-and-drop, real-time plotting, and animated transitions, capabilities. Moreover, framework GUI design libraries such as PyQt and PyQT5 [269], [270], offer polished interface designs that align with contemporary user expectations, that elevate the overall user experience. Furthermore, adopting frameworks like Kivy used by [271] and [272], introduce the possibility of cross-platform deployment, including on Android and iOS, enabling the current desktop-based ThinShadePV to be transformed into a mobile application. This would allow ThinShadePV to be accessible and convenient for field use. Mobile functionality would allow users of ThinShadePV to import images directly from their device's camera roll, streamlining the workflow for the user to predict the power loss at any given thin object shading scenario. This mobile adaptability not only modernises ThinShadePV but greatly expands its reach and usability in real-world applications.

5.4 Conclusion

The purpose of the chapter was to answer RQ.2 outlined below:

RQ.2 - How do variations in thin object shading characteristics such as shadow size and intensity based on distance and object thickness correlate with power loss on PV

modules, and can these parameters be used to effectively predict power output using image-based analysis?

The literature review in Chapter 3 highlighted a gap in existing research, where shadow characteristics are primarily defined by size. This study addressed that limitation by incorporating shadow intensity and differentiating between umbra and penumbra, particularly in the context of thin object shading.

The first part of RQ.2 was addressed by quantifying 104 cases of thin object shading from different sized objects at incremental distances, in Section 5.3.1, later used as training data. The analysis showed that as the distance between the shading object and PV module increases, umbra size and intensity decrease. This results in an increase in the size of the penumbra with lower intensity, replacing the umbra entirely for smaller objects and retaining the loss in power up to around 275 cm. At distance higher than 275 cm, a decrease in power loss is noted, where the penumbra shadow can no longer retain the same effectiveness. This entails that for small thin objects (2.8 mm – 8 mm), up to around 275 cm distance, the loss in shadow intensity is compensated by the increase in shadow size, resulting in retaining a similar power loss compared to 25 cm distance. However, this statement does not hold upwards of 275 cm distance since the power loss decreases due to the shadow (mostly penumbra) is very light in intensity. For larger objects, the umbra remains present over longer distances and significantly contributes to power loss, as the increased size of the penumbra cannot fully offset the diminishing umbra beyond around 175 cm distance.

In Section 5.3.3, using Spearman correlation, object thickness had the strongest positive correlation with power loss, while distance had a weak correlation across object sizes. For small thin objects, penumbra intensity emerged as the highest correlation attributing factor on power loss, whereas for larger thin objects, the size of the umbra shadow was the most influential. Random Forest sensitivity analysis confirmed this, assigning the highest importance to penumbra intensity (54.5%) for small objects and umbra size (40.1%) for large thin objects.

The second part of RQ.2 was addressed in Section 5.3.4, where ThinShadePV, an image analysis-based tool was developed to predict power loss from an input image of a thin

object shadow case. The effectiveness of ThinShadePV in predicting power loss was validated through direct comparison with measured values. The model demonstrated a strong coefficient of determination (R^2) of 0.862 with the training dataset. Furthermore, the Bland-Altman analysis showed that the predicted power loss values varied within a range of −3.68% to +2.71%, thereby validating the accuracy of ThinShadePV for these horizontal shading cases.

In this chapter, evidence has been presented to highlight the critical role of penumbra shadows in the performance of PV modules. Although penumbra shadows are characterised by relatively low intensity, their influence must not be overlooked. The findings demonstrate that, despite their reduced intensity, penumbra shadows exert a significant impact due to their larger spatial coverage. This compensatory effect demonstrates the necessity of considering penumbra shadows when a PV source is under thin object shading conditions. Consequently, the following chapter will focus exclusively on the penumbra shadow, examining its impact in isolation and evaluating whether its behaviour aligns with the simplified representations commonly found in existing literature.

Chapter 6 The Penumbra Shadow Representation

6.1 Introduction

The results presented in Chapter 5 demonstrate that attention should also converge towards penumbra shadow on its own, not merely as a byproduct of partial shading. This observation lies in the findings, which have demonstrated that penumbra shadows become lighter in nature as the shading object moves away from the surface of the PVs, causing a reduction of the power loss impact on PVs. Nonetheless, exclusive penumbra shadows characterised by a gradual decrease in light intensity, have not been extensively investigated in their isolated state from the umbra shadow. This is due to many studies classifying penumbra as a "boundary" [82, p. 1237] or of a "diffused nature" [82, p. 1236], instead of as a detrimental part of a shadow on a PV source. However, the definition of penumbra shadow has been interpreted in multiple ways by different scholars. Authors such as Murali et al. [63], have depicted the penumbra as having a constant-intensity as seen in Figure 6.1a. This definition of penumbra is often intended for visual simplification only, as a true penumbra features a gradual transition in intensity towards the non-shaded region, "no shadow", as in Figure 6.1b. Indeed, Dendrinos [182], has presented penumbra shadow as having a gradient realistic effect such as that captured in Figure 6.1b [258].

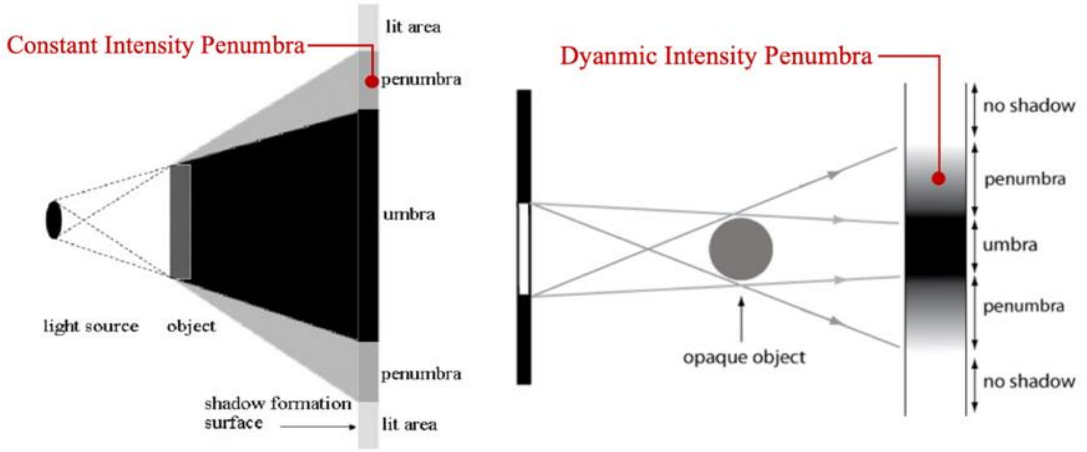


Figure 6.1. (a) The principle of shadow formation indicating umbra and penumbra where penumbra is presented as having a uniform grey intensity value, rather than a gradient effect [63] **(b)** A representation of umbra and penumbra shadow with penumbra being shown as a varying-intensity penumbra shadow [258].

This chapter therefore aims to investigate whether the gradient characteristics inherent to the penumbra region (as defined by Dendrinos [182] and Ramanath et al. [273]) can be represented instead by simply using a shadow of constant-intensity as interpreted by Muali et al. [63]. This will aid in evaluating the scientific validity of the assumption that a penumbra with gradient characteristics, known as varying-intensity penumbra, can be approximated to a single, uniform intensity value. This is mostly applicable to thin object shading since Chapters 4 and 5 have shown substantial complex shadow formation when compared to those found in literature dealing with hard shading or placing an opaque object on the PV module to mimic shading conditions.

Moreover, in order to answer RQ.3: 'In the absence of an umbra shadow, can the impact on a PV module of a penumbra shadow be replicated by using the average constant-intensity value of the corresponding varying-intensity penumbra shadow?', the following hypotheses are proposed:

- **Null Hypothesis (H_0):** There is no statistical significant difference in power loss between penumbra as a varying-intensity shadow and penumbra as a constant-intensity shadow.
- **Alternative Hypothesis (H_1):** There is statistical significant difference in power loss between penumbra as a varying-intensity shadow and penumbra as a constant-intensity shadow.

To elucidate the specific shadow characteristics examined in this chapter and to clarify the two shadow forms, Figure 6.2a starts by demonstrating an image of a penumbra-only case at substantial distance from the PV source. This shadow case shall be referred to as 'varying-intensity penumbra shadow'. In contrast, the corresponding average intensity of the varying-intensity penumbra shadow of Figure 6.2a , shall be termed as 'constant-intensity shadow' and is visualised in Figure 6.2b. The methodology and the main results of this chapter and RQ.3 have been published in the peer-reviewed journal MDPI Applied Science [230].



(a) **(b)**

Figure 6.2. (a) The formation of a sample varying-intensity shadow by a thin sample object. **(b)** the corresponding constant-intensity, bearing the same overall size and average intensity.

The scientific work presented up to Chapter 5, has so far involved casting shadows directly onto the PV module using thin objects and analysing their relationship and correlation between attributing variables and power loss. In contrast, this chapter focuses on replicating penumbra-only shadow cases, similar to that shown in Figure 6.2a, using a controlled method to achieve, constant-intensity shadow. This approach replicates the varying-intensity while preserving the key shadow characteristics of shadow size and light attenuation. To clarify, shadows such as those in Figure 6.2a depicting a varying-intensity penumbra-only shadow, will not use thin objects as a subject to create the shadow, but shall opt for alternative materials capable of attenuating light until the final shadow is comparable to Figure 6.2b. The justification of the material used will be outlined in the subsequent Section 6.2. The goal is to evaluate how well these constant-intensity shadows, created using alternative light-attenuating materials rather than physical thin objects, can replicate the PV performance of varying-intensity penumbra shading.

6.2 Materials and Methods

This section outlines the methods and materials chosen specifically to replicate the varying-intensity penumbra-only shadow. Section 6.2.1 focuses on the appropriate material selection, which was chosen based on an analysis of several options outlined. This is followed by a comprehensive description of the setup conditions in Section 6.2.2. Moreover, Section 6.2.3 quantifies the intensity associated with each of the chosen material grade while Section 6.2.4 presents the method used to directly compare the varying-intensity penumbra with the constant-intensity shadow.

6.2.1 Choosing the Appropriate Material to Replicate a Varying-Intensity Penumbra-Only Shadow

A penumbra is formed when an opaque object partially blocks light from an extended source [274]. Unlike the umbra, which represents total shadow, the penumbra is a region of partial shadow. This effect cannot be produced using a point light source, as that would result only in an umbra. Moreover, since the penumbra shadow gradually transitions from dark to light intensity, the material chosen to replicate the penumbra must be translucent to allow partial light transmission and form a non-black shadow. Moreover, since Gabrijelčič at al. [59] denote a shadow as the absence of light, the material chosen must also be able to reduce the light at a relatively constant manner, according to the intensity of the shadow. This should be done, in particular, throughout the wavelengths of the monocrystalline Si bandgap since this study will analyse the effect on a PV source.

Various translucent materials have been explored for their light transmission, although not necessarily directly in the field of PVs. Serrano et al. [275] denote that traditional substrates such as clear glass offer high visible light transmittance. However, clear glass falls short in reducing light systematically without any additional coatings due to its limited diffusive capacity and poor control over spectral filtering in its raw state. Moreover, Duarte [276] found that clear glass transmitted 74.3% of the source lighting, while tinted and laminated glass can significantly reduce UV radiation. For example, green glass, was found to fully block Ultraviolet A (UVA) wavelengths whilst blue-tinted glass may transmit only 56.8% of the source lighting [276]. However, the amount of light transmittance through glass all depends on the material and composite chosen, introducing spectral mismatch, especially when applying tinted layers. In addition to glass material, Spitz et al. [277] also mentions acrylic polymers, particularly UV-transmitting (UVT) type as a potential translucent material of choice. However, these type of materials have the tendency of suffering degradation in UV transmittance upon prolonged exposure to sunlight, with measurable losses occurring after only several hours, thereby not suitable as a material to constantly reduce light across the wavelengths required.

According to Simonot et al. [278], accurately characterising the optical and visual properties of translucent materials as a function of their shape and thickness remains a significant challenge in scientific research, owing to the difficulty in maintaining a consistent spectral distribution of the transmitted light. One sector that relies extensively on translucent materials and has achieved a high level of engineering precision in controlling light transmittance is photography, in particular the use of photographic filters, engineered for controlled light modulation. Furthermore, the calibrated nature of photographic filters provides the precision and repeatability required for a scientific use.

Among the various photographic translucent filters available, absorption filters are described by Kalyani [279] describes these filters as compounds that consume certain wavelength of lights and transmit others. Thus, they were deemed unsuitable for replicating the penumbra-only shadow transposed on the PV module. This is due to such filters altering the spectral composition by absorbing only specific wavelengths [279]. In the context of this chapter, the focus is specifically on penumbra-only shadows, which, by nature, uniformly attenuate light across all wavelengths due to the partial obstruction of the light source. Given that a shadow represents a reduction in overall light rather than selective wavelength absorption, absorption filters were deemed unsuitable for this study. Likewise, colour compensating and balancing filters, which are designed to adjust RGB colour balance and colour temperature, were not considered appropriate. This is because their primary function is to modify spectral composition rather than reduce light intensity uniformly without introducing chromatic shifts [280].

Optical-grade glass filters and coated polymer filters, such as neutral density (ND) and graduated ND filters, offer standardised and calibrated attenuation across a vast spectrum of light, specifically focusing on visible light (380 nm – 700 nm). Heron et al. [281] defined ND filters as being capable of reducing the intensity of light without changing the colour composition of the original object. These filters are manufactured to strict tolerances, ensuring spectral neutrality and stability over time. Their ability to produce consistent, predictable light transmittance makes them superior to other preceding translucent materials outlined in this section.

Two main types of ND filters are commercially available: constant transmittance filters, which uniformly reduce light across their entire surface (as illustrated in Figure 6.3a), and graduated ND filters, shown in Figure 6.3b. Graduated ND filters feature a transition in light intensity, ranging from full density (black, pixel value 0) to no density (white, pixel value 255), typically positioned at the upper and lower portions of the filter. This gradient closely resembles the varying-intensity profile of a penumbra shadow. Even though the graduated ND filters are suitable to mimic penumbra shadow, the aim of this chapter is to determine whether the average constant-intensity of the penumbra shadow can be utilised to simplify the varying-intensity penumbra shadow. Therefore, instead of opting for graduated ND filters, ND filters having a single constant-intensity were deemed more suitable for the investigation conducted in this chapter.

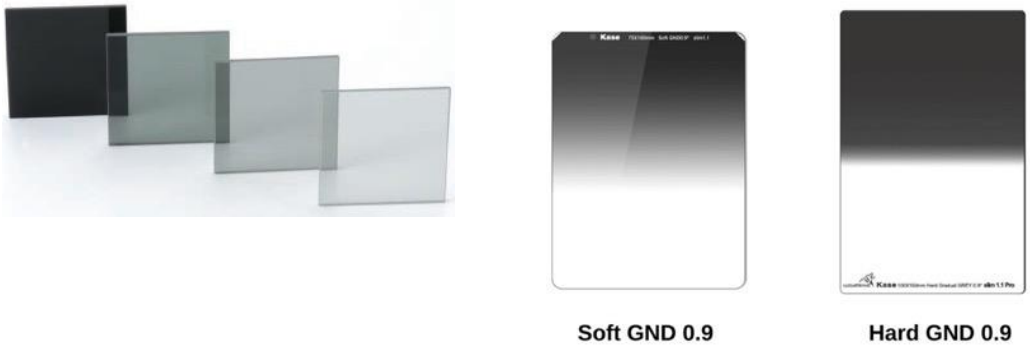


Figure 6.3. (a) A constant transmittance light ND filter [282], **(b)** An ND filter representing a graduated light transmittance [283].

In a 2024 review published by Willey [284], only eight scientific publications were identified as specifically focused on the development of ND filters. In his concluding remarks, Willey affirmed that ND filters exhibit consistent wavelength-independent attenuation, particularly between the 400 and 1000 nm range. This spectral range closely aligns with the effective response window of crystalline silicon PV cells, which spans approximately 300 to 1100 nm, as outlined in Chapter 2, Section 2.1. Consequently, ND filters were identified as suitable candidates for uniformly reducing light intensity without heavily altering the spectral distribution of light, primarily within the visible spectrum [285]. For this reason, they were considered the most appropriate option for replicating varying-intensity penumbra shadows (such as penumbra-only formations) using a constant-intensity approach.

Given the novelty of this methodology in the context of shadow replication, preliminary experimentation was necessary to evaluate the suitability and optical behaviour of ND filters for this purpose, particularly considering the limited literature on their application in simulating penumbral shading. The setup conditions as well as the PV sources used for the forthcoming experimentations will be subsequently presented in Section 6.2.2.

6.2.2 Setup Conditions and PV Sources Utilised

The forthcoming experimentations were conducted at the premises of the ISE on the 4th of July, 2024, under clear sky conditions and without external shading from nearby structures. An on-site weather station equipped with a pyranometer continuously recorded global irradiance, including both direct beam and diffuse components, at 10-minute intervals throughout the testing period. The irradiance data was used to correct the power output to STC, following the method outlined in Procedure 1 of IEC 60891:2021, which employs current and voltage correction equations [216]. Power loss measurements were recorded using a DATAQ DI-808 data logger, with dedicated inputs for both the control and shaded PV modules, similar to the methodology in Chapters 4 and 5.

Both modules were mounted horizontally at a 0° inclination to minimise ground reflected radiation (albedo), thereby reducing its influence on incident light intensity. The experimental procedure for comparing power loss followed the guidelines in Section 4.1 of IEC 60904-1:2020 [137], and was further supported by the fixed load-point measurement methodology detailed in Chapter 5, Section 5.2.1 in Figure 5.2.

To assess differences in power output performance and thereby determine the power loss metric, two identical PV modules were required: one serving as the control and the other as the experimental shaded module, following the methodology established in Chapters 4 and 5. Ideally, the same small-scale PV modules, bearing dimensions 299.0 mm x 662.0 mm, used in Chapter 5 would have been employed throughout this chapter to maintain experimental consistency. However, despite their small size, the overall dimensions of those PV modules exceeded the size of the ND filter sheets provided by the manufacturer (533.0 mm x 610.0 mm).

Consequently, two smaller PV modules, bearing an overall dimension of 235.0 mm x 335.0 mm, were sourced, with their electrical characteristics detailed in Table 6.1. These modules were used exclusively in the preliminary experiment presented in Section 6.3.1.1, which aimed to investigate the impact of varying the vertical elevation of ND filters above the PV surface. To ensure consistency between the control and experimental shaded modules, both of which exhibited near-identical electrical specifications and dimensions, a calibration correction factor was applied. The calibration process resulted in the chosen PV module to act as the shaded PV, generating 0.26% more power than the control PV module both at unshaded conditions. This was calculated by averaging 15 minutes of 1-second interval power data under full illumination. Moreover, to obtain a baseline initial power output for both the PV modules, the power readings of the control PV module were increased by 0.26% to align with the baseline output of the shaded PV module under identical test conditions.

Table 6.1. The electrical characteristics of the PV module used for the preliminary experimentation.

Description	**Symbol**	**Outdoor calibrated at STC**	
Applicable Experiment No.		Section 6.3.1	
Cell Technology		Mono Si	
No. of Series cells		36	
Size of Cells (mm)		52 x 31	
Bypass diodes		0	
Rated Power Output	P	10 W	
Short circuit current	I_{SC}	0.60 A	
Open circuit voltage	V_{OC}	21.1 V	
MPP current	I_{MPP}	0.55 V	
MPP voltage	V_{MPP}	17.2 V	

6.2.3 Quantifying the Intensity Associated with each ND Filter

Due to the novelty of the proposed methodology, preliminary experimentation was necessary to verify the suitability of ND filters as a material capable of attenuating gradient light in order to produce a constant-intensity ND filter shadow. For this purpose, flexible gelatine-based ND filter sheets were sourced from Lee Filters [286], a

subsidiary of the Panavision Group and one of the leading manufacturers of optical filters in the United Kingdom, specialising in optical technology.

The ability of ND filters to reduce visible light is quantified by their optical density (OD), a logarithmic metric that indicates the extent to which light is blocked. For example, an OD value of 0.3 corresponds to approximately 50% light transmission and is typically denoted following the acronym 'ND'. However, for clarity and ease of interpretation in this study, OD values are instead expressed as the percentage of light transmittance reduction (TR), representing the proportion of light blocked, as illustrated in Equation (26).

$$\text{Transmittance Reduction (TR)} = 1 - (10^{-OD}) \quad (26)$$

The first ND filter selected was the lowest TR level commercially available non-opaque option, designed to attenuate sunlight by approximately 95% (ND 1.2), as shown in Figure 6.4. In this figure, it is noticeable that the ND filter is made from a flexible material and exhibits minor surface waviness. However, this did not affect the spatial uniformity of the transmitted light as this was verified by placing a white reference sheet on top of the PV module and the pixel intensities across the recorded images showed no measurable variation in light intensity. The flexible ND material was required because the filters were subsequently cut into specific sizes to replicate the varying intensity shadow patterns presented previously in Chapter 5. Additionally, Edmund Optics, a globally recognised manufacturer of optical components, provides a theoretical basis for logarithmically increasing light attenuation through the stacking of multiple ND filters, thereby enabling multilayer filtration [287]. However, to date, no peer-reviewed scientific studies have validated the reliability or optical consistency of stacked ND filters. While this concept warrants further investigation, it lies beyond the scope of the present study. As a result, a single-layer ND filter configuration was adopted and maintained throughout the experiments described in this chapter.

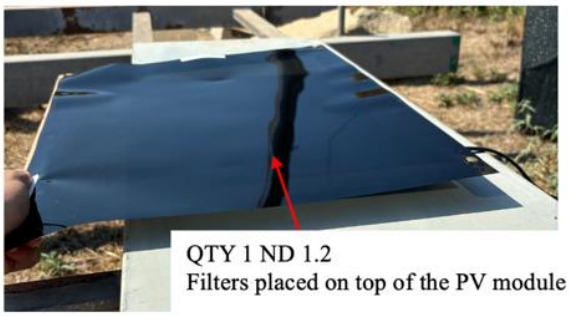


Figure 6.4. A single ND filter rated at 95% TR covering the PV module.

One observation that can be inferred from Figure 6.4, is the lack of space between the ND filter and the PV module. This arises from directly placement of the ND filters on top of the PV module, leaving no physical space for capturing images of the constant-intensity shadow and limiting the ability to measure shadow intensity. Therefore, the setup shown in Figure 6.4 was deemed impractical for image acquisition. To overcome this limitation, a separation distance of 50 cm between the ND filter and the PV module was established, allowing sufficient space to position the camera between the filter and the module for shadow imaging.

To evaluate the impact of this elevation on PV performance, power output differences between the shaded and unshaded modules were measured across varying distances. A range from 10 cm (lower bound) to 50 cm (upper bound) was tested in 10 cm increments, as illustrated in Figure 6.5a and Figure 6.5b. This provided a basis for assessing whether increasing the filter-to-module distance introduced a significant deviation in power output.



(a) **(b)**

Figure 6.5. (a) The ND Filter positioned at 10 cm from the PV module, **(b)** The ND filter repositioned at 50 cm from the PV module to accommodate for image capture.

The 95% TR filter was selected for this evaluation to assess whether variations in filter distance affect the power output of the shaded PV module. This specific grade was chosen due to its dark intensity characteristics, resulting in the highest observed power loss and lowest intensity values, representing a worst-case scenario for ND filter application. To ensure repeatability and accuracy, each experimental condition was subject to 50 readings (a measurement every 0.25 seconds), and the power loss values were averaged into a single value. The results of this preliminary investigation are presented in Section 6.3.1.1.

To facilitate a comparative analysis across different penumbral conditions, a range of constant-intensity ND filter shadows exhibiting varied pixel intensity values was required. Consequently, in addition to the 95% TR filter which was previously used to assess how distance influenced power loss, multiple ND filters with varying TR% grades were additionally sourced. These were required to create a multi intensity dataset of different constant-intensity shadows, with the aim of subsequently replicating the same intensity level of the chosen varying-intensity dataset discussed more in depth in Section 6.2.3. Each filter was used to approximate a uniform, constant-intensity shadow. In contrast to naturally occurring varying-intensity penumbra shadows described earlier in this section, the shadows produced by the ND filters maintain a constant-intensity across the shaded area. The characteristics of each filter and the corresponding intensity values are summarised in Table 6.2.

Table 6.2. The single layer ND filters used during the experimentation with the converted TR level determined using Equation (26).

ND (OD Value)	TR (%)
ND 1.20	≈ 95%
ND 0.90	≈ 90%
ND 0.60	≈ 75%
ND 0.30	≈ 50%
ND 0.15	≈ 30%
ND 0.10	≈ 20%
ND 0.05	≈ 10%
Unshaded	0%

The spectral characteristics of each ND filter are presented in Figure 6.6, based on spectroscopy data provided by the manufacturer, accompanied by a certificate of conformity included in Appendix C. This data is provided to ensure transparency and reproducibility of the methodology. From Figure 6.6, it was observed that all seven ND filters exhibited consistent attenuation across the visible spectrum, with the exception of a slight increase in transmission between 650 nm and 700 nm, an identified limitation of this experimental setup. This limitation spans from material imperfections of the ND filters which is unavoidable, given the ND filter materials chosen where one of the highest quality found on the commercial market at the time of this thesis.

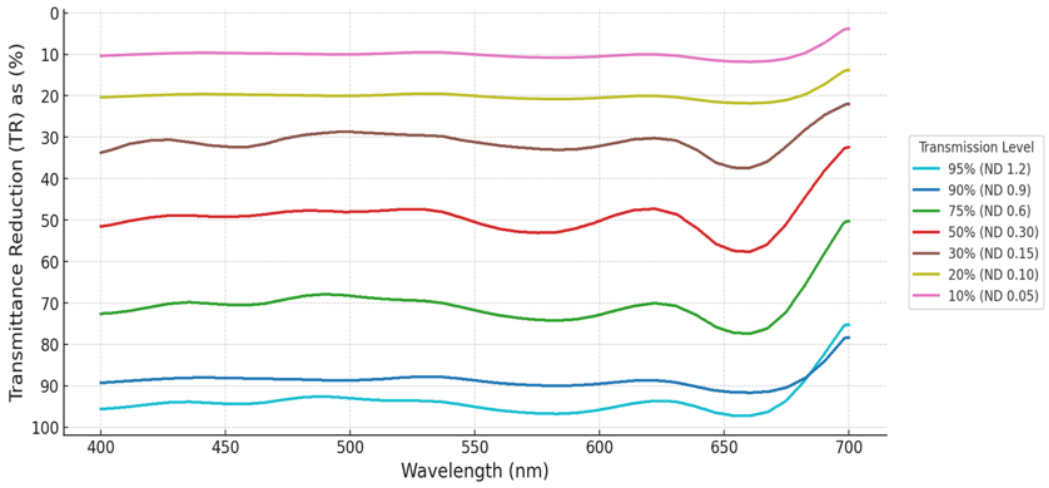


Figure 6.6. Spectroscopy data for the ND filters used in this work as provided by the manufacture.

In addition to the specified TR levels, it was necessary to determine the intensity values of the constant-intensity ND filter shadows produced by the full range of ND filters to enable a direct comparison with the corresponding varying-intensity penumbra shadow cases, as detailed in the subsequent Section 6.2.4.

In contrast to the preliminary experimentation, where the ND filter cast a shadow directly onto the PV module surface, this second procedure employed a uniform white surface sheet placed over the module. This modification was introduced since the reflective properties and surface texture of the PV module were found to introduce visual distortions that could compromise the reliability of intensity measurements; therefore, a white surface sheet was used to provide a consistent and controlled imaging background. Each ND filter listed in Table 6.2 was individually positioned at a fixed distance of 50 cm above the PV module surface, and a corresponding image was captured for each case, as illustrated in Figure 6.7. To maintain uniformity and ensure reproducibility, all images were acquired using the same portable device used throughout Chapter 5, the Apple iPhone 15, bearing camera settings of ISO 200, shutter speed 1/60s, aperture f/1.6. Following the image analysis approach outlined in [170] and [169], each RGB image was converted into an 8-bit greyscale format using the OpenCV (cv2) library in Python, in accordance with the methodology described in [288].

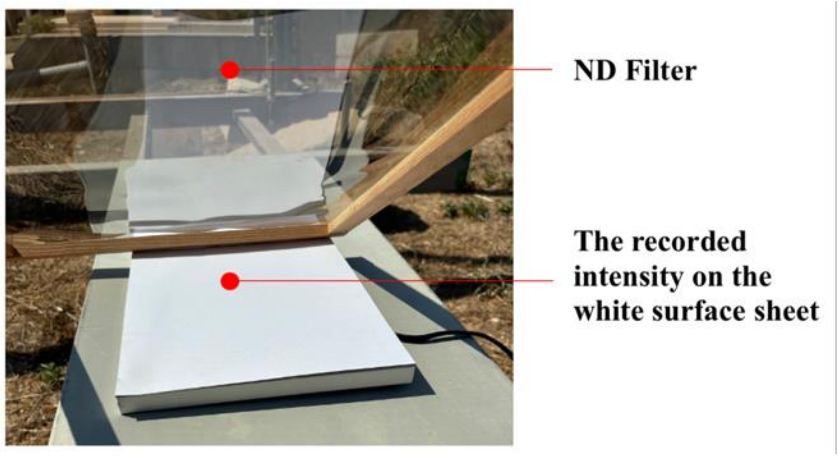


Figure 6.7. The image capture setup involving a white surface sheet placed over the PV module, with an ND filter positioned on top.

A dataset of pixel intensity values corresponding to the full range of ND filters was compiled, with the results presented in Section 6.3.1.2. However, as noted by Soni et al.

[289], raw pixel values (ranging from 0 to 255) obtained from images captured using the portable devices, (such as the iPhone 15), do not directly represent actual light intensity due to the nonlinear response of the camera sensor. This nonlinearity is primarily introduced by gamma correction. The latter is a standard image processing technique applied to align captured luminance data with the human visual system's sensitivity, particularly enhancing detail in darker regions [289], [290].

The iPhone 15 used in this study applies a default gamma correction factor of 2.2 to smooth the transition from black to white on digital displays [82], [83]. As a result, it is necessary to invert this gamma correction when processing the intensity values derived from the captured images. This inversion removes the portable devices' built-in correction and restores the true, real-world intensity values, ensuring accurate scientific measurement of pixel intensity, as emphasised by Carlos et al. [83] and Farid [291]. The conversion from camera-recorded pixel intensity to the real life intensity is performed using Equation (27), as previously applied by Farid [291]. In this equation, u represents the normalised pixel intensity (ranging from 0 to 1) as recorded by the iPhone 15 camera, and γ is the gamma correction factor, in this case, 2.2 [83]. By applying gamma correction, this study mathematically reverses the perceptual adjustments introduced by the iPhone 15 camera, allowing pixel values to reflect true physical light intensity.

$$g^{-1}(u) = u^{\frac{1}{\gamma}} \tag{27}$$

As a result, Section 6.3.1.2 includes a comparative comparison of gamma-corrected pixel intensities against the raw values, to ensure that the measured intensity more accurately reflects true light attenuation caused by the ND filters.

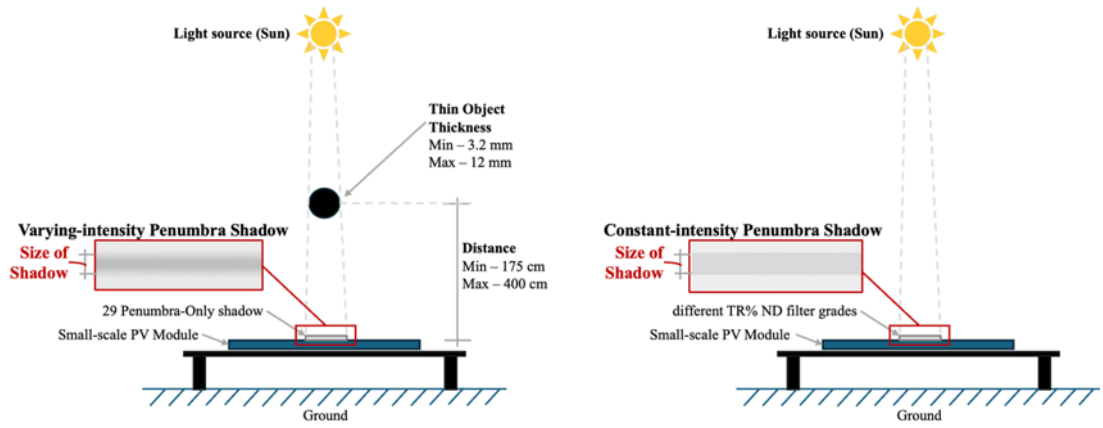
6.2.4 Direct Comparable Method used Between a Varying-Intensity Penumbra Shadow and Constant-Intensity Shadow

This section aims to determine whether the null or alternative hypothesis identified in Section 6.1. should be accepted, in response to the research gap identified. To support the comparative experimental analysis between the varying-intensity penumbra and the constant-intensity penumbra, Table 6.3 presents the relevant variables, that is, thickness,

distance and power loss, along with the sources from which their values were derived. Each column in the table will be explained in detail in the subsequent discussion. Moreover, Figure 6.8a presents a visual comparative diagram of the setup representing the penumbra-only varying-intensity penumbra shadow cases, while compariably Figure 6.8b illustrates the constant-intensity shadow setup using the ND filters.

Table 6.3. Comparative value sourcing table between the varying-intensity penumbra shadow and the constant-intensity shadow.

	Chapter 5 Penumbra-only cases (29)			**Maintaining Size**		**Maintaining Intensity**	
Variables	Thickness	Distance	Power Loss	Varying-intensity penumbra shadow	Constant-intensity shadow	Varying-intensity penumbra shadow	Constant-intensity shadow
Source of Value	Chapter 5 Figure 5.29	Chapter 5 Figure 5.29	Chapter 5 Figure 5.29	Chapter 5 Figure 5.32 Figure 5.36	This Chapter Figure 6.15	Chapter 5 Figure 5.32 Figure 5.36	This Chapter Figure 6.14



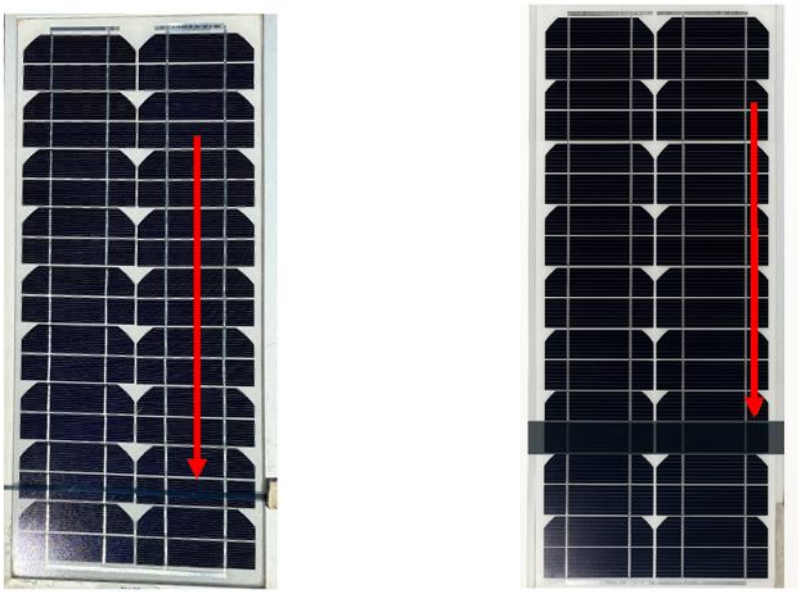
(a) **(b)**

Figure 6.8. A visual comparison between **(a)** the setup used for penumbra-only cases and **(b)** the setup used for replicating the shadow transposed using the ND filter.

The varying-intensity penumbra shadow dataset used in this analysis, corresponding to the experimental setup shown in Figure 6.8a, was sourced from Chapter 5, Section 5.3.1. In the latter, 104 cases of thin-object shading were quantified. From these, 29 cases were identified as penumbra-only shadows, based on their light intensity profiles. These cases

varied in object thickness, distance from the PV module, and associated percentage power loss, as detailed in the first three columns of Table 6.3. The remaining 75 cases were excluded from this comparative analysis due to the presence of both umbra and penumbra regions within the shadow formation. The selected 29 penumbra-only cases occurred predominantly at distances between 175 cm and 400 cm, as indicated in Figure 6.8a. The upper bound of this distance range (400 cm) was set as a constraint, owing to the physical limitation incurred when the projected penumbra shadow exceeded the 100% surface area of the quarter-cut solar cell used in the small-scale PV module. Additionally, the thickness of the thin objects for the chosen 29 penumbra-only cases ranged from ⌀3.2 mm to ⌀12 mm, as illustrated by the examples shown in Figure 6.8a.

The objective was to preserve the two most critical attributes identified in Chapter 5, shadow size and intensity, for both the varying-intensity penumbra shadow (represented in blue in Table 6.3) and the constant-intensity penumbra shadow (represented in red in Table 6.3). The fourth and fifth columns of Table 6.3 present the source data used to replicate the size of the varying-intensity penumbra shadows. The shadow sizes for all 29 penumbra-only cases were extracted from Chapter 5 Figure 5.32 and Figure 5.36. Accordingly, 29 distinct shadow sizes were required to be replicated. To achieve this, ND filter sheets were cut into horizontal strips corresponding to each of the 29 shadow sizes and applied to the surface of the PV module, as illustrated in Figure 6.8b. Furthermore, Figure 6.9 offers a visual representation of the placement of the ND filter strips on the small-scale PV module. An example of minimal (10%) coverage of the PV module by the ND filter strips is shown in Figure 6.9a, while the maximum possible constant shadow, whereby an ND filter strip covers 100% of a single solar cell, is illustrated in Figure 6.9b.



(a) **(b)**

Figure 6.9. The PV module covered with strips of ND filters replicating the constant-intensity ND filter shadow consisting of a single intensity where **(a)** represents a coverage of 10% by the shaded strip on the PV module and **(b)** represents a fully shaded PV row with 100% coverage by the strip.

The sixth and seventh columns of Table 6.3 present the source values for the intensity attribute of both the varying-intensity and constant-intensity penumbra shadow. To replicate the intensity of the penumbra-only shadow, the gamma-corrected intensity values of each ND filter, derived from Section 6.2.3, were categorised to correspond with the nearest matching penumbra-only case. A visual example of a varying-intensity penumbra shadow and its corresponding constant-intensity shadow, matched in both size and average intensity, is shown with a red border in Figure 6.8a and Figure 6.8b, respectively. By closely matching both the size and intensity of the varying-intensity penumbra shadow, the constant-intensity shadow replicated using ND filter strips was applied to the small-scale PV module. The resulting power loss measurements are analysed using a regression model in Section 6.3.2 to evaluate the relationship between the two scenarios.

This regression model of best fit was employed to facilitate both visual interpretation and quantitative analysis. This approach enables a comparative assessment of the relationships and supports hypothesis testing through statistical metrics such as the coefficient of determination (R^2) and residual analysis. Regression analysis is a widely accepted method for modelling relationships between variables, accounting for

experimental variability, and improving the reproducibility and interpretability of results, as demonstrated by Alshammari et al. [292] and Ayyub et al. [293]. Furthermore, statistical tests will also be applied to the regression models to numerically evaluate the significance of differences between the varying-intensity penumbra shadow and the constant-intensity ND filter shadow generated by the ND filters.

The results of the previously described methodology, encompassing both the preliminary and comparative analyses, are presented and discussed in the following Section 6.3.

6.3 Results and Discussions

This section aims to provide empirical evidence, through a comparative analysis using the methodology outlined in Section 6.2, to determine whether there is a statistically significant difference between the varying-intensity penumbra shadow and the constant-intensity shadow. To illustrate the forthcoming sequence of results, Figure 6.10 presents an overview. The steps outlined in the methodology are highlighted with blue borders, while those that will be presented and discussed in this section are marked with red borders. As indicated by the blue-bordered elements, each respective dataset has been described, and a decision was made to use 29 penumbra-only cases from Chapter 5, Section 5.3.1, as representative of the varying-intensity penumbra in the analysis that follows. Moreover, Section 6.3.1 details the preliminary experiments conducted to evaluate the effect of raising the ND filter from the PV module and to determine the intensity values associated with each ND filter. Section 6.3.2 then presents a comparative analysis between the varying-intensity penumbra shadow and constant-intensity shadow datasets, based on the 29 penumbra-only cases. Finally, a comprehensive statistical analysis is performed to assess the relationship and effect size between the two scenarios, ultimately determining whether to accept the null hypothesis (H_0) or the alternative hypothesis (H_1).

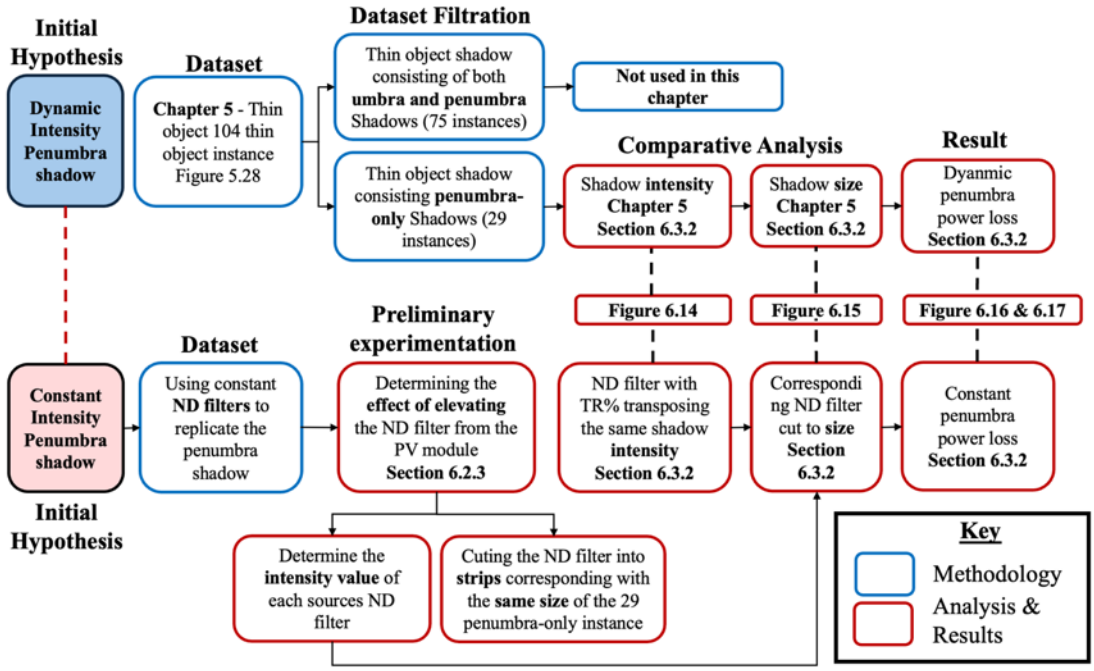


Figure 6.10. Flowchart outlining the methodological steps illustrated by the blue border and the forthcoming results represented by the process with the red border.

6.3.1 Preliminary Experimentation results and Discussion for ND Filters

The preliminary experimentation aims to assess two fundamental aspects of using ND filters on a PV module. First, it investigates whether elevating the ND filter at a distance of 50cm from the surface of the PV module (detailed in Section 6.3.1.1) affects both the transposed shadow intensity and the resulting power loss when the entire module is shaded. Second, it seeks to determine the specific intensity value associated with each of the seven ND filters by capturing an image of the shadow cast on a white surface sheet.

6.3.1.1 Determining the Effect of Elevating the ND Filter from the PV Module

The TR 95% ND filter was selected as the filter under evaluation for this experiment. This is because it represents the highest transmission reduction level readily available on the market and produces the darkest shadow on the PV module, making it the most effective at uniformly reducing light across the entire surface. The filter was cut to match

the exact dimensions of the PV module and positioned at heights ranging from 10 cm to 50 cm above the module, in 10 cm increments. Shadow intensity was measured using ThinShadePV, while power loss was quantified by calculating the percentage difference between the output of the control PV module and that of the experimental shaded module.

As shown in Table 6.4, the pixel intensity values (middle column) captured at all distances showed a level of consistency, indicating that varying the ND filter distance from the PV module up to 50 cm had no effect on the shadow intensity cast on the white surface sheet. This finding is particularly important, as Section 6.3.1.2 will determine the intensity values for all seven ND filters, which will then be used to replicate the intensities of the 29 penumbra-only cases. Additionally, the variation in power loss across all distances was minimal, with a maximum difference of only 0.43%. This negligible change demonstrates that elevating the ND filter up to 50 cm above the PV module during image capture neither affected the light intensity measurements nor compromised the accuracy of the data. These results provide a critical foundation for the subsequent experiments involving the characterisation of pixel intensity values for each sourced ND filter.

Table 6.4. The resultant intensity level and power loss difference when elevating the ND filter from the PV module between 10 cm and 50 cm; in increments of 10 cm for the 95% TR ND filter.

Filter utilised: 95% TR		
Distance between ND filter and white surface (cm)	**Recorded Intensity (Pixel Value)**	**Power Loss (%)**
10	154	93.57
20	154	93.54
30	154	93.52
40	154	93.17
50	154	93.14

Following the results in Table 6.4, where no direct comparison with the varying-intensity penumbra shadow was undertaken so far, the small-scale PV modules previously used in Chapter 5 and having electrical characteristics detailed in Table 5.1, were employed for the analysis in Section 6.3.2. These modules were ideal for facilitating a direct comparison between the varying-intensity penumbra shadow and constant-intensity shadows, given that the baseline data for the varying-intensity penumbra shadow is sourced from Chapter 5, Section 5.3.1. The continued use of the same PV module in Section 6.3.2 ensured experimental consistency by maintaining the same PV source throughout both the varying-intensity penumbra shadow and the constant-intensity shadow cases.

6.3.1.2 Determining the Intensity Value for the Range of ND filters (on the White Surface Sheet)

Each of the seven ND filters listed in Section 6.2.3 Table 6.2, and supported by the corresponding spectroscopy data shown in Figure 6.6, were positioned at 50 cm above a white surface sheet on top of the PV module. This setup mirrors the configuration previously illustrated in Figure 6.5b of the same section. Subsequently, an image was captured using the iPhone 15 portable camera described in Section 6.2.3 of the methodology, and was then converted to 8-bit greyscale. Finally, using ThinShadePV, the intensity values were determined, and inverse gamma correction was applied (as explained in Section 6.2.3).

To visualise the results of both the original camera-captured intensity values and the corrected intensity values after inverse gamma correction, Figure 6.11 was compiled. The orange line represents the raw intensity values captured by the iPhone camera, while the blue line shows the corresponding values after gamma correction. Moreover, it is worth noting that certain intermediate TR levels, specifically 40%, 70%, and 80% were not included, as ND filters with these specifications could not be sourced within the timeframe of the study. This represents an initial limitation. Nevertheless, the dataset includes a broad range of TR percentages, effectively covering both the minimum and maximum transmission levels relevant to this analysis.

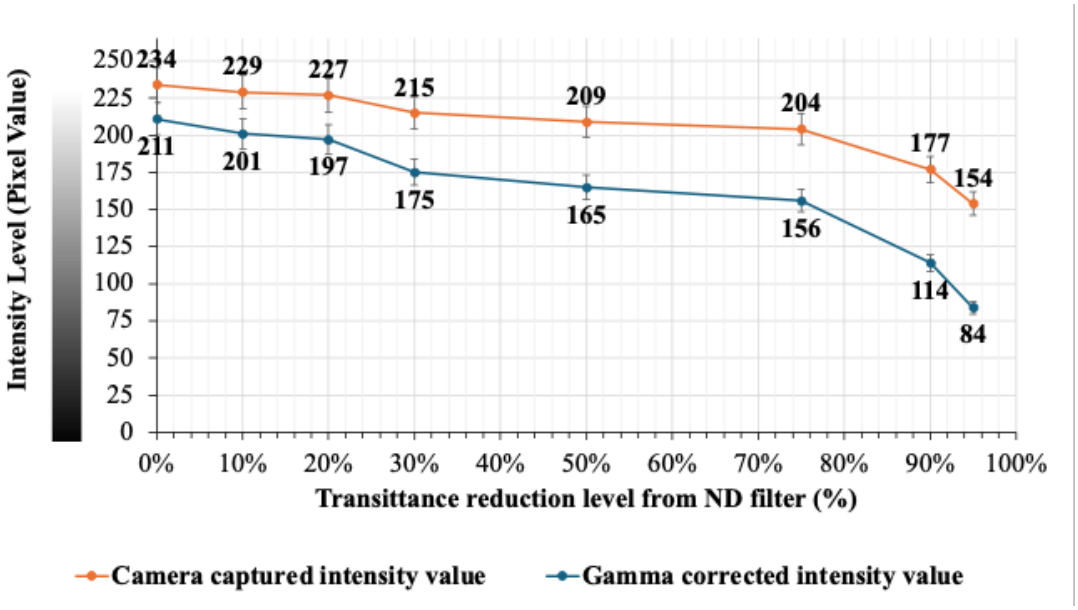


Figure 6.11. The image captured intensity (orange) and the gamma-corrected pixel intensity values (blue) plotted against each ND filter TR level sourced.

An initial observation reveals that the rate of change between the original intensity values and the gamma-corrected values is not constant. This is since the gamma correction formula, as previously defined in Equation (27), represents a nonlinear transformation. As a result, equal increments in input intensity do not produce equal changes in the output.

It is evident that the raw intensity values illustrated by the orange line in Figure 6.11 shift downwards due to a pixel intensity decrease with increasing TR%, providing a more accurate representation of real-world intensity values compared to the camera-captured intensity values. Taken as a baseline measurement prior to applying any ND filter to the PV module, the observed intensity at 0% TR does not reach the maximum possible pixel intensity of 255. Instead, the camera-captured intensity measures 234, while the gamma-corrected value is 211. This deviation may be attributed to internal iPhone camera exposure settings designed to prevent sensor saturation, transmission losses through optical components, or the reflectance properties of the white surface sheet used. While these factors highlight the limitations of the iPhone for precise intensity measurements, it was nonetheless chosen in Chapter 5 as a practical means to capture shadow images which were essential for the ThinShadePV image analysis phase. Therefore, even though the SLR camera from Chapter 4 would have offered more

controlled manual settings, the iPhone camera was retained due to the limiting factor to directly compare with the varying-intensity penumbra image acquired previously in Chapter 5.

As the TR level increases across the x-axis in Figure 6.11, the decline in intensity follows a non-linear trend, with a significantly sharper drop observed beyond the 75% TR level. For example, the gamma-corrected intensity decreases from 156 at 75% TR to 84 at 95% TR, indicating substantial sensitivity to light attenuation at higher TR percentages. This behaviour can be attributed to the camera sensor's limited response under low-light conditions, as discussed by Rezagholizadeh et al. [294]. At these darker levels, photon noise and read noise become more pronounced, and the sensor's response becomes less consistent. This nonlinearity is further amplified by the gamma correction process, which disproportionately affects lower intensity values due to its exponential nature. As such, applying gamma correction is essential when working with variable lighting conditions to ensure accurate intensity measurements.

It is notable that when using ND filters having a TR of 95%, the camera captured pixel intensity is observed to have the lightest recorded pixel value of 154. The gamma-corrected intensity of the same ND filter reduces the value from 154 to 84, incurring a difference of 70 pixel value. Comparatively, the 70 pixel value difference is almost three times the difference between the baseline pixel values at 0% TR, where a 23 pixel value difference was observed. This difference is significant and a pixel value of 84 is considerably dark in nature when referring to the 0 – 255 scale on the left side of Figure 6.11. Therefore, to compare varying-intensity penumbra shadows with constant-intensity shadows, the subsequent section will also need to determine which of the gamma-corrected pixel intensity values correspond to the penumbra-only shadow being replicated.

6.3.2 Comparative Analysis of the Intensities Between a Varying-Intensity Penumbra-Only Shadow and a Constant-Intensity Shadow

Building on the preliminary experimental results discussed in Sections 6.3.1, this section directly addresses the hypothesis introduced at the end of Section 6.1. The objective is

to replicate the size and intensity of the 29 penumbra-only thin-object shading cases extracted from Chapter 5, Section 5.3.1, using ND filters, as described in the methodology in Section 6.2.4. The analysis then compares the power loss between these 29 varying-intensity penumbra-only shadow cases and their corresponding constant-intensity shadow which is created using the various TR levels of ND filters employed in this chapter.

Firstly, the power loss across the 29 penumbra-only cases was illustrated in Figure 6.12. The object thicknesses of the 29 cases ranged from ⌀3.2 mm to ⌀12.0 mm at distances beginning at 175 cm and extending until the shadow covers the whole solar cell area at a maximum limit of 375 cm. Beyond a thickness of ⌀12.0 mm, the thin objects were observed to produce either a predominantly umbra shadow or, during the transition to penumbra, generate a shadow that exceeds the surface width of the solar cell. Therefore, if any of the two latter observations was noted, the respective shadow cases were not considered as penumbra-only shadows and were discarded as previously visualised in the flow chart in Figure 6.10. To visualise a penumbra-only shadow, Figure 6.13a demonstrates a case where the shadow is varying in intensity, contrasting to the shadow produced by the ND filters in Figure 6.13b. The procedure to determine the size and averaged intensity of each shadow will be replicated for all the 29 varying-intensity shadow cases as previously explained in Section 6.2.4 and more specifically in Table 6.3. The uncertainty for each power loss value was derived from Appendix B.1 of the appendix, where an average uncertainty of ±2.43% was calculated.

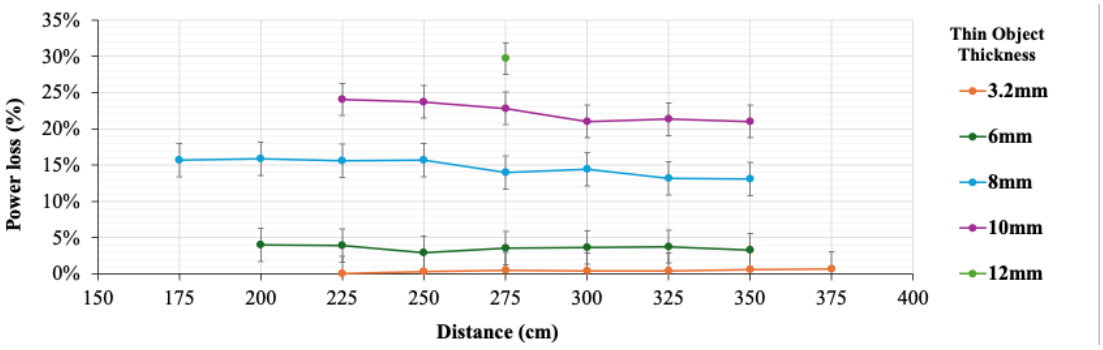


Figure 6.12. The extracted power loss from each of the 29 varying-intensity penumbra-only cases in Chapter 5 Section 5.3.1 .

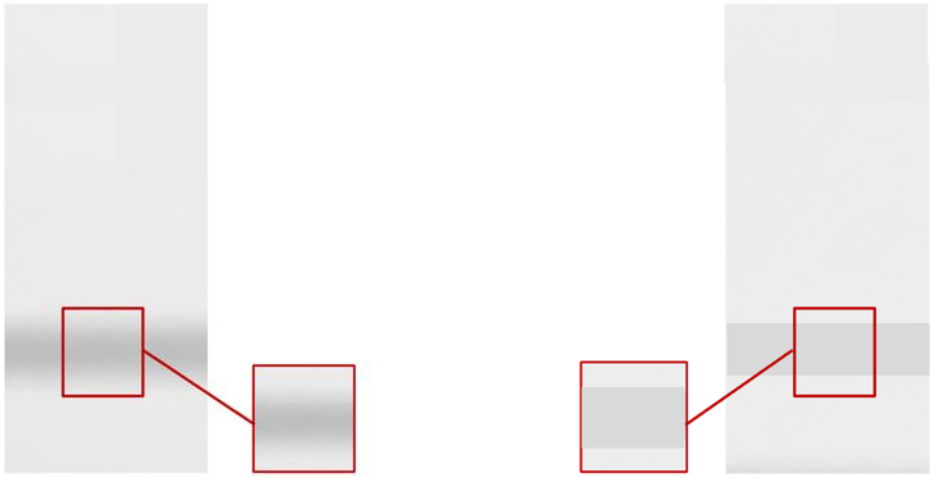


Figure 6.13. (a) A penumbra-only shadow created by the thin object, **(b)** the constant-intensity shadow using ND filter strips.

The first main attributing factor of the penumbra-only shadows is the intensity of the shadow of the 29 cases. Mapping was performed between the intensity values of the seven ND filters shown in Figure 6.11 and the varying-intensity values represented by the blue curve in Figure 6.14. This mapping aimed to identify the closest corresponding transmittance percentage (TR%) for each varying-intensity shadow case, thereby aligning each of the 29 varying-intensity shadows with a comparable constant-intensity shadow. This approach ensured that the intensity levels being compared were closely matched, enabling a comparable basis of the attributing factors of a shadow for the subsequent analysis.

The blue line in Figure 6.14 illustrates the intensity values of each of the 29 penumbra-only cases, sorted in descending order from the highest to lowest gamma-corrected intensity value. The lightest intensity case observed from the 29 penumbra-only case was a pixel value of 209 shown as the first left hand side point on the blue line of Figure 6.14. Referring to the gamma-corrected blue line previously shown in Figure 6.11, the closest intensity value corresponding with the 209 pixel value generated by an ND was 10% TR (excluding the 0% TR no shadow), demonstrating an intensity of 201. With just 8 pixel value difference from the lightest pixel intensity of the 29 cases, the TR 10% will be the upper limit to replicate the penumbra-only intensity of the 29 cases.

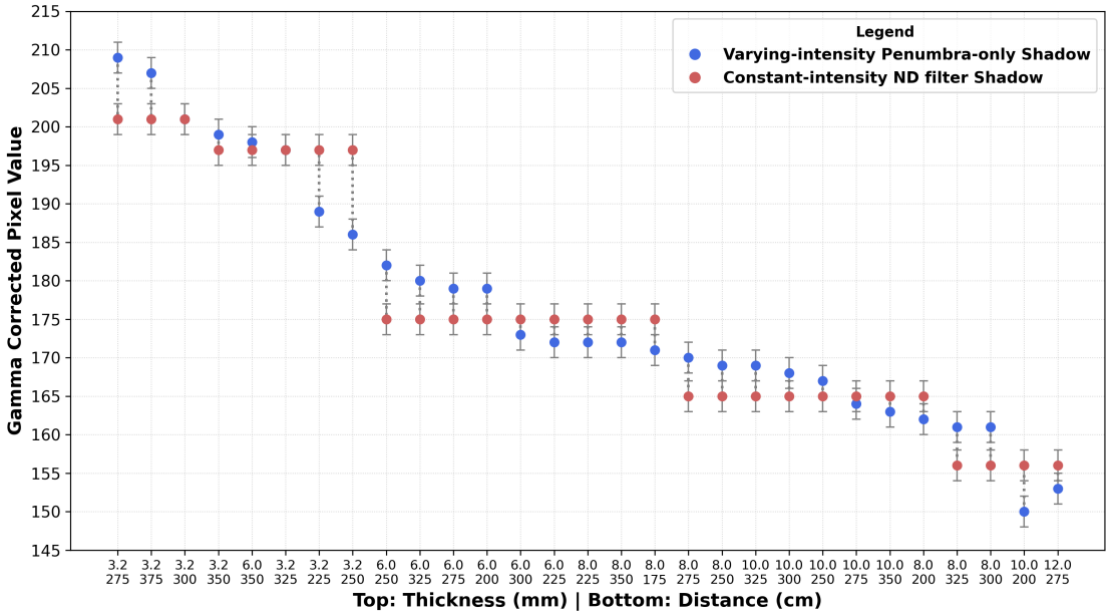


Figure 6.14. A graph comparing the gamma-corrected intensity values of the 29 penumbra-only cases represented as the varying-intensity penumbra-only shadow in blue and the constant-intensity ND filter intensities shown in red.

On the other hand, the darkest penumbra-only case recorded in Figure 6.14 produced an intensity value of 153. The closest matching TR level in Figure 6.11 was 75%, producing an intensity of 156. Therefore, a TR level of 75% was selected as the lower bound for replicating penumbra-only intensity values. Higher TR levels, such as at 90% and 95%, produced much darker intensities of 114 and 84, respectively, well below the penumbra-only range, and were thus deemed too dark to accurately replicate any of the 29 penumbra-only cases.

Consequently, TR levels of 10%, 20%, 30%, 50%, and 75% were found to fall within the appropriate intensity range for replication. The intensity of these five ND filters, previously shown in Figure 6.11, was each matched (binned) to the closest corresponding intensity values from the 29 penumbra-only cases, as explained prior. This mapping is illustrated in Figure 6.14, where the penumbra-only cases are denoted in blue, and the binned ND filter intensities are shown in red, demonstrating close alignment. The maximum pixel difference between the two categories was 11 and a minimum of 0. These results confirm that the five selected ND filters successfully replicated the intensity range of the 29 penumbra-only shadow cases with acceptable accuracy.

6.3.3 Comparative Analysis of the Size of a Varying-Intensity Penumbra-Only Shadow and a Constant-Intensity Shadow

The second defining attributing factor of the penumbra-only shadow is its size. It is essential that the replicated constant-intensity shadow closely matches the area coverage of the 29 penumbra-only cases. In Figure 6.15, the blue scatter plot represents the percentage area coverage of the solar cell for all 29 penumbra-only cases extracted from Chapter 5, Section Section 5.3.1. The five ND filters which were binned to the 29 penumbra-only intensities demonstrated in Section 6.3.2 were employed in this section to replicate these shadow cases. These ND filters were cut into strips closely matching the dimensions of the original penumbra-only cases, implementing the methodology described in Section 6.2.4. The corresponding percentage coverage for each ND filter strip is represented by the red scatter points in Figure 6.15, which closely align to the blue scatter points representing the 29 varying-intensity penumbra shadows. The analysis revealed a maximum difference of +4.98%, a minimum difference of -4.98%, and an average difference of approximately -0.36% between the two datasets. These results indicate that the ND filters produced shadows with solar cell area coverage acceptably similar to that of the penumbra-only cases, complementing the previous outcomes in Section 6.3.2 with regards to intensity .

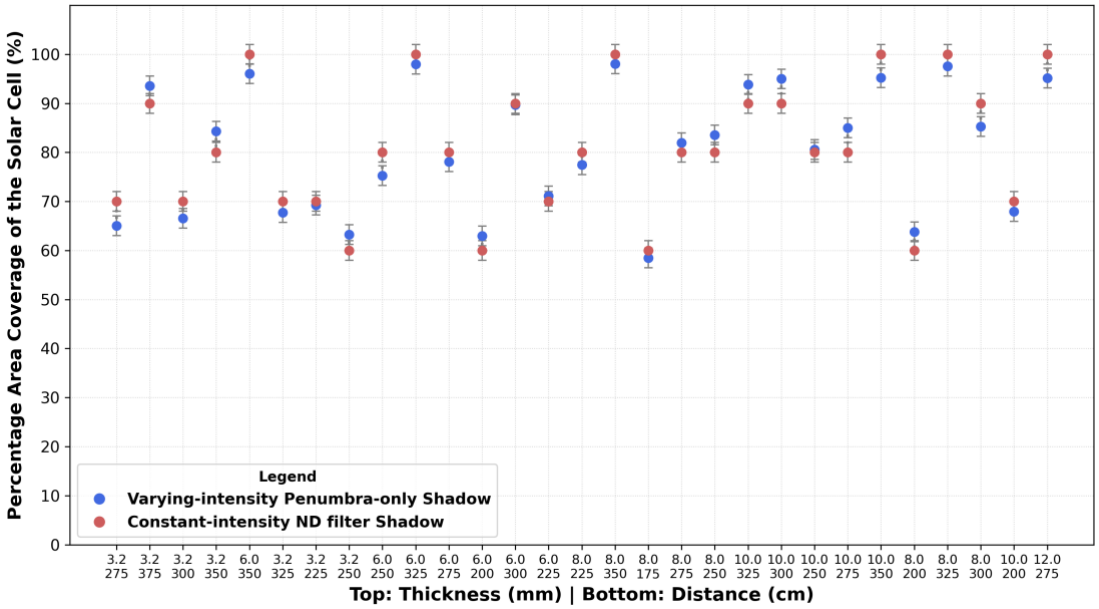


Figure 6.15. Comparison of percentage area covered by the shadow on the solar cell for the varying-intensity penumbra-only shadow and the constant-intensity shadow produced from the ND filter strips.

With size and intensity successfully replicated to an acceptable rate of accuracy as seen in Figure 6.14 and Figure 6.15, the ND filters were subsequently placed on top of the PV module in the middle of the solar cell as visualised in Section 6.2.4 in Figure 6.5 and the setup presented in Figure 6.8. The power loss difference between the control and experimental PV modules, at identical calibrated power outputs, was subsequently retrieved from the constant-intensity shadows created on the PV module. A comparison of the percentage power loss between the varying-intensity penumbra-only shadow and the constant-intensity shadow created by the ND filters is visualised in Figure 6.16. The uncertainty for each power loss value was derived from Appendix B.1 of the appendix and shown as error bars in Figure 6.16. As a value representation, the average uncertainty of ±2.48% was calculated for the varying-intensity shadow previously observed from the extracted data in Chapter 5 Section 5.3.1. Moreover, an average uncertainty of ±2.34% power loss was observed for the constant-intensity shadows.

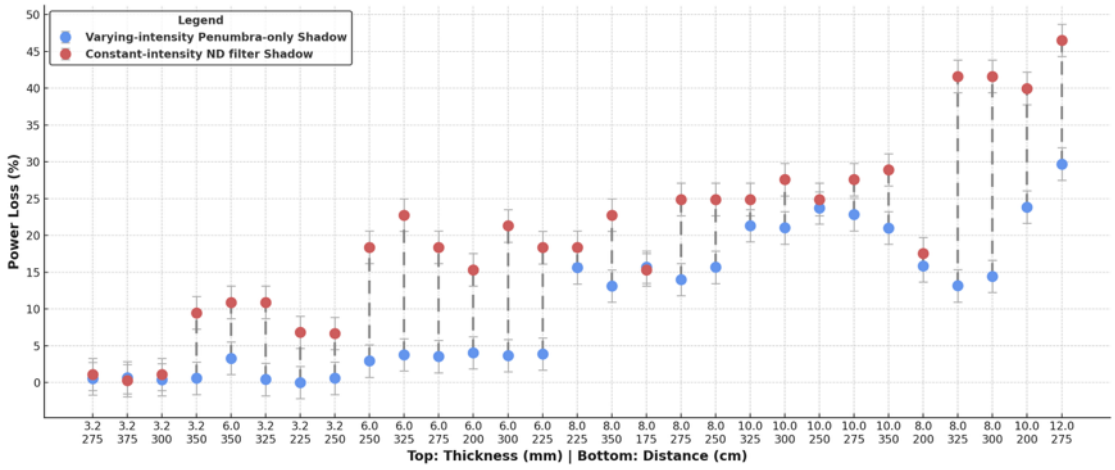


Figure 6.16. Comparison of the percentage power loss for the varying-intensity penumbra-only shadow and the constant-intensity shadows created by the ND filters.

Figure 6.16 reveals a clear discrepancy in power loss between the two shading conditions. A comparative analysis between varying and constant-penumbra power loss revealed a maximum difference of +0.38% power loss, a minimum difference of -28.46% power loss, and an mean difference of -9.65% power loss. Although some penumbra measurements showed significant deviations from the mean difference, multiple cases were analysed to obtain a reliable average difference between the constant-intensity and varying-intensity ND filters. Both the extreme deviations and the closely matched instances observed in Figure 6.16 can be attributed to the combined

limitations of not perfectly replicating the shadow's intensity and size, together with the performance characteristics of the ND filter itself. While some measurements appear closely aligned in Figure 6.16, these are offset by the substantial maximum differences. Therefore, the average across all penumbra cases provides a reliable indication of the difference between the constant and varying intensity penumbra.

In almost all cases, the constant-intensity ND filter shadow resulted in greater power loss when compared to the varying-intensity penumbra-only shadow. This suggests that, even when the size and intensity of both types of shadows are closely matched, the constant-intensity ND shadow imposed a more pronounced negative impact on the PV module's performance. Furthermore, despite the differences in magnitude, a similar trend between the power loss percentage of varying-intensity penumbra and constant-intensity shadows can be observed in Figure 6.16. This indicates a potential underlying relationship warranting further statistical analysis to determine the consistency and to assess the significance of the observed power loss differences. Consequently, Section 6.3.4 shall elaborate further into such analysis to comprehend the trends and statistical differences between the varying and constant-intensity shadow.

6.3.4 Analysing the Difference in Power Loss Between the Varying-Intensity Shadow and the Constant-Intensity Shadow created by the ND filters.

To analyse the differences and relative magnitudes between the varying-intensity shadow and the constant-intensity shadow produced by the ND filters, Figure 6.17 was created to illustrate and quantify the observable trends, as well as to assess the statistical significance in power loss of the two shadow types. The varying-intensity penumbra shadow is represented by the blue point markers, while the constant-intensity shadow instances are shown using red point markers on the graph.

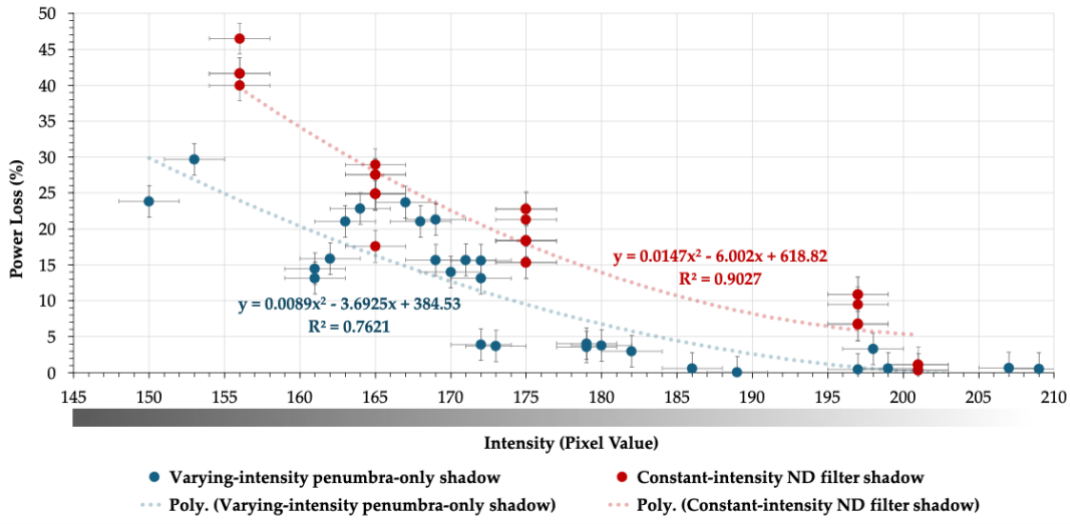


Figure 6.17. Comparison between varying-intensity shadow and constant-intensity shadow created by ND filters.

Initially, a second-degree polynomial regression model was fitted to each dataset to evaluate the predictive relationship between percentage power loss and pixel intensity values. This curve fitting can be visualised in the dotted curved in Figure 6.17. To assess the predictive accuracy of each model, error analysis was performed using MAE and RMSE, as previously described in Chapter 5, Section 5.2.2.4. The varying-intensity penumbra shadow model achieved an MAE of 3.74% and an RMSE of 4.43%, while the constant-intensity ND-filter shadow model achieved an MAE of 2.92% and an RMSE of 3.72%. These results indicate that the constant-intensity ND-filter shadow model provides slightly more accurate predictions overall, with lower average and squared error values, while the varying-intensity penumbra model exhibits greater variability and thus reduced predictive reliability. Moreover, while the constant-intensity shadow was well captured by the polynomial curve, with an R^2 value of 0.9027, the varying-intensity penumbra shadow exhibited greater irregularity, resulting in a lower R^2 of 0.7621. This reduced fit corresponds to the noticeable deviations observed in the intensity range between 161 and 172 on the x-axis. Higher-degree polynomial models were also tested to improve the fit; however, no significant improvement was achieved. These results suggest that polynomial curve fitting lacks sufficient precision to reliably differentiate between the two shadow types.

To enable a more rigorous comparison, statistical analyses were conducted to evaluate the relationship between the varying-intensity and constant-intensity shadows using the original data points, rather than relying solely on the fitted second-degree regression models. Table 6.5 summarises the earlier regression results in the first two rows and, more importantly, presents the outcomes of the statistical analyses in the last two rows, which are discussed in detail in the following section.

Table 6.5. Comparative summary of model fit, group statistical differences, and prediction errors for the varying-intensity penumbra-only shadow and the constant-intensity ND shadows.

Category	Metric	Varying-intensity penumbra-only Shadow	Constant-Intensity ND filter Shadow
Prediction error	MAE (Mean Absolute Error) (%)	3.74	2.92
	RMSE (Root Mean Squared Error) (%)	4.43	3.72
Relationship between the second-degree polynomial regression fits	R^2 (Individual fitted curve)	0.762	0.903
Testing for normality of the distribution	Shapiro-Wilk Test (p-value)	0.0032	
Comparative statistical test	Mann-Witney U test (p-value)	0.00229	
	Cohen's d (Effect Size)	-0.893	

The first statistical test required was the normality test, which determines the most appropriate comparative statistical method to use. To assess the normality of the varying-intensity penumbra shadow in terms of percentage power loss, two statistical methods were applied. The Shapiro-Wilk test yielded a p-value of 0.0032, indicating a statistically significant deviation from normality ($p < 0.05$). This conclusion is further supported by visual inspection through a histogram plot of the power loss, which revealed clear left-skewness and deviation from the normal curve. Therefore, since the

use of traditionally used Welch t-test must satisfy normality assumption, it cannot be used when the Shapiro-Wilk test results in a non normally distributed data, as is the case in this section. Alternatively, West [295] suggests the use of the Mann–Whitney U-test which is almost as powerful and has no distributional assumptions. Oti et al. [296] and Fang [297] demonstrated the effectiveness of the Mann-Whitney U-test in anomaly detection for non-normally distributed data, highlighting its advantages over parametric methods, specifically in complex PV fault detection scenarios. Building on this, Yang and Fang [297] introduced a nonlinear fault detection model using the Mann-Whitney test, achieving improved accuracy by reducing false positives and missed faults, thus reinforcing its robustness in complex PV fault detection scenarios. Therefore, the Mann-Whitney U-test was performed for the two groups of shadows, yielding a U-statistic of 268.5 and confirming a statistically significant difference between the groups ($p = 0.00229$). Assumptions required for these tests, including variance equality (Levene's test, $p = 0.542$) and sample size adequacy (small sample size required), were checked and satisfied.

Moreover, apart from the significance p-value, research conducted by Sullivan et al. [298] and Lakens [299] denoted that the 'effect size' helps in understanding the magnitude of differences found, whereas statistical significance examines whether the findings are likely to be due to chance. In this way the Cohen's d test was chosen to determine the effect size, complimenting the significance level between both varying-intensity penumbra shadow and constant-intensity shadow groups. The magnitude of this difference was quantified using Cohen's d, which yielded a value of -0.893, reflecting a large effect size and strong practical significance.

These results strongly suggest that the type of shadow has a statistically and practically significant impact on power loss. Therefore, the constant-intensity ND shadow does not result in the same power loss effect on a PV source even though both intensity and size are kept relatively the same.

6.4 Conclusion

The purpose of Chapter 6 was to answer outlined below:

RQ.3 In the absence of an umbra shadow, can the impact of a penumbra shadow on a PV module be replicated by using the mean constant-intensity value of the corresponding varying-intensity penumbra shadow?

RQ.3 was addressed across the relevant sections, beginning with Section 6.3.1.1, where the preliminary experimentation confirmed that the variations in elevating the ND filters by 50 cm from the white surface sheet, resulted in negligible changes in recorded pixel intensity values and consistent power loss measurements, thereby validating the experimental setup for image capture and analysis. Furthermore in Section 6.3.1.2, the intensity values of the original seven ND filters sourced were successfully retrieved. Moreover, a comparative analysis between the captured pixel values and the implemented gamma correction ($\gamma = 2.2$), demonstrated effective adjustment to the pixel intensities, to more accurately represent actual light attenuation.

Furthermore, following the preliminary experimentations conducted, Section 6.3.2 was directly linked to answering RQ.3, the size and intensity of the 29 penumbra-only shadow cases were confirmed to be effectively replicated. A statistical analysis revealed that even through the relationship of both models were similar, the constant-intensity ND shadow produced statistically significant different power loss as confirmed by the Mann-Whitney U test ($p = 0.00229$).

Based on the experimental results, the null hypothesis (H_0), which stated that there is no statistically significant difference in power loss between varying-intensity penumbra shadow and constant-intensity shadows, was rejected. The alternative hypothesis (H_1) was accepted, indicating that the varying characteristics of the penumbra do significantly influence PV performance. These findings demonstrate that simplifying the penumbra to a constant-intensity shadow introduces a measurable deviation in power output, thereby answering Research Question 3.

Chapter 7 Conclusions

This concluding chapter summarises the principal findings of the study in relation to the stated research aim, objectives, and contributions to knowledge. The research questions and the ways in which they were addressed have been outlined at the end of each chapter. In addition, this chapter articulates the study's objectives and outlines the methods and results found, with particular emphasis on the implications of shading caused by thin objects. It also offers a reflection on the study's limitations and proposes potential avenues for future research.

7.1 Achieved Aims and Objectives

This study aimed to investigate a specific subset of the broader phenomenon of partial shading namely, shading caused by thin objects. More specifically, the objectives were to firstly examine the differences in shadow formation and corresponding power loss between outdoor and laboratory environments, secondly to explore the relationship and correlation between various contributing factors of thin object shading and the resulting power loss on applicable PV sources, and thirdly to evaluate the scientific validity of simplifying the varying penumbra shadow as a constant intensity shadow.

The research objectives were successfully met as described below:

O.1 Analyse how the size and intensity of horizontal thin object shadows influence the power loss when observed at incremental distances in both outdoor and laboratory experimental settings.

The literature review revealed a clear research gap: while partial shading has been widely studied, limited attention has been given specifically to thin object shading. Although both laboratory and outdoor environments have been used to investigate partial and, to a lesser extent, thin object shading, direct comparisons between the two, particularly in terms of shadow formation, are rare. Furthermore, no existing studies

were found to compare the effects of thin object shading on any PV source across both environments. Accordingly, the first part of this research was dedicated to addressing this gap.

To ensure a consistent and repeatable experimental setup, a single 156.0 × 156.0 mm solar cell with a maximum output power of 4.156 W, calibrated at STC conditions, was used in both laboratory and outdoor environments as outlined in Chapter 4. Initial unshaded measurements achieved an MPP of 4.156 W in a laboratory environment and 3.982 W outdoors, indicating a baseline difference of 0.174 W or 4.37%. A direct comparison of 56 thin object shading cases across distances of 10–40 cm from the PV source and object thicknesses of ⌀2–⌀20 mm showed consistent differences in power output, with power measurements taken outdoor exceeding laboratory results by a range of 0.34 W to 0.67 W. Additionally, the outdoor setup exhibited a steeper linear power response, with a gradient of 0.0181, compared to 0.0110 for the laboratory environment.

Apart from the quantifiable power loss of each thin object shading scenario, the overall size and intensity of the shadow case were considered and analysed. A Combined Shadow Factor (CSF) score introduced in Chapter 4, accounting for both the size and intensity, was calculated for 56 thin object shading scenarios. The analysis confirmed that shadow intensity significantly influences the CSF score and the resultant shading impact on the solar cell. Across all object thicknesses, outdoor conditions consistently produced more intense shadows and higher CSF values. While CSF effectively combines shadow size and intensity into a single metric, it lacks the resolution to differentiate between umbra and penumbra regions, the issue of which has been addressed through a refined methodology in Chapter 5.

The observed discrepancies in shadow formation between laboratory and outdoor environments carried out in Chapter 4, were attributed to differences in light source collimation and diffraction. Outdoor shadows, shaped by the sun's highly collimated light, maintained a well-defined umbra even at a distance of 40 cm. In contrast, laboratory shadows at the same distance exhibited interference fringes and fragmented

patterns, particularly for thin objects (e.g.: ⌀2 mm), where laboratory histograms showed multiple intensity peaks versus a single peak outdoors. These optical distinctions led to measurable variations in shading effects, with outdoor CSF values reaching up to 12.31 for ⌀20 mm objects, compared to 8.28 in a laboratory environment , indicating stronger and more coherent shadows with greater impact on PV performance in the outdoor environment.

This comprehensive comparison of power loss between laboratory and outdoor conditions effectively addressed Objective O.1 of this study. The quantification aspect of thin object shading as an underexplored avenue of partial shading and some preliminary results were presented at the 2024 WSED Young Energy Efficiency conference in Wels, Austria. The methodology and more complete results were then published in the MDPI peer-reviewed journal Energies [208].

In Chapter 5, this thesis addressed objectives O.2 and O.3, outlined below, focusing the development of an effective image analysis tool to quantify shadow formation comprising both umbra and penumbra regions.

O.2 Develop an innovative image analysis tool capable of quantifying the approximate size of umbra and penumbra shadows in thin object shading scenarios, measuring shadow intensity in terms of pixel darkness value and using a predictive model to estimate the worst-case scenario power loss based on changing parameters in horizontal thin object shading.

O.3 Validate the innovative image analysis tool by creating realistic scenarios with various thin objects and verifying that the predicted power loss aligns, within acceptable limits, with actual measured values.

A review of the literature, specifically in Chapter 3 Sections 3.2 revealed that most existing studies [24], [97], [98], [100], [130], evaluate power loss by placing opaque objects directly on solar cells and calculating power loss based on the percentage of cell

area covered. However, thin objects were found to cast shadows with varying intensity profiles, including distinct umbra and penumbra regions, which necessitated a more comprehensive method of shadow quantification.

By integrating several concepts from the literature, such as sigmoidal fitting functions and intersection points on sigmoidal curves, a comprehensive methodology was formulated to improve the CSF metric used in Chapter 4 Section 4.2.5. This led to the creation of ThinShadePV, an image analysis tool designed to quantify shadow formation from captured images.

A training dataset comprising of 104 cases of thin object shading was compiled, with corresponding power loss values recorded. Results indicated that, at distances ranging from 25 cm to 150 cm and for thin objects with thicknesses between ⌀2.8 mm and ⌀16 mm, the power loss was relatively consistent. This suggests that the reduction in intensity with increasing distance is largely compensated by the expanding penumbra region. Beyond 175 cm, shading from the larger thin objects (⌀12–⌀16 mm) caused the PV module to exhibit a measurable decline in power output, indicating that the penumbra shadow at these distances was no longer sufficient to offset the reduction in umbra intensity.

In Chapter 5 Section 5.3.3, using a Spearman correlation matrix, it was found that for both small (2.8 – 8 mm) and large (10 – 16 mm) thin object categories, object thickness was the most influential parent variable, with correlation coefficients of 0.75 and 0.96, for the small and large thin objects respectively. As expected, distance, exhibited a weak correlation with power loss, at 0.15 and 0.37 for the small and large categories, respectively. For small thin objects, the most significant contributing factor was penumbra intensity (0.61), while other variables such as umbra size, penumbra size, and umbra intensity showed a very weak correlation with values under a correlation of 0.05.

This finding was further supported by a sensitivity analysis based on the Random Forest model as demonstrated in Chapter 5 Section 5.3.3, which identified penumbra intensity

as the highest contributing factor (54.5%) for power loss prediction in the small object category. In contrast, for large thin objects, both umbra size and penumbra size showed meaningful correlations with power loss. The sensitivity analysis revealed that umbra size (40.1%) and umbra intensity (26.6%) were the most significant predictors in this category. Furthermore, the successful quantification and relationship understanding of umbra and penumbra size and intensity using ThinShadePV fulfilled Objective O.2 of this research.

The performance of the ThinShadePV Random Forest model was validated using 15 real-world thin object shading cases in Chapter 5 Section 5.3.4. Visual inspection of the 15 validation cases of thin object shading, confirmed that ThinShadePV successfully identified the umbra and penumbra boundaries for all cases. Additionally, the predicted power loss values were compared against measured power losses on a large-scale PV module with equivalent shadow coverage percentages to those used in the training dataset.

Using Bland–Altman analysis, the mean difference between measured and predicted power loss was found to be 0.48%, with limits of agreement ranging from −3.68% to +2.71%, indicating an acceptable level of predictive accuracy. This successful validation of ThinShadePV and its ability to produce reliable power loss estimates fulfilled Objective O.3 of this study.

The concept and methodology behind ThinShadePV were first presented at the 2024 EU PVSEC, following which the EU PVSEC Scientific Committee recommended the work for publication in a special issue of the peer-reviewed journal EPJ Photovoltaics [2].

O.4 Replicate the varying gradient intensity behaviour of penumbra-only shadows using a constant average intensity approximation, and evaluate whether the constant intensity simplification is a scientifically valid simplification.

Chapter 6 investigated whether a constant-intensity penumbra shadow could serve as a scientifically valid simplification of the varying penumbra shadow. A gap in the existing literature was identified, wherein the penumbra shadow has often been represented as both a varying-intensity shadow [258] and constant-intensity shadow [63], with no consensus reached between scholars. Even though, the physics of shadow formation clearly indicates that the penumbra exhibits varying variations in intensity.

Following a comprehensive analysis of potential materials suitable for replicating a penumbra shadow in Chapter 6 Section 6.2.1, ND filters were identified as the most appropriate option. To construct a dataset of varying-intensity penumbra shadows, 29 penumbra-only cases were extracted from the full set of 104 shadow cases presented in Chapter 5 Section 5.2.1. A total of seven different ND filters with varying transmission reduction (TR) levels were initially sourced, of which five were found to adequately replicate the intensity profiles of all 29 penumbra-only cases, achieving an intensity replication accuracy within ±11 pixel values. Shadow replication involved maintaining consistent shadow size, whereby the average penumbra dimensions previously established in Chapter 5 Section 5.2.2.2, were reproduced by cutting strips of ND filters corresponding to the 29 penumbra-only cases. This method achieved a mean coverage accuracy deviation of just 3.37%. Furthermore in Chapter 6 Section 6.2.1, a second-degree polynomial regression model was plotted for both varying and constant-intensity shadow data against power loss as a function of shadow intensity.

The results demonstrated that, when attributing factors were maintained at relatively consistent levels (size and intensity), both shadow scenarios exhibited a similar relationship between shadow intensity and power loss. This was reflected in the adjusted R^2 values: 0.743 for the varying-intensity penumbra-only shadow and 0.895 for the constant-intensity ND filter shadow. However, despite the apparent similarity in trends, the constant-intensity penumbra shadow consistently resulted in higher power loss measurements. This observation was further supported by the Cohen's d effect size of -0.893, indicating a large and statistically significant difference between the two conditions as summarised in Chapter 6 Section 6.3.4.

These findings suggest that, although the representation of the penumbra shadow as a constant-intensity shadow is frequently used in research, it does not accurately reproduce the power loss effects associated with a physically accurate varying penumbra shadow. The novelty of the methodology employed, along with the findings discussed above, have been submitted for publication in the MDPI peer-reviewed journal Applied Sciences and the paper is currently under review.

7.2 Contribution to Knowledge and Key Findings

In summary, the contributions of this research to the field of knowledge of thin object shading can be outlined as below. These are based on the methods and materials used in this study, including the measurement of shading effects under STC at fixed load points and when the shadow impact is most pronounced:

- Using the outlined methodology, horizontally oriented thin objects (⌀2 – ⌀20.0 mm thick) placed 10–40 cm above a 156.0 mm × 156.0 mm, 4.2 W solar cell resulted in power losses ranging from **0.34 W to 0.67 W**, equivalent to 8.18% to 16.13% respectively.

- Recreating thin object shading by placing an **opaque** object horizontally atop a PV source is only valid for thin objects positioned at a distance of approximately **150 cm** from the PV source.

- Using a 20 W small-scale PV module, **distance**, as a parent variable, exhibited a weak negative correlation with power loss, with correlation coefficients of **–0.15** for ⌀2.8 – ⌀8.0 mm thick and **–0.37** for ⌀10 – ⌀16.0 mm thick objects .

- For small thin objects (⌀2.8 – ⌀8.0 mm thick), power loss correlates most **strongly** with the **size** of the **penumbra** (**0.61**), whereas for larger thin objects (⌀10 – ⌀16.0 mm), the **size** of the **umbra** shows the highest correlation with power loss (**0.69**).

- Sensitivity analysis of the Random Forest model showed that, for small thin objects, **penumbra intensity** was the most influential feature (**54.5%**), while for large thin objects, **umbra size** was the most influential (**40.1%**).

- The developed **ThinShadePV** image analysis tool is capable of predicting the impact of horizontal thin object shading with an accuracy range of **–3.68% to +2.71%**, based on the outlined methodology. Further refinement is required for potential commercial application.

- ND filters used to simulate constant-intensity shadows showed a strong correlation with varying-intensity penumbra shadows (adjusted R^2 = **0.743 vs. 0.895**), but failed to replicate their magnitude, with a large **effect size** observed (Cohen's d = **–0.893**).

7.3 Research Limitations

This subsection outlines the limitations associated with the findings of this research, providing context for their interpretation and applicability. Moreover, the points identified below apply for the broader aspect of the study, building upon limitational aspects identified in each chapter.

- The selected small-scale PV modules used in Chapters 5 and 6 provided a reliable representation of PV output, whilst the DATAQ DI-808 datalogger facilitated precise voltage and current measurements through fixed and shunt resistors. Despite this, the absence of I-V curve plotting due to the logger's limitation limited the interpretability of the MPP point. Employing a device similar to the Seaward PV200, but more adaptable to voltage ranges of small-scale PV modules, would allow for I-V curve capture, thereby improving result interpretability and analysis.

- Applicable throughout all the chapters, the power loss due to thin object shading was assessed during a single time frame, deliberately focusing on when the

shadow is most effective during the time of day and year. Consequently, variations in PV installation angles and shadow positions throughout the day were not examined. While the findings offer a foundational understanding of shading impacts based on object size and distance, they should be interpreted cautiously, as real-world conditions such as ambient light variation, may yield different results. This underscores the need for further research under diverse conditions and with various PV configurations to expand upon these findings.

- Due to time constraints and with the focus being on establishing a scientific basis for analysing thin object shading via image analysis, this study was limited to horizontal shading fully spanning the PV module's width. As a result, ThinShadePV currently applies only to this specific scenario. In practice, however, thin objects may cast diagonal, vertical, or multiple overlapping shadows. Adapting ThinShadePV to these shadow scenarios would have expanded the tool's applicability had the study been allocated more time.

- In Chapter 6, ND filter strips were precisely cut in 10% increments based on a quarter-cut solar cell with a width of 31 mm. However, when comparing these with varying-intensity penumbra shadows, discrepancies of up to 3% occurred. This could have been reduced by using larger PV modules with standard 156×156 mm cells, where 10% equates to 15.6 mm, allowing for finer subdivisions (e.g. 5%) and improving strip accuracy to within 1% for more precise shadow size replication.

- Furthermore, in Chapter 6, the ND filter grades (transmittance levels) were selected based on market availability and manufacturer-provided spectral data, which confirmed a relatively consistent light reduction in the visible light wavelength range. However, no data conformity was provided for IR or UV wavelengths. Due to time constraints, independent spectroscopic analysis using a spectrometer could not be performed to verify filter performance across the full spectrum.

7.4 Recommendations for Future Work

- The recommendations in this subsection build upon the future work directions identified in Chapters 4 to 6. The aim is to encourage continued research that advances the capabilities of this study and more specifically the ThinShadePV tool, particularly given that the foundational outline of the image analysis based tool has already been established in Chapter 5.

- The work conducted in Chapter 4 could involve replicating the laboratory thin object shading analysis using a full-scale PV module instead of a single solar cell. This would allow comparison with the original results to assess whether the observed discrepancies scale with module size. Additionally, the dataset could be expanded to examine whether the fringe effect persists at greater distances beyond 40 cm. This could involve physically modifying the solar simulator setup to accommodate thin objects positioned at distances up to 200 cm, enabling investigation of the fringe behaviour at extended ranges.

- Chapter 5 Section 5.3.4.4 outlines future improvements aimed at expanding the dataset and exploring the commercial potential of the ThinShadePV tool. Commercialisation would require shifting from single PV module analysis to multi-array PV systems affected by thin object shading. Similar image-based methodologies could be adapted to accommodate varying shading patterns and the diverse electrical characteristics of larger PV systems. This would improve ThinShadePV's applicability beyond single-module or residential use, positioning it for broader adoption in mass-market and utility-scale applications.

- Future work could include integrating standard PV shading mitigation technologies, such as MPPT algorithms, bypass diodes, and power optimisers into the thin object shading analysis to improve the practical utility of the training model. Reassessing the relationship between thin object shading and power output in systems equipped with these technologies would offer deeper insights into their effectiveness and interaction under thin object shading conditions.

- Building on the work in Chapter 6, further research could investigate the point at which penumbra-only shadows no longer cause significant power loss. This could involve testing larger PV modules while significantly increasing the distance between the shading object and the module to generate penumbra-only shadows. Such experiments would help determine the distance beyond which thin object shading becomes negligible for each object thickness, establishing thresholds where thin objects no longer significantly impact the performance of the PV source.

- A proposed improvement on the work caried out in Chapter 6 could incorporate a wider range of ND-filter increments to enable finer control over light-intensity reduction. Introducing more intermediate ND-filter steps would allow for more precise replication of both the size and intensity gradients characteristic of penumbra conditions. This expanded filter set could improve accuracy when reproducing varying penumbra intensities. By comparing these intermediate transmittance levels with the penumbra-only shading scenarios analysed in Chapter 5, future research could better validate the underlying hypotheses and improve the understanding of the impact of varying penumbra on photovoltaics.

7.5 Final Remarks

This research has contributed novel insights to the scientific community, particularly in the realm of thin object shading on PVs. For the first time, a comparative study was conducted evaluating the effects and shadow formation of various thin object shading scenarios in both laboratory and outdoor environments. Additionally, the development of the image analysis tool ThinShadePV, designed to quantify and predict power losses caused by horizontal thin object shading, offers researchers and PV system owners a practical method to assess the detrimental impact of such conditions.

ThinShadePV serves not only as a prototype tool but also as a foundation for future development. Its continued refinement, especially through the expansion of the training

dataset, will improve its predictive accuracy and adaptability across diverse thin object shading scenarios. Moreover, ThinShadePV holds potential for integration into established commercial simulation software such as PVsyst or PVSol, functioning as a submodule to predict umbra and penumbra characteristics, as well as their corresponding power losses. Ultimately, the findings of this thesis fulfil the stated research objectives and address the identified research gap by contributing meaningfully to the growing body of knowledge on partial shading in PV applications.

References

[1] Met Office, "Malta weather," Met Office. Accessed: Dec. 31, 2024. [Online]. Available: https://www.metoffice.gov.uk/weather/travel/holiday-weather/europe/malta

[2] Statista, "Malta: renewable energy capacity 2023," Statista. Accessed: Dec. 28, 2024. [Online]. Available: https://www.statista.com/statistics/864751/total-renewable-capacity-in-malta/?utm_source=chatgpt.com

[3] "Renewable energy statistics." Accessed: Dec. 31, 2024. [Online]. Available: https://ec.europa.eu/eurostat/statistics-explained/index.php?title=Renewable_energy_statistics

[4] EWA, "National Policy for the Deployment of Offshore Renewable Energy Launched at the National Energy Conference," EWA. Accessed: Dec. 31, 2024. [Online]. Available: https://energywateragency.gov.mt/national-policy-for-the-deployment-of-offshore-renewable-energy-launched-at-the-national-energy-conference/

[5] "National energy and climate plans." Accessed: Dec. 31, 2024. [Online]. Available: https://commission.europa.eu/energy-climate-change-environment/implementation-eu-countries/energy-and-climate-governance-and-reporting/national-energy-and-climate-plans_en

[6] Eurostat, "Short assessment of renewable energy sources (SHARES) - Energy - Eurostat," Energy Additional data. Accessed: Nov. 28, 2025. [Online]. Available: https://ec.europa.eu/eurostat/web/energy/database/additional-data#Short%20assessment%20of%20renewable%20energy%20sources%20(SHARES)

[7] E. H. Sepúlveda-Oviedo, "Impact of environmental factors on photovoltaic system performance degradation," *Energy Strategy Reviews*, vol. 59, p. 101682, May 2025, doi: 10.1016/j.esr.2025.101682.

[8] "DC2015 by Planning Authority - Issuu." Accessed: Feb. 15, 2023. [Online]. Available: https://issuu.com/planningauthority/docs/dc2015_851e7b0de470e8

[9] "LEĠIŻLAZZJONI MALTA." Accessed: Feb. 15, 2023. [Online]. Available: https://legislation.mt/eli/sl/545.11/20150827/eng

[10] A. Dolara, G. C. Lazaroiu, and E. Ogliari, "Efficiency analysis of PV power plants shaded by MV overhead lines," *Int J Energy Environ Eng*, vol. 7, no. 2, pp. 115–123, Jun. 2016, doi: 10.1007/s40095-016-0208-2.

[11] Legislation, "Work place (minimum health and safety requirements) regulations." Legizlazzjoni Malta, 2024. Accessed: Mar. 29, 2025. [Online]. Available: https://legislation.mt/eli/sl/424.15/eng/pdf

[12] United Nations (UN), "luss." Accessed: May 13, 2023. [Online]. Available: https://sdgs.un.org/goals

[13] M. K. Al-Smadi and Y. Mahmoud, "Analysis of Photovoltaic Systems Power Losses in Partial Shading Conditions," in *IECON 2018 - 44th Annual Conference of the IEEE Industrial Electronics Society*, Oct. 2018, pp. 1699–1704. doi: 10.1109/IECON.2018.8591806.

[14] D. Craciunescu and L. Fara, "Investigation of the Partial Shading Effect of Photovoltaic Panels and Optimization of Their Performance Based on High-

Efficiency FLC Algorithm," *Energies*, vol. 16, no. 3, p. 1169, Jan. 2023, doi: 10.3390/en16031169.

[15] PVSyst SA, "PVSyst 7 – Photovoltaic System Design Software: Solar Module Model Documentation," PVSyst SA, Geneva, Switzerland, 2020. [Online]. Available: https://www.pvsyst.com

[16] A. Ramadan, "Rooftop solar PV system planning with 3D visualization using PVSOL (Case study in Syria)," 2024.

[17] MathWorks Inc., *MATLAB® R2024b Simscape*. (2024). MathWorks Inc., Natick, MA, USA. [Online]. Available: https://www.mathworks.com/products/matlab.html

[18] PVsyst, "Thin objects: effect on the electrical losses (Module strings calculation)." Accessed: Dec. 31, 2021. [Online]. Available: https://www.pvsyst.com/help/shadings_thinobjects.htm

[19] K. S. Anderson, C. W. Hansen, W. F. Holmgren, A. R. Jensen, M. A. Mikofski, and A. Driesse, "pvlib python: 2023 project update," *JOSS*, vol. 8, no. 92, p. 5994, Dec. 2023, doi: 10.21105/joss.05994.

[20] A. Aronescu and J. Appelbaum, "Shading on Photovoltaic Collectors on Rooftops," *Applied Sciences*, vol. 10, p. 2977, Apr. 2020, doi: 10.3390/app10082977.

[21] K. Brecl, M. Bokalič, and M. Topič, "Annual energy losses due to partial shading in PV modules with cut wafer-based Si solar cells," *Renewable Energy*, vol. 168, pp. 195–203, May 2021, doi: 10.1016/j.renene.2020.12.059.

[22] J. Hofer, A. Groenewolt, P. Jayathissa, Z. Nagy, and A. Schlueter, "Parametric analysis and systems design of dynamic photovoltaic shading modules," *Energy Science & Engineering*, vol. 4, no. 2, pp. 134–152, Mar. 2016, doi: 10.1002/ese3.115.

[23] J. Teneta, W. Kreft, and M. Janowski, "Partial Shading of Photovoltaic Modules with Thin Linear Objects: Modelling in MATLAB Environment and Measurement Experiments," *Energies*, vol. 17, no. 14, 2024, doi: 10.3390/en17143546.

[24] A. Dolara, G. C. Lazaroiu, S. Leva, and G. Manzolini, "Experimental investigation of partial shading scenarios on PV (photovoltaic) modules," *Energy*, vol. 55, pp. 466–475, Jun. 2013, doi: 10.1016/j.energy.2013.04.009.

[25] A. Gutiérrez Galeano, M. Bressan, F. Jiménez Vargas, and C. Alonso, "Shading Ratio Impact on Photovoltaic Modules and Correlation with Shading Patterns," *Energies*, vol. 11, no. 4, p. 852, Apr. 2018, doi: 10.3390/en11040852.

[26] R. T. Marcus, "chapter 2 - The Measurement of Color," in *AZimuth*, vol. 1, K. Nassau, Ed., North-Holland, 1998, pp. 31–96. doi: 10.1016/S1387-6783(98)80005-6.

[27] "What is The Difference Between Natural Light and Artificial Light?" Accessed: Mar. 31, 2024. [Online]. Available: https://chromaviso.com/en/knowledge-about-light/what-is-the-difference-between-natural-light-and-artificial-light

[28] L. Maierova, "Public Lighting, Public Health," in *2018 VII. Lighting Conference of the Visegrad Countries (Lumen V4)*, Trebic: IEEE, Sep. 2018, pp. 1–5. doi: 10.1109/LUMENV.2018.8521032.

[29] J. Widén and J. Munkhammar, *Solar Radiation Theory*. Uppsala University, 2019. doi: 10.33063/diva-381852.

[30] S. Sobek and S. Werle, “Comparative Review of Artificial Light Sources for Solar-Thermal Biomass Conversion Research Applications,” *Ecological Chemistry and Engineering S*, vol. 26, no. 3, pp. 443–453, Sep. 2019, doi: 10.1515/eces-2019-0033.

[31] A. K. R. Choudhury, “6 - Colour measurement instruments,” in *Principles of Colour and Appearance Measurement*, A. K. R. Choudhury, Ed., Woodhead Publishing, 2014, pp. 221–269. doi: 10.1533/9780857099242.221.

[32] U. America, “UXL Xenon Short Arc | Ushio America, Inc.” Accessed: Apr. 02, 2025. [Online]. Available: https://www.ushio.com/product/uxl-xenon-short-arc/

[33] C. A. Figueiredo Ramos, A. Alcaso, and A. J. M. Cardoso, “Photovoltaic-thermal (PVT) technology: Review and case study,” *IOP Conference Series: Earth and Environmental Science*, vol. 354, p. 012048, Oct. 2019, doi: 10.1088/1755-1315/354/1/012048.

[34] O. Dupré, R. Vaillon, and M. Green, “Physics of the temperature coefficients of solar cells,” *Solar Energy Materials and Solar Cells*, Mar. 2015, doi: 10.1016/j.solmat.2015.03.025.

[35] P. Yang, S. Razzaq, R. Jiao, Y. Hu, L. Liu, and J. Tao, “UV Light-Induced Degradation of Industrial Silicon HJT Solar Cells: Degradation Mechanism and Recovery Strategies,” *Journal of Solar Energy Research Updates*, vol. 10, pp. 36–45, Jul. 2023, doi: 10.31875/2410-2199.2023.10.04.

[36] E. Elsarrag, “Spectrum splitting for eicient utilization of solar radiation: a novel photovoltaic–thermoelectric power generation system,” *Renewables: Wind, Water and Solar*, vol. 2, Nov. 2015, doi: 10.1186/s40807-015-0016-y.

[37] S. Asumadu Sarkodie, “Design and synthesis of low-band gap perylene imides,” 2016. doi: 10.13140/RG.2.2.12563.43048.

[38] A. Métioui and L. Trudel, “The Model of the Rectilinear Propagation of Light and The Study of the Variation of the Size of a Shadow,” *US-China Education Review B*, vol. 2, pp. 173–186, Feb. 2012.

[39] I. Ourraoui and A. Ali, “Investigation of the feasibility and potential use of sun tracking solutions for concentrated photovoltaic Case study Fez Morocco,” *Energy Reports*, vol. 8, pp. 1412–1425, Nov. 2022, doi: 10.1016/j.egyr.2022.08.071.

[40] C. Yousif, G. O. Quecedo, and J. B. Santos, “Comparison of solar radiation in Marsaxlokk, Malta and Valladolid, Spain,” *Renewable Energy*, vol. 49, pp. 203–206, Jan. 2013, doi: 10.1016/j.renene.2012.01.031.

[41] M. Ernst, X. Liu, C.-A. Asselineau, D. Chen, C. Huang, and A. Lennon, “Accurate modelling of the bifacial gain potential of rooftop solar photovoltaic systems,” *Energy Conversion and Management*, vol. 300, p. 117947, Jan. 2024, doi: 10.1016/j.enconman.2023.117947.

[42] Eoul Energy, “Bifacial Solar Panel Double Sided Solar Panels.” Accessed: Apr. 02, 2025. [Online]. Available: https://couleenergy.net/bifacial-solar-panel-double-sided-solar-panels/

[43] A. Marsh, “PD: 3D Sun-Path.” Accessed: Jan. 12, 2025. [Online]. Available: https://andrewmarsh.com/apps/staging/sunpath3d.html

[44] V. Quaschning, *Understanding renewable energy systems.* Earthscan, 2005.

[45] M. Kamran, “Chapter 5 - Planning and modeling of solar energy systems,” in *Fundamentals of Smart Grid Systems*, M. Kamran, Ed., Academic Press, 2023, pp. 219–270. doi: 10.1016/B978-0-323-99560-3.00004-1.

[46] M. Z. A. A. Kadir and Y. Rafeeu, “A review on factors for maximizing solar fraction under wet climate environment in Malaysia,” *Renewable and Sustainable Energy Reviews*, vol. 14, no. 8, pp. 2243–2248, Oct. 2010, doi: 10.1016/j.rser.2010.04.009.

[47] A. Tonkoshkur, L. Nakashydze, A. Ivanchenko, A. Lyashkov, and I. Gomilko, *Application of polymer posistor nanocomposites in systems for protecting photovoltaic components of solar arrays from electrical overloads*. 2021. doi: 10.46299/978-1-63972-054-5.

[48] H. Zsiborács, N. Hegedűsné Baranyai, S. Csányi, A. Vincze, and G. Pintér, “Economic Analysis of Grid-Connected PV System Regulations: A Hungarian Case Study,” *Electronics*, vol. 8, no. 2, 2019, doi: 10.3390/electronics8020149.

[49] S. Saravanan and N. Ramesh Babu, “Maximum power point tracking algorithms for photovoltaic system – A review,” *Renewable and Sustainable Energy Reviews*, vol. 57, pp. 192–204, May 2016, doi: 10.1016/j.rser.2015.12.105.

[50] S. M. Ferdous, M. A. Mohammed, F. Nasrullah, A. Saleque, and A. S. Muttalib, *Design and simulation of an open voltage algorithm based maximum power point tracker for battery charging PV system*. 2012, p. 911. doi: 10.1109/ICECE.2012.6471698.

[51] “Photovoltaic Efficiency: Maximum Power Point Fundamentals Article,” TeachEngineering.org. Accessed: Feb. 09, 2023. [Online]. Available: https://www.teachengineering.org/lessons/view/cub_pveff_lesson03

[52] “The solar cells output parameters.” Accessed: Feb. 09, 2023. [Online]. Available: https://www2.pvlighthouse.com.au/resources/courses/altermatt/The%20PV%20Principle/The%20solar%20cells%20output%20parameters.aspx

[53] M. A. A. Mamun, M. Hasanuzzaman, and J. Selvaraj, “Experimental investigation of the effect of partial shading on photovoltaic performance,” *IET Renewable Power Generation*, vol. Volume 11, pp. 912–921, Jun. 2017, doi: 10.1049/iet-rpg.2016.0902.

[54] T. A. Kumar, Ch. S. N. Murthy, and A. Mangalpady, “Performance analysis of PV panel under varying surface temperature,” *MATEC Web Conf.*, vol. 144, 2018, doi: 10.1051/matecconf/201714404004.

[55] M. Chegaar, A. Hamzaoui, A. Namoda, P. Petit, M. Aillerie, and A. Herguth, “Effect of Illumination Intensity on Solar Cells Parameters,” *Energy Procedia*, vol. 36, pp. 722–729, Jan. 2013, doi: 10.1016/j.egypro.2013.07.084.

[56] Z. Li, J. Yang, and P. Dezfuli, “Study on the Influence of Light Intensity on the Performance of Solar Cell,” *International Journal of Photoenergy*, vol. 2021, pp. 1–10, Feb. 2021, doi: 10.1155/2021/6648739.

[57] M. Wolf and M. A. Rauschenbach, H., “Series Resistance Effects on Solar Cell Measurements,” *Advanced Energy Conversion*, vol. 3, pp. 846–854, 1963, doi: 10.1063/1.349645.

[58] C. Saiprakash, A. Mohapatra, B. Nayak, S. B. Thanikanti, and H. Haes Alhelou, “A Novel Benzene Structured Array Configuration for Harnessing Maximum Power From PV Array Under Partial Shading Condition With Reduced Number

of Cross Ties," *IEEE Access*, vol. PP, pp. 1–1, Jan. 2022, doi: 10.1109/ACCESS.2022.3228049.

[59] V. Štampfl, H. Gabrijelčič, and J. Ahtik, "The Role of Light and Shadow in the Perception of Photographs," *Tehnicki Vjesnik*, vol. 30, pp. 1347–1356, Aug. 2023, doi: 10.17559/tv-20221014154132.

[60] Z. Liu, K. Huang, T. Tan, and L. Wang, *Cast Shadow Removal with GMM for Surface Reflectance Component*. 2006, p. 730. doi: 10.1109/ICPR.2006.357.

[61] R. Pogge, "Eclipses of the Sun & Moon," Introduction to Solar System Astronomy. Accessed: Feb. 19, 2023. [Online]. Available: https://www.astronomy.ohio-state.edu/pogge.1/Ast161/Unit2/eclipses.html

[62] J. Hernán, "Calculation of the shadow-penumbra relation and its application on efficient architectural design," *Solar Energy*, vol. 110, pp. 139–150, Dec. 2014, doi: 10.1016/j.solener.2014.08.043.

[63] S. Murali, G. V K, and S. Kalady, "A Survey on Shadow Detection Techniques in a Single Image," *Information Technology And Control*, vol. 47, Mar. 2018, doi: 10.5755/j01.itc.47.1.15012.

[64] O. L. Carlos. R and steven L.rickman, "Method of calculation of spacecraft umbra and penumbra shadow termination point," *NASA Center for AeroSpace Information, 800 Elkridge Landing Road, Linthicum Heights, MD 21090-2934 (301) 621-0390.*, Apr. 1995.

[65] P. Blaszczyk and A. Petiurenko, *Bridging Classical and Modern Approaches to Thales' Theorem*. 2025. doi: 10.48550/arXiv.2503.16684.

[66] "En savoir plus: Le calcul des rayons de l'ombre et de la pénombre." Accessed: Apr. 30, 2025. [Online]. Available: https://media4.obspm.fr/public/ressources_lu/pages_eclipses-soleil/stlp-rayons-ombre-penombre.html

[67] "In Depth | Sun – NASA Solar System Exploration." Accessed: Sep. 22, 2022. [Online]. Available: https://solarsystem.nasa.gov/solar-system/sun/in-depth/

[68] J. P. Rozelot, A. G. Kosovichev, and A. Kilcik, "A brief history of the solar diameter measurements: a critical quality assessment of the existing data.," p. 17.

[69] J. Demouth, O. Devillers, H. Everett, M. Glisse, S. Lazard, and R. Seidel, "Between umbra and penumbra," *Proceedings of the Annual Symposium on Computational Geometry*, pp. 265–274, Jun. 2007, doi: 10.1145/1247069.1247117.

[70] J. Tian and Y. Tang, *Linearity of each channel pixel values from a surface in and out of shadows and its applications*. 2011, p. 992. doi: 10.1109/CVPR.2011.5995622.

[71] R. C. Gonzalez, R. E. Woods, and B. R. Masters, "Digital Image Processing, Third Edition," *J. Biomed. Opt.*, vol. 14, no. 2, p. 029901, 2009, doi: 10.1117/1.3115362.

[72] J. C. Grande, "Principles of Image Analysis," *Metallography, Microstructure, and Analysis*, vol. 1, no. 5, pp. 227–243, Oct. 2012, doi: 10.1007/s13632-012-0037-5.

[73] S. Chandran, *Color Image to Grayscale Image Conversion*. 2010, p. 199. doi: 10.1109/ICCEA.2010.192.

[74] M. Rahman, M. Mohamed, and J. Shin, “The Impact of State-of-the-Art Techniques for Lossless Still Image Compression,” *Electronics*, vol. 10, p. 360, Feb. 2021, doi: 10.3390/electronics10030360.

[75] L. Tan and J. Jiang, “Chapter 14 - Image Processing Basics,” in *Digital Signal Processing (Second Edition)*, L. Tan and J. Jiang, Eds., Boston: Academic Press, 2013, pp. 683–765. doi: 10.1016/B978-0-12-415893-1.00014-7.

[76] F. Baskoro, B. Suprianto, A. B. Pratiwi, L. Anifah, A. P. Nurdiansyah, and M. Rohman, “Analysis of Motion Detection System Sensitivity with Light Intensity,” in *2021 Fourth International Conference on Vocational Education and Electrical Engineering (ICVEE)*, Oct. 2021, pp. 1–6. doi: 10.1109/ICVEE54186.2021.9649674.

[77] K. Kainth and B. Singh, “Analysis of CCD and CMOS Sensor Based Images from Technical and Photographic Aspects,” *SSRN Electronic Journal*, Jan. 2020, doi: 10.2139/ssrn.3559236.

[78] R. Fisher, S. Perkins, and A. Walker, “Image Analysis - Intensity Histogram.” Accessed: Jan. 03, 2025. [Online]. Available: https://homepages.inf.ed.ac.uk/rbf/HIPR2/histgram.htm

[79] s Alsiya, C. Lekshmi, B. Priya, and R. Mehta, “Image Processing Algorithm for Fringe Analysis in Photoelasticity,” *Scholars Journal of Engineering and Technology*, vol. 4, pp. 325–328, Jul. 2016, doi: 10.21276/sjet.2016.4.7.5.

[80] T. Hussein, H. Omar, and K. Jihad, “A study on image noise and various image denoising techniques,” vol. 11, pp. 27–42, Nov. 2021, doi: 10.17605/OSF.IO/87XGJ.

[81] X. Liu *et al.*, “The real-time shadow detection of the PV module by computer vision based on histogram matching and gamma transformation method,” *Scientific Reports*, vol. 14, no. 1, p. 21781, Sep. 2024, doi: 10.1038/s41598-024-71710-x.

[82] Z. Wang, Y. Zhou, F. Wang, S. Wang, G. Qin, and J. Zhu, “Shadow Detection and Reconstruction of High-Resolution Remote Sensing Images in Mountainous and Hilly Environments,” *IEEE Journal of Selected Topics in Applied Earth Observations and Remote Sensing*, vol. 17, pp. 1233–1243, 2024, doi: 10.1109/JSTARS.2023.3338976.

[83] J. Carlos and J. C. Fernandes, “Linear versus Non-Linear Digital Image Processing Methods”.

[84] M. Mafi, H. Martin, M. Cabrerizo, J. Andrian, A. Barreto, and M. Adjouadi, “A comprehensive survey on impulse and Gaussian denoising filters for digital images,” *Signal Processing*, vol. 157, pp. 236–260, Apr. 2019, doi: 10.1016/j.sigpro.2018.12.006.

[85] P. Luo, X. Zhang, Z. Chang, and W. Liu, “Research on Salt and Pepper Noise Removal Method Based on Adaptive Fuzzy Median Filter,” in *2021 IEEE 5th Advanced Information Technology, Electronic and Automation Control Conference (IAEAC)*, Mar. 2021, pp. 387–392. doi: 10.1109/IAEAC50856.2021.9390923.

[86] N. Nelfy, A. Achmadi, Y. Prihhapso, W. Farhania, D. Suryani, and H. Zaini, “The effect of glass neutral density filter on illuminance measurement error,” *Journal of Physics: Conference Series*, vol. 1918, p. 022028, Jun. 2021, doi: 10.1088/1742-6596/1918/2/022028.

[87] S. Monicka, M. .D, and K. .M, "Detection of Microcracks in Silicon Solar Cells using Otsu-Canny Edge Detection Algorithm," *Renewable Energy Focus*, vol. 43, Sep. 2022, doi: 10.1016/j.ref.2022.09.002.

[88] M. I. Ameerdin, M. H. Jamaluddin, A. Z. Shukor, L. Al Hakim Kamaruzaman, and S. Mohamad, "Towards Efficient Solar Panel Inspection: A YOLO-based Method for Hotspot Detection," in *2024 IEEE 14th Symposium on Computer Applications & Industrial Electronics (ISCAIE)*, May 2024, pp. 367–372. doi: 10.1109/ISCAIE61308.2024.10576312.

[89] W. Yin, S. Lingxin, L. Maohuan, S. Qianlai, and L. Xiaosong, "PV-YOLO: Lightweight YOLO for Photovoltaic Panel Fault Detection," *IEEE Access*, vol. 11, pp. 10966–10976, 2023, doi: 10.1109/ACCESS.2023.3240894.

[90] Aurora Solar, "Shading Losses in PV Systems, and Techniques to Mitigate Them." [Online]. Available: https://aurorasolar.com/blog/shading-losses-in-pv-systems-and-techniques-to-mitigate-them/

[91] Gary Reysa, "Effect of Power Line Wire Shadows on PV Array Output." [Online]. Available: https://www.builditsolar.com/Experimental/PVShading/PVShading.htm

[92] M. Aljumaili, A. Abdalkafor, and M. Taha, "Analysis of the Hard and Soft Shading Impact on Photovoltaic Module Performance Using Solar Module Tester," *International Journal of Power Electronics and Drive Systems*, vol. 10, Jun. 2019, doi: 10.11591/ijpeds.v10.i2.pp1014-1021.

[93] Y. Sun, S. Chen, L. Xie, R. Hong, and H. Shen, "Investigating the Impact of Shading Effect on the Characteristics of a Large-Scale Grid-Connected PV Power Plant in Northwest China," *International Journal of Photoenergy*, vol. 2014, pp. 1–9, 2014, doi: 10.1155/2014/763106.

[94] A. Zulu and G. Kashweka, "The Influence of Artificial Light and Shading on Photovoltaic Solar Panels," *International Journal of Energy Engineering*, vol. 2013, pp. 15–20, Jan. 2013, doi: 10.5923/j.ijee.20130301.03.

[95] S. Bimenyimana, G. N. O. Asemota, M. C. Kemunto, and L. Li, "Shading effects in photovoltaic modules: Simulation and experimental results," in *2017 2nd International Conference on Power and Renewable Energy (ICPRE)*, Chengdu: IEEE, Sep. 2017, pp. 904–909. doi: 10.1109/ICPRE.2017.8390665.

[96] M. R. Maghami, H. Hizam, C. Gomes, M. A. Mohd Radzi, S. Rezadad, and S. Hajighorbani, "Power Loss Due to Soiling on Solar Panel: A review," *Renewable & Sustainable Energy Reviews*, vol. 59, pp. 1307–1316, Jan. 2016, doi: 10.1016/j.rser.2016.01.044.

[97] S. Abdulridha, S. Tuma, and O. Abdulrazzaq, "Study of the Partial Shading Effect on the Performance of Silicon PV Panels String," *JASN*, vol. 1, no. 1, pp. 32–42, Apr. 2021, doi: 10.53293/jasn.2021.11022.

[98] P. R. Kareem, "Performance of PV panel under shaded condition," *Open Access*, vol. 1, no. 1, p. 9.

[99] M. A. Ismail, N. L. J. Adil, F. Y. Yan, N. Amaludin, N. Bohari, and S. Sar-ee, "Analysis of the Effects of Hard Shading Pattern on I–V Performance Curve," *Applied Solar Energy*, vol. 59, no. 4, pp. 369–377, Aug. 2023, doi: 10.3103/S0003701X23700020.

[100] A. H. Numan, Z. S. Dawood, and H. A. Hussein, "Theoretical and experimental analysis of photovoltaic module characteristics under different partial shading

conditions," *IJPEDS*, vol. 11, no. 3, p. 1508, Sep. 2020, doi: 10.11591/ijpeds.v11.i3.pp1508-1518.

[101] K. Osmani, A. Haddad, H. Jaber, T. Lemenand, B. Castanier, and M. Ramadan, "Mitigating the effects of partial shading on PV system's performance through PV array reconfiguration: A review," *Thermal Science and Engineering Progress*, vol. 31, p. 101280, Jun. 2022, doi: 10.1016/j.tsep.2022.101280.

[102] A. Bidram, A. Davoudi, and R. Balog, "Control and Circuit Techniques to Mitigate Partial Shading Effects in Photovoltaic Arrays," *IEEE Journal of Photovoltaics*, vol. 2, pp. 532–546, Oct. 2012, doi: 10.1109/JPHOTOV.2012.2202879.

[103] M. Baka, P. Manganiello, D. Soudris, and F. Catthoor, "A cost-benefit analysis for reconfigurable PV modules under shading," *Solar Energy*, vol. 178, pp. 69–78, Nov. 2018, doi: 10.1016/j.solener.2018.11.063.

[104] S. B, M. Ansari M, and K. P., "Analysis of Passive Partial Shading Mitigation Technique for PV Array," *JREE*, vol. 11, no. 1, Jan. 2024, doi: 10.30501/jree.2023.400223.1599.

[105] M. Dhimish, M. Theristis, and V. d'Alessandro, "Photovoltaic hotspots: A mitigation technique and its thermal cycle," *Optik*, vol. 300, p. 171627, Apr. 2024, doi: 10.1016/j.ijleo.2024.171627.

[106] W. Herrmann, W. Wiesner, and W. Vaassen, "Hot spot investigations on PV modules-new concepts for a test standard and consequences for module design with respect to bypass diodes," in *Conference Record of the Twenty Sixth IEEE Photovoltaic Specialists Conference - 1997*, Oct. 1997, pp. 1129–1132. doi: 10.1109/PVSC.1997.654287.

[107] M. Alonso-Garcia, W. Herrmann, W. Böhmer, and B. Proisy, "Thermal and electrical effects caused by outdoor Hot-spot testing in associations of photovoltaic cells," *Progress in Photovoltaics: Research and Applications*, vol. 11, pp. 293–307, Jul. 2003, doi: 10.1002/pip.490.

[108] M. Simon and E. L. Meyer, "Detection and analysis of hot-spot formation in solar cells," *Solar Energy Materials and Solar Cells*, vol. 94, no. 2, pp. 106–113, Feb. 2010, doi: 10.1016/j.solmat.2009.09.016.

[109] A. H. Numan, H. Hussein, and Z. Dawood, "Hot Spot Analysis of Photovoltaic Module under Partial Shading Conditions by Using IR-Imaging Technology," vol. 39, pp. 1338–1344, Sep. 2021, doi: 10.30684/etj.v39i9.8410.

[110] C. E. Clement, J. P. Singh, E. Birgersson, Y. Wang, and Y. S. Khoo, "Hotspot development and shading response of shingled PV modules," *Solar Energy*, vol. 207, pp. 729–735, Sep. 2020, doi: 10.1016/j.solener.2020.06.078.

[111] K. Itako and A. Alhabib, "A New Method of Detecting Hot Spots in PV Generation System Utilizing AI," *IOP Conf. Ser.: Earth Environ. Sci.*, vol. 581, no. 1, p. 012006, Nov. 2020, doi: 10.1088/1755-1315/581/1/012006.

[112] P. A. A. Pramana and R. Dalimi, "Hotspot Detection Method in Large Capacity Photovoltaic (PV) Farm," *IOP Conf. Ser.: Mater. Sci. Eng.*, vol. 982, no. 1, p. 012019, Dec. 2020, doi: 10.1088/1757-899X/982/1/012019.

[113] Admin, "Half-Cut Solar Cells: Next Step in Solar Module Performance? - Novergy," Novergy Solar. Accessed: Jan. 17, 2025. [Online]. Available: https://www.novergysolar.com/half-cut-solar-cells-improve-solar-module-performance/

[114] J. C. Teo, R. H. G. Tan, V. H. Mok, V. K. Ramachandaramurthy, and C. Tan, "Impact of bypass diode forward voltage on maximum power of a photovoltaic system under partial shading conditions," *Energy*, vol. 191, p. 116491, Jan. 2020, doi: 10.1016/j.energy.2019.116491.

[115] R. Vieira, F. Araújo, M. Dhimish, and M. I. Guerra, "A Comprehensive Review on Bypass Diode Application on Photovoltaic Modules," *Energies*, vol. 13, p. 2472, May 2020, doi: 10.3390/en13102472.

[116] G. Daniel, N. Rosmarie, and M. Urs, "The Bypass Diode – A Weakness in today's PV Systems," presented at the Laboratory for Photovoltaic Systems, Photovoltaic Modules and BoS Components. [Online]. Available: http://www.pvtest.ch/Dokumente/Publikationen/269_EUPVSEC20_Bypass-Diodes.pdf

[117] F. Fadliondi, H. Isyanto, and B. Budiyanto, "Bypass Diodes for Improving Solar Panel Performance," *International Journal of Electrical and Computer Engineering (IJECE)*, vol. 8, p. 2703, Oct. 2018, doi: 10.11591/ijece.v8i5.pp2703-2708.

[118] C. Deline, "Partially shaded operation of a grid-tied PV system," in *2009 34th IEEE Photovoltaic Specialists Conference (PVSC)*, Philadelphia, PA, USA: IEEE, Jun. 2009, pp. 001268–001273. doi: 10.1109/PVSC.2009.5411246.

[119] S. Ghosh, V. K. Yadav, and V. Mukherjee, "Improvement of partial shading resilience of PV array though modified bypass arrangement," *Renewable Energy*, vol. 143, pp. 1079–1093, Dec. 2019, doi: 10.1016/j.renene.2019.05.062.

[120] G. H. Shinde and D. M. Sonje, "A consequence of partial shading on the attribute curves of a photovoltaic panel," *Global Transitions Proceedings*, vol. 2, no. 2, pp. 571–578, Nov. 2021, doi: 10.1016/j.gltp.2021.08.053.

[121] A. Ahmad, M. Khattak, M. Zeeshan, M. Salman, and K. Alam, "Techniques to Mitigate Problem of Partial Shading and Soiling on PV Module: A Review," *International Journal of Engineering*, vol. 6, pp. 148–152, Apr. 2019, doi: 10.34259/ijew.19.605148152.

[122] H.-S. Lee and J.-J. Yun, "Advanced MPPT Algorithm for Distributed Photovoltaic Systems," *Energies*, vol. 12, p. 3576, Sep. 2019, doi: 10.3390/en12183576.

[123] A. Fri, R. El Bachtiri, and el ghzizal Abdelaziz, "Improved MPPT Algorithm for Controlling a PV System Grid Connected for Rapid Changes of Irradiance," *International Review of Automatic Control (IREACO)*, vol. 9, p. 11, Jan. 2016, doi: 10.15866/ireaco.v9i1.7921.

[124] N. Tait, "Robert Lusser and Lusser's Law," *Safety and Reliability*, vol. 15, no. 2, pp. 15–18, Sep. 1995, doi: 10.1080/09617353.1995.11690648.

[125] J. Li, Y. Wu, M. Suliang, M. Chen, B. Zhang, and B. Jiang, "Analysis of photovoltaic array maximum power point tracking under uniform environment and partial shading condition: A review," *Energy Reports*, vol. 8, pp. 13235–13252, Nov. 2022, doi: 10.1016/j.egyr.2022.09.192.

[126] P. Guerriero, S. Daliento, V. d'Alessandro, and G. Vallone, "A simple test-bench to evaluate partial shading effects on the MPPT efficiency of a PV inverter," in *2013 International Conference on Clean Electrical Power (ICCEP)*, Alghero, Italy: IEEE, Jun. 2013, pp. 20–23. doi: 10.1109/ICCEP.2013.6586959.

[127] A. M. Eltamaly, M. S. Al-Saud, and A. G. Abokhalil, "A Novel Bat Algorithm Strategy for Maximum Power Point Tracker of Photovoltaic Energy Systems Under Dynamic Partial Shading," *IEEE Access*, vol. 8, pp. 10048–10060, 2020, doi: 10.1109/ACCESS.2020.2964759.

[128] N. Shankar and N. SaravanaKumar, "Reduced Partial shading effect in Multiple PV Array configuration model using MPPT based Enhanced Particle Swarm Optimization Technique," *Microprocessors and Microsystems*, p. 103287, Sep. 2020, doi: 10.1016/j.micpro.2020.103287.

[129] N. Gupta and M. Khatri, "An Experimental Analysis of Shading on Solar Photovoltaic System," pp. 226–228, Jan. 2017.

[130] C. Luo *et al.*, "Influence and characteristic of shading on photovoltaic performance of bifacial modules and method for estimating bifacial gain," *Build. Simul.*, Feb. 2023, doi: 10.1007/s12273-022-0966-0.

[131] K. Sinapis, G. Litjens, M. Donker, W. Folkerts, and W. Sark, "Outdoor characterization and comparison of string and MLPE under clear and partially shaded conditions," *Energy Sci Eng*, vol. 3, no. 6, pp. 510–519, Nov. 2015, doi: 10.1002/ese3.97.

[132] A. Dolara, G. C. Lazaroiu, and E. Ogliari, "Efficiency analysis of PV power plants shaded by MV overhead lines," *Int J Energy Environ Eng*, vol. 7, no. 2, pp. 115–123, Jun. 2016, doi: 10.1007/s40095-016-0208-2.

[133] X. Feng and T. Ma, "Solar photovoltaic system under partial shading and perspectives on maximum utilization of the shaded land," *International Journal of Green Energy*, vol. 20, no. 4, pp. 378–389, Mar. 2023, doi: 10.1080/15435075.2022.2047977.

[134] A. Cabrera-Tobar, A. Dolara, S. Leva, D. Mazzeo, and E. Ogliari, "Comparative analysis of half-cell and full-cell PV commercial modules for sustainable mobility applications: Outdoor performance evaluation under partial shading conditions," *Sustainable Energy Technologies and Assessments*, vol. 71, p. 103981, Nov. 2024, doi: 10.1016/j.seta.2024.103981.

[135] M. Mittag, "Techno-Economic Analysis of Half Cell Modules - the Impact of Half Cells on Module Power and Costs," 2019.

[136] F. Plag *et al.*, "Comprehensive analysis of a pulsed solar simulator to determine measurement uncertainty components".

[137] INTERNATIONAL STANDARD, *Part 1: Measurement of photovoltaic current-voltage characteristics.*, IEC 60904-1:2020, Geneva, Switzerland., 2020.

[138] N. Kumari, S. K. Singh, S. Kumar, and V. K. Jadoun, "Performance analysis of partially shaded high-efficiency mono PERC/mono crystalline PV module under indoor and environmental conditions," *Scientific Reports*, vol. 14, no. 1, p. 21587, Sep. 2024, doi: 10.1038/s41598-024-72502-z.

[139] M. A. A. Mamun, M. Hasanuzzaman, and J. Selvaraj, "Experimental investigation of the effect of partial shading on photovoltaic performance," *IET Renewable Power Generation*, vol. 11, no. 7, pp. 912–921, Jun. 2017, doi: 10.1049/iet-rpg.2016.0902.

[140] J. Demouth, O. Devillers, H. Everett, M. Glisse, S. Lazard, and R. Seidel, "On the complexity of umbra and penumbra," *Computational Geometry*, vol. 42, no. 8, pp. 758–771, Oct. 2009, doi: 10.1016/j.comgeo.2008.04.007.

[141] E. Hecht, *Optics.*, 3rd ed.. Addison-Wesley, 1998.

[142] N. Jakica, "State-of-the-art review of solar design tools and methods for assessing daylighting and solar potential for building-integrated photovoltaics," *Renewable and Sustainable Energy Reviews*, vol. 81, pp. 1296–1328, Jan. 2018, doi: 10.1016/j.rser.2017.05.080.

[143] Building Regulation Office and Ministry for Transport and Infrastructure, "Nearly-Zero Energy Buildings Plan for Malta," Government of Malta, Valletta, Malta, 2015. [Online]. Available: https://energy.ec.europa.eu/system/files/2018-11/malta_en_version_0.pdf

[144] A. Grover, A. Khosla, and D. Joshi, "Design and simulation of 20MW photovoltaic power plant using PVSyst," *Indonesian Journal of Electrical Engineering and Computer Science*, vol. 19, p. 58, Jul. 2020, doi: 10.11591/ijeecs.v19.i1.pp58-65.

[145] R. Chedid, R. Tajeddine, F. Chaaban, and R. Ghajar, *Modeling and simulation of PV arrays under varying conditions*. 2014, p. 542. doi: 10.1109/MELCON.2014.6820592.

[146] K. Singh, T. Chandel, M. Mallick, and M. Siddiqui, "Effect of Bypass Diode under Partial Shading in SPV Module," vol. 8, pp. 2215–2219, Jun. 2019.

[147] M. Zebiri, M. Mediouni, and H. Idadoub, "Modeling and simulation of the shading effect on the performance of a photovoltaic module in the presence of the bypass diode.," *E3S Web Conf.*, vol. 37, p. 06002, 2018, doi: 10.1051/e3sconf/20183706002.

[148] Z. Alqaisi and Y. Mahmoud, "Comprehensive Study of Partially Shaded PV Modules With Overlapping Diodes," *IEEE Access*, vol. 7, pp. 172665–172675, 2019, doi: 10.1109/ACCESS.2019.2956916.

[149] M. Alonso-Garcia, J. Ruiz, and W. Herrmann, "Computer simulation of shading effects in photovoltaic arrays," *Renewable Energy*, vol. 31, pp. 1986–1993, Oct. 2006, doi: 10.1016/j.renene.2005.09.030.

[150] M. Silva, J. J. Roberts, and P. O. Prado, "Calculation of the Shading Factors for Solar Modules with MATLAB," *Energies*, vol. 14, no. 15, p. 4713, Aug. 2021, doi: 10.3390/en14154713.

[151] P. Singh, "Analyse the Effects of Partial Shading Conditions on Solar Photovoltaic Panels," *IJRASET*, vol. 9, no. VI, pp. 4167–4172, Jun. 2021, doi: 10.22214/ijraset.2021.35972.

[152] M. Sameeullah and A. Swarup, "Modeling of PV module to study the performance of MPPT controller under partial shading condition," in *2014 IEEE 6th India International Conference on Power Electronics (IICPE)*, Kurukshetra, India: IEEE, Dec. 2014, pp. 1–6. doi: 10.1109/IICPE.2014.7115792.

[153] R. K. Pachauri *et al.*, "Impact of Partial Shading on Various PV Array Configurations and Different Modeling Approaches: A Comprehensive Review," *IEEE Access*, vol. 8, pp. 181375–181403, 2020, doi: 10.1109/ACCESS.2020.3028473.

[154] Ajithgopi, K. Sudhakar, and N. Wai Keng, "Design and simulation of solar roof-top projects for an energy self-reliant university campus," *IOP Conference Series: Materials Science and Engineering*, vol. 1078, p. 012013, Feb. 2021, doi: 10.1088/1757-899X/1078/1/012013.

[155] S. Wolk, Z. Berzolla, L. Carethers, and C. Reinhart, *Accelerating photovoltaic potential simulations for urban building energy modeling to inform policymakers*. 2023. doi: 10.26868/25222708.2023.1389.

[156] R. Sharma and S. Goel, "Performance analysis of a 11.2 kWp roof top grid-connected PV system in Eastern India," *Energy Reports*, vol. 3, pp. 76–84, Nov. 2017, doi: 10.1016/j.egyr.2017.05.001.

[157] P. Axaopoulos, E. Fylladitakis, and K. Gkarakis, "Accuracy analysis of software for the estimation and planning of photovoltaic installations," *International Journal of Energy and Environmental Engineering*, vol. 5, Jan. 2014, doi: 10.1186/2251-6832-5-1.

[158] B. Alsayid, S. Alsadi, J. Jallad, and M. Dradi, "Partial Shading of PV System Simulation with Experimental Results," *Smart Grid and Renewable Energy*, vol. 04, pp. 429–435, Jan. 2013, doi: 10.4236/sgre.2012.46049.

[159] S. Freitas, F. Serra, and M. C. Brito, "Multi-Objective Genetic Algorithm for the Optimization of a PV System Arrangement," in *Proceedings of the ISES Solar World Congress 2015*, Daegu, Korea: International Solar Energy Society, 2016, pp. 1–7. doi: 10.18086/swc.2015.05.16.

[160] J. Robledo, J. Leloux, and E. Lorenzo, "3D simulation of complex shading affecting PV systems taking benefit from the power of graphics cards developed for the video game industry," *arXiv preprint arXiv:1410.5780*, 2014.

[161] A. Kour, V. Yv, V. Maheshwari, and D. Prashar, "A Review on Image Processing," *International Journal of Electronics Communication and Computer Engineering*, vol. 4, pp. 2278–4209, Jan. 2012.

[162] M. Abdelsattar, A. Abdelmoety, and A. Emad-Eldeen, *A Review on Detection of Solar PV Panels Failures Using Image Processing Techniques*. 2023, p. 6. doi: 10.1109/MEPCON58725.2023.10462371.

[163] A. Latoui and M. E. H. Daachi, "Real-time monitoring of partial shading in large PV plants using Convolutional Neural Network," *Solar Energy*, vol. 253, pp. 428–438, Mar. 2023, doi: 10.1016/j.solener.2023.02.041.

[164] A. Salazar and E. Q. Macabebe, "Hotspots Detection in Photovoltaic Modules Using Infrared Thermography," *MATEC Web of Conferences*, vol. 70, p. 10015, Jan. 2016, doi: 10.1051/matecconf/20167010015.

[165] S. G. Monicka, D. Manimegalai, M. Karthikeyan, and R. Gunasekari, "Image Processing Based Hot-Spot Detection on Photovoltaic Panels," *International Journal of Intelligent Systems and Applications in Engineering*.

[166] S. Salamanca, P. Merchan, and I. Garcia, "On the detection of solar panels by image processing techniques," in *2017 25th Mediterranean Conference on Control and Automation (MED)*, Valletta, Malta: IEEE, Jul. 2017, pp. 478–483. doi: 10.1109/MED.2017.7984163.

[167] C. Henry, S. Poudel, S.-W. Lee, and H. Jeong, "Automatic Detection System of Deteriorated PV Modules Using Drone with Thermal Camera," *Applied Sciences*, vol. 10, no. 11, 2020, doi: 10.3390/app10113802.

[168] M. Premkumar and R. Sowmya, "An effective maximum power point tracker for partially shaded solar photovoltaic systems," *Energy Reports*, vol. 5, pp. 1445–1462, Nov. 2019, doi: 10.1016/j.egyr.2019.10.006.

[169] Á. Bognár, R. C. G. M. Loonen, R. M. E. Valckenborg, and J. L. M. Hensen, "An unsupervised method for identifying local PV shading based on AC power and

regional irradiance data," *Solar Energy*, vol. 174, pp. 1068–1077, Nov. 2018, doi: 10.1016/j.solener.2018.10.007.

[170] K. Sinapis *et al.*, "A comprehensive study on partial shading response of c-Si modules and yield modeling of string inverter and module level power electronics," *Solar Energy*, vol. 135, pp. 731–741, Oct. 2016, doi: 10.1016/j.solener.2016.06.050.

[171] A. Gutiérrez Galeano, M. Bressan, F. Jiménez Vargas, and C. Alonso, "Shading Ratio Impact on Photovoltaic Modules and Correlation with Shading Patterns," *Energies*, vol. 11, no. 4, p. 852, Apr. 2018, doi: 10.3390/en11040852.

[172] J. Tian, L. Zhu, and Y. Tang, "Outdoor shadow detection by combining tricolor attenuation and intensity," *EURASIP J. Adv. Signal Process.*, vol. 2012, no. 1, p. 116, Dec. 2012, doi: 10.1186/1687-6180-2012-116.

[173] A. Zbeeb, V. Devabhaktuni, and A. Sebak, "Improved photovoltaic MPPT algorithm adapted for unstable atmospheric conditions and partial shading," in *2009 International Conference on Clean Electrical Power*, Jun. 2009, pp. 320–323. doi: 10.1109/ICCEP.2009.5212035.

[174] J. Ma, Z. Bi, K. L. Man, Y. Yue, and J. S. Smith, "Automatic Shading Detection System for Photovoltaic Strings," in *2018 International SoC Design Conference (ISOCC)*, Nov. 2018, pp. 176–177. doi: 10.1109/ISOCC.2018.8649960.

[175] W. Al Abri, R. A. Abri, H. Yousef, and A. Al-Hinai, "A Simple Method for Detecting Partial Shading in PV Systems," *Energies*, vol. 14, no. 16, p. 4938, Aug. 2021, doi: 10.3390/en14164938.

[176] N. Hussain Dar, *Image segmentation Techniques and its application*. 2020.

[177] S. Kesler, S. Kivrak, H. Gurleyen, F. Dincer, S. Yilmaz, and H. R. Ozcalik, "A Low Cost Shading Analyzer and Site Evaluator Design to Determine Solar Power System Installation Area," *International Journal of Photoenergy*, vol. 2015, no. 1, p. 126373, Jan. 2015, doi: 10.1155/2015/126373.

[178] S. Sural, Gang Qian, and S. Pramanik, "Segmentation and histogram generation using the HSV color space for image retrieval," in *Proceedings. International Conference on Image Processing*, Sep. 2002, p. II–II. doi: 10.1109/ICIP.2002.1040019.

[179] H. Rehman *et al.*, "Neighboring-Pixel-Based Maximum Power Point Tracking Algorithm for Partially Shaded Photovoltaic (PV) Systems," *Electronics*, vol. 11, no. 3, p. 359, Jan. 2022, doi: 10.3390/electronics11030359.

[180] A. Sinha, "Comparison of techniques used in shadow detection in an image," *ICETCSE*, vol. 14, no. Special Issue International Journal of Computer Science and Information Security (IJCSIS), 2016.

[181] J. Yousefi, *Image Binarization using Otsu Thresholding Algorithm*. 2015. doi: 10.13140/RG.2.1.4758.9284.

[182] D. Dendrinos, "ON THE FUZZY NATURE OF SHADOWS," *academia.edu*, Mar. 2017.

[183] Xiang Huang, Gang Hua, J. Tumblin, and L. Williams, "What characterizes a shadow boundary under the sun and sky?," in *2011 International Conference on Computer Vision*, Barcelona, Spain: IEEE, Nov. 2011, pp. 898–905. doi: 10.1109/ICCV.2011.6126331.

[184] K. Mirylenka, G. Giannakopoulos, and T. Palpanas, "SRF: A Framework for the Study of Classifier Behavior under Training Set Mislabeling Noise," in *Advances*

in Knowledge Discovery and Data Mining, vol. 7301, P.-N. Tan, S. Chawla, C. K. Ho, and J. Bailey, Eds., in Lecture Notes in Computer Science, vol. 7301. , Berlin, Heidelberg: Springer Berlin Heidelberg, 2012, pp. 109–121. doi: 10.1007/978-3-642-30217-6_10.

[185] Gursharn Singh and Anand Mittal, "Various Image Enhancement Techniques - A Critical Review," *International Journal of Innovation and Scientific Research*, vol. 10, no. 2, pp. 267–274, 2014.

[186] P. Sathya, M. Bhuvaneswari, G. K. G K, and K. Saravanan, "A review on image enhancement using sharpening techniques," *International Journal of Computer Vision*, pp. 78–84, Jan. 2014.

[187] X. Liu, M. Pedersen, and R. Wang, "Survey of natural image enhancement techniques: Classification, evaluation, challenges, and perspectives," *Digital Signal Processing*, vol. 127, p. 103547, Jul. 2022, doi: 10.1016/j.dsp.2022.103547.

[188] K. A. Panetta, E. J. Wharton, and S. S. Agaian, "Human Visual System-Based Image Enhancement and Logarithmic Contrast Measure," *IEEE Transactions on Systems, Man, and Cybernetics, Part B (Cybernetics)*, vol. 38, no. 1, pp. 174–188, Feb. 2008, doi: 10.1109/TSMCB.2007.909440.

[189] M. Nurfakhrian Aziz, T. Purboyo, and A. Prasasti, "A survey on the implementation of image enhancement," *International Journal of Applied Engineering Research*, vol. 12, pp. 11451–11459, Jan. 2017.

[190] M. Ramkumar and B. Karthikeyan, "A survey on image enhancement methods," *International Journal of Engineering and Technology*, vol. 5, pp. 960–962, Jan. 2013.

[191] S. Dubey and M. Dixit, "Image Enhancement Techniques: An Exhaustive Review," 2020, pp. 363–375. doi: 10.1007/978-3-030-44758-8_34.

[192] S. -C. Huang, F. -C. Cheng, and Y. -S. Chiu, "Efficient Contrast Enhancement Using Adaptive Gamma Correction With Weighting Distribution," *IEEE Transactions on Image Processing*, vol. 22, no. 3, pp. 1032–1041, Mar. 2013, doi: 10.1109/TIP.2012.2226047.

[193] S. S. Al-amri and N. V. Kalyankar, "Image Segmentation by Using Thershod Techniques," vol. 2, no. 5, 2010.

[194] T. Celebi, I. Shayea, A. A. El-Saleh, S. Ali, and M. Roslee, "Histogram Equalization for Grayscale Images and Comparison with OpenCV Library," in *2021 IEEE 15th Malaysia International Conference on Communication (MICC)*, Dec. 2021, pp. 92–97. doi: 10.1109/MICC53484.2021.9642082.

[195] C. Bishop, "Pattern Recognition and Machine Learning," in *Journal of Electronic Imaging*, vol. 16, 2006, pp. 140–155. doi: 10.1117/1.2819119.

[196] W. Wu, X. Wu, and Y. Wan, "Single-image shadow removal using detail extraction and illumination estimation," *The Visual Computer*, vol. 38, Mar. 2021, doi: 10.1007/s00371-021-02096-4.

[197] S. A. Anwar and M. Z. Abdullah, "Micro-crack detection of multicrystalline solar cells featuring an improved anisotropic diffusion filter and image segmentation technique," *EURASIP Journal on Image and Video Processing*, vol. 2014, no. 1, p. 15, Mar. 2014, doi: 10.1186/1687-5281-2014-15.

[198] Z. Ju, L. Gun, A. Hussain, M. Mahmud, and C. Ieracitano, "A Novel Approach to Shadow Boundary Detection Based on an Adaptive Direction-Tracking Filter

for Brain-Machine Interface Applications," *Applied Sciences*, vol. 10, no. 19, 2020, doi: 10.3390/app10196761.

[199] J.-F. Lalonde, A. Efros, and S. Narasimhan, *Detecting Ground Shadows in Outdoor Consumer Photographs*, vol. 6312. 2010, p. 335. doi: 10.1007/978-3-642-15552-9_24.

[200] T. Kappler, A. S. Starosta, N. Munzke, B. Schwarz, and M. Hiller, "Detection of shading for short-term power forecasting of photovoltaic systems using machine learning techniques," *EPJ Photovolt.*, vol. 15, 2024, doi: 10.1051/epjpv/2024013.

[201] T. Kappler, A. Starosta, N. Munzke, B. Schwarz, and M. Hiller, *Detection of Shading for Solar Power Forecasting Using Machine Learning Techniques*. 2023. doi: 10.4229/EUPVSEC2023/4AO.9.6.

[202] J. Olivares, T. Depe, K. Sood, and R. Mahto, "Predictive Modeling of Shading Effects on Photovoltaic Panels Using Regression Analysis," Dec. 10, 2024, *arXiv*: arXiv:2412.17828. doi: 10.48550/arXiv.2412.17828.

[203] J. Gaboitaolelwe, A. M. Zungeru, A. Yahya, C. K. Lebekwe, D. N. Vinod, and A. O. Salau, "Machine Learning Based Solar Photovoltaic Power Forecasting: A Review and Comparison," *IEEE Access*, vol. 11, pp. 40820–40845, 2023, doi: 10.1109/ACCESS.2023.3270041.

[204] Z. Mustafa, M. Azzouz, A. Awad, and A. Azab, "A Scalable Random Forest-Based Scheme to Detect and Locate Partial Shading in Photovoltaic Systems," *SSRN Journal*, 2022, doi: 10.2139/ssrn.4272809.

[205] T. Adenekan, "Advanced Detection of Faults and Partial Shading in Photovoltaic Systems," Oct. 2024.

[206] B. K. Karmakar and A. Pradhan, "Detection and Classification of Faults in Solar PV Array Using Thevenin Equivalent Resistance," *IEEE Journal of Photovoltaics*, vol. PP, pp. 1–11, Mar. 2020, doi: 10.1109/JPHOTOV.2019.2959951.

[207] G. M. Tina, C. Ventura, S. Ferlito, and S. De Vito, "A State-of-Art-Review on Machine-Learning Based Methods for PV," *Applied Sciences*, vol. 11, no. 16, 2021, doi: 10.3390/app11167550.

[208] M. Axisa, M. Demicoli, and L. Mule'Stagno, "Analysing the Effects of Thin Object Shading on PV Sources: A Dual Approach Combining Outdoor and Laboratory Solar Simulator Experimentation," *Energies*, vol. 17, no. 9, 2024, doi: 10.3390/en17092069.

[209] A. Duhis and M. Alkafaji, "Increasing photovoltaic system power output with white paint albedo -a scenario in Al-Mausaib City using PVSyst. software," *International Journal of Power Electronics and Drive Systems*, vol. 14, pp. 1149–1159, Jun. 2023, doi: 10.11591/ijpeds.v14.i2.pp1149-1159.

[210] Y. Kotak, M. Gul, T. Muneer, and S. Ivanova, *Investigating the Impact of Ground Albedo on the Performance of PV Systems*. 2015.

[211] Y. Chua, K. Chin, and T. Tay, *Investigating effect of different reflective surfaces on solar thermal collector*, vol. 1902. 2017. doi: 10.1063/1.5010675.

[212] C. A. Reynaud, R. Clerc, P. B. Lechêne, M. Hébert, A. Cazier, and A. C. Arias, "Evaluation of indoor photovoltaic power production under directional and diffuse lighting conditions," *Solar Energy Materials and Solar Cells*, vol. 200, p. 110010, Sep. 2019, doi: 10.1016/j.solmat.2019.110010.

[213] S. R. Wenham, *Applied photovoltaics*, 2nd ed.. Earthscan, 2007.

[214] University of Malta, "University of Malta - Weather Station," University of Malta - Weather Station. Accessed: May 02, 2025. [Online]. Available: https://www.um.edu.mt/ise/weatherstation/realtime.html

[215] International Electrotechnical Commission, "IEC 60891:2021 - Photovoltaic devices – Procedures for temperature and irradiance corrections to measured I-V characteristics," Oct. 2021, [Online]. Available: https://webstore.iec.ch/en/publication/61766

[216] S. Luciani, G. Coccia, S. Tomassetti, M. Pierantozzi, and G. Di Nicola, "Correction Procedures for Temperature and Irradiance of Photovoltaic Modules: Determination of Series Resistance and Temperature Coefficients by Means of an Indoor Solar Flash Test Device," *TI-IJES*, vol. 65, no. 2–4, pp. 264–270, Jul. 2021, doi: 10.18280/ti-ijes.652-419.

[217] "Photo Emission Tech – Solar Simulator, Simulator Solar, Light Source, Full Spectrum Light, Solar Simulation Systems, IV Measurement System - Solar Simulator Model SS150AAA." Accessed: May 02, 2025. [Online]. Available: https://www.photoemission.com/SS150A.html

[218] D. Rangelov, S. Waanders, K. Waanders, M. van Keulen, and R. Miltchev, "Impact of Camera Settings on 3D Reconstruction Quality: Insights from NeRF and Gaussian Splatting," *Sensors*, vol. 24, no. 23, 2024, doi: 10.3390/s24237594.

[219] C. Giraud-Carrier, R. Vilalta, and P. Brazdil, "Introduction to the Special Issue on Meta-Learning," *Machine Learning*, vol. 54, pp. 187–193, Mar. 2004, doi: 10.1023/B:MACH.0000015878.60765.42.

[220] G. Di Leo and F. Sardanelli, "Statistical significance: p value, 0.05 threshold, and applications to radiomics—reasons for a conservative approach," *European Radiology Experimental*, vol. 4, p. 18, Mar. 2020, doi: 10.1186/s41747-020-0145-y.

[221] S. Sinzinger, "3.02 - Diffractive and Defractive Micro-optics," in *Comprehensive Microsystems*, Y. B. Gianchandani, O. Tabata, and H. Zappe, Eds., Oxford: Elsevier, 2008, pp. 65–99. doi: 10.1016/B978-044452190-3.00033-1.

[222] B. Reinhardt, R. Buras-Schnell, L. Bugliaro, and B. Mayer, "Determination of the Sunshape from Meteosat Second Generation," Jan. 2012.

[223] M. Mussard and O. J. Nydal, "Influence of Solar Tracking Inaccuracy and Sun Rays Modeling on the Efficiency of a Small-scale Parabolic Trough," *Energy Procedia*, vol. 57, pp. 1508–1515, Jan. 2014, doi: 10.1016/j.egypro.2014.10.143.

[224] C. Aime, E. Aristidi, and Y. Rabbia, "The Fresnel Diffraction: A Story of Light and Darkness," *EAS Publications Series*, vol. 59, pp. 37–58, Mar. 2013, doi: 10.1051/eas/1359003.

[225] "Photo Emission Tech., Inc.CELL TESTER MODEL # CT150AAA," Specification sheet of CELL TESTER MODEL # CT150AAA. [Online]. Available: https://photoemission.com/wp-content/uploads/2025/07/CT150AAA_Cell_Tester_Rev._G_Specs.pdf

[226] F. L. Anderson, "Huygens' Principle geometric derivation and elimination of the wake and backward wave," *Scientific Reports*, vol. 11, no. 1, p. 20257, Oct. 2021, doi: 10.1038/s41598-021-99049-7.

[227] A. G. Sedukhin, "Discontinuity-free edge-diffraction model for characterization of focused wave fields," *J. Opt. Soc. Am. A*, vol. 27, no. 3, pp. 622–631, Mar. 2010, doi: 10.1364/JOSAA.27.000622.

[228] M. Gu and X. S. Gan, “Fresnel diffraction by circular and serrated apertures illuminated with an ultrashort pulsed-laser beam,” *J. Opt. Soc. Am. A*, vol. 13, no. 4, pp. 771–778, Apr. 1996, doi: 10.1364/JOSAA.13.000771.

[229] X.-H. Luo, H. Mei, Q.-D. Zhu, S.-S. Wang, and Y.-L. Hou, “Quantum-mathematical model of edge and peak point in Fresnel diffraction through a slit,” *Chinese Physics B*, vol. 26, p. 054202, May 2017, doi: 10.1088/1674-1056/26/5/054202.

[230] M. Axisa, L. Mule’Stagno, and M. Demicoli, “Quantifying the effect of shadow formation on photovoltaic sources under thin object shading: an image analysis approach,” *EPJ Photovolt.*, vol. 16, 2025, doi: 10.1051/epjpv/2025005.

[231] M. Axisa, L. Mule’Stagno, and M. Demicoli, *Correlating field experimentation and image analysis for the assessment of induced losses from thin object shading on photovoltaic sources*. 2024. doi: 10.4229/EUPVSEC2024/3DO.20.2.

[232] M. Seyedmahmoudian *et al.*, “Simulation and Hardware Implementation of New Maximum Power Point Tracking Technique for Partially Shaded PV System Using Hybrid DEPSO Method,” *IEEE Transactions on Sustainable Energy*, vol. PP, pp. 1–13, Jul. 2015, doi: 10.1109/TSTE.2015.2413359.

[233] D. Mahmoud, A. Bouchelaghem, and G. Abderezak, “A Novel Method to obtain Reverse bias I-V Curves for Single Cells Integrated in Photovoltaic Modules Power Electronics and Drives,” *Power Electronics and Drives*, vol. 9, Jul. 2024, doi: 10.2478/pead-2024-0027.

[234] K. Lappalainen and S. Valkealahti, “Experimental study of the maximum power point characteristics of partially shaded photovoltaic strings,” *Applied Energy*, vol. 301, p. 117436, Nov. 2021, doi: 10.1016/j.apenergy.2021.117436.

[235] J. Gallon, “PV Module Hotspot Detection,” p. 1.

[236] A. Heck, “Point tracking and image rectification in video activities,” *PLOS Biology - PLOS BIOL*, Jan. 2005.

[237] C. Wang, Y. Ding, K. Cui, J. Li, Q. Xu, and J. Mei, “A Perspective Distortion Correction Method for Planar Imaging Based on Homography Mapping,” *Sensors*, vol. 25, no. 6, p. 1891, 2025, doi: 10.3390/s25061891.

[238] K. Bedrich, “Quantitative Electroluminescence Measurements of PV Devices,” 2017. doi: 10.13140/RG.2.2.33490.25280.

[239] ImageOnline.io, “Perspective Tool – Online Perspective Correction Utility.” [Online]. Available: https://imageonline.io/perspective-tool/

[240] T. Kumar and K. Verma, “A Theory Based on Conversion of RGB image to Gray image,” *International Journal of Computer Applications*, vol. 7, Sep. 2010, doi: 10.5120/1140-1493.

[241] J. Zar, “Spearman Rank Correlation,” in *Encycl Biostat*, vol. 5, 2005. doi: 10.1002/0470011815.b2a15150.

[242] D. J. Sheskin, *Handbook of parametric and nonparametric statistical procedures*. Chapman and hall/CRC, 2003.

[243] A. Field, *Discovering statistics using SPSS.*, 2nd ed. in ISM introducing statistical methods. Sage, 2005.

[244] J. F. Hair, *Research Methods for Business*. John Wiley & Sons, 2007. [Online]. Available: https://archive.org/details/researchmethodsf0000unse_j4k9/page/358/mode/2up?q=moderate

[245] Z. Mustafa, M. Azzouz, A. Awad, and A. Azab, “A Scalable Random Forest-Based Scheme to Detect and Locate Partial Shading in Photovoltaic Systems,” *SSRN Journal*, 2022, doi: 10.2139/ssrn.4272809.

[246] V. F. Rodriguez-Galiano, B. Ghimire, J. Rogan, M. Chica-Olmo, and J. P. Rigol-Sanchez, “An assessment of the effectiveness of a random forest classifier for land-cover classification,” *ISPRS Journal of Photogrammetry and Remote Sensing*, vol. 67, pp. 93–104, Jan. 2012, doi: 10.1016/j.isprsjprs.2011.11.002.

[247] L. Breiman, “Random Forests,” *Machine Learning*, vol. 45, no. 1, pp. 5–32, Oct. 2001, doi: 10.1023/A:1010933404324.

[248] D. K. Bilolikar, A. More, A. Gong, and J. Janssen, “How to out-perform default random forest regression: choosing hyperparameters for applications in large-sample hydrology,” *arXiv preprint arXiv:2305.07136*, 2023.

[249] M. Guillame-Bert, S. Bruch, R. Stotz, and J. Pfeifer, “Yggdrasil decision forests: A fast and extensible decision forests library,” presented at the Proceedings of the 29th ACM SIGKDD Conference on Knowledge Discovery and Data Mining, 2023, pp. 4068–4077.

[250] K. Basaran, A. Çelikten, and H. Bulut, “A short-term photovoltaic output power forecasting based on ensemble algorithms using hyperparameter optimization,” *Electrical Engineering*, vol. 106, pp. 5319–5337, Feb. 2024, doi: 10.1007/s00202-024-02281-3.

[251] G. Sahin, G. Isik, and W. G. J. H. M. Van Sark, “Predictive modeling of PV solar power plant efficiency considering weather conditions: A comparative analysis of artificial neural networks and multiple linear regression,” *Energy Reports*, vol. 10, pp. 2837–2849, Nov. 2023, doi: 10.1016/j.egyr.2023.09.097.

[252] T. Chai and R. Draxler, “Root mean square error (RMSE) or mean absolute error (MAE)?,” *Geosci. Model Dev.*, vol. 7, Jan. 2014, doi: 10.5194/gmdd-7-1525-2014.

[253] N. R. Draper and H. Smith, *Applied Regression Analysis*. in Wiley Series in Probability and Statistics. Wiley, 1998. [Online]. Available: https://books.google.com.mt/books?id=d6NsDwAAQBAJ

[254] K. Song, J. Jeong, J.-H. Moon, S.-C. Kwon, and H. Kim, “DTTrans: PV Power Forecasting Using Delaunay Triangulation and TransGRU,” *Sensors*, vol. 23, no. 1, 2023, doi: 10.3390/s23010144.

[255] C. Idogho *et al.*, “Machine Learning-Based Solar Photovoltaic Power Forecasting for Nigerian Regions,” *Energy Science & Engineering*, vol. 13, no. 4, pp. 1922–1934, Apr. 2025, doi: 10.1002/ese3.70013.

[256] K. Bot, A. Ruano, and M. D. Ruano, “Short-Term Forecasting Photovoltaic Solar Power for Home Energy Management Systems,” *Inventions*, vol. 6, no. 1, 2021, doi: 10.3390/inventions6010012.

[257] E. A. Setiawan, M. Fathurrahman, R. F. Pamungkas, and S. Ma’arif, “Fast Partial Shading Detection on PV Modules for Precise Power Loss Ratio Estimation Using Digital Image Processing,” *Journal of Electrical and Computer Engineering*, vol. 2024, no. 1, p. 9385602, Jan. 2024, doi: 10.1155/2024/9385602.

[258] “Geometrical Optics Laboratory.” Accessed: Jan. 07, 2025. [Online]. Available: https://www.animations.physics.unsw.edu.au/labs/geometrical-optics/geometrical-optics-lab.html

[259] Dr. M. K. Salama, “Optimization of Regression Models Using Machine Learning: A Comprehensive Study with Scikit-learn,” *International Uni-Scientific Research Journal*, vol. 5, Sep. 2024, doi: 10.59271/s45500.024.0624.16.

[260] T. B. Nadeem, S. U. Ali, M. Asif, and H. K. Suberi, “Forecasting daily solar radiation: An evaluation and comparison of machine learning algorithms,” *AIP Advances*, vol. 14, no. 7, p. 075010, Jul. 2024, doi: 10.1063/5.0211723.

[261] A. Lari, “Forecasting and Prediction of Solar Energy Generation using Machine Learning Techniques,” PhD, Swansea University, Swansea, 2024. doi: 10.23889/SUThesis.66094.

[262] H. Belyadi and A. Haghighat, “Chapter 5 - Supervised learning,” in *Machine Learning Guide for Oil and Gas Using Python*, H. Belyadi and A. Haghighat, Eds., Gulf Professional Publishing, 2021, pp. 169–295. doi: 10.1016/B978-0-12-821929-4.00004-4.

[263] A. Osadolor, A. Showole, T. Eze, R. Owulo, and G. Asamoah, “Illuminating the Future: Predictive Modelling of PV Output Using Machine Learning Techniques,” *European Journal of Artificial Intelligence and Machine Learning*, vol. 3, pp. 9–13, Jun. 2024, doi: 10.24018/ejai.2024.3.2.41.

[264] H. Shareef, A. H. Mutlag, and A. Mohamed, “Random Forest-Based Approach for Maximum Power Point Tracking of Photovoltaic Systems Operating under Actual Environmental Conditions,” *Computational Intelligence and Neuroscience*, vol. 2017, pp. 1–17, 2017, doi: 10.1155/2017/1673864.

[265] S. Kumar, S. Gupta, V. Pratik, and P. Brunet, “Comparative Study of MPPT and Parameter Estimation of PV cells,” *arXiv preprint arXiv:2304.07817*, 2023.

[266] P. S. Myles and J. Cui, “I. Using the Bland–Altman method to measure agreement with repeated measures,” *BJA: British Journal of Anaesthesia*, vol. 99, no. 3, pp. 309–311, Sep. 2007, doi: 10.1093/bja/aem214.

[267] J. Van Der Donckt, J. Van Der Donckt, E. Deprost, and S. Van Hoecke, “Plotly-resampler: Effective visual analytics for large time series,” presented at the 2022 IEEE Visualization and Visual Analytics (VIS), IEEE, 2022, pp. 21–25.

[268] L. Addepalli *et al.*, “Assessing the Performance of Python Data Visualization Libraries: A Review,” *International Journal of Computer Engineering in Research Trends*, vol. 10, pp. 28–39, Jan. 2023, doi: 10.22362/ijcert/2023/v10/i01/v10i0104.

[269] M. Summerfield, “Rapid GUI programming with Python and Qt: the definitive guide to PyQt programming,” Jan. 2007.

[270] Soliev Bakhromjon Nabijonovich and G‘iyosiddinov Najmiddin, “Optimizing PyQt5 development with Qt Designer,” *Web teach.*, vol. 2, no. 4, pp. 254–259, Apr. 2024.

[271] D. Phillips, *Creating apps in Kivy: mobile with Python*. O’Reilly Media, Inc., 2014.

[272] S. F. M, S. P. R, S. Shanmugavadivel, and M. S. M. Sivaraja, “No-Code Cross-Platform Application Framework for Customizable User Interfaces,” in *2024 International Conference on Recent Innovation in Smart and Sustainable Technology (ICRISST)*, Mar. 2024, pp. 1–6. doi: 10.1109/ICRISST59181.2024.10921839.

[273] R. Ramanath and M. S. Drew, “Penumbra and Umbra,” in *Computer Vision: A Reference Guide*, K. Ikeuchi, Ed., Boston, MA: Springer US, 2014, pp. 589–590. doi: 10.1007/978-0-387-31439-6_513.

[274] A. De Rosa, A. Bortot, and F. Bergamo, *In Praise of Penumbra*. John Wiley & Sons, 2023.

[275] M.-A. Serrano and J. C. Moreno, “Spectral transmission of solar radiation by plastic and glass materials,” *Journal of Photochemistry and Photobiology B: Biology*, vol. 208, p. 111894, Jul. 2020, doi: 10.1016/j.jphotobiol.2020.111894.

[276] I. Duarte, A. Rotter, A. Malvestiti, and M. Hafner, “The role of glass as a barrier against the transmission of ultraviolet radiation: An experimental study,” *Photodermatology, photoimmunology & photomedicine*, vol. 25, pp. 181–4, Sep. 2009, doi: 10.1111/j.1600-0781.2009.00434.x.

[277] B. Littlejohn, K. Heeger, T. Wise, E. Gettrust, and M. Lyman, “UV degradation of the optical properties of acrylic for neutrino and dark matter experiments,” *Journal of Instrumentation*, vol. 4, no. 09, p. T09001, 2009.

[278] L. Simonot, M. Hébert, S. Mazauric, and R. D. Hersch, “Assessing the proper color of translucent materials by an extended two-flux model from measurements based on an integrating sphere,” *Electronic Imaging*, vol. 2017, pp. 48–56, Jan. 2017, doi: 10.2352/ISSN.2470-1173.2017.8.MAAP-291.

[279] V. Kalyani and V. Sharma, “Different types of Optical Filters and their Realistic Application,” *Journal of Management Engineering and Information Technology*, vol. 3, Jun. 2016.

[280] E. Y. Lam and G. S. K. Fung, “Automatic white balancing in digital photography,” in *Single-Sensor Imaging: Methods and Applications for Digital Cameras*, 2008, pp. 267–294.

[281] G. Heron and G. N. Dutton, “The Pulfrich phenomenon and its alleviation with a neutral density filter.,” *Br J Ophthalmol*, vol. 73, no. 12, p. 1004, Dec. 1989, doi: 10.1136/bjo.73.12.1004.

[282] Murakami Color Research Laboratory, “ND filter.” [Online]. Available: https://www.mcrl.co.jp/english/products/p_standard/detail/NDfilters.html

[283] Kase Filters, “Using Graduated ND Filters.” [Online]. Available: https://kasefilters.eu/nice-to-know/guides/using-graduated-nd-filters/

[284] R. Willey, “Designing Metallic Neutral Density Filters with Constant Optical Density Versus Wavelength,” *Space Science Journal*, vol. 1, pp. 01–07, Jul. 2024, doi: 10.33140/SSJ.01.02.08.

[285] J. E. Shelby, “OPTICAL MATERIALS | Color Filter and Absorption Glasses,” in *Encyclopedia of Modern Optics*, R. D. Guenther, Ed., Oxford: Elsevier, 2005, pp. 440–446. doi: 10.1016/B0-12-369395-0/00871-X.

[286] “Lee Filters,” LEE Filters UK and shop for high-quality lighting and camera filters. [Online]. Available: https://leefiltersdirect.com

[287] “Understanding Neutral Density Filters | Edmund Optics.” Accessed: May 08, 2025. [Online]. Available: https://www.edmundoptics.com/knowledge-center/application-notes/optics/understanding-neutral-density-filters/?srsltid=AfmBOorwBdA2g5zdwLEDddyzul6popAOdCHe_N_jGyJezKwTqgpO72Dj

[288] K. Khobragade, *A Comparative study of Converting Coloured Image to Gray-scale Image using Different Technologies*. 2012.

[289] S. Soni, P. Singh, and A. Waoo, “Review of gamma correction techniques in digital imaging,” *ShodhKosh: Journal of Visual and Performing Arts*, vol. 5, May 2024, doi: 10.29121/shodhkosh.v5.i5.2024.1902.

[290] J. Singnoo and G. Finlayson, *Understanding the Gamma Adjustment of Images*. 2010.

[291] H. Farid, “Blind inverse gamma correction,” *IEEE transactions on image processing : a publication of the IEEE Signal Processing Society*, vol. 10, pp. 1428–33, Feb. 2001, doi: 10.1109/83.951529.

[292] A. Alshammari, “Implementation of Curve Fitting using Polynomial Regression in Python,” *International Journal of Computer Applications*, vol. 186, pp. 27–32, Jan. 2024, doi: 10.5120/ijca2024923400.

[293] B. Ayyub and R. Mccuen, “Curve Fitting and Regression Analysis,” 2015, pp. 331–394. doi: 10.1201/b19115-10.

[294] M. Rezagholizadeh and J. Clark, “Image Sensor Modeling: Color Measurement at Low Light Levels,” *Color and Imaging Conference*, vol. 58, Nov. 2014, doi: 10.2352/J.ImagingSci.Technol.2014.58.3.030401.

[295] R. M. West, “Best practice in statistics: Use the Welch t-test when testing the difference between two groups,” *Ann Clin Biochem*, vol. 58, no. 4, pp. 267–269, Jul. 2021, doi: 10.1177/0004563221992088.

[296] E. U. Oti, M. O. Olusola, and P. A. Esemokumo, “Statistical Analysis of the Median Test and the Mann-Whitney U Test,” vol. 7, no. 9, 2021.

[297] C. Yang and H. Fang, “A New Nonlinear Model-Based Fault Detection Method Using Mann–Whitney Test,” *IEEE Transactions on Industrial Electronics*, vol. 67, pp. 10856–10864, Dec. 2020, doi: 10.1109/TIE.2019.2958297.

[298] G. M. Sullivan and R. Feinn, “Using Effect Size—or Why the *P* Value Is Not Enough,” *Journal of Graduate Medical Education*, vol. 4, no. 3, pp. 279–282, Sep. 2012, doi: 10.4300/JGME-D-12-00156.1.

[299] D. Lakens, “Calculating and reporting effect sizes to facilitate cumulative science: a practical primer for t-tests and ANOVAs,” *Frontiers in Psychology*, vol. Volume 4-2013, 2013, [Online]. Available: https://www.frontiersin.org/journals/psychology/articles/10.3389/fpsyg.2013.00863

[300] J. P. Holman, *Experimental methods for engineers*, 8. ed. in McGraw Hill Series in Mechanical Engineering. New York: McGraw-Hill, 2012.

[301] Canon Europe, “Canon EOS 6D Specifications.” Accessed: Nov. 29, 2025. [Online]. Available: https://www.canon-europe.com/for_home/product_finder/cameras/digital_slr/eos_6d/specifications/

Appendices

Appendix A

Peer-reviewed publications related to this research:

- M. Axisa, M. Demicoli, and L. Mule'Stagno, "Analysing the Effects of Thin Object Shading on PV Sources: A Dual Approach Combining Outdoor and Laboratory Solar Simulator Experimentation," Energies, vol. 17, no. 9, 2024, doi: 10.3390/en17092069.

- M. Axisa, L. Mule'Stagno, and M. Demicoli, "Quantifying the effect of shadow formation on PV sources under thin object shading: an image analysis approach," *EPJ Photovolt.*, vol. 16, 2025, doi: 10.1051/epjpv/2025005.

- M. Axisa, L. Mule' Stagno, and M. Demicoli, "Penumbra shadow imaging: new insights into the limitations of conventional shadowgraph intensity," Applied Sciences, vol. 15, no. 17, p. 9820, 2025.

Conference papers:

- M. Axisa, "Correlating field experimentation and image analysis for the assessment of induced losses from thin object shading on photovoltaic sources," 2024. doi: 10.4229/EUPVSEC2024/3DO.20.2.

- M. Axisa, M. Demicoli, and L. Mule'Stagno, "Enhancing Photovoltaic Energy Efficiency through Thin Object Shade Analysis," *World Sustainable Energy Days (WSED), Young Energy Researchers at Wels/Austria*, March. 2024.

Conferences and events attended and presented:

- Presented the research concept at the 2023 SEA-EU Doctoral Students Training event in Cadiz, Spain.

- Presented a poster illustrating the initial findings of Chapter 4 at the University of Malta research EXPO 2023 in Valletta, Malta.

- Delivered an oral presentation at the 2024 World Sustainability Energy Days (WSED), Young Energy Researchers related to Chapter 4 of this research in Wels, Austria.

- Delivered an oral presentation about the initial findings of Chapter 5 at the University of Malta (UM) research EXPO 2024 in Valletta, Malta.

- Delivered an oral presentation related to the findings of Chapter 5 at the 2024 first 'Being Sea-EU' conference in Valletta, Malta.

- Delivered an oral presentation on the finalised findings of Chapter 5 at the 41st edition of EU PVSEC 2024 conference in Vienna, Austria.

- Successfully completed the UoM introduction, intermediate and advanced statistical SPSS courses delivered by Prof. Liberato Camilleri in 2024.

Funding acquired:

- Tertiary Education Scholarship Scheme (TESS) funding the tuition fees throughout the 3-year PhD.
- Fully funded conference WSED Conference 2024 by the scientific committee.

- Research, Innovation and Development Trust (RIDT) Overseas Conference Grants for Doctoral Students subsidizing 75% of the expenses incurred for the EU PVSEC conference in Vienna, Austria.

- Subsidised journal article processing charge (APC) for publication in EPJ Photovoltaics, awarded for being one of the most representative papers submitted to the EU PVSEC 2024 Conference.

Appendix B

The experimental procedures described in this thesis have been subjected to repeated measurements in order to minimise the potential impact of anomalies and outliers in the collected data. Nevertheless, a degree of uncertainty remains in the power loss measurements due to the use of different measuring devices. Consequently, the following subsections will henceforth analyse the associated uncertainties in relation to the experimental methodology employed.

Appendix B.1 - Uncertainty Analysis for Chapter 4 Section 4.3.3, Chapter 5 Section 5.3.1, Chapter 5, Section 5.3.4 and Chapter 6 Section 6.3

The experimental setup described in Chapter 4 Section 4.3.3, and Chapter 5, Section 5.3.1, both utilised the same data logging device with high-accuracy voltage measurement capabilities (±[0.05% of span + 10 µV]). While the data logger was not capable of directly measuring current, it measured the voltage drop across a known shunt resistor, as detailed in Chapter 4, Section 4.2.2. This allowed for the derivation of the PV module's current output under fixed load conditions.

The uncertainties associated with the components within the electrical circuit were identified based on their specified accuracy levels, as these were deemed to influence the calculated power loss. The key sources of uncertainty include:

- Fixed load resistors: Specified accuracy of ±1%, as provided by the manufacturer.
- Shunt resistors: Specified accuracy of ±1%, according to manufacturer specifications.
- Data logging device (DATAQ DI-808): Accuracy of ±(0.05% of span + 10 µV), as stated in the manufacturer datasheet.

In addition, certain uncertainties were classified as excluded uncertainties based on the assumption that their impact on the overall power loss is negligible. These are outlined as follows:

- Resistance of the DC circuit cables: The cables connecting the electrical box to the data logger are less than 0.1 meters in length, and their resistance is considered minimal.
- Resistance of the MC4 connectors: Used to interface the PV module with the circuit box (which includes the data logger, fixed load resistors, and shunt), these connectors contribute negligible resistance.
- Resistance of the DC cable between the MC4 connectors and the circuit box: This segment of the wiring was also determined to have an insignificant effect on measurement accuracy since the length is under 1 meter.

To evaluate the relative power loss between the control and shaded PV source and to quantify the associated uncertainty, the method of uncertainty propagation was employed, following the approach outlined in Holman's Experimental Methods for Engineers, specifically Example 3.2 [300, p. 67].

The first source of uncertainty considered was the voltage drop which was measured using the DATAQ DI-808, with a specified accuracy of ±(0.05% of span + 10 μV). Given that the additional 10 μV is negligible in comparison to 0.05% of the measurement span, it was deemed insignificant and excluded from the uncertainty calculation, in accordance with Holman's guidance at the bottom of page [300, p. 67]. The second source of uncertainty, relates to the resistance value of the shunt resistor. This resistor had a known value with a specified accuracy of ±1%. In Holman's Section 3.4 Example 3.2, an uncertainty equation based on the principle of the following power equation was derived, as explained subsequently.

$$P = \frac{V^2}{R}$$

Now the uncertainty partial derivative formula must be applied:

Since the variable P (Power) depends on two independent variables, V (Voltage) and R (Resistance), there are two possible first-order partial derivatives.

The partial derivative with respect to Voltage (V), R is treated as a constant and V^2 is differentiated as seen below:

$$\frac{\partial P}{\partial V} = \frac{1}{R}\frac{\partial}{\partial V}(V^2)$$

$$\frac{\partial P}{\partial V} = \frac{1}{R}(2V)$$

Resultant:

$$\frac{\partial P}{\partial V} = \frac{2V}{R}$$

Partial derivative with respect to Resistance (R) can be found by treating V as a constant and differentiate $\frac{1}{R}$ (which is R^{-1}).

$$\frac{\partial P}{\partial R} = V^2\frac{\partial}{\partial R}(R^{-1}) = -\frac{V^2}{R^2}$$

The general formula used by Holman (Example 3.2) was used for the uncertainty (w_P) of a function P(V, R) is the square root of the sum of the squares of the partial derivatives multiplied by their uncertainties:

$$w_P = \sqrt{(\frac{\partial P}{\partial V}\, w_V)^2 + (\frac{\partial P}{\partial R}\, w_R)^2}$$

From the previous discussion, the derivatives for $P = \frac{V^2}{R}$ where found to be:

$$\frac{\partial P}{\partial V} = \frac{2V}{R}, \frac{\partial P}{\partial R} = -\frac{V^2}{R^2}$$

The above are substituted into the general formula:

$$w_P = \sqrt{(\frac{2V}{R} w_V)^2 + (-\frac{V^2}{R^2} w_R)^2}$$

Moreover, once the power uncertainties for both the control PV source and the shaded PV source were established, the power loss ratio was calculated using the below equation:

$$\text{Power loss ratio} = 1 - \frac{P_{\text{shaded}}}{P_{\text{control}}}$$

The final step is to determine the uncertainty associated with the power loss as a ratio, the power uncertainties of both the control and shaded PV sources must be taken into account as outlined the below equation:

$$w_{\text{Loss}} = \sqrt{(\frac{w_{P_{\text{shaded}}}}{P_{\text{shaded}}})^2 + (\frac{w_{P_{\text{control}}}}{P_{\text{control}}})^2}$$

The final value power loss uncertainty is expressed as a '±' value alongside the power loss expressed as a ratio of the shaded and control power loss. This is applied for each power loss measurement in Chapter 4 Section 4.3.3, Chapter 5 Section 5.3.1, Chapter 5, Section 5.3.4 and Chapter 6 Section 6.3.

Appendix B.2 - Uncertainty Analysis for Chapter 4 Section 4.3.1 and 4.3.3

The uncertainty analysis previously presented was specifically developed for the outdoor experiments conducted on small-scale PV sources, based on the measurement circuit used to determine power loss via a data logger. In contrast, the experiments described in Chapter 4 Section 4.3.1 and 4.3.3, were conducted in a laboratory environment using a Photo Emission Tech solar simulator in complimentary I–V measurement system (CC Series models).

The uncertainties in both voltage and current measurements were determined based on the theoretical derivation provided by the manufacturer, specifically outlined in Section V of the operating manual. Measurements were conducted using manual range selection, tailored to the specifications of the tested solar cell. Voltage was measured directly at the busbars of the solar cell using one of the predefined measurement ranges. The lower limit of the range consisted of 1 V (with the signal amplified by a factor of 5) and the upper as 10 V (with the signal attenuated by a factor of 0.5). Given that the Data Acquisition card (DAQ) card of the I-V measurement system is equipped with its own amplifiers, these standard ranges can be further customised by the user to define intermediate ranges. As such, a 0.8 V range was determined to be the most suitable for the solar cell under test, aligning with its expected output characteristics.

According to the specifications of the DAQ system, the analog-to-digital converter (ADC) operates with a 16-bit resolution over a fixed full-scale input range of ±5 V, resulting in a fundamental quantisation step size of the equation below.

$$\frac{10V}{65{,}536} \approx 0.15mV$$

However, since input signals such as voltage and current are scaled to fit within the ±5 V range of the ADC based on the selected measurement range, the actual resolution at the physical signal level is dependent on this scaling. For voltage measurements, a range of ±0.8 V was selected, in accordance with the specifications of the single solar cell used as the PV source. This scaling implies that the input voltage was amplified by a factor

of 6.25 (i.e., 5 V / 0.8 V), resulting in an effective voltage resolution at the signal level of the equation below.

$$\frac{0.15mV}{6.25} = 24\mu V \tag{28}$$

Therefore, the voltage uncertainty can be classified as 24 μV. Similarly, the current measurement was conducted using the ±10 A range. Current was measured indirectly by capturing the voltage drop across a precise four-wire shunt resistor connected in series with the solar cell, for which the I–V characteristics were being evaluated. The small differential signal across the shunt resistor was amplified using a high-precision instrumentation amplifier. Assuming a linear scaling across the ±10 A range, the corresponding quantization step size for the current measurement is denoted in equation below.

$$\frac{20A}{65{,}536} \approx 0.31mA \tag{29}$$

These values represent the ideal, resolution-limited uncertainties associated with each measurement. This resolution is adequate for large signal values (e.g., 8 A), where the resulting relative uncertainty is minimal (less than 0.01%). However, if small signals were measured without appropriately adjusting the measurement range, the quantisation error would become significant. Therefore, these calculations provide a baseline estimate of the expected uncertainty when using the solar simulator in conjunction with the I–V measurement device. They also support the decision to manually select the narrowest possible measurement ranges to maximize accuracy, rather than relying on automatic range selection.

The current and voltage uncertainties measured using the I–V tester are notably low, reflecting the high precision expected in a controlled experimental setup. To evaluate power output and power loss ratio uncertainties between the control and shaded conditions, the same method outlined previously in the final two equations of Appendix

B.1. Furthermore, the uncertainty level was indicated as error bars in the figures outlining results in Chapter 4 Section 4.3.1 and 4.3.3.

Appendix B.3 - Uncertainty Analysis for Chapter 4 Section 5.3.3 Sensitivity Analysis

The uncertainty analysis in Chapter 5, Section 5.3.3 evaluated the feature importance of the four contributing factors to power loss from thin-object shading, using the Random Forest model. As the sensitivity analysis depends on the robustness of the model, its results are also subject to uncertainty. To quantify this, a bootstrap resampling approach was employed. In this context, bootstrapping involves training each decision tree on a random sample (with replacement) from the dataset.

First, two independent Random Forest models were trained on the dataset from Chapter 5 Section 5.3.1, split into small and large thin objects, to establish baseline feature importance values. To estimate the variability of these values, a bootstrap procedure was performed over 30 iterations. In each iteration, the training data was resampled with replacement to generate a new dataset of equal size.

A new Random Forest model was trained on each resampled dataset, and the resulting feature importances were recorded, generating a distribution for each input variable. The standard deviation of each distribution was computed to represent the uncertainty in the corresponding importance score. These uncertainties were visualised as error bars in the final sensitivity plot, with each bar labelled to clearly convey the variability in each feature's estimated influence on the target variable.

As shown in Figure 5.39 and more prominently in Figure 5.40, the error bars indicate substantial uncertainty. This is primarily due to the relatively small sample sizes used in the Random Forest models: 59 cases for small thin objects and 45 for large thin objects. Future studies using larger datasets could reduce uncertainty and improve the reliability of the sensitivity analysis. Nonetheless, the most prominent attributing factors still retain there role as the most important attributing factors, namely the penumbra intensity for

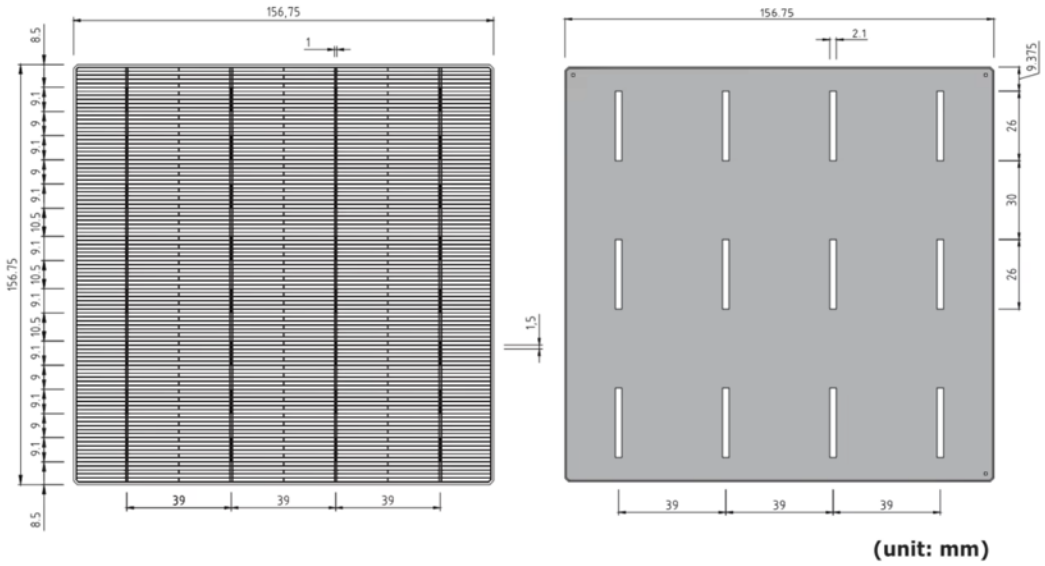
small thin objects and the percentage umbra for large thin objects, emerging as the most important contributors within their respective thin object shading categories.

The uncertainty analysis for the validation process in Chapter 5 was integrated into the sensitivity analysis Python script, which can be referred to in Appendix H.

Appendix C - Datasheets and Conformities

The single solar cell used in Chapter 4 for both the laboratory and outdoor environment:

Moreover, the electrical specifications of the 156.0 mm x 156.0 mm solar cell where retrieved using the solar simulator coupled with the I-V tester and the monocrystalline reference cell to calibrate based on STC conditions.



Dimension	156.75 mm X 156.75 mm ± 0.25 mm
Thickness	200 μm ± 30 μm
Front	Four 1mm wide bus bars(silver) with distance 39mm, acid texturized surface with blue silicon nitride AR coating
Back	2.1mm wide silver/aluminum soldering pads,aluminum back surface field

The Dataq Instruments DI-808 used in outdoor experimentations for Chapter 4, 5 and 6:



DI-808 Description

Web-based, Device-independent Operation

Model DI-808 is a giant step forward in the evolution of data logger technology toward autonomous and device-independent operation. Its built-in web server allows you to access, configure, manage, and oversee in real time all aspects of the instrument's measurement process using any device with a web browser running under any operating system. Just as you can navigate to Yahoo! using your favorite smart device, that same device can be used without exception with the DI-808. And because intelligence is built into the instrument, third party cloud services with their associated security risks and fee-based structures are avoided entirely. You stay in control at all levels, from device configuration and real time monitoring, to the acquired data and alarms the DI-808 places on your smart device. The DI-808's Ethernet interface allows it to integrate with any existing local area network (LAN) or virtual private network (VPN.) And simple port forwarding exposes the instrument to the Internet, allowing remote access from any location on the planet.

Measurement Flexibility

Built around the DI-808's web server is a powerful data logger engine that adapts to a wide range of analog and pulse measurements. Eight analog input channels feature channel-independent voltage and thermocouple configurations. Voltage measurements support ±10 mV to ±50 V measurements across twelve programmable ranges. Thermocouple configurations support J,K,T,B,R,S,E, and N types. Full channel isolation allows virtually any measurement in tough industrial environments: grounded thermocouples, powered thermocouples, off-ground current shunts, as well as unexpected and unknown ground potential differences. Complementing the analog input channels are four pulse inputs. Each can be independently programmed for simple state detection, to operate as a counter, or make a frequency measurement. Use these functions to acquire, for example, volume data from a flow sensor (count), and flow rate (frequency.) Other examples are rpm measurements or simple counting in production or product life test applications. Both analog and pulse measurements are reported synchronously in the same sampling interval, and all measurements are time-and-date-stamped. Sampling intervals are programmable as often as once every 25 mS or as infrequently as once every hour, with 18 selectable intervals in between. There's even an external option to synchronize sampling to external events.



Alarm Outputs with E-mail/Text Alerts

The DI-808 also provides four alarm output channels that can be used to flag exceptions during a recording. Each discrete output can be used to signal a PLC, turn on an alarm, or otherwise used as demanded by the application. Each alarm output is also linked to the web interface, where an email alert (or text alert, if supported by your provider) can be triggered when the alarm activates.

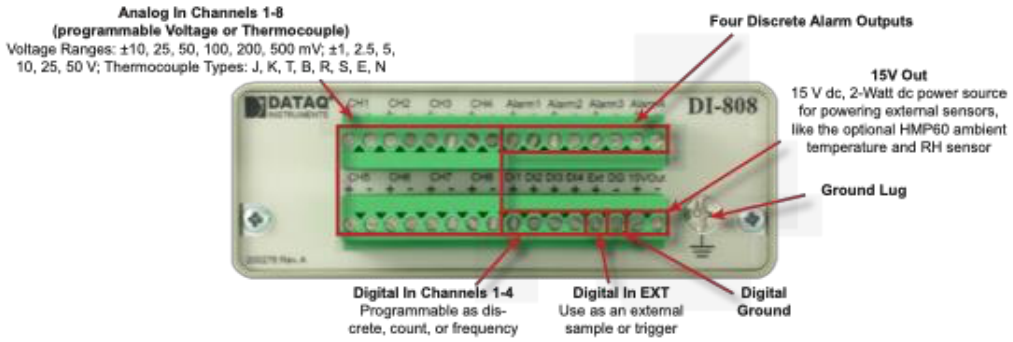
So, even though you may be miles from the instrument, you're only a few swipes on your smart device away from real time process updates.

Triggering Flexibility Adapts the DI-808 To Your Needs

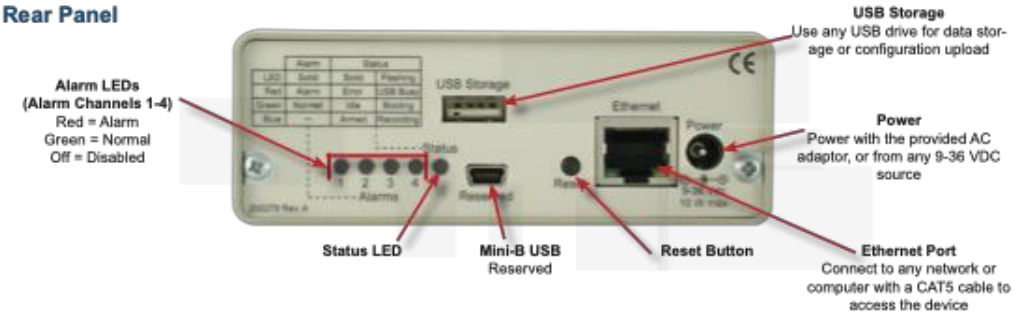
The DI-808 supports exceptional triggering flexibility to determine when the data logger should start and stop recording data, and when alarms should be activated. All or any subset of analog and pulse input channels can be tested, and conditions that stop and start recording can be entirely different. The start and stop recording processes can be a function of input levels, an alarm state, a specific date and time and day-of-the-week. Level tests support single and dual modes. Single levels support above- and below-threshold tests. Dual levels test inside or outside a trigger window. All enabled trigger conditions per analog or digital input can be combined in a selectable Boolean AND/OR function to further refine trigger definitions. So, if you want to begin recording when channel 2 exceeds 34 psi AND when channel 5 is greater than 84 but less than 127 pounds, and then stop recording at 10 pm on Sunday evening, you can do it. You can even configure the instrument to re-trigger itself automatically. Finally, when the DI-808 completes a start/stop recording cycle it can be configured to send data to one or all of five destinations ranging from local to remote servers, multiple email addresses, and even a USB drive with built-in flash memory (4GB standard, 32GB optionally) providing transparent backup.

DI-808 Close-up

Front Panel

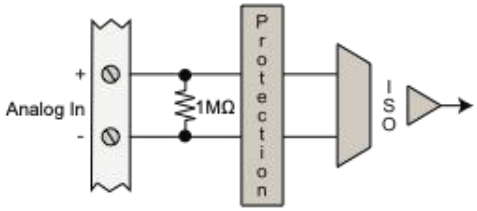


Rear Panel

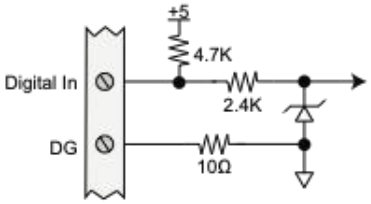


DI-808 I/O Equivalent Circuits

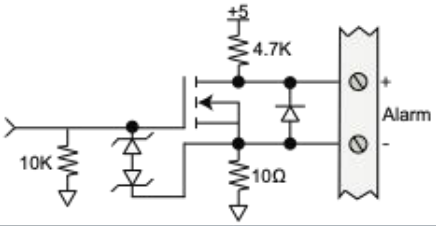
Analog Input



Pulse Input



Alarm Out

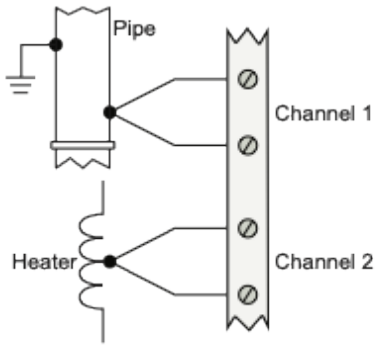


Analog Input Channels (continued)

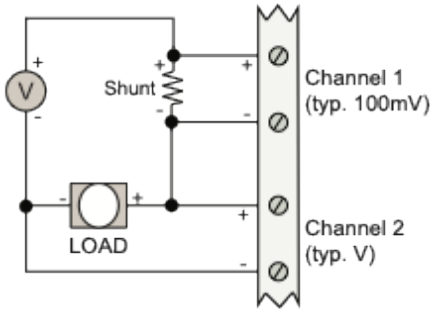
Typical Analog Channel Connections

The isolation, range, and multi-function nature of the eight DI-808 analog input channels allows a wide range of measurement possibilities. Here are just a few:

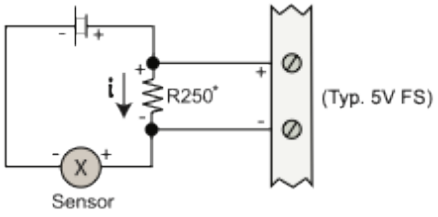
Grounded or Powered Thermocouples



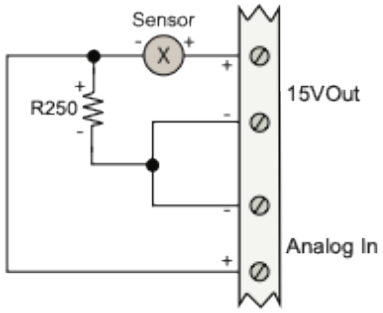
Simultaneous Voltage and Current



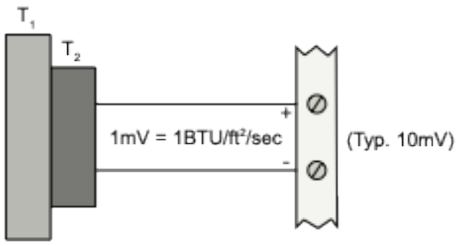
4-20 mA Process Current (externally-powered)



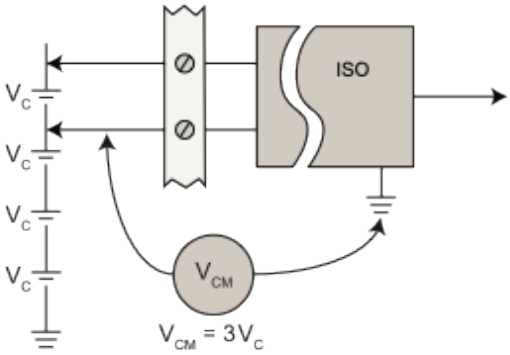
4-20 mA Process Current (powered by DI-808)



Heat Flux Sensor



Stacked Power Cells



* Optional model R250 250 Ω process current shunt resistor

DI-808 Specifications

Analog Inputs

Number of Channels: 8

Configuration: Differential, Isolated

Isolation: Input-to-output, channel-to-channel

Measurement type per channel: Voltage, Thermocouple

Programmable thermocouple types and measurement range per channel:

Over 25 ±3 °C ambient temperature range
Stable ambient temperature
Following 60 minutes warm-up
Excluding common mode error
Excluding thermocouple error

TC type	Temperature Measurement range (°C)	Accuracy (°C)
J	-190 to 1200	±(0.1% of span + 2)
K	-180 to 1360	
T	-190 to 400	±(0.1% of span + 1)
B	600 to 1000	±(0.2% of span + 4)
	1001 to 1810	±(0.1% of span + 3)
R	-40 to 300	±(0.2% of span + 6)
	301 to 1760	±(0.1% of span + 3)
S	-40 to 400	±(0.2% of span + 6)
	401 to 1750	±(0.1% of span +3)
E	-160 to 990	±(0.1% of span + 1)
N	-170 to 50	±(0.1% of span + 3)
	51 to 1290	±(0.1% of span + 1)

Programmable voltage ranges per channel:

At 25 °C ambient temperature
Following 30 minutes warm-up
Excluding common mode error

Range (±)	Accuracy
10 mV	±(0.05% of span + 10 µV)
25 mV	
50 mV	
100 mV	
250 mV	
500 mV	
1 V	
2.5 V	
5 V	
10 V	
25 V	
50 V	

Input impedance: 1MΩ all ranges

Absolute maximum input without damage: 120 V (±dc or rms)

Maximum common mode voltage: 120 V (±dc or rms)

Minimum common mode rejection: (330Ω unbalance) >100 dB (dc to 60 Hz)

Channel-to-channel crosstalk rejection: (Rsource ≤ 330Ω; Freqsource ≤ 60 Hz) >110 dB

Alarm and trigger hysteresis: Voltage: ±0.5% of the full scale range; Temperature: ±0.3 °C

Digital/Pulse Inputs

Number of channels: 4

Pull-up value: 4.7 kΩ

Isolation: None

Input high voltage threshold: 1.80 V minimum

Input low voltage threshold: 1.40 V maximum

Absolute voltage (V) input without damage: 0 ≤ V ≤ 30 V

Maximum count value: 2^{32} - 1 (.csv format)
65,535 (WinDaq format)

Maximum measured frequency: >100 kHz (.csv format)
65,565 Hz (WinDaq format)

Alarm Outputs

Number of channels: 4

Maximum drain voltage: 30 V

Maximum sink current: 100 mA

ADC Characteristics

Voltage measurement Resolution:

Range (±)	Resolution	Units
10 mV	305	nV
25 mV	763	
50 mV	1.52	µV
100 mV	305	
250 mV	763	
500 mV	15.3	
1 V	30.5	
2.5 V	76.3	
5 V	152.6	
10 V	305	
25 V	763	
50 V	1.53	mV

Minimum temperature measurement resolution:

TC type	Resolution	Units
J	0.086	°C
K	0.096	
T	0.037	
B	0.096	
R/S	0.111	
E	0.073	
N	0.092	

4-20 mA current loop resolution: (±5 V range with 250Ω shunt resistor) 26,214 ADC counts over the 4-20 mA range

Programmable sampling intervals: 25, 50, 100, 250, 500 mS
1, 2, 5, 10, 20, 30 S
1, 2, 5, 10, 20, 30 minutes
1 hour, External

Internal Memory

Type: Non-volatile flash

Size: 4 GB (standard); 32 GB (optional)

Use: Automatic backup of recorded data

Indicators and Controls

Signal I/O: Dual, removable 16-position screw terminal connectors

Power connector: 2.0 mm center pin, 5 mm shell

Status light: One multicolor LED indicating status

Alarm lights: 4 multicolor LEDs

Ethernet interface connector: RJ45

USB drive receptacle: Type A male

USB connector: Mini B style (usage is reserved)

Control button: Push type to set device operating mode

Ground: Screw terminal to establish Earth ground.

Power I/O

Input power requirements: 9-36 V dc @ 7.5 Watts
9-36 V dc @ 10 Watts (w/excitation)

Excitation power supply output: 15 V, 130 mA max, 13 mA min

Environmental

Operating temperature range: 0 to 70 °C (32 to 158°F)

Storage temperature: -20 to 70 °C (-4 to 158°F)

Storage humidity: 0-90%RH, non-condensing

Physical Characteristics

Enclosure: All-metal. Steel top, aluminum base

Mounting: Desktop, Bulkhead with optional brackets

Dimensions: 5⁷/₁₆ D × 4³/₈ W × 1½ H inches
13.81D × 10.48W × 3.81H cm

Weight: <1 lb. (<453 grams)

330-668-1444 13 www.dataq.com

DI-808 Specifications (continued)

Configurable Components

Network variables:	IP address, Subnet mask, Gateway, DNS
Account log-on information:	For FTP, SFTP, SMB, SMTP
User log-on information:	User and administrator names and passwords

Supported Standards

Network Time Protocol (NTP):	Syncs internal time and date clock to Internet time
File Transfer Protocol (FTP): Secured File Transfer Protocol (SFTP): Server Message Block (SMB) protocol:	Allows the instrument to push recorded data to an FTP/SFTP server Allows the instrument to record data to a local server drive
Simple Mail Transfer Protocol (SMTP):	Allows the instrument to send data and alarms to multiple email addresses

Display Subsystem

Digital display:	Numeric display of acquired values scaled into engineering units in real time. Selectable precision of 1 to four digits to the right of the decimal point.
Waveform display:	Scrolling plot of selected channel data in real time versus time of day.
Alarms status:	Virtual LEDs display the status of the four alarm outputs

Channel Settings Subsystem

Analog channel configuration:	Voltage and measurement range, temperature and thermocouple type, moving average filter, engineering units, channel label
Digital/pulse channels:	Discrete, count, count with reset, frequency, engineering units, channel label

Trigger Subsystem

Start or stop recording trigger conditions:	Level: Above/below level, In/out window Alarm: Upon alarm activation Date/time: Specific date and time. Daily selection External
Auto rearm:	Enabled or disabled

Alarm Subsystem

Level or edge selection:	Level: Alarm is activated when alarm condition is met on first encounter Edge: Alarm is activated only after first not being met.
Analog/pulse channel levels:	Above/below level, In/out window
Thermocouple burnout:	Any burnout detected on a TC channel
Selectable alarm ports:	1-4
Alarm hold:	Enable/disable

File Subsystem

File browse/download:	Browse files on the DI-808 internal flash memory or connected USB drive and allow selectable downloads to the client device.
Format local file storage:	Formats internal flash memory, erasing previously recorded files and reallocating file space for new recorded data.
Get local file space:	Returns the available file space.
Base file name:	Allows recorded files to be assigned a definable file name, and to optionally have date and time appended.
File type:	Allows the recorded file format to be defined as either ASCII CSV or binary WDH.

Device Subsystem

Device settings and information:	Program device sampling interval, temperature units (°F/°C), enable or disable auto start on boot feature, time/date/ synched to connected PC or NTP server, reboot device.
Network configuration:	Configure device IP address, DNS, Subnet mask, Gateway.
Users and accounts:	Configure user and administrator names and passwords.

Ordering Guide

Description	Order No.	Description	Order No.
DI-808 Web-based Data logger with 4GB Memory Includes DI-808, ac adaptor, NIST-traceable calibration certificate. Provides 4 GB of non-volatile internal data file storage.	DI-808	**DI-808 Web-based Data logger with 32GB Memory** Includes DI-808, ac adaptor, NIST-traceable calibration certificate. Provides 32 GB of non-volatile internal data file storage.	DI-808-32
250Ω 4-20 mA shunt resistor ±0.1%, 0.5 Watts max., ±50 ppm/°C	R250	**Power Connector** Dc power connector for powering the DI-808 from a source other than the provided ac adaptor.	200300
Ambient Temp and RH Sensor -40 to +60 °C, 0 to 100% RH Measurement Range. Powered by the DI-808.	HMP60	**Bottom Screw Terminal Block** Spare 16-port removable screw terminal block for BOTTOM of DI-808 screw terminal block receptacle.	100995-MCVW
Mounting bracket Right-angle mounting brackets for bulkhead mounting model DI-808.	100947-1	**Top Screw Terminal Block** Spare 16-port removable screw terminal block for TOP of DI-808 screw terminal block receptacle.	100995-MCVR

The small scale PV module used in Chapter 5:

Solar

Photovoltaics is our passion

ET Module

ET-M53605	5Wp
ET-M53610	10Wp
ET-M53620	20Wp
ET-M53640	40Wp



FEATURES

- Low voltage-temperature coefficient enhances high-temperature operation
- Exceptional low-light performance and high sensitivity to light across the entire solar spectrum maximize yearly energy delivery
- 25-year limited warranty on power output, 2-year limited warranty on materials and workmanship

MARTERIALS

- Highest quality, high-transmission tempered glass provides enhanced stiffness and impact resistance
- Advanced EVA encapsulation system with multi-layer back sheet meets the most stringent safety requirements for high-voltage operation
- A sturdy, anodized aluminum frame allows modules to be easily roof-mounted with a variety of standard mounting systems
- Ultra reliable bypass diodes prevent damage through overheating due to shaded or defective cells



BENEFITS

- Manufactured in an ISO 9001:2000 certified plant
- High efficiency, high safety, high reliability
- Output power tolerance of +/-3%
- Conformity with CE

www.etsolar.com

ET SOLAR GROUP

ET Solar China
24F, A2 World Trade Center Mansion, 67 Shanxi RD, Nanjing 210005, China
Tel: +86 25 86898096 Fax: +86 25 86898097 E-mail: sales@etsolar.com

ET Solar USA
4900 Hopyard Road, Suite 290, Pleasanton, CA 94588, USA
Tel: +1 925 4609898 Fax: +1 925 4609929 Email: sales@etsolar.us

ET Module

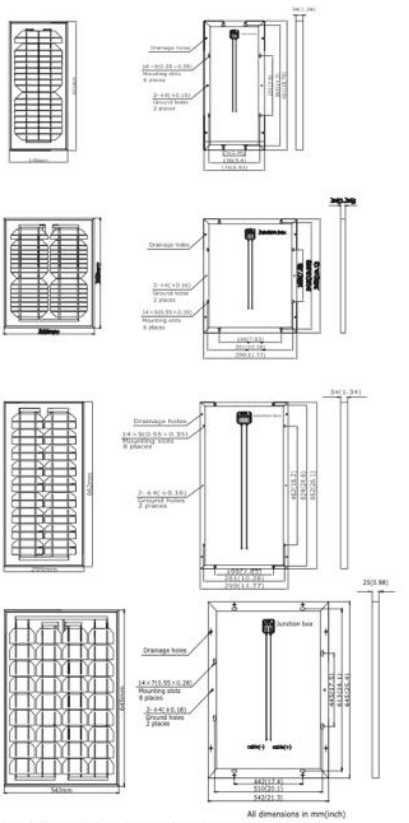
ET-M53605 ET-M53610 ET-M53620 ET-M53640

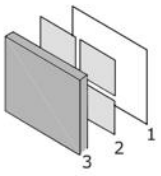
SPECIFICATIONS

Model type	ET-M53605	ET-M53610	ET-M53620	ET-M53640
Peak power(Pmax)	5W	10W	20W	40W
Weight	1.2kg	1.7kg	2.7kg	4.6kg
Dimensions	401×176×34mm	383×299×34mm	662×299×34mm	645×542×25mm
Maximum power voltage (Vmp)	17.82V			
Maximum power current (Imp)	0.285A	0.57A	1.14A	2.27A
Open circuit voltage (Voc)	21.96V			
Short circuit current (Isc)	0.315A	0.63A	1.27A	2.54A
Maximum system voltage	750V			
Temp. Coeff. of Isc (TK Isc)	0.058 %/℃			
Temp. Coeff. of Voc (TK Voc)	-0.367 %/℃			
Temp. Coeff. of Pmax (TK Pmax)	-0.485 %/℃			
Normal Operating Cell Temperature	44.4 ℃			

Note: the specifications are obtained under the Standard Test Conditions (STCs): 1000 W/m2 solar irradiance, 1.5 Air Mass, and cell temperature of 25 ℃.

PHYSICAL CHARACTERISTICS





1] Front: tempered glass
2] monocrystalline solar cells
125 mm x 125 mm embedded
in EVA
3] Rear: Tedlar foil

Certifications

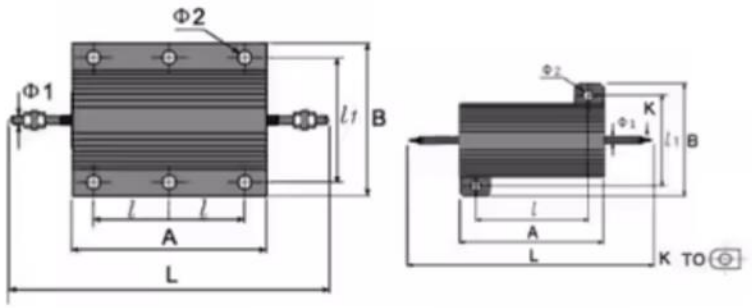
Conformity with

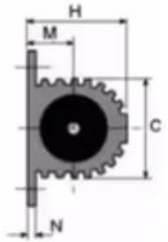
CE

Please contact Support@etsolar.com for technical support

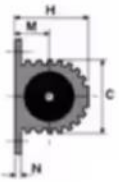
The fixed resistive load resistors used in experimentations conducted in Chapter 4 - 6:

Product picture (aluminum housing resistor)



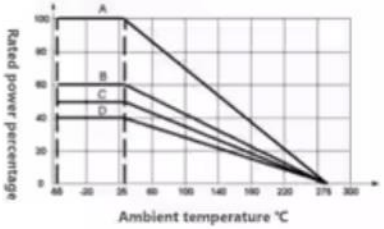


100W---500W



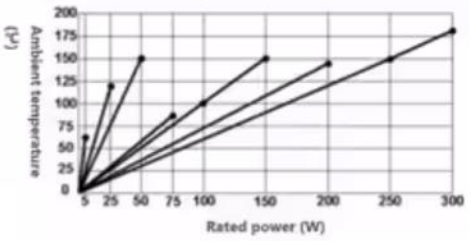
10W---50W

Power reduction curve



A Suitable for all power resistors with heat sink
B is 5W and 10W without heat sink
C is 25W without heat sink
D is 50W~500W without heat sink

Surface temperature rise
(the figure is applicable to the installation with standard heat sink plate)



Dimensions

Model	Rated power (W) at 25℃ with heat sink	Dimensions (mm)											
		Resistor body										Standard heat sink (aluminum)	
		A	B	L	H	C	1	11	M	N	Φ1	Φ2	Surface area (cm2)	Thickness (mm)
	5	19		60	10	11							400	1
	10	19	20	33	10	11	14	16	5	2	2	2.5	415	
	25	27	27	52	15.5	16	21	19	8	2	2	3.5	535	
	50	50	27	75	15.5	16	41	19	8	2	2	3.5	995	
	100	100	52	135	29	32	82	42	13	2	M3	4.4	995	
	200	165	52	195	29	32	143	42	13	2	M3	5.5	3750	
	300	195	52	225	29	32	173	42	13	2	M3	5.5	5780	
	500	250	52	280	29	32	228	42	13	2	M3	5.5	8500	

■ Main Specifications

Model	Rated power at 25°C (W)		Resistance range (Ω)	Resistance tolerance (%)	Temperature Coefficient (×10 -6 /°C)	Withstand voltage (V)
	With heat sink	Without heat sink				
	5	3	0.01~1K	±1，±5	±100，±50	1000
	10	8	0.01~1.5K			
	25	12.5	0.01～10K			
	50	20	0.01～33K			
	100	50	0.01～51K			2000
	200	50	0.01～62K			
	300	75	0.01～75K			
	500	200	0.01～82K			

■ Main inspection items, test methods and performance requirements

Test items	Performance requirements	experiment method
Solderability	The solder can flow freely and wet with the leads	Slot welding 235±5°C，2s
Terminal strength	△R ≤ ±(1%R+0.05Ω)	40N
Rapid temperature change	△R ≤ ±(1%R+0.05Ω)	-55°C/+155°C，5 cycles
Short-time overload	△R ≤ ±(1%R+0.05Ω)	10P R 5s
Constant heat and humidity	△R ≤ ±(5%R+0.1Ω)	40±2°C 93 eq\o(\s\up 7(+2),\s\do 3(-3)) +2-3 % 21天
Shock	△R ≤ ±(1%R+0.05Ω)	490m/s 2 11ms 18次
Vibration	△R ≤ ±(1%R+0.05Ω)	10—50Hz 98 m/s 2 6h
Room temperature durability	△R ≤ ±(5%R+0.1Ω)	Room temperature P R 1000h
Resistance to welding heat	△R ≤ ±(1%R+0.05Ω)	350±10°C 3.5±0.5s
Surface temperature rise	≤ 275°C	V R

The consolidated specifications of the SLR camera used for image acquisition in Chapter 4, for the full specification of the camera refer to [301]**:**

Sensor & Imaging

- Sensor: Full-frame CMOS, approx. 35.8 × 23.9 mm Canon+
- Effective resolution: ~ 20.2 megapixels
- Maximum image size: 5472 × 3648 pixels (3:2 aspect ratio)
- File formats: JPEG, RAW (14-bit), RAW + JPEG simultaneous recording

Image Processing & Lens

- Image processor: DIGIC 5+
- Lens mount: Canon EF (does not support EF-S / EF-M lenses)
- Crop factor: 1.0× (full-frame)

ISO & Sensitivity

- Native ISO: 100 – 25,600
- Expanded ISO: ISO 50 (Low), ISO 51,200 (H1), ISO 102,400 (H2)

Shutter & Shooting Performance

- Shutter speed: 30 s – 1/4000 s, plus Bulb
- Continuous shooting: up to approx. 4.5 frames per second
- Metering system: 63-zone iFCL metering (dual-layer, using AF and colour info)

Autofocus & Viewfinder

- Autofocus: 11-point AF system; centre point is cross-type, sensitive down to –3
- Viewfinder: Optical pentaprism, approx. 97 % coverage, 0.71× magnification

LCD & Live View

- Rear LCD: 3.0″ fixed TFT screen, approx. 1,040,000 dots
- Live View: Yes

Video Recording

- Video resolutions / frame rates:
  - Full HD 1920 × 1080 at 24/25/30 fps
  - HD 1280 × 720 at 50/60 fps
  - SD 640 × 480 at 25/30 fps
- Video format: H.264 codec

Storage & Media

- Recording media: SD, SDHC, SDXC — UHS-I compatible

Connectivity & Additional Features

- Built-in Wi-Fi (wireless LAN) and GPS receiver for location tagging and remote operation
- Dust-reduction system (sensor cleaning / low-pass filter vibration)
- Exposure modes: Program, Aperture-Priority, Shutter-Priority, Manual, plus Self-timer/Remote, Bulb, and Silent Shooting.
- Exposure compensation & bracketing: Exposure compensation ±5 EV; Auto-exposure bracketing (AEB) possible.

Body & Physical Specs

- Body type: Digital single-lens reflex (DSLR), weather-sealed/water-resistant (splash/dust resistant) magnesium alloy + polycarbonate top cover design (relatively compact for a full-frame DSLR) Canon
- Weight: approx. 680 g (body only) / ~770 g with battery (varies by spec source)
- Dimensions: ~ 145 × 111 × 71 mm
- Battery: Rechargeable Lithium-Ion pack (LP-E6), rated for ~ 1090 shots per charge

The full-scale PV module used in the validation section of Chapter 5:

www.hhi-green.com/solar/en
www.facebook.com/hyundaisolar.eu

Hyundai Solar Module

Hyundai Heavy Industries was founded in 1972 and is a Fortune 500 company. The company employs more than 48,000 people, and has a global leading 6 business divisions with sales of 49.9 Billion USD in 2014. As one of our core businesses of the company, Hyundai Heavy Industries is committed to develop and invest heavily in the field of renewable energy.
Hyundai Solar is the largest and the longest standing PV cell and module manufacturer in South Korea. We have 600 MW of module production capacity and provide high-quality solar PV products to more than 3,000 customers worldwide. We strive to achieve one of the most efficient PV modules by establishing an R&D laboratory and investing more than 20 Million USD on innovative technologies.

Black-Black RG-Series

Multi-crystalline Type
HiS-M245RG (BK) | HiS-M250RG (BK) | HiS-M255RG (BK)

Mono-crystalline Type
HiS-S250RG (BK) | HiS-S255RG (BK) | HiS-S260RG (BK) | HiS-S265RG (BK)

Mechanical Characteristics

Dimensions	998 mm (39.29")(W) x 1,640 mm (64.57")(L) x 35 mm (1.38")(H)
Weight	Approx. 18.7 kg (41.2 lbs)
Solar cells	60 cells in series (6 x10 matrix)
Output cables	4 mm² (12AWG) cables with polarized weatherproof connectors, IEC certified (UL listed), Length 1.0 m (39.4"), MC4 compatible connectors
Junction box	IP67, weatherproof, IEC certified (UL listed)
Bypass diodes	3 bypass diodes to prevent power decrease by partial shade
Construction	Front : High transmission low-iron tempered glass, 3.2 mm (0.13") Encapsulant : EVA Back Sheet : Weatherproof film (Black)
Frame	Clear anodized aluminum alloy type 6063 (Black)

High Quality

- IEC 61215 (Ed.2) and IEC 61730 Certified by VDE
- Output power tolerance +3/-0 %
- ISO 9001:2008, ISO 14001:2004 and ISO 50001:2011 Certified
- OHSAS 18001:2007 Certified
- Advanced Mechanical Test (5,400 Pa) Passed (IEC 61215)
- IEC 62716 (Ammonia Corrosion Test) Certified
- IEC 61701 (Salt Mist Corrosion Test) Certified

Accredited Test Lab

- VDE (Test Data Acceptance Program)
- UL (Witness Test Data Program)

Limited Warranty

- 10 years for product defect
- 10 years for 90 % of warranted min. power
- 25 years for 80 % of warranted min. power

※ Important Notice on Warranty
The warranties apply only to the PV modules with Hyundai Heavy Industries Co., Ltd's logo (shown below) and product serial number on it.



HYUNDAI HEAVY INDUSTRIES

Electrical Characteristics

| Multi-crystalline Type |

		HiS-M□□□RG (BK)		
		245	250	255
Nominal output (Pmpp)	W	245	250	255
Voltage at Pmax (Vmpp)	V	30.7	30.9	31.0
Current at Pmax (Impp)	A	8.0	8.1	8.2
Open circuit voltage (Voc)	V	37.3	37.4	37.6
Short circuit current (Isc)	A	8.5	8.7	8.8
Output tolerance	%	+3/-0		
No. of cells & connections	pcs	60 in series		
Cell type	-	6" Multi-crystalline silicon		
Module efficiency	%	15.0	15.3	15.6
Temperature coefficient of Pmpp	%/K	-0.41	-0.41	-0.41
Temperature coefficient of Voc	%/K	-0.32	-0.32	-0.32
Temperature coefficient of Isc	%/K	0.039	0.039	0.039

※All data at STC (Standard Test Conditions). Above data may be changed without prior notice.

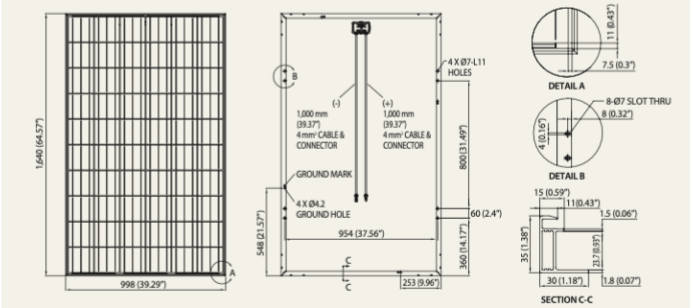
| Mono-crystalline Type |

		HiS-S□□□RG (BK)			
		250	255	260	265
Nominal output (Pmpp)	W	250	255	260	265
Voltage at Pmax (Vmpp)	V	30.9	31.0	31.1	31.3
Current at Pmax (Impp)	A	8.1	8.2	8.4	8.5
Open circuit voltage (Voc)	V	37.6	37.8	37.9	38.1
Short circuit current (Isc)	A	8.7	8.8	8.9	9.0
Output tolerance	%	+3/-0			
No. of cells & connections	pcs	60 in series			
Cell type	-	6" Mono-crystalline silicon			
Module efficiency	%	15.3	15.6	15.9	16.2
Temperature coefficient of Pmpp	%/K	-0.42	-0.42	-0.42	-0.42
Temperature coefficient of Voc	%/K	-0.30	-0.30	-0.30	-0.30
Temperature coefficient of Isc	%/K	0.047	0.047	0.047	0.047

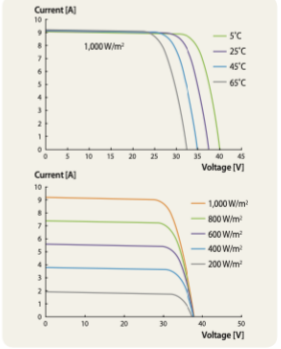
※All data at STC (Standard Test Conditions). Above data may be changed without prior notice.

| Module Diagram |

(unit : mm, inch)



| I-V Curves |



| Installation Safety Guide |

- Only qualified personnel should install or perform maintenance.
- Be aware of dangerous high DC voltage.
- Do not damage or scratch the rear surface of the module.
- Do not handle or install modules when they are wet.

Nominal Operating Cell Temperature	46°C ± 2
Operating Temperature	-40 - 85°C
Maximum System Voltage	DC 1,000 V (IEC) DC 600 V (UL)
Maximum Reverse Current	15 A

[Printed Date : December 2015]

Printed on FSC certified eco-friendly paper.

Sales & Marketing
Hyundai Bldg., 75, Yulgok-ro, Jongno-gu, Seoul 03058, Korea
Tel : +82-2-746-7563, 4517 Fax : +82-2-746-7675

HYUNDAI HEAVY INDUSTRIES

The 10W PV module used in Chapter 6 to conduct preliminary experimentations:

Go Power!®

GP-PV-10M

SOLAR MODULE

Reliable

The GP-PV-10M Solar Module from Go Power! is a high-efficiency monocrystalline solar module that provides outstanding performance and cost-effective solar power for off-grid and mobile applications. The Go Power! GP-PV-10M Solar Module is built to last and features a 10-year limited power output warranty.

Durable

To ensure long life, the high-efficiency solar cells are encapsulated between a special tempered, low-iron solar glass and a Tedlar® / polyester backing material. The mounting frame, manufactured from anodized marine-grade aluminum, allows the GP-PV-10M to be installed in extreme conditions.

The GP-PV-10M is ideal for:

- RV/Marine
- 12/24 Volt battery systems
- OEM
- Security Trailers
- Telecommunications
- Water pumping
- Other off-grid applications



GP-PV-10M SOLAR MODULE

Features:

- Compact and rugged design
- Dual positive + negative bare wire connectors
- Lightweight anodized aluminum frame
- High transmissivity tempered glass
- 7m cable with built-in fuse
- Junction box with bypass and blocking diodes
- 10 year limited power output warranty

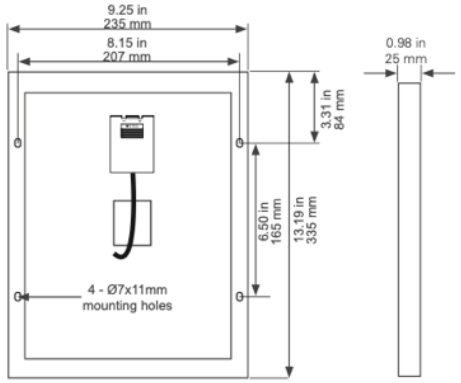
REPRESENTED IN YOUR REGION BY:

Go Power! (A wholly-owned subsidiary of Vattera Products, LLC) | gpelectric.com

GP-PV-10M
SOLAR MODULE

SPECIFICATIONS	
Rated power (Pm)	10W
Maximum power voltage (Vmp)	17.5V
Maximum power current (Imp)	0.57A
Open circuit voltage (Voc)	21V
Short circuit current (Isc)	0.62A
Cell type	Monocrystalline
Module efficiency	17.30%
Maximum system voltage	600VDC
Weight	1.76 lb (0.8 kg)
Dimensions	13.19 x 9.25 x 0.98 in 335 x 235 x 25 mm
Frame type / material	Clear anodized aluminum frame

Power Specifications calculated at STC:
- *Irradiance: 1000 W/m2*
- *Cell Temperature: 77 °F (25 °C)*
- *Air Mass: 1.5*



Rear profile *Side profile*

Specifications subject to local environmental conditions.
Specifications may be subject to change.

© 2018, Go Power!
Document: SPEC_GP-PV-10M_RevA.v1

Go Power! (A wholly-owned subsidiary of Valterra Products, LLC.) | gpelectric.com

The certificate of conformity for the ND filters used in Chapter 6 based on the spectroscopy data outlined in the chapter:

LEE Filters

CERTIFICATE OF CONFORMITY

LEE Filters certifies that their lighting products manufactured by themselves comply with the specifications, requirements and performance data shown in their published Technical Data Information Sheet supplied to our customers and representatives.

Furthermore, we confirm *LEE* Filters products are in accordance with our Company standards, drawings, specifications, processes, methods and procedures.

All other parts not manufactured by *LEE* Filters are under the warranty of the specific manufacturer and shall be the responsibility of that manufacturer.



Craig Thornhill
Operations Manager

***LEE* Filters**, Central Way, Walworth Business Park, Andover, Hampshire SP10 5AN, England
Telephone: +44 (0)1264 366245 www.leefilters.com
Registered Office: Panavision Europe Limited, Corporate Office, Metropolitan Centre, Bristol Road, Greenford, Middlesex, UB6 8GU Registered in England No 2532311

Appendix D – Tabulated Laboratory Dataset

The dataset for the primary laboratory environmental setup described in Section 4.3.3 is presented below, summarising the results of the three individual experimental tests. The first column shows the distance between the thin object and the solar cell, while the second column indicates the thin object's diameter (thickness). The third, fourth, and fifth columns list the solar cell's power output when shaded by the thin object, and the sixth column provides the corresponding average power output.

As discussed in the main body of the thesis, the seventh column presents the extracted P_{load}, which denotes the average power output under a fixed load condition, as explained in the methodology Section 4.2.3. This allows direct comparison with the outdoor environment results presented in Section 4.3.3. The final column reports the percentage power loss relative to the unshaded experimental scenario.

Distance (cm)	**Thickness** (mm)	**Exp. Round 1** (W)	**Exp. Round 2** (W)	**Exp. Round 3** (W)	**Average Power Output** (W)	**Extracted P_{load}** (W)	**Power Loss** (%)
---	Unshaded	4.18	4.14	4.15	4.16	---	---
10	2	4.08	4.01	4.11	4.07	4.05	2.50
15		4.10	4.04	4.02	4.05	4.04	2.87
20		4.07	4.03	4.08	4.06	4.05	2.68
25		4.07	4.02	4.00	4.03	4.01	3.45
30		4.06	4.05	4.02	4.04	4.03	3.11
35		4.00	4.07	4.07	4.05	4.03	3.00
40		4.00	4.09	4.09	4.06	4.04	2.77
10	2.3	4.11	4.04	4.04	4.07	4.06	2.27
15		4.10	4.04	4.03	4.06	4.05	2.51
20		4.10	4.03	4.04	4.06	4.05	2.52
25		4.10	4.04	4.03	4.06	4.05	2.52
30		4.10	4.03	4.03	4.05	4.05	2.57
35		4.11	4.02	4.02	4.05	4.05	2.65
40		4.02	4.08	4.04	4.05	4.04	2.77
10	2.8	4.08	4.04	4.03	4.05	4.04	2.91
15		4.08	4.04	4.01	4.04	4.03	3.04
20		4.08	4.03	4.01	4.04	4.03	3.12
25		4.10	4.02	4.00	4.04	4.03	3.11
30		4.08	4.10	4.02	4.06	4.05	2.53

35		4.01	4.09	4.02	4.04	4.03	3.09
40		3.99	3.99	3.99	3.99	4.03	3.17
10		4.01	4.05	4.07	4.04	4.02	3.36
15		4.03	4.01	4.03	4.02	4.00	3.86
20		4.01	4.01	4.05	4.02	4.00	3.87
25	3.2	4.01	4.03	4.01	4.02	3.99	3.95
30		4.01	4.02	4.01	4.02	3.99	4.00
35		4.01	3.99	3.99	4.00	4.00	3.67
40		3.99	4.01	3.99	4.00	4.01	3.61
10		4.09	3.98	3.98	4.02	4.01	3.58
15		4.11	4.01	3.98	4.03	4.02	3.21
20		4.09	3.99	3.97	4.01	4.01	3.64
25	4.4	4.12	3.99	3.98	4.03	4.02	3.34
30		4.08	3.99	3.97	4.01	4.00	3.66
35		3.97	3.97	3.98	3.97	3.97	4.57
40		4.08	3.99	3.98	4.02	4.01	3.62
10		4.06	3.99	3.97	4.01	3.99	3.94
15		4.06	3.98	3.95	4.00	3.98	4.32
20		4.06	3.97	3.96	4.00	3.98	4.23
25	4.6	4.07	3.97	3.96	4.00	3.98	4.20
30		4.04	3.97	3.96	3.99	3.97	4.44
35		4.05	3.97	3.95	3.99	3.97	4.46
40		3.96	3.96	3.95	3.95	3.94	5.30
10		4.07	3.94	3.93	3.98	3.95	4.93
15		3.98	3.93	3.93	3.95	3.92	5.71
20		3.98	3.92	3.93	3.94	3.92	5.81
25	6	4.01	3.91	3.93	3.95	3.92	5.60
30		4.01	3.91	3.93	3.95	3.92	5.61
35		3.98	3.89	3.93	3.93	3.91	6.04
40		3.98	3.89	3.93	3.93	3.90	6.10
10		3.99	4.09	4.13	4.07	3.96	4.83
15		4.11	4.12	4.10	4.11	3.97	4.45
20		4.11	4.10	4.10	4.10	3.95	4.93
25	6.4	4.09	4.10	4.10	4.10	3.94	5.18
30		4.09	4.10	4.09	4.09	3.94	5.22
35		4.08	4.05	4.08	4.07	3.93	5.57
40		4.07	4.06	4.08	4.07	3.93	5.54
10		3.94	3.94	3.94	3.94	3.91	5.99
15		3.93	3.92	3.93	3.93	3.91	5.99
20	7.2	3.93	3.93	3.93	3.93	3.89	5.93
25		3.91	3.90	3.92	3.91	3.93	6.44
30		4.05	3.89	3.91	3.95	3.88	5.49

35		3.91	3.88	3.90	3.90	3.87	6.69
40		3.90	3.86	3.89	3.89	3.86	7.00
10		3.87	3.89	3.90	3.89	3.77	9.33
15		3.89	3.88	3.89	3.89	3.77	9.32
20		3.87	3.88	3.87	3.88	3.76	9.59
25	8	3.86	3.86	3.89	3.87	3.75	9.67
30		3.87	3.87	3.87	3.87	3.76	9.64
35		3.86	3.86	3.86	3.86	3.74	9.93
40		3.87	3.86	3.87	3.86	3.75	9.84
10		3.89	3.84	3.83	3.85	3.70	11.06
15		3.91	3.86	3.83	3.86	3.71	10.84
20		3.84	3.84	3.83	3.84	3.68	11.44
25	10	0.00	3.84	3.82	2.55	3.68	11.49
30		3.89	3.81	3.80	3.83	3.68	11.53
35		3.90	3.81	3.88	3.86	3.71	10.79
40		3.81	3.80	3.81	3.81	3.65	12.07
10		3.85	3.79	3.80	3.81	3.62	12.84
15		3.86	3.78	3.76	3.80	3.61	13.15
20		3.85	3.80	3.78	3.81	3.61	13.06
25	12	3.84	3.77	3.77	3.79	3.60	13.36
30		3.82	3.75	3.78	3.78	3.59	13.53
35		3.81	3.76	3.75	3.77	3.58	13.80
40		3.82	3.77	3.76	3.79	3.59	13.54
10		3.80	3.71	3.74	3.75	3.49	16.12
15		3.80	3.73	3.72	3.75	3.48	16.18
20		3.77	3.71	3.72	3.73	3.47	16.50
25	14	3.78	3.70	3.71	3.73	3.47	16.56
30		3.76	3.70	3.71	3.72	3.46	16.76
35		3.75	3.69	3.71	3.71	3.45	16.90
40		3.76	3.69	3.69	3.71	3.45	16.97
10		3.47	3.48	3.49	3.48	3.17	23.78
15		3.48	3.48	3.48	3.48	3.17	23.83
20		3.46	3.46	3.47	3.46	3.15	24.21
25	20	3.45	3.46	3.44	3.45	3.14	24.54
30		3.44	3.44	3.45	3.44	3.13	24.67
35		3.42	3.42	3.43	3.43	3.11	25.14
40		3.41	3.41	3.42	3.41	3.11	25.26

Appendix E – Supporting Calculations for Key Chapter Developments

The following sections present the key supporting calculations used in the development of each chapter of this thesis.

Appendix E.1 - The One-Way Anova used in Section 4.3.1

A sample calculation of the one-way Anova is presented below. The example is based on the absorbent colour thin object against the reflective colour. The same adaptable calculation applies also to the statistical analysis between horizontal and vertically positioned thin objects on the solar cell analysed in Section 4.3.1.

Measurements were taken at five thickness levels (2, 6, 10, 14, and 20 mm), with seven repeated measurements at each thickness, representing the distance between the thin object and the solar cell between 10 - 40 cm at a 5 cm increment.

Thus:

Absorbent thin object: $5 \times 7 = 35$ observations

Reflective thin object: $5 \times 7 = 35$ observations

Total observations: $N = 70$

To obtain the group totals and means, let:

- Group 1 = Black, $n_1 = 35$
- Group 2 = Silver, $n_2 = 35$

The individual values within each group in of Figure 4.15 in Section 4.3.1 were summed to obtain the total scores:

$$\sum X_1 = 368.64 \sum X_2 = 382.96$$

To compute the mean for each group, the total score was divided by the number of observations in that group using the formula:

$$\bar{X} = \frac{\sum X}{n}$$

Thus:

$$\bar{X}_1 = \frac{368.64}{35} = 10.5326$$

$$\bar{X}_2 = \frac{382.96}{35} = 10.9417$$

Grand mean (the average power loss across all observations, regardless of group):

$$\sum X = 368.64 + 382.96 = 751.60$$

$$\bar{X} = \frac{751.60}{70} = 10.7371$$

Between-groups sum of squares (SS_B) which measures how far the group means are from the grand mean.

For a one-way ANOVA:

$$SS_B = \sum_{j=1}^{k} n_j(\bar{X}_j - \bar{X})^2$$

where $k = 2$, since only two groups are being used in the one-way anova:

$$SS_B = 35(10.5326 - 10.7371)^2 + 35(10.9417 - 10.7371)^2$$

Deviations from the grand mean:

$$10.5326 - 10.7371 = -0.2046$$

$$10.9417 - 10.7371 = 0.2046$$

Therefore:

$$SS_B = 35(0.2046^2) + 35(0.2046^2) = 70(0.04185) = 2.9295$$

As an interpretation, the group means are very close to the grand mean. Therefore, surface finish explains very little of the total variability.

Now, the variability inside each group is calculated by the sum of squares (SS_W)

$$SS_W = \sum_{j=1}^{k} \sum_{i=1}^{n_j} (X_{ij} - \bar{X}_j)^2$$

Using the observed data:

Absorbent: $SS_{W1} = \sum(X_{i1} - \bar{X}_1)^2 = 1942.4649$

Reflective: $SS_{W2} = \sum(X_{i2} - \bar{X}_2)^2 = 2134.0505$

Thus:

$$SS_W = 1942.4649 + 2134.0505 = 4076.5154$$

The next step is to calculate the Degrees of freedom (df), which represent the number of independent pieces of information available to estimate variability after accounting for constraints imposed by the model.

Between Groups:

The between-groups degrees of freedom depend on the number of group means being compared. Although there are $k = 2$ group means (Absorbent and Reflective), once one group mean is known, the other is fixed relative to the grand mean. Therefore, only one group mean can vary independently.

$$df_B = k - 1 = 2 - 1 = 1$$

This single degree of freedom represents the one independent comparison between the two group means.

Within Groups:

The within-groups degrees of freedom reflect the variability of individual observations around their respective group means. There are $N = 70$ total observations. However,

estimating the means for the $k = 2$ groups uses up two degrees of freedom—one for each group mean.

The remaining independent observations are used to estimate within-group variability:

$$df_W = N - k = 70 - 2 = 68$$

Mean squares (Mean squares convert sums of squares into variance estimates):

Between groups: $MS_B = \frac{SS_B}{df_B} = \frac{2.9295}{1} = 2.9295$

Within groups: $MS_W = \frac{SS_W}{df_W} = \frac{4076.5154}{68} = 59.9488$

F-statistic: the ratio of two variance estimates in a one-way ANOVA. It compares how much variability exists between group means to how much variability exists within the groups.

The formula for the F-statistic is:

$$F = \frac{MS_B}{MS_W}$$

where:

- MS_B (between-groups mean square) estimates variance due to differences between group means
- MS_W (within-groups mean square) estimates variance due to random variation within groups

From the previous calculations:

$$MS_B = 2.9295$$
$$MS_W = 59.9488$$

Substituting into the formula:

$$F = \frac{2.9295}{59.9488} = 0.04887$$

p-value and statistical decision:

For an F-distribution with $(1,68)$ degrees of freedom:

$$p = P(F_{(1,68)} \geq 0.04887) = 0.8257$$

Using a significance level of $\alpha = 0.05$:

$$p \geq \alpha$$

Therefore:

There is no statistically significant difference in power loss between absorbent and reflective surface finish of a thin shading object when thickness levels at the given object thickness and distance from the PV source.

Appendix E.2 – Additional information on the Random Forest Prediction Model used in Section 5.3.2

Random Forest regression is used to model power loss prediction as a nonlinear function of the input variables of umbra and penumbra size and intensity. A Random Forest is an ensemble learning method composed of multiple decision trees, each trained on a randomly resampled subset of the data.

Before model training, all input features are standardised using z-score normalisation:

$$x_{\text{scaled}} = \frac{x - \mu_x}{\sigma_x}$$

where x is the original feature value, μ_x is the mean of that feature, and σ_x is its standard deviation. This step ensures that variables with different units and numerical ranges contribute comparably during tree construction.

Each decision tree in the Random Forest recursively partitions the feature space by selecting split points that minimise the Mean Squared Error (MSE), defined as:

$$\text{MSE} = \frac{1}{n}\sum_{i=1}^{n} (y_i - \hat{y}_i)^2$$

In this expression, n is the number of samples at a given node, y_i is the observed Power_Loss value, and $\hat{y}_i$ is the predicted value. At each candidate split, the reduction in prediction error is evaluated as:

$$\Delta\text{MSE} = \text{MSE}_{\text{parent}} - (\frac{n_L}{n}\text{MSE}_L + \frac{n_R}{n}\text{MSE}_R)$$

where n_L and n_R represent the number of samples in the left and right secondary nodes, respectively, and MSE_L and MSE_R are the corresponding errors after splitting.

For the provided dataset in Section 5.3.1, these error-reducing splits frequently occur for the input variables reflecting transitions between different shading sizes and intensities. By averaging predictions across 100 independently trained trees, the Random Forest model captures the nonlinear relationships and interactions between variables that cannot be represented by linear models.

Appendix E.3 – Spearman Correlation Matrix used in Section 5.3.3

Spearman rank correlation is used to quantify the relationships between pairs of variables without assuming linear behavior or normal data distributions. This method is particularly suitable for the dataset presented in Chapter 5, which contains nonlinear trends and repeated zero values (e.g., when the size of the umbra is zero due to a large distance between the thin object and the PV source).

For any two variables X_i and X_j, the Spearman rank correlation coefficient ρ_{ij} is computed as:

$$\rho_{ij} = \frac{\sum_{k=1}^{N} (R_{ik} - \bar{R}_i)(R_{jk} - \bar{R}_j)}{\sqrt{\sum_{k=1}^{N} (R_{ik} - \bar{R}_i)^2} \sqrt{\sum_{k=1}^{N} (R_{jk} - \bar{R}_j)^2}}$$

Here, N denotes the total number of observations in the dataset, and k is the index of an individual observation. The terms R_{ik} and R_{jk} represent the ranked values of the k-th observation of variables i and j, respectively. The quantities $\bar{R}_i$ and $\bar{R}_j$ denote the mean ranks of variables i and j.

In the context of this dataset, raw values such as thickness (2.8–16.0 mm) and power loss are first converted into ranks. The correlation is then computed using these ranks rather than the original magnitudes. As a result, consistent trends, such as the increase in power loss with increasing thickness, produce high correlation values even when the relationship is nonlinear. Conversely, variables whose values are zero beyond certain distances (e.g., the total umbra size) exhibit less rank variability, which affects the resulting correlation magnitude.

The Spearman correlation matrix therefore provides a rank-based, descriptive measure of dependence between variables but does not account for multivariable interactions or conditional effects.

Appendix E.4 – Sensitivity Analysis used in Section 5.3.3

The sensitivity analysis quantifies how variations in the parameters of the shadow influence power loss. The analysis considers the following input variables:

- Thickness (mm)
- Distance (cm)
- Penumbra Size (%)
- Umbra Size (%)
- Umbra Intensity (pixel value)

- Penumbra Intensity (pixel value)

The objective of the sensitivity analysis is to determine which of these variables most strongly influence power loss.

The data is prepared and dived as follows:

- Predictors (X)**:** Thickness, Distance, Penumbra Size, Umbra Size, Umbra intensity, and Penumbra intensity
- Response (y)**:** Power_Loss

All predictor variables are standardised using z-score normalisation to ensure that variables with different physical units (e.g., millimeters, percentages, intensity values) contribute comparably to the learning process.

A Random Forest Regressor is used to model the relationship between the input variables and power loss. This model is particularly suitable since power loss depends nonlinearly on shading size and intensity and between the geomatertic parameters thickness and distance.

Feature importance in the Random Forest represents how much each variable reduces prediction error across all decision trees.

Bootstrap Resampling for Robustness:

To ensure stability and quantify uncertainty in the sensitivity estimates:

- The training dataset is resampled 30 times using bootstrap sampling
- A new Random Forest model is trained for each resampled dataset
- Feature importance values are extracted from each model

This approach captures variability caused by sampling fluctuations and avoids reliance on a single model.

Sensitivity Metrics:

For each input variable:

- The mean feature importance across all bootstrap runs represents its overall sensitivity with respect to power loss
- The standard deviation represents the uncertainty in that sensitivity estimate

Variables with higher mean importance values exert a stronger influence on power loss, while larger standard deviations indicate sensitivity that varies across operating conditions.

Visualisation and Ranking:

The sensitivity results are visualised using a horizontal bar chart:

- Bar length corresponds to mean feature importance
- Error bars represent ± one standard deviation
- Variables are ranked from least to most influential

This visualisation in Section 5.3.3 clearly identifies the dominant contributors to power loss and highlights which parameters are most critical in a thin object shading scenario.

Appendix E.5 – Bland-Altman Analysis used in Section 5.3.4.2

The Bland–Altman Analysis was used to compare the predicted power loss values from ThinShadePV with the measured values from the validation process in Section 5.3.4.2. Fifteen paired observations were obtained, where each instance consists of a predicted value and a measure value.

Let:

- $n = 15$
- Differences defined as:

$$d_i = \text{Measured}_i - \text{Predicted}_i$$

Computing means and differences:

For each instance:

$$\text{Mean}_i = \frac{\text{Predicted}_i + \text{Measured}_i}{2}$$

$$d_i = \text{Measured}_i - \text{Predicted}_i$$

Table of pared values:

Instance	Predicted Power Loss (%)	Measured Power Loss (%)	Mean	Difference (d_i)
1	2.42	4.13	3.28	1.71
2	1.68	1.32	1.50	−0.36
3	7.77	7.93	7.85	0.16
4	7.12	7.48	7.30	0.36
5	5.32	4.50	4.91	−0.82
6	1.36	0.95	1.16	−0.41
7	13.96	13.94	13.95	−0.02
8	16.67	13.14	14.91	−3.53
9	6.37	7.16	6.77	0.79
10	5.44	6.05	5.75	0.61
11	1.71	1.31	1.51	−0.40
12	20.25	21.81	21.03	1.56
13	31.43	27.95	29.69	−3.48
14	29.69	26.84	28.27	−2.85
15	29.67	29.10	29.39	−0.57

Mean difference (bias):

All individual differences are summed:

$$\sum_{i=1}^{15} d_i = 1.71 - 0.36 + 0.16 + 0.36 - 0.82 - 0.41 - 0.02 - 3.53 + 0.79 + 0.61 - 0.40 + 1.56 - 3.48 - 2.85 - 0.57$$

$$\sum_{i=1}^{15} d_i = -7.25$$

Divide by the number of observations:

The mean difference is obtained by dividing the total by the number of paired observations:

$$\bar{d} = \frac{1}{n}\sum_{i=1}^{n} d_i$$

$$\bar{d} = \frac{-7.25}{15} = 0.483$$

This indicates that, on average, the measured values are 0.48% lower than the predicted values.

Standard deviation of the differences:

$$s_d = \sqrt{\frac{1}{n-1}\sum_{i=1}^{n} (d_i - \bar{d})^2}$$

$$s_d = 1.66$$

Limits of agreement:

The 95% limits of agreement are calculated as:

$$\text{Upper LoA} = \bar{d} + 1.96 s_d$$
$$\text{Lower LoA} = \bar{d} - 1.96 s_d$$

Substituting numerical values:

$$\text{Upper LoA} = 0.48 + 1.96(1.66) = 2.7$$

$$\text{Lower LoA} = 0.48 - 1.96(1.66) = -3.7$$

Horizontal reference lines indicate:

- Mean difference (bias)
- Upper and lower limits of agreement

All points fall within the 95% limits of agreement, indicating good agreement between predicted and measured values across the observed range.

Appendix E.6 – Mann–Whitney U Test used in Section 6.3.4

This analysis compares power loss measured under two independent operating conditions:

- Varying-intensity penumbra
- Constant-intensity penumbra

Each condition produced 29 independent observations, giving a total of N = 58 measurements. These represent power loss values (%) recorded across a range of operating intensities.

Rationale for statistical methods since:

- The two groups are independent,
- A small sample sizes ($n = 29$ per group)
- Normality assumptions are violated

The Mann–Whitney U test was selected to assess whether the distributions of power loss differ between varying-intensity and constant-intensity penumbra. Moreover, while the Mann–Whitney U test determines statistical significance, it does not quantify the magnitude of the observed difference. Therefore, Cohen's d was additionally calculated as a standardised effect size to support practical interpretation in Appendix E.7 in the subsequent appendix section.

Ranking procedure:

All 58 power loss observations from both groups were pooled into a single ordered list and ranked from smallest to largest. Where identical values occurred, average ranks were assigned to preserve rank integrity.

Let:

- $n_1 = 29$: varying-intensity penumbra sample size
- $n_2 = 29$: constant penumbra sample size
- R_1: sum of ranks assigned to the varying-intensity group
- R_2: sum of ranks assigned to the constant-intensity group

Calculation of the U statistic:

The Mann–Whitney U statistic for each group is computed as:

$$U_1 = n_1 n_2 + \frac{n_1(n_1 + 1)}{2} - R_1$$

$$U_2 = n_1 n_2 + \frac{n_2(n_2 + 1)}{2} - R_2$$

The test statistic is defined as the smaller of the two values:

$$U = \min(U_1, U_2)$$

For the present dataset, this yields:

$$U = 224$$

This value represents the degree of rank separation between the two distributions.

Hypothesis testing and significance:

The null hypothesis (H_0) for the Mann–Whitney U test states that the two samples are drawn from identical distributions.

A two-sided test was performed, resulting in:

$$p = 0.002296$$

Using a significance threshold of $\alpha = 0.05$:

$$p < \alpha$$

The null hypothesis is therefore rejected which means that there is a statistically significant difference in penumbra power loss between varying-intensity and constant-intensity penumbra shadows.

Appendix E.7 – Cohen's Effect Size Analysis used in Section 6.3.3

While statistical significance indicates the presence of a difference, effect size quantifies its practical importance. Cohen's d expresses the mean difference between groups relative to the pooled variability of the data.

Group means:

Let the two independent samples be:

- Group 1: Varying-intensity penumbra power loss, size $n_1 = 29$
- Group 2: Constant-intensity penumbra power loss, size $n_2 = 29$

The mean for each group is defined as:

$$\bar{X}_1 = \frac{1}{n_1}\sum_{i=1}^{n_1} X_{1i}, \bar{X}_2 = \frac{1}{n_2}\sum_{i=1}^{n_2} X_{2i}$$

Using the dataset, the sample means are:

$$\bar{X}_{\text{varying intensity penumbra}} = 10.67$$
$$\bar{X}_{\text{constant intensity penumbra}} = 20.32$$

These means represent the average power loss (%) observed under each operating condition.

Pooled standard deviation (combined variability):

Cohen's d uses a single standard deviation representing the typical within group spread across both samples. This is the pooled standard deviation, computed from the two sample variances:

$$s_p = \sqrt{\frac{(n_1 - 1)s_1^2 + (n_2 - 1)s_2^2}{n_1 + n_2 - 2}}$$

Explanation of the terms:

- s_1^2 and s_2^2 are the sample variances
- Each variance is weighted by its degrees of freedom $(n - 1)$
- The denominator $(n_1 + n_2 - 2)$ is the total degrees of freedom for two independent samples

Using sample standard deviations calculated the pooled standard deviation is:

$$s_p = 10.80$$

This value represents the overall within-condition variability in power loss.

Computation of Cohen's d (standardised mean difference):

Cohen's d expresses the difference in group means in standard deviation units, allowing interpretation independent of the measurement scale.

$$d = \frac{\bar{X}_{\text{dynamic}} - \bar{X}_{\text{constant}}}{s_p}$$

Substituting the numerical values:

$$d = \frac{10.67 - 20.32}{10.80}$$

$$d = \frac{-9.65}{10.80} = -0.893$$

Interpretation of sign and magnitude:

The negative sign indicates that the varying intensity penumbra has a lower mean power loss than the constant condition. Moreover, the magnitude of d = -0.893 indicates that the difference in means is approximately 0.89 pooled standard deviations, which is interpreted as a large effect (using conventional thresholds: 0.2 small, 0.5 medium, 0.8 large).

Therefore:

Varying intensity penumbra results in substantially lower power loss compared with constant intensity penumbra operation, with a large practical effect size**.**

Appendix F - CSF Score Script

The full source code script for the CSF score introduced in Chapter 4, Section 4.2.5 is outlined below and can also be accessed via a GitHub repository at: **https://github.com/mattaxi/CSF-Score**

Moreover, since not all readers may have access to or be proficient in Python, a text version of the code is provided below. Moreover, lines in the script that begin with the '#' symbol and formatted to bold text, serve as comments to guide the reader of this thesis in understanding the purpose of the subsequent lines of code.

```
1: import easygui
2: from PIL import Image
3: import numpy as np
4: import pandas as pd
5:
6: def calculate_background_intensity(image_array):
7:     """Calculate background intensity using a robust method (95th percentile)."""
8:     background_intensity = np.percentile(image_array, 95)
9:     return background_intensity
10:
11: def calculate_shadow_factor(image_path):
12:     """Calculate Combined Shadow Factor (CSF) based on intensity and size."""
13:     try:
14:         # Load image and convert to greyscale
15:         image = Image.open(image_path).convert('L')
16:         image_array = np.array(image, dtype=np.int32)
17:
18:         # Calculate background intensity
19:         background_intensity = calculate_background_intensity(image_array)
20:
21:         # Calculate darkness relative to background intensity
22:         darkness = background_intensity - image_array
23:
24:         # Normalise darkness by dividing by the global maximum possible darkness (255)
25:         normalised_darkness = darkness / 255.0  # Normalise to [0, 1]
26:
27:         normalised_darkness = np.clip(normalised_darkness, 0, 1)  # Clip negative values to zero
28:
29:         # Intensity Factor (IF): Average darkness of shadow pixels
30:         shadow_pixels = normalised_darkness[normalised_darkness > 0]  # Only consider shadow pixels
31:         if len(shadow_pixels) > 0:
32:             intensity_factor = np.mean(shadow_pixels)
33:         else:
34:             intensity_factor = 0
35:
36:         # Size Factor (SF): Proportion of shadow pixels in the image
37:         total_pixels = image_array.size
38:         size_factor = len(shadow_pixels) / total_pixels
39:
40:         # Combined Shadow Factor (CSF)
41:         combined_shadow_factor = intensity_factor * size_factor
42:
43:         # Multiply by 100 to express as percentage-like value
44:         combined_shadow_factor *= 100
45:
46:         return combined_shadow_factor
47:
48:     except FileNotFoundError:
```

```
49:         easygui.msgbox(f"Error: Image file not found at {image_path}", title="Error")
50:         return None
51:     except Exception as e:
52:         easygui.msgbox(f"Error processing image {image_path}: {e}", title="Error")
53:         return None
54:
55: def process_images():
56:     """Opens a file dialog, processes selected images, calculates CSF, and displays a table using easygui."""
57:     image_paths = easygui.fileopenbox(msg="Select one or more image files",
58:                                       title="Shadow Factor Calculator",
59:                                       multiple=True,
60:                                       filetypes=["*.png", "*.jpg", "*.jpeg", "*.bmp", "*.tiff"])
61:
62:     if not image_paths:
63:         easygui.msgbox("No images selected.", title="Information")
64:         return
65:
66:     results = []
67:     for image_path in image_paths:
68:         score = calculate_shadow_factor(image_path)
69:         if score is not None:
70:             results.append({
71:                 "Image Filename": image_path.split("/")[-1],  # Extract filename
72:                 "Shadow Factor (%)": f"{score:.2f}%"  # Display score with two decimal places
73:             })
74:
75:     if results:
76:         df = pd.DataFrame(results)
77:         df.set_index("Image Filename", inplace=True)
78:         table_string = df.to_string()
79:         easygui.textbox(msg="Shadow Factor Results",
80:                         title="Shadow Factor Calculator",
81:                         text=table_string)
82:     else:
83:         easygui.msgbox("No images processed successfully.", title="Information")
84:
85: # Run the image processing function
86: if __name__ == "__main__":
87:     process_images()
```

Appendix G - ThinShadePV Script

The complete source code for the ThinShadePV application has been made publicly available on GitHub, an online platform widely used for version control and collaborative software development. Hosting the script on GitHub improves transparency, reproducibility, and accessibility for researchers and developers who may wish to examine, replicate, or build upon this work.

The repository can be accessed at: **https://github.com/mattaxi/ThinShadePV**

For reference to readers of this thesis and other researchers attempting to continue on this study, the full source code is also included below. As previously explained in Appendix F, lines in the script that begin with the '#' symbol and formatted to bold text, serve as comments to guide the reader of this thesis in understanding the purpose of the subsequent lines of code.

```
from tkinter import Label, Tk, messagebox
from PIL import Image, ImageTk
import pandas as pd
import numpy as np
from sklearn.ensemble import RandomForestRegressor
from sklearn.model_selection import train_test_split
import matplotlib.pyplot as plt
from scipy.optimize import curve_fit
from sklearn.linear_model import LinearRegression
from collections import Counter
import os
import cv2
import easygui
from sklearn.metrics import mean_squared_error, r2_score
from tkinter import ttk
from matplotlib.figure import Figure
from matplotlib.backends.backend_tkagg import FigureCanvasTkAgg
import matplotlib.image as mpimg
from sklearn.metrics import mean_squared_error, mean_absolute_error, r2_score

# The Function to train the Random Forest model
def train_random_forest(data_path):
    import pandas as pd
    from sklearn.model_selection import train_test_split
    from sklearn.ensemble import RandomForestRegressor
    from sklearn.metrics import mean_squared_error, mean_absolute_error, r2_score

    # Dataset being loaded
    data = pd.read_excel(data_path)
    data.fillna(0, inplace=True)

    # column names for debugging
    print("Columns in dataset:", data.columns)

    # Verify the required columns exist, otherwise an error is printed
    required_columns = ['Thickness', 'Distance', 'Total_penumbra_percentage',
                        'Total_umbra_percentage', 'Umbra_Intensity', 'Penumbra_Intensity',
                        'Power_Loss']
    missing_columns = [col for col in required_columns if col not in data.columns]
```

```
    if missing_columns:
        raise KeyError(f"The following required columns are missing in the dataset: {missing_columns}")

    # Features and targets
    X = data[['Total_umbra_percentage', 'Total_penumbra_percentage',
              'Umbra_Intensity', 'Penumbra_Intensity']]
    y = data[['Power_Loss', 'Distance', 'Thickness']]  # Multiple outputs

    # Split the dataset
    X_train, X_test, y_train, y_test = train_test_split(X, y, test_size=0.2, random_state=42)

    # Train the Random Forest model
    rf_model = RandomForestRegressor(n_estimators=100, random_state=42)
    rf_model.fit(X_train, y_train)

    # Evaluate the model
    y_pred = rf_model.predict(X_test)
    rmse = np.sqrt(mean_squared_error(y_test["Power_Loss"], y_pred[:, 0]))
    mae = mean_absolute_error(y_test["Power_Loss"], y_pred[:, 0])
    r2 = r2_score(y_test["Power_Loss"], y_pred[:, 0])
    print(f"root mean squared: {rmse}")
    print(f"MAE: {mae:.2f}")
    print(f"R² Score: {r2:.2f}")

    return rf_model, X_test, y_test, mae, r2, rmse

# GUI Function
def create_gui():
    global rf_model, X_test, y_test  # Declare globals first
    rf_model, X_test, y_test, mae, r2, rmse = train_random_forest("Training data.xlsx")

    # Main application window
    root = tk.Tk()
    root.title("Power Loss Predictor for Thin Object Shadows")
    root.geometry("900x1000")

    # Center the window on the screen
    screen_width = root.winfo_screenwidth()
    screen_height = root.winfo_screenheight()
    window_width = 900
    window_height = 1000
    x_coordinate = (screen_width // 2) - (window_width // 2)
    y_coordinate = (screen_height // 2) - (window_height // 2)
    root.geometry(f"{window_width}x{window_height}+{x_coordinate}+{y_coordinate}")

    # Creation of a scrollable canvas
    canvas = tk.Canvas(root, bg="#FFFFFF")
    scrollbar = tk.Scrollbar(root, orient="vertical", command=canvas.yview)
    scrollable_frame = tk.Frame(canvas, bg="#FFFFFF")

    # Configure scrolling
    scrollable_frame.bind(
        "<Configure>",
        lambda e: canvas.configure(scrollregion=canvas.bbox("all"))
    )
    canvas.create_window((0, 0), window=scrollable_frame, anchor="nw")
    canvas.configure(yscrollcommand=scrollbar.set)

    # Pack the canvas and scrollbar
    canvas.pack(side="left", fill="both", expand=True)
    scrollbar.pack(side="right", fill="y")

    # Function to switch frames
    def show_frame(frame):
        frame.tkraise()

    # Three GUI frames are created
    frame1 = tk.Frame(scrollable_frame, bg="#FFFFFF")
    frame2 = tk.Frame(scrollable_frame, bg="#FFFFFF")
    frame3 = tk.Frame(scrollable_frame, bg="#FFFFFF")

    for frame in (frame1, frame2, frame3):
        frame.grid(row=0, column=0, sticky="nsew")

    frame1.tkraise()  # Ensures the main menu is displayed first
```

```
115:
116:    # -------- Top Logo (Shared Between Frames) --------
117:
118:    # Loading the top logo
119:    logo_path = "ThinShadePV LOGO.png"
120:    original_logo = Image.open(logo_path)
121:    resized_logo = original_logo.resize((400, 100))
122:    resized_logo_tk = ImageTk.PhotoImage(resized_logo)
123:
124:    # The top logo is included to each frame
125:    for frame in (frame1, frame2, frame3):
126:        top_logo_label = tk.Label(frame, image=resized_logo_tk, bg="#FFFFFF")
127:        top_logo_label.image = resized_logo_tk
128:        top_logo_label.pack(pady=20)
129:
130: # -------- Frame 1: Main Menu --------
131:
132:    note_label = tk.Label(
133:        frame1,
134:        text="Press one of the two buttons below to indicate current status of your PV system",
135:        font=("Arial", 14, "bold"),  # Bold text
136:        fg="#333333",  # Dark grey text color for better readability
137:        bg="#FFFFFF",  # White background
138:        justify="center",  # Center alignment
139:        wraplength=700  # Ensures text wraps neatly if too long
140:    )
141:    note_label.pack(pady=10)
142:
143:     # The icon image is loaded
144:    icon_path = "PV on roof.png"
145:    icon_image = Image.open(icon_path).resize((150, 200))  # the icon can be resized as needed
146:    icon_image_tk = ImageTk.PhotoImage(icon_image)
147:
148:    # A frame to hold the button and the icon side by side
149:    button_frame = tk.Frame(frame1, bg="#FFFFFF")
150:    button_frame.pack(pady=10)
151:
152:    # Button for Existing PV on Roof
153:    pre_pv_button = tk.Button(
154:        button_frame,
155:        text="Existing PV on roof",
156:        font=("Arial", 14, "bold"),
157:        command=lambda: show_frame(frame3),  # Switch to frame3
158:        width=20, height=2,
159:        bg="#4CAF50",  # Background color
160:        fg="black",  # Text color
161:        relief="flat",
162:        padx=10, pady=10
163:    )
164:    pre_pv_button.pack(side="left", padx=5)
165:
166:    # Label for the icon
167:    icon_label = tk.Label(
168:        button_frame,
169:        image=icon_image_tk,
170:        bg="#FFFFFF"  # Match the background color
171:    )
172:    icon_label.image = icon_image_tk
173:    icon_label.pack(side="left", padx=5)
174:
175:    # Adding a note (non-bold, non-italic)
176:    note_label = tk.Label(frame1, text="Note: Existing PV on roof refers to the instance where the PV system has been
installed \nand remedial actions are being considered by the user to reduce the power loss at a \nparticular thin object shading
instance", font=("Arial", 12), fg="#333333", bg="#FFFFFF")
177:    note_label.pack(pady=5)
178:
179:        #  "Pre Installation of PV on roof" button
180:    icon_path_post = "No PV on roof.png"
181:    post_icon_image = Image.open(icon_path_post).resize((150, 200))  # The icon can be resized as needed
182:    post_icon_image_tk = ImageTk.PhotoImage(post_icon_image)
183:
184:    # Create a frame to hold the button and the icon side by side
185:    post_button_frame = tk.Frame(frame1, bg="#FFFFFF")
186:    post_button_frame.pack(pady=10)
187:
```

```
    # Button for Pre Installation of PV on Roof
    post_pv_button = tk.Button(
        post_button_frame,
        text="Design stage of PV system",
        font=("Arial", 14, "bold"),
        command=lambda: show_frame(frame2),
        width=20,
        height=2,
        bg="#4CAF50",
        fg="black",
        relief="flat",
        padx=10,
        pady=10
    )
    post_pv_button.pack(side="left", padx=5)

    # Label for the icon
    post_icon_label = tk.Label(
        post_button_frame,
        image=post_icon_image_tk,
        bg="#FFFFFF"  # Match the background color
    )
    post_icon_label.image = post_icon_image_tk
    post_icon_label.pack(side="left", padx=5)

    # Note (non-bold, non-italic)
    note_label = tk.Label(frame1, text="Note: The design stage of a PV system refers to the phase when the rooftop owner \nintends to install solar panels and seeks an estimate of potential power loss caused \nby the identified thin object crossing the planned installation area. \n\nThe decision to remove, relocate, or retain this object rests solely with the rooftop owner.", font=("Arial", 12), fg="#333333", bg="#FFFFFF")
    note_label.pack(pady=1)

    # Open the logo image using Pillow
    logo_image = Image.open("ISE Logo.png")

    if logo_image.mode == 'RGBA':

        white_background = Image.new('RGBA', logo_image.size, (255, 255, 255, 255))  # White background
        white_background.paste(logo_image, (0, 0), logo_image)

        logo_image = white_background.convert("RGB")

    # Resize the logo image
    logo_image = logo_image.resize((100, 60))

    # Convert to Tkinter-compatible image
    logo_image_tk = ImageTk.PhotoImage(logo_image)

    # A label with the logo and placed in Frame 1 (at the bottom)
    logo_label = tk.Label(frame1, image=logo_image_tk, anchor="center", bg="#FFFFFF")  # White background for the label
    logo_label.image = logo_image_tk
    logo_label.pack(side=tk.BOTTOM, pady=100)  # Adjust padding as needed

# Frame 3: Pre PV Installation----------

    # A container for the image panel and label
    image_panel_container = tk.Frame(frame3, bg="#FFFFFF")
    image_panel_container.pack(side="left", padx=(10, 0), pady=0, anchor="nw")

    # The bordered white image frame (same as before)
    image_frame = tk.Frame(image_panel_container, bg="#FFFFFF", relief="groove", bd=2, width=500, height=450)
    image_frame.pack()
    image_frame.pack_propagate(False)

    # image label (shown inside image_frame)
    input_image_label = tk.Label(image_frame, bg="#FFFFFF")
    input_image_label.pack(pady=(10, 5))

    # instructions label (shown inside image_frame)
    instructions = tk.Label(
        image_frame,
        text="Insert Image with the following conditions:\n"
             "• Background of image must be white in colour\n"
             "• Shadow must be as horizontally aligned as possible\n"
```

```
259:            "• No foreign objects must be displayed in the image",
260:        font=("Arial", 10),
261:        bg="#FFFFFF",
262:        justify="left"
263:    )
264:    instructions.pack(pady=(10, 0))
265:
266:    # The shadow label placed under the white box (outside image_frame)
267:    shadow_type_label = tk.Label(
268:        image_panel_container,
269:        text="",
270:        font=("Segoe UI", 12, "bold"),
271:        fg="#222222",
272:        bg="#f0f0f0",
273:        relief="groove",
274:        padx=10,
275:        pady=5
276:    )
277:    shadow_type_label.pack(pady=(10, 0))
278:
279:    # label for displaying notes in the image frame
280:    image_note_label = tk.Label(
281:        image_frame,
282:        text=(
283:            "Insert Image with the following conditions:\n"
284:            " \n"
285:            "• Background of image must be white in colour\n"
286:            "• Shadow must be as horizontally aligned as possible\n"
287:            "• No foreign objects must be displayed in the image"
288:        ),
289:        font=("Arial", 16, "bold"),
290:        bg="#FFFFFF",
291:        fg="#000000",  # Light grey text color
292:        justify="center",
293:        wraplength=450  # Ensures text wraps within the frame
294:    )
295:    image_note_label.pack(expand=True, fill="both")
296:
297:    # label to display the loaded image inside the image frame
298:    image_display_label = tk.Label(image_frame, bg="#FFFFFF")
299:    image_display_label.place(relx=0.5, rely=0.5, anchor="center")
300:
301:    # Updated load_images function to display the first image
302:    def load_images():
303:        # Reset all labels
304:        reset_labels()
305:        shadow_type_label.config(text="")  # Reset label when a new image is loaded
306:
307:        global image_paths
308:        file_paths = easygui.fileopenbox(
309:            msg="Select Images",
310:            title="Image Selector",
311:            filetypes=["*.png", "*.jpg", "*.jpeg"],
312:            multiple=True,
313:        )
314:        if file_paths:
315:            image_paths = list(file_paths)
316:            messagebox.showinfo("Images Selected", f"{len(image_paths)} image(s) selected.")
317:
318:            # Display the first image in the GUI
319:            first_image_path = image_paths[0]
320:            img = Image.open(first_image_path)
321:
322:            # Resize the image to fit the frame, maintaining aspect ratio
323:            frame_width, frame_height = 500, 400  # Frame size
324:            img.thumbnail((frame_width, frame_height))  # Resize the image to fit within the frame
325:            img_tk = ImageTk.PhotoImage(img)
326:
327:            # Update the label to display the resized image
328:            image_display_label.config(image=img_tk)
329:            image_display_label.image = img_tk
330:
331:            # Hide the note label
332:            image_note_label.pack_forget()
333:        else:
```

```
334:            messagebox.showinfo("No Selection", "No images were selected.")
335:
336:    # Define the prediction function
337:    def predict_features():
338:        try:
339:            # Fetch values from the input labels (replace "N/A" with 0 if no data exists)
340:            total_umbra_percentage = float(total_umbra_value_frame3.cget("text").replace("N/A", "0").replace("%", ""))
341:            total_penumbra_percentage = float(total_penumbra_value_frame3.cget("text").replace("N/A", "0").replace("%", ""))
342:            umbra_intensity = float(umbra_intensity_value_frame3.cget("text").replace("N/A", "0"))
343:            totalpenumbra_intensity = float(penumbra_intensity_value_frame3.cget("text").replace("N/A", "0"))
344:
345:            # Prepare input features for the model
346:            input_features = np.array([[total_umbra_percentage, total_penumbra_percentage, umbra_intensity,
totalpenumbra_intensity]])
347:
348:            # Use the trained model to predict power loss, distance, and thickness
349:            predicted_values = rf_model.predict(input_features)[0]
350:
351:            # Debug: Print predicted values
352:            print("Predicted Values:", predicted_values)
353:
354:            # Update the labels with predictions
355:            power_loss_label.config(text=f"Predicted Power Loss: {predicted_values[0]:.2f}%")
356:
357:            # --- Compute performance metrics for the validation set ---
358:
359:        except Exception as e:
360:            # Handle any errors gracefully
361:            messagebox.showerror("Prediction Error", f"An error occurred: {e}")
362:
363:    # Define the parent frame for predictions with fixed width
364:    predictions_frame = tk.Frame(frame3, bg="#FFFFFF", padx=2, pady=2, width=300)  # Fixed width
365:    predictions_frame.pack(side="right", anchor="ne", fill="y")  # Align to the right
366:
367:
368:    # Container frame for right-aligned elements
369:    right_aligned_frame = tk.Frame(predictions_frame, bg="#FFFFFF", width=300)
370:    right_aligned_frame.pack(fill="y", padx=2, pady=2)  # Avoid `expand=True` to prevent stretching
371:
372:
373:    # Define a function to create styled labels
374:    def create_styled_label(parent, text, font=("Arial", 14, "bold"), fg="#000000", bg="#FFFFFF", anchor="e", width=25,
pady=5):
375:        label = tk.Label(
376:            parent,
377:            text=text,
378:            font=font,
379:            fg=fg,
380:            bg=bg,
381:            anchor=anchor,
382:            width=width
383:        )
384:        label.pack(fill="x", pady=pady, anchor="e")
385:        return label
386:
387:
388:    # Add a moderately sized "Load Images" button
389:    load_images_button = tk.Button(
390:        right_aligned_frame,
391:        text="Load Images",  # Concise but descriptive text
392:        font=("Arial", 14, "bold"),  # Moderate font size
393:        command=lambda: load_images(),
394:        bg="#FFC107",
395:        fg="black",
396:        relief="flat",
397:        padx=10,  # Adjusted padding for moderate size
398:        pady=5
399:    )
400:    load_images_button.pack(anchor="e", pady=5)
401:
402:
403:    # note for dimension input
404:    dimension_note = tk.Label(
405:        right_aligned_frame,
406:        text="Ensure Image is croped to the overall \nsize of one single solar cell \n ",  # Instructional note
```

```
407:        font=("Arial", 11, "bold"),
408:        bg="#FFFFFF",  # Matching background color
409:        fg="black",  # Matching text color
410:        justify="left"
411:    )
412:    dimension_note.pack(anchor="e", pady=5)
413:
414:    def process_and_predict():
415:        process_images()
416:        predict_features()
417:
418:    process_and_predict_button = tk.Button(
419:        right_aligned_frame,
420:        text="Process & Predict",
421:        command=process_and_predict,
422:        bg="#696969",  # Dark grey background
423:        fg="#000000",  # White text for better contrast
424:        activebackground="#505050",  # Slightly darker grey when pressed
425:        activeforeground="#FFFFFF",  # Keep text white when pressed
426:        font=("Arial", 14, "bold"),  # Moderate font size
427:        relief="raised",  # Raised button style for 3D effect
428:        bd=3,  # Moderate border depth
429:        padx=10,  # Adjusted padding for moderate size
430:        pady=5
431:    )
432:    process_and_predict_button.pack(anchor="e", pady=5)
433:
434:    # Helper function to create labeled value pairs
435:    def create_labeled_value_pair(parent, label_text, value_text, label_font=("Arial", 14, "bold"),
436:                                  value_font=("Arial", 14, "bold"), label_fg="#000000", label_bg="#FFFFFF",
437:                                  value_fg="#000000", value_bg="#E0F7E0", label_width=18, value_width=10, pady=5):
438:        """Creates a label and a value pair in a frame."""
439:        frame = tk.Frame(parent, bg=label_bg)
440:        frame.pack(fill="x", pady=pady, anchor="e")
441:
442:        # Label for the description
443:        label = tk.Label(
444:            frame,
445:            text=label_text,
446:            font=label_font,
447:            fg=label_fg,
448:            bg=label_bg,
449:            anchor="e",
450:            width=label_width  # Adjusted width for the label
451:        )
452:        label.pack(side="left", padx=5)
453:
454:        # Label for the value
455:        value = tk.Label(
456:            frame,
457:            text=value_text,
458:            font=value_font,
459:            fg=value_fg,
460:            bg=value_bg,
461:            anchor="e",
462:            width=value_width  # Adjusted width for the value box
463:        )
464:        value.pack(side="left", padx=5)
465:
466:        return label, value
467:
468:    # Add Total Umbra Percentage, Total Penumbra Percentage, Umbra Intensity, and Penumbra Intensity with
styled labels
469:    total_umbra_label_frame3, total_umbra_value_frame3 = create_labeled_value_pair(
470:        right_aligned_frame, "Total Umbra %:", "N/A", label_width=18, value_width=10
471:    )
472:    total_penumbra_label_frame3, total_penumbra_value_frame3 = create_labeled_value_pair(
473:        right_aligned_frame, "Total Penumbra %:", "N/A", label_width=18, value_width=10
474:    )
475:    umbra_intensity_label_frame3, umbra_intensity_value_frame3 = create_labeled_value_pair(
476:        right_aligned_frame, "Umbra Intensity:", "N/A", label_width=18, value_width=10
477:    )
478:    penumbra_intensity_label_frame3, penumbra_intensity_value_frame3 = create_labeled_value_pair(
479:        right_aligned_frame, "Penumbra Intensity:", "N/A", label_width=18, value_width=10
480:    )
```

```
481:
482:    # Adjusted labels with shorter widths
483:    power_loss_label = create_styled_label(
484:        right_aligned_frame,
485:        "Power Loss (%): N/A",  # Shortened text
486:        bg="#32CD32",  # Green background
487:        fg="#FFFFFF",  # White text
488:        width=18  # Compact width for the green background
489:    )
490:
491:    # Varying labels for performance metrics (initially blank)
492:    label_rmse = create_styled_label(
493:        right_aligned_frame,
494:        f"RMSE: {rmse:.2f}",
495:        width=18,
496:        fg="#000000",
497:        bg="#FFFFFF"
498:    )
499:    label_rmse.pack(pady=2)
500:
501:    label_mae = create_styled_label(
502:        right_aligned_frame,
503:        f"MAE: {mae:.2f}",
504:        width=18,
505:        fg="#000000",
506:        bg="#FFFFFF"
507:    )
508:    label_mae.pack(pady=2)
509:
510:    label_r2 = create_styled_label(
511:        right_aligned_frame,
512:        f"R²: {r2:.3f}",
513:        width=18,
514:        fg="#000000",
515:        bg="#FFFFFF"
516:    )
517:    label_r2.pack(pady=2)
518:
519:    # Back to Main Menu function
520:    def back_to_main_menu():
521:        try:
522:            # function correctly linked to raise frame1
523:            show_frame(frame1)
524:        except Exception as e:
525:            print(f"Error: {e}")  # Debugging aid to catch any issues
526:
527:    # Back to Main Menu button to the bottom of the right-aligned frame
528:    back_button = tk.Button(
529:        right_aligned_frame,
530:        text="Back to Main Menu",
531:        command=back_to_main_menu,  # Updated function call for back navigation
532:        bg="#696969",  # Dark grey background
533:        fg="#000000",  # White text for contrast
534:        activebackground="#505050",  # Slightly darker grey when pressed
535:        activeforeground="#FFFFFF",  # Keep text white when pressed
536:        font=("Arial", 12, "bold"),  # Bold font for emphasis
537:        relief="raised",  # Raised style for 3D effect
538:        bd=3,  # Border thickness for tactile appearance
539:        padx=20,  # Add horizontal padding
540:        pady=10  # Add vertical padding
541:    )
542:    back_button.pack(side="bottom", anchor="s", pady=10, fill="x")  # Anchor it to the bottom
543:
544:    # Global Variables
545:    global image_paths
546:    image_paths = []  # Initialize the image paths list
547:
548:    def reset_labels():
549:        """Reset all labels to their default state."""
550:        # Reset the text values of all labels
551:        total_umbra_value_frame3.config(text="N/A")
552:        total_penumbra_value_frame3.config(text="N/A")
553:        umbra_intensity_value_frame3.config(text="N/A")
554:        penumbra_intensity_value_frame3.config(text="N/A")
555:
```

```
    # All labels remain visible and reset to their default text
    for label in [
        total_umbra_label_frame3,
        total_umbra_value_frame3,
        total_penumbra_label_frame3,
        total_penumbra_value_frame3,
        umbra_intensity_label_frame3,
        umbra_intensity_value_frame3,
        penumbra_intensity_label_frame3,
        penumbra_intensity_value_frame3,
    ]:
        label.pack(pady=5)

def process_images():
    """Process selected images and update the labels."""
    if not image_paths:
        # Error message if no images are selected
        messagebox.showwarning("No Images Selected", "Please load images before processing.")
        return


    results_list = []
    # Define column names explicitly
    column_names = [
        'Image', 'Rapid_Increase_Start_Above', 'Rapid_Increase_End_Above',
        'Rapid_Increase_Start_Below', 'Rapid_Increase_End_Below',
        'Denormalised_Start_Y_Above', 'Denormalised_End_Y_Above',
        'Denormalised_Start_Y_Below', 'Denormalised_End_Y_Below',
        'Umbra_Value_Limit', 'Penumbra_Only_Value', 'Total_Pixels',
        'Percentage_Penumbra_Only', 'Total_length_of_Image_100',
        'Total_length_of_penumbra', 'Total_penumbra_percentage',
        'Total_length_of_umbra', 'Total_umbra_percentage', 'umbra_intensity', 'penumbra_intensity',
        'Average Penumbra Only Intensity Value',
        'Normalised % Average Penumbra Only Intensity Value',
        'Only_penumbra_present'
    ]

    # Process each selected image
    for image_path in image_paths:
        try:
            print(f"Processing image: {image_path}")  # Debugging message
            result = create_guide_plot_dual(image_path, pixels_above_darkest=5000)
            print(f"Processed result for {image_path}: {result}")  # Debugging message
            results_list.append((os.path.basename(image_path), *result))
        except Exception as e:
            # Handle individual image processing errors
            messagebox.showerror("Processing Failed", f"Failed to process {image_path}: {e}")
            print(f"Error processing {image_path}: {e}")
            continue  # Skip to the next image

    if results_list:
        try:
            # DataFrame for results
            results_df = pd.DataFrame(results_list, columns=column_names)
            results_df.fillna(0, inplace=True)  # Fill NaN values to avoid issues

            # Extract metrics
            total_umbra_percentage = results_df['Total_umbra_percentage'].mean()
            total_penumbra_percentage = results_df['Total_penumbra_percentage'].mean()
            penumbra_only_percentage = results_df['Percentage_Penumbra_Only'].mean()
            average_penumbra_only_intensity = results_df['Average Penumbra Only Intensity Value'].mean()

            # Debugging outputs
            print("Metrics:")
            print(f"Total Umbra Percentage: {total_umbra_percentage}")
            print(f"Total Penumbra Percentage: {total_penumbra_percentage}")
            print(f"Penumbra Only Percentage: {penumbra_only_percentage}")

            # Retrieve values for further decision-making
            umbra_value_limit = results_df['Umbra_Value_Limit'].iloc[0]
            denormalised_end_y_above = results_df['Denormalised_End_Y_Above'].iloc[0]
            denormalised_end_y_below = results_df['Denormalised_End_Y_Below'].iloc[0]

            # Decide whether to show Penumbra Only or both Umbra and Penumbra labels
```

```
630:             if abs(umbra_value_limit - denormalised_end_y_above) <= 1 or abs(umbra_value_limit -
denormalised_end_y_below) <= 1:
631:                 # Penumbra Only condition
632:                 reset_labels()  # Reset to hide Umbra-related labels
633:                 total_penumbra_value_frame3.config(text=f"{penumbra_only_percentage:.2f}%")
634:                 penumbra_intensity_value_frame3.config(text=f"{average_penumbra_only_intensity:.2f}")
635:             else:
636:                 # Show both Umbra and Penumbra
637:                 total_umbra_value_frame3.config(text=f"{total_umbra_percentage:.2f}%")
638:                 total_penumbra_value_frame3.config(text=f"{total_penumbra_percentage:.2f}%")
639:                 umbra_intensity_value_frame3.config(text=f"{results_df['umbra_intensity'].mean():.2f}")
640:                 penumbra_intensity_value_frame3.config(text=f"{results_df['penumbra_intensity'].mean():.2f}")
641:
642:             # Save results to Excel
643:             results_excel_path = os.path.join(desktop_path, "Processed_Results.xlsx")
644:             results_df.to_excel(results_excel_path, index=False)
645:             messagebox.showinfo("Processing Complete", f"Results saved to:\n{results_excel_path}")
646:         except Exception as e:
647:             # Handle errors during DataFrame processing or saving
648:             messagebox.showerror("Error", f"An error occurred while saving results: {e}")
649:
650:
651: def predict_power_loss(rf_model, total_umbra, total_penumbra, umbra_intensity, penumbra_intensity):
652:     try:
653:         # Prepare input features
654:         input_features = np.array([[total_umbra, total_penumbra, umbra_intensity, penumbra_intensity]])
655:
656:         # Predict power loss
657:         predicted_loss = rf_model.predict(input_features)[0]
658:         return predicted_loss
659:     except Exception as e:
660:         messagebox.showerror("Error", f"Prediction failed: {e}")
661:         return None
662:
663: # Function to normalise data
664: def normalise_data(data):
665:     min_val = np.min(data)
666:     max_val = np.max(data)
667:     normalised_data = 1 - (data - min_val) / (max_val - min_val)
668:     return normalised_data
669:
670: # Function to denormalise data
671: def denormalise_data(normalised_data, original_data):
672:     min_val = np.min(original_data)
673:     max_val = np.max(original_data)
674:     denormalised_data = min_val + (1 - normalised_data) * (max_val - min_val)
675:     return denormalised_data
676:
677: # Sigmoid function
678: def sigmoid(x, L, k, x0):
679:     y = L / (1 + np.exp(-k * (x - x0)))
680:     return y
681:
682: # Fit sigmoidal curves to data above and below the darkest pixel
683: def fit_dual_sigmoid_curves(x, y):
684:
685:     p0_above = [np.max(y), 0.001, np.median(x)]
686:     p0_below = [np.min(y), -0.001, np.median(x)]
687:
688:     # Fit sigmoidal curve for data above the darkest pixel
689:     params_above, _ = curve_fit(sigmoid, x[x <= np.median(x)], y[x <= np.median(x)], p0_above, method='trf',
maxfev=6000)
690:
691:     # Fit sigmoidal curve for data below the darkest pixel
692:     params_below, _ = curve_fit(sigmoid, x[x > np.median(x)], y[x > np.median(x)], p0_below, method='trf',
maxfev=6000)
693:
694:     return params_above, params_below
695:
696: def rotate_image(image):
697:     # GObtain the height and width of the image
698:     height, width = image.shape
699:
700:     # Find the darkest pixel in each column
701:     darkest_pixels = np.argmin(image, axis=0)
```

```
702:
703:        # Prepare the data for linear regression
704:        X = np.arange(width).reshape(-1, 1)
705:        y = darkest_pixels
706:
707:        # Perform linear regression to find the line of best fit
708:        reg = LinearRegression().fit(X, y)
709:        slope = reg.coef_[0]
710:
711:        # Calculate the angle to rotate
712:        angle = np.degrees(np.arctan(slope))
713:
714:        # Find the most common pixel intensity value
715:        pixels_above_150 = image[image > 150]
716:        if len(pixels_above_150) > 0:
717:            most_common_pixel = int(Counter(pixels_above_150).most_common(1)[0][0])
718:        else:
719:            most_common_pixel = 255
720:
721:        # Center of the image
722:        center = (width // 2, height // 2)
723:
724:        # Calculate the rotation matrix
725:        rotation_matrix = cv2.getRotationMatrix2D(center, angle, 1.0)
726:
727:        # Perform the rotation with the most common pixel value as border
728:        rotated_image = cv2.warpAffine(image, rotation_matrix, (width, height), borderMode=cv2.BORDER_CONSTANT,
borderValue=(most_common_pixel,))
729:
730:        return rotated_image
731:
732:    def create_guide_plot_dual(image_path, pixels_above_darkest=5000):
733:        # Load the image, convert to greyscale, and convert to numpy array
734:        img = Image.open(image_path)
735:        img_grey = img.convert('L')
736:        img_array = np.array(img_grey)
737:
738:        # Rotate the image
739:        img = rotate_image(img_array)
740:
741:        # Save the rotated image to the desktop folder
742:        rotated_image_path = os.path.join(desktop_path, f"Rotated_{os.path.basename(image_path)}")
743:        cv2.imwrite(rotated_image_path, img)
744:
745:        # Average out all the pixel values from left to right
746:        avg_column = np.mean(img_array, axis=1)
747:
748:        # Find the index of the darkest pixel in the averaged column
749:        darkest_pixel_index = np.argmin(avg_column)
750:
751:        # Select the pixels vertically above and below the darkest pixel
752:        selected_pixels = avg_column[darkest_pixel_index-pixels_above_darkest:darkest_pixel_index+pixels_above_darkest]
753:
754:        # Normalise the data
755:        normalised_data = normalise_data(selected_pixels)
756:
757:        # Create a DataFrame
758:        df = pd.DataFrame({'y': normalised_data})
759:        df['x'] = np.arange(0, len(df['y']))
760:
761:        # Fit the dual sigmoidal curves
762:        params_above, params_below = fit_dual_sigmoid_curves(df['x'], df['y'])
763:
764:        x_fit_above = np.linspace(df['x'].min(), np.median(df['x']), 1000)
765:        y_fit_above = sigmoid(x_fit_above, *params_above)
766:
767:        x_fit_below = np.linspace(np.median(df['x']), df['x'].max(), 1000)
768:        y_fit_below = sigmoid(x_fit_below, *params_below)
769:
770:        # new function for automating start
771:
772:        # Determine flat regions
773:        num_points = len(df['y'])
774:        left_end = df['y'][:num_points // 10]
775:        right_end = df['y'][-num_points // 10:]
```

```
776:
777:        # Take the higher of the two flat-region max values
778:        flat_max = max(np.max(left_end), np.max(right_end))
779:        threshold = flat_max + 0.05
780:
781:        # Find first index where the curve exceeds this threshold
782:        threshold_cross_index = np.argmax(df['y'] > threshold)
783:        start_x = df['x'].iloc[threshold_cross_index]
784:
785:        # Find the index where the curve starts to increase rapidly for the curve above the darkest pixel
786:        rapid_increase_start_above = start_x
787:        rapid_increase_start_y_above = np.interp(start_x, x_fit_above, y_fit_above)
788:
789:        # Find the index where the curve levels off for the curve above the darkest pixel
790:        threshold_end_above = 0.95 * (np.max(y_fit_above) - np.min(y_fit_above)) + np.min(y_fit_above)
791:        rapid_increase_end_index_above = np.argmax(y_fit_above >= threshold_end_above)
792:        rapid_increase_end_above = x_fit_above[rapid_increase_end_index_above]
793:        rapid_increase_end_y_above = y_fit_above[rapid_increase_end_index_above]
794:
795:        # Find the index where the curve starts to increase rapidly for the curve below the darkest pixel
796:        # Compute flat max from both ends again (reuse if needed)
797:        flat_max = max(np.max(left_end), np.max(right_end))
798:        threshold = flat_max + 0.05
799:
800:        # Find index where the BOTTOM curve drops below the threshold, from right to left
801:        threshold_cross_index_below = len(df['y']) - np.argmax(df['y'][::-1] > threshold) - 1
802:        start_x_below = df['x'].iloc[threshold_cross_index_below]
803:
804:        # Interpolate from sigmoid fit for below curve
805:        rapid_increase_start_below = start_x_below
806:        rapid_increase_start_y_below = np.interp(start_x_below, x_fit_below, y_fit_below)
807:
808:        # Find the index where the curve levels off for the curve below the darkest pixel
809:        threshold_end_below = 0.95 * (np.max(y_fit_below) - np.min(y_fit_below)) + np.min(y_fit_below)
810:        rapid_increase_end_index_below = len(x_fit_below) - np.argmin(y_fit_below[::-1] < threshold_end_below)
811:        rapid_increase_end_below = x_fit_below[rapid_increase_end_index_below]
812:        rapid_increase_end_y_below = y_fit_below[rapid_increase_end_index_below]
813:
814:        # Denormalise the start and end values
815:        denormalised_start_y_above = denormalise_data(rapid_increase_start_y_above, selected_pixels)
816:        denormalised_end_y_above = denormalise_data(rapid_increase_end_y_above, selected_pixels)
817:        denormalised_start_y_below = denormalise_data(rapid_increase_start_y_below, selected_pixels)
818:        denormalised_end_y_below = denormalise_data(rapid_increase_end_y_below, selected_pixels)
819:
820:        # Calculate total length of Image (100%)
821:        total_length_image_100 = len(avg_column)
822:
823:        # Calculate total pixels
824:        height, width = img_array.shape
825:        total_pixels = height * width
826:
827:        # Count pixels Total Penumbra
828:
829:        # Determine the range for counting the penumbra above the darkest pixel
830:        penumbra_above_range = avg_column[darkest_pixel_index:]
831:
832:        # Calculate the penumbra above the darkest pixel within the specified range
833:        penumbra_above = np.sum((penumbra_above_range > denormalised_end_y_above + 1) & (penumbra_above_range <=
denormalised_start_y_above))
834:
835:        # Determine the range for counting the penumbra below the darkest pixel
836:        penumbra_below_range = avg_column[darkest_pixel_index:]
837:
838:        # Calculate the penumbra above the darkest pixel within the specified range
839:        penumbra_below = np.sum((penumbra_below_range > denormalised_end_y_below + 1) & (penumbra_below_range <=
denormalised_start_y_below))
840:
841:        total_length_penumbra = penumbra_above + penumbra_below
842:
843:        # Count pixels in only penumbra
844:        darkest_pixel_index = np.argmin(avg_column)
845:
846:        # Determine the range for counting the penumbra above the darkest pixel
847:        penumbra_only_above_range = avg_column[darkest_pixel_index:]
848:
```

```
849:        # Calculate the penumbra above the darkest pixel within the specified range
850:        penumbra_only_above = np.sum((penumbra_only_above_range > avg_column[darkest_pixel_index]) &
(penumbra_only_above_range <= denormalised_start_y_above))
851:
852:        # Determine the range for counting the penumbra below the darkest pixel
853:        penumbra_only_below_range = avg_column[darkest_pixel_index:]
854:
855:        # Calculate the penumbra below the darkest pixel within the specified range
856:        penumbra_only_below = np.sum((penumbra_only_below_range > avg_column[darkest_pixel_index]) &
(penumbra_only_below_range <= denormalised_start_y_below))
857:
858:        penumbra_only_value = penumbra_only_above + penumbra_only_below
859:        percentage_penumbra_only = penumbra_only_value / total_length_image_100 * 100
860:
861:
862:        # Count pixels in umbra
863:
864:        # Determine the range for counting the penumbra above the darkest pixel
865:        umbra_above_range = avg_column[darkest_pixel_index::-1]
866:
867:        # Calculate the penumbra above the darkest pixel within the specified range
868:        umbra_above = np.sum((umbra_above_range > avg_column[darkest_pixel_index]) & (umbra_above_range <=
denormalised_end_y_above))
869:
870:        # Determine the range for counting the penumbra below the darkest pixel
871:        umbra_below_range = avg_column[darkest_pixel_index:]
872:
873:    # Calculate the penumbra below the darkest pixel within the specified range
874:        umbra_below = np.sum((umbra_below_range > avg_column[darkest_pixel_index]) & (umbra_below_range <=
denormalised_end_y_below))
875:
876:        total_length_umbra = umbra_below + umbra_above
877:
878:
879:        # Total penumbra percentage
880:        Total_penumbra_percentage = total_length_penumbra / total_length_image_100 * 100
881:
882:        # Calculate Total umbra %
883:        total_umbra_percentage = total_length_umbra / total_length_image_100 * 100
884:
885:        # Find the index of the whole number rounded value of Denormalised_End_Y from the top
886:        umbra_boundary_index_top = np.where(avg_column <= np.round(denormalised_end_y_above))[0][-1]
887:
888:        # Find the index of the whole number rounded value of Denormalised_Start_Y from the top
889:        penumbra_boundary_index_top = np.where(avg_column <= np.round(denormalised_start_y_above))[0][-1]
890:
891:        # Reverse the array to find indices from the top
892:        avg_column_reversed = avg_column[::-1]
893:
894:        # Find the index of the whole number rounded value of Denormalised_End_Y from the bottom
895:        umbra_boundary_index_bottom = len(avg_column) - np.where(avg_column_reversed <=
np.round(denormalised_end_y_above))[0][-1]
896:
897:        # Find the index of the whole number rounded value of Denormalised_Start_Y from the bottom
898:        penumbra_boundary_index_bottom = len(avg_column) - np.where(avg_column_reversed <=
np.round(denormalised_start_y_above))[0][-1]
899:
900:
901:        def debug_log(message):
902:            with open("debug_log.txt", "a") as f:
903:                f.write(f"{message}\n")
904:
905:        # Determine whether to show only Penumbra or both Umbra and Penumbra boundaries
906:        umbra_value_limit = np.min(avg_column)
907:        if abs(umbra_value_limit - denormalised_end_y_above) <= 2 or abs(umbra_value_limit - denormalised_end_y_below)
<= 2 :
908:            show_umbra = False
909:            only_penumbra_present = 1
910:
911:        else:
912:            show_umbra = True
913:            only_penumbra_present = 0
914:
915:        if only_penumbra_present == 1:
```

```
            filtered_pixels = [pixel for pixel in avg_column if pixel <= max(denormalised_start_y_below, denormalised_start_y_above)]
            if not filtered_pixels:
                average_penumbra_intensity = 0  # Safe fallback
                debug_log("Filtered pixels empty; setting average_penumbra_intensity to 0")
            else:
                average_penumbra_intensity = np.mean(filtered_pixels)
        else:
            average_penumbra_intensity = 0  # Default to zero


        if only_penumbra_present == 1:
            shadow_type_label.config(text="Detected: Penumbra only")
        else:
            shadow_type_label.config(text="Detected: Umbra & Penumbra")

            debug_log(f"Processing image: {image_path}")
            debug_log(f"Darkest pixel index: {darkest_pixel_index}")
            debug_log(f"Selected pixels size: {len(selected_pixels)}")
            debug_log(f"Normalised data size: {len(normalised_data)}")
            debug_log(f"Params above: {params_above}, Params below: {params_below}")
            debug_log(f"Penumbra only value: {penumbra_only_value}")
            debug_log(f"Total pixels: {total_pixels}, Percentage penumbra only: {percentage_penumbra_only}")

            debug_log(f"Threshold for penumbra only: {denormalised_start_y_above}, {denormalised_start_y_below}")
        if abs(denormalised_start_y_above - avg_column[darkest_pixel_index]) < 1e-6:
            debug_log("Threshold for penumbra only appears to be zero or too close to the darkest pixel intensity.")


        # Calculate the normalised percentage for the average penumbra intensity value
        if only_penumbra_present == 0:
            normalised_percentage_average_penumbra = 'N/A'
        elif only_penumbra_present == 1:
            # Normalise the average penumbra intensity value
            normalised_average_penumbra = (average_penumbra_intensity / 255) * 100
            normalised_percentage_average_penumbra = normalised_average_penumbra
        else:
            raise ValueError("Invalid value for Only_penumbra_present")

         # Calculating the Umbra intensity

        umbra_intensity = ((denormalised_end_y_above + umbra_value_limit)/2)

        # Calculating the Penumbra Intensity

        penumbra_intensity = ((denormalised_start_y_above + denormalised_end_y_above)/2 + (denormalised_start_y_below + denormalised_end_y_below)/2)/2

        # Plot the data and the fitted curves with normalised y-axis
        plt.scatter(df['x'], df['y'], color='blue', label='Original Data')
        plt.plot(x_fit_above, y_fit_above, 'r--', label=f'Above Darkest Pixel\nk = {params_above[1]:.4f}')
        plt.plot(x_fit_below, y_fit_below, 'g--', label=f'Below Darkest Pixel\nk = {params_below[1]:.4f}')
        plt.xlabel('Distance (Pixels)')
        plt.ylabel(f'Normalised Y ({pixels_above_darkest}th above Darkest=0, Darkest=1)')
        plt.title('Normalised Data and Fitted Curves')

        # Scatter points for rapid increase and leveling off above the darkest pixel
        # Scatter point for the new "start" of the curve (from either side flat threshold)
        plt.scatter(rapid_increase_start_above, rapid_increase_start_y_above, color='red', marker='o',
                    label=f'Rapid Increase Start Above\nY = {rapid_increase_start_y_above:.4f}')
        plt.scatter(rapid_increase_end_above, y_fit_above[rapid_increase_end_index_above], color='purple', marker='o',
                    label=f'Rapid Increase End Above\nY = {y_fit_above[rapid_increase_end_index_above]:.4f}')

        plt.scatter(rapid_increase_start_below, rapid_increase_start_y_below, color='orange', marker='o',
                    label=f'Rapid Increase Start Below\nY = {rapid_increase_start_y_below:.4f}')
        plt.scatter(rapid_increase_end_below, y_fit_below[rapid_increase_end_index_below], color='yellow', marker='o',
                    label=f'Rapid Increase End Below\nY = {y_fit_below[rapid_increase_end_index_below]:.4f}')


        plt.legend(loc='upper left', bbox_to_anchor=(1, 1))
        # Save the plot with a fixed aspect ratio
        plt.savefig(os.path.join(desktop_path, f"Fitted_Curve_{os.path.basename(image_path)}.png"), bbox_inches='tight', pad_inches=0.1)
        plt.close()

```

```
        # Create an image for single averaged pixel column
        plt.imshow(np.expand_dims(avg_column, axis=1), cmap='grey', aspect='auto', vmin=0, vmax=255)
        plt.xlabel('Averaged Pixel Column')
        plt.ylabel('Pixel Length (pixels)')
        plt.title('Averaged Pixel Column')
        if show_umbra:
            plt.axhline(y=umbra_boundary_index_top, color='r', linestyle='-', linewidth=0.5, label='Umbra Boundary')
            plt.axhline(y=penumbra_boundary_index_top, color='b', linestyle='-', linewidth=0.5, label='Penumbra Boundary')
            plt.axhline(y=umbra_boundary_index_bottom, color='r', linestyle='-', linewidth=0.5)
            plt.axhline(y=penumbra_boundary_index_bottom, color='b', linestyle='-', linewidth=0.5)
            plt.text(1.1, 0.5, f'Total Penumbra %: {total_length_penumbra / total_length_image_100 * 100:.2f}\nTotal Umbra %: {total_umbra_percentage:.2f}', transform=plt.gca().transAxes, bbox=dict(facecolor='white', alpha=0.5))
        else:
            plt.axhline(y=penumbra_boundary_index_top, color='r', linestyle='-', linewidth=0.5, label='penumbra Boundary')
            plt.axhline(y=penumbra_boundary_index_bottom, color='r', linestyle='-', linewidth=0.5)
            plt.text(1.1, 0.5, f'Penumbra Only %: {percentage_penumbra_only:.2f}', transform=plt.gca().transAxes, bbox=dict(facecolor='white', alpha=0.5))
        plt.legend(bbox_to_anchor=(1.05, 1), loc='upper left')
        plt.gca().xaxis.set_tick_params(width=0.1)
        plt.savefig(os.path.join(desktop_path, f"Averaged_Pixel_Column_{os.path.basename(image_path)}.png"), bbox_inches='tight', pad_inches=0.1)
        plt.close()

        return (rapid_increase_start_above, rapid_increase_end_above,
                rapid_increase_start_below, rapid_increase_end_below,
                denormalised_start_y_above, denormalised_end_y_above, denormalised_start_y_below, denormalised_end_y_below,
                umbra_value_limit, penumbra_only_value, total_pixels, percentage_penumbra_only, total_length_image_100, total_length_penumbra, Total_penumbra_percentage, total_length_umbra,
                total_umbra_percentage, umbra_intensity, penumbra_intensity, average_penumbra_intensity,normalised_percentage_average_penumbra, only_penumbra_present)

    # Define the path to the desktop directory
    desktop_path = os.path.join(os.path.expanduser("~"), "Desktop", "Normalised_Plots_20.02.24")


    # Create the directory
    os.makedirs(desktop_path, exist_ok=True)

    # Define the DataFrame to store the results
    results_df = pd.DataFrame(columns=['Image', 'Rapid_Increase_Start_Above', 'Rapid_Increase_End_Above',
                                       'Rapid_Increase_Start_Below', 'Rapid_Increase_End_Below',
                                       'Denormalised_Start_Y_Above', 'Denormalised_End_Y_Above',
                                       'Denormalised_Start_Y_Below', 'Denormalised_End_Y_Below',
                                       'Umbra_Value_Limit', 'Denormalised_Start_Y', 'Denormalised_End_Y',
                                       'Penumbra_Only_Value', 'Total_Pixels', 'Percentage_Penumbra_Only',
                                       'Total_length_of_Image_100', 'Total_length_of_penumbra',
                                       'Total_penumbra_percentage', 'Total_length_of_umbra',
                                       'Total_umbra_percentage', 'umbra_intensity', 'penumbra_intensity', 'average_penumbra_intensity', 'normalised_percentage_average_penumbra', 'Only_penumbra_present'])

    results_df.replace(['N/A', None], np.nan, inplace=True)
    results_df = results_df.fillna(0)

    # Define an empty list to store the results
    results_list = []

    # For each image, calculate and store the necessary values
    for image_path in image_paths:
        # Call create_guide_plot_dual function
        (rapid_increase_start_above, rapid_increase_end_above,
        rapid_increase_start_below, rapid_increase_end_below,
        denormalised_start_y_above, denormalised_end_y_above, denormalised_start_y_below, denormalised_end_y_below,
        umbra_value_limit, penumbra_only_value, total_pixels, percentage_penumbra_only, total_length_image_100, total_length_penumbra,
        Total_penumbra_percentage, total_length_umbra, total_umbra_percentage, umbra_intensity, penumbra_intensity, average_penumbra_intensity, normalised_percentage_average_penumbra, only_penumbra_present) = create_guide_plot_dual(image_path, pixels_above_darkest=5000)

        # Append the values to the results list as a dictionary
        results_list.append({'Image': os.path.basename(image_path),
                             'Rapid_Increase_Start_Above': rapid_increase_start_above,
                             'Rapid_Increase_End_Above': rapid_increase_end_above,
                             'Rapid_Increase_Start_Below': rapid_increase_start_below,
                             'Rapid_Increase_End_Below': rapid_increase_end_below,
```

```
                    'Denormalised_Start_Y_Above': denormalised_start_y_above,
                    'Denormalised_End_Y_Above': denormalised_end_y_above,
                    'Denormalised_Start_Y_Below': denormalised_start_y_below,
                    'Denormalised_End_Y_Below': denormalised_end_y_below,
                    'Umbra_Value_Limit': umbra_value_limit,
                    'Penumbra_Only_Value': penumbra_only_value,
                    'Total_Pixels': total_pixels,
                    'Percentage_Penumbra_Only': percentage_penumbra_only,
                    'Total_length_of_Image_100': total_length_image_100,
                    'Total_length_of_penumbra': total_length_penumbra,
                    'Total_penumbra_percentage': Total_penumbra_percentage,
                    'Total_length_of_umbra': total_length_umbra,
                    'Total_umbra_percentage': total_umbra_percentage,
                    'umbra_intensity': umbra_intensity,
                    'penumbra_intensity': penumbra_intensity,
                    'Average Penumbra Only Intensity Value': average_penumbra_intensity,
                    'Normalised % Average Penumbra Only Intensity Value': normalised_percentage_average_penumbra,
                    'Only_penumbra_present': only_penumbra_present})

    # Convert the list of dictionaries into a DataFrame
    results_df = pd.DataFrame(results_list)

    # Save the DataFrame to Excel
    results_excel_path = os.path.join(desktop_path, "Normalised_Plots_Results.xlsx")
    results_df.to_excel(results_excel_path, index=False)

    # Footer logo at the bottom of Frame 3

    logo_label = tk.Label(frame3, image=logo_image_tk, anchor="center", bg="#FFFFFF")  # White background for the
label
    logo_label.image = logo_image_tk
    logo_label.pack(side=tk.BOTTOM, pady=10)


# -------- Frame 2: Post PV Installation --------

    # Function to train the Random Forest model
    # Paths to resources
    excel_path2 = "Training data.xlsx"
    image_path2 = "PV scene frame.png"

    # Load and train the model
    def train_random_forest2(excel_path):
        try:
            df = pd.read_excel(excel_path)
            X = df[['Distance', 'Thickness']]
            y = df[['Total_umbra_percentage', 'Umbra_Intensity', 'Total_penumbra_percentage', 'Penumbra_Intensity',
'Power_Loss']]
            rf_model = RandomForestRegressor(n_estimators=100, random_state=42)
            rf_model.fit(X, y)
            return rf_model
        except Exception as e:
            messagebox.showerror("Error", f"Failed to load data or train the model: {str(e)}")
            return None

    rf_model_2 = train_random_forest2(excel_path2)

    print("Feature importances:", rf_model_2.feature_importances_)


    # -------- Create Shadow Factor Input Function --------


    def train_power_loss_model_scaled_area(df):
        # Reference panel area
        ref_area = 125 * 31  # mm²

        # Scale umbra/penumbra % to mm² using reference area
        df["Scaled_Umbra"] = df["Total_umbra_percentage"] / 100 * ref_area
        df["Scaled_Penumbra"] = df["Total_penumbra_percentage"] / 100 * ref_area

        # Inputs: scaled area in mm² + intensities
        X = df[["Scaled_Umbra", "Umbra_Intensity", "Scaled_Penumbra", "Penumbra_Intensity"]]
        y = df["Power_Loss"]

```

```
1126:       model = RandomForestRegressor(n_estimators=100, random_state=42)
1127:       model.fit(X, y)
1128:       return model
1129:
1130:   # Train second model using the same Excel data
1131:   rf_model_powerloss = train_power_loss_model_scaled_area(pd.read_excel(excel_path2))
1132:
1133:
1134:   # -------- Create Shadow Factor Input Function --------
1135:   # Load the image to calculate aspect ratio
1136:   img2 = mpimg.imread(image_path2)
1137:   img2_height, img2_width, _ = img2.shape
1138:   aspect_ratio = img2_width / img2_height
1139:
1140:   # Matplotlib figure and axis
1141:   # Adjust the Matplotlib figure size to reduce vertical space
1142:   fig = Figure(figsize=(5, 4 / aspect_ratio), dpi=100)
1143:   ax = fig.add_subplot(111)
1144:
1145:   # Display the image as the background
1146:   ax.imshow(img2, extent=[0, 1000, -300, 500], aspect='auto')
1147:
1148:   # Set up graph limits
1149:   ax.set_xlim(0, 1000)
1150:   ax.set_ylim(-250, 550)
1151:   ax.set_title("Adjustable Line with Thickness and Shadow")
1152:   ax.set_ylabel("Distance from object (cm)")
1153:
1154:   # y-axis ticks to increments of 25 cm
1155:   y_ticks = list(range(0, 551, 25))
1156:   y_labels = [f"{val}" if 0 <= val <= 500 else "" for val in y_ticks]
1157:   ax.set_yticks(y_ticks)
1158:   ax.set_yticklabels(y_labels)
1159:
1160:   # Remove x-axis labels entirely
1161:   ax.set_xticks([])
1162:
1163:   # Plot the initial horizontal red line
1164:   x = [0, 1000]
1165:   y = [0, 0]
1166:   line, = ax.plot(x, y, 'r-', linewidth=2, label="Thin Object")
1167:
1168:   # Add the shadow lines
1169:   shadow_initial_y = -200
1170:   shadow_center_line, = ax.plot(x, [shadow_initial_y, shadow_initial_y], 'k-', linewidth=6, label="Shadow Center")
1171:   shadow_top_line, = ax.plot(x, [shadow_initial_y + 5, shadow_initial_y + 5], 'grey', linewidth=2, label="Shadow Top")
1172:   shadow_bottom_line, = ax.plot(x, [shadow_initial_y - 5, shadow_initial_y - 5], 'grey', linewidth=2, label="Shadow
Bottom")
1173:
1174:   # Add a label for the shadow line
1175:   shadow_label = ax.text(
1176:       0, shadow_initial_y + 10, "Shadow", color="black", fontsize=10, ha="left", va="center",
1177:       bbox=dict(facecolor="white", edgecolor="black", boxstyle="round,pad=0.3")
1178:   )
1179:
1180:   # Add a dynamic label for thickness
1181:   thickness_label = ax.text(
1182:       500, -80, "Thin object thickness: 2 mm", color="black", fontsize=10, ha="center", va="center",
1183:       bbox=dict(facecolor="white", edgecolor="black", boxstyle="round,pad=0.3")
1184:   )
1185:
1186:   # Embed the Matplotlib figure into Tkinter
1187:   canvas = FigureCanvasTkAgg(fig, master=frame2)
1188:   canvas_widget = canvas.get_tk_widget()
1189:   canvas_widget.pack(side="left", fill="both", expand=True)
1190:
1191:   # Add a note above the Distancea label
1192:   note_label = tk.Label(frame2, text="Input Variable Factors:", bg="#FFFFFF", fg="#000000", font=("Arial", 14,
"bold"))  # White background, black italic text
1193:   note_label.pack(pady=5, anchor="w")
1194:
1195:       # Create a frame for number inputs
1196:   input_frame = tk.Frame(frame2, bg="#FFFFFF", padx=5, pady=5)
1197:   input_frame.pack(side="right", fill="y", expand=False)
1198:
```

```
    # Create a new frame to hold both distance and thickness inputs side by side
dt_frame = tk.Frame(input_frame, bg="#FFFFFF")
dt_frame.pack(pady=5, anchor="w")
# --- Solar Cell Size Inputs (now placed after Distance and Thickness) ---
solar_cell_width = tk.StringVar()
solar_cell_length = tk.StringVar()

solar_cell_note = tk.Label(
    input_frame,
    text="Input Solar Cell Size (mm):",
    font=("Arial", 11, "bold"),
    bg="#FFFFFF",
    fg="black"
)
solar_cell_note.pack(anchor="w", pady=(10, 0))

solar_cell_frame = tk.Frame(input_frame, bg="#FFFFFF")
solar_cell_frame.pack(anchor="w", pady=5)

solar_cell_width_entry = tk.Entry(
    solar_cell_frame,
    textvariable=solar_cell_width,
    width=5,
    font=("Arial", 12),
    bg="#D3D3D3",
    fg="black",
    relief="flat"
)
solar_cell_width_entry.pack(side="left")

x_label = tk.Label(
    solar_cell_frame,
    text="x",
    font=("Arial", 12, "bold"),
    bg="#FFFFFF",
    fg="black"
)
x_label.pack(side="left", padx=5)

solar_cell_length_entry = tk.Entry(
    solar_cell_frame,
    textvariable=solar_cell_length,
    width=5,
    font=("Arial", 12),
    bg="#D3D3D3",
    fg="black",
    relief="flat"
)
solar_cell_length_entry.pack(side="left")


# Distance input
label_distancea = tk.Label(dt_frame, text="Distance (cm):", bg="#FFFFFF", fg="#000000")
label_distancea.pack(side="left", padx=(0, 5))

entry_distancea = tk.Entry(dt_frame, width=6, bg="#FFFFFF", fg="#000000", relief="solid")
entry_distancea.pack(side="left", padx=(0, 15))

# Thickness input
label_thicknessa = tk.Label(dt_frame, text="Thickness (mm):", bg="#FFFFFF", fg="#000000")
label_thicknessa.pack(side="left", padx=(0, 5))

entry_thicknessa = tk.Entry(dt_frame, width=6, bg="#FFFFFF", fg="#000000", relief="solid")
entry_thicknessa.pack(side="left")


def update_line_position(new_y, new_thickness):
    try:
        # Update graphical elements (apply changes logic)
        distancea_cm = float(entry_distancea.get())
        if -100 <= distancea_cm <= 400:
            new_y = distancea_cm
            line.set_ydata([new_y, new_y])
            shadow_y = -200 + ((new_y + 100) / 500) * 125
            shadow_center_line.set_ydata([shadow_y, shadow_y])
```

```
            shadow_top_line.set_ydata([shadow_y + 5, shadow_y + 5])
            shadow_bottom_line.set_ydata([shadow_y - 5, shadow_y - 5])
            shadow_label.set_y(shadow_y + 10)
            thickness_label.set_y(new_y + 20)
        else:
            messagebox.showerror("Input Error", "Distancea is out of range (-100 to 400 cm).")
            return
    except ValueError:
        messagebox.showerror("Input Error", "Invalid input for Distancea. Please enter a numeric value.")
        return

    try:
        thicknessa_mm = float(entry_thicknessa.get())
        if 2 <= thicknessa_mm <= 125:
            thin_linewidth = thicknessa_mm / 10.0
            line.set_linewidth(thin_linewidth)
            thickness_label.set_text(f"Thin object thickness: {int(thicknessa_mm)} mm")
        else:
            messagebox.showerror("Input Error", "Thicknessa is out of range (2 to 125 mm).")
            return
    except ValueError:
        messagebox.showerror("Input Error", "Invalid input for Thicknessa. Please enter a numeric value.")
        return

    canvas.draw()

def predict_factors():
    try:
        distancea_cm = float(entry_distancea.get())
        thicknessa_mm = float(entry_thicknessa.get())

        update_line_position(distancea_cm, thicknessa_mm)

        if rf_model_2 is None:
            messagebox.showerror("Error", "Model not trained.")
            return

        # Create input DataFrame
        input_data = pd.DataFrame([[distancea_cm, thicknessa_mm]], columns=["Distance", "Thickness"])
        predictions = rf_model_2.predict(input_data)[0]

        # Extract predictions
        predicted_umbra_percent = predictions[0]
        predicted_umbra_intensity = predictions[1]
        predicted_penumbra_percent = predictions[2]
        predicted_penumbra_intensity = predictions[3]

        # Fill GUI output entries
        prediction_outputs["Umbra Size"].delete(0, tk.END)
        prediction_outputs["Umbra Size"].insert(0, f"{predicted_umbra_percent:.2f}")

        prediction_outputs["Umbra Intensity"].delete(0, tk.END)
        prediction_outputs["Umbra Intensity"].insert(0, f"{int(round(predicted_umbra_intensity))}")

        prediction_outputs["Penumbra Size"].delete(0, tk.END)
        prediction_outputs["Penumbra Size"].insert(0, f"{predicted_penumbra_percent:.2f}")

        prediction_outputs["Penumbra Intensity"].delete(0, tk.END)
        prediction_outputs["Penumbra Intensity"].insert(0, f"{int(round(predicted_penumbra_intensity))}")

        # Automatically scale after predicting
        scale_shadow_size()

    except Exception as e:
        messagebox.showerror("Error", f"Prediction failed: {str(e)}")


def scale_shadow_size():
    try:
        # Get user solar cell dimensions
        user_width = float(solar_cell_width.get().strip())
        user_height = float(solar_cell_length.get().strip())

        if user_width <= 0 or user_height <= 0:
            messagebox.showerror("Input Error", "Solar cell dimensions must be greater than 0.")
```

```
            return

        ref_width = 125  # mm
        ref_height = 31  # mm
        ref_area = ref_width * ref_height

        # Get original umbra and penumbra % from model (based on 125x31mm)
        predicted_umbra_percent = float(prediction_outputs["Umbra Size"].get())
        predicted_penumbra_percent = float(prediction_outputs["Penumbra Size"].get())

        # Convert to mm²

        umbra_area_ref = (predicted_umbra_percent / 100) * ref_area
        penumbra_area_ref = (predicted_penumbra_percent / 100) * ref_area

        # New user panel area
        user_area = ref_width * user_height  # width is fixed to training setup

        # Scale shadow area against new total area
        umbra_scaled_percent = (umbra_area_ref / user_area) * 100
        penumbra_scaled_percent = (penumbra_area_ref / user_area) * 100

        # Update GUI
        prediction_outputs["Umbra Size"].delete(0, tk.END)
        prediction_outputs["Umbra Size"].insert(0, f"{umbra_scaled_percent:.2f}")

        prediction_outputs["Penumbra Size"].delete(0, tk.END)
        prediction_outputs["Penumbra Size"].insert(0, f"{penumbra_scaled_percent:.2f}")

        print("Ref area:", ref_area)
        print("User area:", user_width * user_height)
        print("Umbra area (ref):", umbra_area_ref)
        print("Scaled %:", umbra_scaled_percent)

    except Exception as e:
        messagebox.showerror("Scaling Error", f"Failed to scale shadow sizes: {str(e)}")


def predict_power_loss2():
    try:
        # Get scaled percentage values from GUI (already rescaled for display)
        scaled_umbra_percent = float(prediction_outputs["Umbra Size"].get())
        scaled_penumbra_percent = float(prediction_outputs["Penumbra Size"].get())
        umbra_intensity = float(prediction_outputs["Umbra Intensity"].get())
        penumbra_intensity = float(prediction_outputs["Penumbra Intensity"].get())

        # Use fixed reference area (same as used in training)
        ref_area = 125 * 31  # mm²

        # Convert scaled percentages back to mm² based on reference panel (not user panel)
        umbra_mm2 = (scaled_umbra_percent / 100) * ref_area
        penumbra_mm2 = (scaled_penumbra_percent / 100) * ref_area

        # Prepare input for prediction
        input_df = pd.DataFrame([[umbra_mm2, umbra_intensity, penumbra_mm2, penumbra_intensity]],
                                columns=["Scaled_Umbra", "Umbra_Intensity", "Scaled_Penumbra", "Penumbra_Intensity"])

        # Predict power loss
        predicted_loss = rf_model_powerloss.predict(input_df)[0]

        # Update the Power Loss field
        prediction_outputs["Power Loss"].delete(0, tk.END)
        prediction_outputs["Power Loss"].insert(0, f"{predicted_loss:.2f}")

    except Exception as e:
        messagebox.showerror("Prediction Error", f"Failed to predict power loss: {str(e)}")

# Initialize the dictionary to store output entries
prediction_outputs = {}

 # Create a frame for prediction outputs
output_frame = tk.Frame(input_frame, bg="#FFFFFF", padx=5, pady=5)  # Create a nested frame for better spacing
output_frame.pack(fill="both", expand=True, pady=10)

# Add labels and styled entry fields with units
```

```
    for label_text in ["Umbra Size", "Umbra Intensity", "Penumbra Size", "Penumbra Intensity", "Power Loss"]:

        if label_text == "Power Loss":

            # --- Predicted Factors ---
            predict_and_apply_button = tk.Button(
                output_frame,
                text="Predicted Factors",
                command=predict_factors,
                bg="#696969",
                fg="#000000",
                activebackground="#505050",
                activeforeground="#FFFFFF",
                font=("Arial", 12, "bold"),
                relief="raised",
                bd=3,
                padx=10,
                pady=5
            )
            predict_and_apply_button.pack(pady=(10, 5), fill="x")

            predict_and_apply_button = tk.Button(
                output_frame,
                text="Predicted Power Loss",
                command=predict_power_loss2,  # ← New function
                bg="#696969",
                fg="#000000",
                activebackground="#505050",
                activeforeground="#FFFFFF",
                font=("Arial", 12, "bold"),
                relief="raised",
                bd=3,
                padx=10,
                pady=5
            )
            predict_and_apply_button.pack(pady=(10, 5), fill="x")

        # Create a row for each label and entry
        row_bg = "#FFFFFF"  # Default row background
        label_fg = "#000000"  # Default label text color
        entry_bg = "#F0F0F0"  # Default entry background
        entry_fg = "#000000"  # Default entry text color
        unit_fg = "#000000"   # Default unit text color

        if label_text == "Power Loss":
            # Set vibrant green for Power Loss row
            row_bg = "#32CD32"  # Vibrant lime green
            label_fg = "#FFFFFF"
            entry_bg = "#90EE90"
            entry_fg = "#006400"
            unit_fg = "#FFFFFF"

        row_frame = tk.Frame(output_frame, bg=row_bg, pady=5)
        row_frame.pack(fill="x", pady=5)

        label = tk.Label(
            row_frame,
            text=f"{label_text}:",
            bg=row_bg,
            fg=label_fg,
            font=("Arial", 12, "bold"),
            anchor="w",
            width=16
        )
        label.pack(side="left", padx=5)

        entry = tk.Entry(
            row_frame,
            width=6,
            bg=entry_bg,
            fg=entry_fg,
            relief="groove",
            font=("Arial", 12)
        )
        entry.pack(side="left", padx=5)
```

```
1499:
1500:     if label_text == "Umbra Intensity" or label_text == "Penumbra Intensity":
1501:         unit_label = tk.Label(
1502:             row_frame,
1503:             text="Pixel Intensity Value \n 0 = Black 255 = White",
1504:             bg=row_bg,
1505:             fg=unit_fg,
1506:             font=("Arial", 10, "bold")
1507:         )
1508:         unit_label.pack(side="left", padx=5)
1509:
1510:     if label_text == "Umbra Size" or label_text == "Penumbra Size":
1511:         unit_label = tk.Label(
1512:             row_frame,
1513:             text="% of total solar cell size",
1514:             bg=row_bg,
1515:             fg=unit_fg,
1516:             font=("Arial", 10, "bold")
1517:         )
1518:         unit_label.pack(side="left", padx=5)
1519:
1520:     if label_text == "Power Loss":
1521:         unit_label = tk.Label(
1522:             row_frame,
1523:             text="%",
1524:             bg=row_bg,
1525:             fg=unit_fg,
1526:             font=("Arial", 10, "bold")
1527:         )
1528:         unit_label.pack(side="left", padx=5)
1529:
1530:     prediction_outputs[label_text] = entry
1531:
1532: # Back to Main Menu button
1533: def back_to_main_menu():
1534:     try:
1535:         # function linked to raise frame1
1536:         show_frame(frame1)
1537:     except Exception as e:
1538:         print(f"Error: {e}")  # Debugging aid to catch any issues
1539:
1540: # Back to Main Menu button
1541: input_frame = tk.Frame(frame2, bg="#FFFFFF", padx=5, pady=5)
1542: input_frame.pack(side="right", fill="y", expand=False)
1543:
1544: # Add the Back to Main Menu button below the Power Loss label
1545: back_button = tk.Button(
1546:     output_frame,
1547:     text="Back to Main Menu",
1548:     command=lambda: show_frame(frame1),  # Replace frame1 with your actual main menu frame
1549:     bg="#696969",  # Dark grey background
1550:     fg="#000000",  # White text for contrast
1551:     activebackground="#505050",  # Slightly darker grey when pressed
1552:     activeforeground="#FFFFFF",  # Keep text white when pressed
1553:     font=("Arial", 12, "bold"),  # Bold font for emphasis
1554:     relief="raised",  # Raised style for 3D effect
1555:     bd=3,  # Border thickness for tactile appearance
1556:     padx=20,  # Add horizontal padding
1557:     pady=20    # Add vertical padding
1558: )
1559: back_button.pack(pady=10, fill="x")  # Ensure proper spacing below the output labels
1560:
1561:     # note below the Back to Main Menu button
1562: info_label = tk.Label(
1563:     output_frame,
1564:     text="Advice: If the thin object causes significant power loss \nby shading the PV module, reposition or remove it.",
1565:     bg="#FFFFFF",  # Match the frame's background
1566:     fg="#000000",  # Red text for emphasis
1567:     font=("Arial", 12, "bold"),  # Slightly smaller bold font
1568:     anchor="center"  # Center align the text
1569: )
1570: info_label.pack(pady=10, fill="x")  # Add padding below the note
1571:
1572:
1573: # Function to load and resize the logo image
```

```
    def load_logo():
        global resized_logo_tk

        try:
            # Specify the path to the logo
            logo_path = "ISE Logo.png"

            # Load the logo image using Pillow
            original_logo = Image.open(logo_path)

            # Resize the logo to desired dimensions (e.g., 300x100 pixels)
            resized_logo = original_logo.resize((300, 100))

            # Convert the resized image to a format usable by Tkinter
            resized_logo_tk = ImageTk.PhotoImage(resized_logo)
        except Exception as e:
            print(f"Error loading or resizing logo: {e}")
            resized_logo_tk = None

        # Add the logo to the bottom-right corner of frame2
        if resized_logo_tk:
            logo_label = tk.Label(
                frame2,
                image=resized_logo_tk,
                bg="#FFFFFF"  # Match the frame's background color
            )
            logo_label.image = resized_logo_tk  # Prevent garbage collection
            # position closer to the note
            logo_label.place(relx=0.98, rely=0.87, anchor="se")  # Lift the logo closer to the note

    # Call the function after initializing frame2
    load_logo()

    # Run the app
    root.mainloop()

create_gui()
```

Appendix H - Other Supporting Scripts Used in this Thesis

Apart from the CSF Score generator and ThinShadePV scripts, the following scripts were used for various parts of this thesis. Each supporting script outlined below can be accessed via the GitHub repository in: **https://github.com/mattaxi/PhD-Supporting-scripts**

These custom scripts where instrumental for the methodology and data analyses of the following parts of this thesis:

Chapter	Script Name	Description
4 & 5	Sunpath Generator 2024. py	A custom-built sun path generator was developed to determine the solar altitude angle at specific geographic coordinates, in this case, for Malta. The basis of the tool was determined from the explanation conducted in Chapter 2 Section 2.1.2. This script played a critical role in the data analysis process by enabling the calculation of a sun path correction factor. This factor adjusts the measured power loss from the PV module to a common reference time of day, thereby allowing consistent comparison of shading impact under varying solar positions. Once the altitude angle was retrieved for different times of the day, the corresponding correction factor was applied to compensate for the effect of the sun's changing position.
4 & 6	Image to pixel.py	An image-to-pixel processing script was developed to facilitate the conversion of standard RGB images into analysable greyscale data. Initially, each RGB image was transformed into an 8-bit greyscale image, reducing the colour information to a single intensity channel. This conversion allowed each pixel to be represented by a value ranging from 0 (black) to 255 (white), corresponding to its intensity. This process was fundamental for quantifying shadow formations in the images used throughout the study. By extracting pixel intensity values, it became possible to measure the relative darkness of each shadow cast on the PV module surface. These intensity metrics were subsequently used to assess the correlation between shadow characteristics and PV performance degradation

4	Image to histogram.py	To analyse the shadow formation patterns produced by 54 individual thin object shadow cases demonstrated in Chapter 4, a systematic image-to-histogram conversion approach was employed. Each captured image of a shadow was processed to generate a corresponding histogram, representing the distribution of pixel intensity values across the image. This visual and quantitative representation enabled the identification of irregularities in the shadow profiles, including inconsistencies in density and shape. More importantly, the histograms provided a clear means to the fringe effect, often characteristic of laboratory environment shadow behaviour.
4	Pixel distribution.py	Pixel distribution analysis supported the histogram method by highlighting anomalies or outliers in the shadow images. This ensured that any non-representative data, such as external dust depositions or lighting inconsistencies, were identified and excluded, preserving the accuracy of the shading analysis.
4 & 5	Intersect point of I-V curve with R_{Load}.py	Due to equipment constraints in not being able to generate an I-V curve in the outdoor environment, a fixed load point was used. To ensure comparability, the corresponding R_{load} was derived from the PV module's voltage and current characteristics. The intersection of this diagonal R_{load} with the I–V curve defined the operating power at that point. This approach enabled consistent comparison between laboratory and outdoor conditions and supported the validation presented in Chapter 4 and 5.
4	Heatmap generator.py	A heatmap generator was used to visualise variations in output power across a single solar cell. This method provided a clear representation of localised performance differences, enhancing the reader's understanding of power distribution across the 54 thin object shadow cases analysed.

5	Rotate image from diagonal.py	To ensure consistent shadow positioning, the horizontal shadow on the white reference surface was rotated until it was perfectly horizontal. This precise alignment maintained uniformity in shadow placement across all measurements.
5	Spearman Correlation Matrix.py	A Spearman correlation matrix was generated using Python to visualise the relationships between each parent variable and contributing factor, relative to the dependent variable, power loss. This provided insight into which variables most strongly influenced the power loss.
5	Creating Random Forest predictive model.py	The Random Forest algorithm was a key component of this thesis, enabling power loss prediction based on the size and intensity of both umbra and penumbra regions. As such predictive modelling is not feasible in Excel, Python was used to implement the algorithm. The model was integrated into the ThinShadePV script to produce a holistic analysis.